Residual stress measurements using the contour method

A thesis submitted to the University of Manchester for the degree of Ph.D.
in the Faculty of Engineering and Physical Sciences

2008

Gregory Johnson
School of Materials

Table of Contents

List of Figures

Abstract

Gregory Johnson / Residual stress measurements using the contour method

University of Manchester / 2008 / PhD

The aim of this dissertation is to explore and evaluate the contour method, a recently developed destructive technique for measuring residual stresses. It is a valuable addition to the suite of tools available to the researcher.

This work includes validation of the contour method against both the predictions of analytical models and measurements made by complementary techniques. The accuracy of the method has been evaluated, and a number of algorithms have been developed to facilitate the process of converting the raw measured data into stress maps.

A number of different aspects of the contour method have been explored. By way of introduction, a comparison has been performed between the analytical stresses expected in a bent bar, a numerical model of four point bending, and a physical bent bar measured with the contour method, which shows good agreement across the bulk of the sample. The contour method is then used to assess the claims of residual stress relief by cryogenic treatment in aluminium beams. The expected stress profile of a quenched beam is seen, but no significant reduction in stresses is effected by the cryogenic treatment.

The ability of the contour method, which requires the very precise cutting of the sample, to work with larger samples is examined by studying two inertia friction welds. These highlight both the importance of cutting technique and the ability of the contour method to accommodate poor quality source data if sufficient filtering is performed. Good agreement with neutron diffraction data is highlighted.

Linear friction welds are then examined to assess the effects of post weld heat treatment, and evaluate the ability of the contour method to resolve very high stress gradients. Comparisions with synchrotron diffraction data are made which reveal that limitations in the surface fitting algorithms and finite element mesh sizes can have adverse effects on the efficacy of the contour method.

Near the surface of a sample, contour method measurements are critically affected by measurement accuracy, data processing, and modelling fidelity. The laser shock peening of aluminium introduces near-surface compressive stresses, so is a natural case study for the contour method. Excellent agreement is found, even to depths as shallow as 100μm, with synchrotron diffraction measurements.

As a direct consequence of the work performed in this thesis, a flexible and easy-to-use toolkit of software routines has been developed over the course of this work with the express purpose of lowering the barrier to future researchers in using this technique.

Declaration & Copyright

No portion of the work referred to in this thesis has been submitted in support of an application for another degree or qualification in this or any other university or other institute of learning.

Acknowledgements

I am truly indebted to so many people who helped me during the course of this work. They made my life tolerable when it might have been barely so, enjoyable when it might have been blasé, and a sheer delight when it might have simply been nice. Thank you, all of you.

In particular, and by geography:

America

Well, thanks are of course due to Mike Prime, source of much contour inspiration and conversation. Also *grimpeur extraordinaire* - didn't I do a good Evel Knievel impression? Let's do it right some day...

St Andrews

Duncan Robertson educated me in the Scottish spirit, and encouraged me in the months when the distance to Manchester seemed a curse. Tee Gatewood prescribed adrenalin and endorphins as the drugs to remedy ennui, and the doctor was correct. Thanks for the friendship. Paul Cruickshank for the umpteen croissants and lemon-curd yogurts. Alan, for the many occasions when you "left your wallet in the office", and the life-giving convos at the Whey Pat.

France

Wow, so many friends in France before we even arrived - a great gift.Thanks to Wolfgang, Linne, and the boys for the exciting domestic distractions. *Merci à Noëlle, Jean-Yves, Louise, et Clem pour l'hospitalité et l'amitié - le monstre de la couverture s'a échappé finalement. 2008 - vraiement...*

Canada

My Mum and Dad have been steadfast in their support, not least in the last four years. Thanks for all the opportunities.

Manchester

To Phil, my supervisor and boss - it's been a fun few years, and the way you treat we who work for you is a big part of that. Thanks for both the 'hands-off' time and the periods of intense scrutiny. I look forward to the next phase together! Sue Edwards, our antipodean secretary, who went far beyond the call of duty in helping me out. Latterly, Rachel, who became the Printing Queen. Mark - whom I educated on the contour method, and then was re-educated by in turn. Without men like Stuart Morse, nothing would get done in the world. Thanks for the patience and the help with the kit. Mallik, I never got you to Scotland - it would have been a small token of thanks for all the help you gave me. Laurent, we moved on to something new at the same time - but I hope we'll work and play together again. Andy. Where to begin? The hospitality and pleasure of cooking? The horrendous month in the lab? Experiments, matlab sessions, beers? It was all good. Let's do it all again sometime. Okay, not quite all... (and thanks for the pics). To Sam, particularly for your eagle-eye in these last few months. Alex, for not running away when I screamed, and the hospitality in Grenoble. Dan, those first years in Manchester, your home was a haven for me - thank you. Philipp - it's going to be my turn to do some favours. I'm sure you'd be justified in complaining by now! Matt, the 'secretary' - so many helping hands you gave. Richard - for numerous helping hands in the final stages. Chris, for errands and papers. Michael - spending time with you continues to be a pleasure, even after invading the Hotel Preuss on so many occasions. Long techinical talks that I forgot we had (but must have made an impression), cultural observations, eating together. I appreciate your friendship - and the great honour of Julian. The times I was thrashed by you on the squash court are not a pleasant memory, João, but I think all the others are! Your patience and encouragement has been so valuable - and the comments that kept me thinking about the big picture. And everyone else in E30 - it's been great to share the years with you!

The Boatie Rows and Pré Borel

Well, Kirstin. The end of a long road, but just part of the longer one. I'm happiest travelling with you, no matter the twists and turns. With my love and gratitude.

Dedication

For Kirstin.
You are a great Gift

take these shoes
click clacking down some dead end street
take these shoes
and make them fit
take this shirt
polyester white trash made in nowhere
take this shirt
and make it clean, clean
take this soul
stranded in some skin and bones
take this soul
and make it sing

YAHWEH, YAHWEH
always pain before a child is born
YAHWEH, YAHWEH
still I'm waiting for the dawn

"YAHWEH"
U2 2004

1 Introduction

The contour method is a recent technique for measuring the residual stresses normal to a cut surface. Invented by Prime in 2001, it consists of cutting a sample, measuring the distortion on that cut surface that arises due to stress relaxation, and calculating what stresses were present before cutting.

While the contour method is elegantly simple in concept, in practise the difficulties of execution appear to have contributed to its limited uptake outside Los Alamos National Laboratory, where it was invented. A number of other laboratories have made use of the contour method to evaluate residual stress fields, but none seem to have continued beyond the efforts of a single practitioner. Part of the reason for this is the combination of skills needed to apply this technique. The instrumentation requirements are modest and do not need to be in-house: access to a good wire-EDM facility and an appropriate surface measurement instrument, whether a conventional CMM or an optical profiler. However, there is a considerable amount of work needed to clean the point cloud measured, align and combine the two surface datasets, perform the surface fitting, and then integrate with a finite element modelling package to apply many thousands of different boundary conditions - a task not suited to manual editing.

There are two aims for the work presented in this dissertation. The first is to evaluate the efficacy of the contour method and develop it further in a number of different areas and applications: near-surface measurements, high gradient stress fields, sample size limitations, etc. It is hoped that this will contribute to the nascent community of contour method users and assist those deciding whether their application suits the technique. The second aim is to facilitate the technical deployment of the contour method. A website (http://pwlinda.mt.umist.ac.uk/contourmethod) has been created where the software tools developed over the

course of this project are available. These tools make it possible for the newcomer to the field to be able to start making contour method measurements quickly and easily. In fact, once the cutting and measurement have been done, the data processing and modelling can now be accomplished within a matter of hours.

1.1 Layout of dissertation

The next chapter contains an overview of residual stresses and surveys a number of techniques for measuring them. It concludes with a comparison of the relative merits of each. Chapter 3 is an introduction to the contour method itself, and both explains the basis of the technique as well as briefly discussing the work that has been done using this method. The technical details of the technique and the implementation of it by this author are shown through the examination of the classic four-point bent bar in Chapter 4.

Chapter 5 examines the claim of cryogenic 'stress relief' in quenched aluminium, dealing with a straightforward stress profiles that can be predicted analytically. Chapters 6 and 7 deal with friction welded samples, wherein large areas of low stress gradients are surrounded by small regions of very high stress gradients. The inertia friction welds examined in Chapter 6 test the ability of the contour method to deal with large cut surfaces. The linear friction weld results are also compared with synchrotron measurements.

To assess the efficacy of the contour method close to the surface of samples, the final application is to laser shock peened aluminium (Chapter 8). Comparisons of the contour method with synchrotron x-ray measurements are also made.

The dissertation is concluded in Chapter 9, where a summary of the results is made. Following this is the bibliography and the appendices, which contain the source code that was written over the period of this thesis in addition to a reference section on surface metrology and finite element analysis.

2 Residual Stresses and their measurement

The aim of this chapter is to outline the origin and nature of residual stresses in engineering components and to review a number of techniques for measuring them, both destructive and non-destructive. This brief discussion sets the context for introducing the newly developed contour method, in the following chapter.

2.1 Residual stresses

Residual stresses are those stresses that remain once a body is at rest and at equilibrium with its surroundings (without mechanical loading) (Withers 2001).

They may be broadly characterised, by the length scales over which the stress self-equilibrates, into three groups (Maserauch 1986) (shown schematically in Figure 2-1):

- Type I: vary over distances that are large relative to the microstructure of the material
- Type II: vary from grain to grain in the material
- Type III: vary within a single grain

All of these stresses are caused by misfits (Figure 2-2), whether of micro- or macro-structural dimensions.

Type I stresses, with which this thesis is concerned, are caused by many manufacturing processes such as forging, welding, casting, and rolling (see Figure 2-2 for some examples). They may be introduced during service by wear or damage, or introduced intentionally during processing. Tensile residual stresses are generally regarded as problematic, adversely affecting fatigue life and causing stress corro-

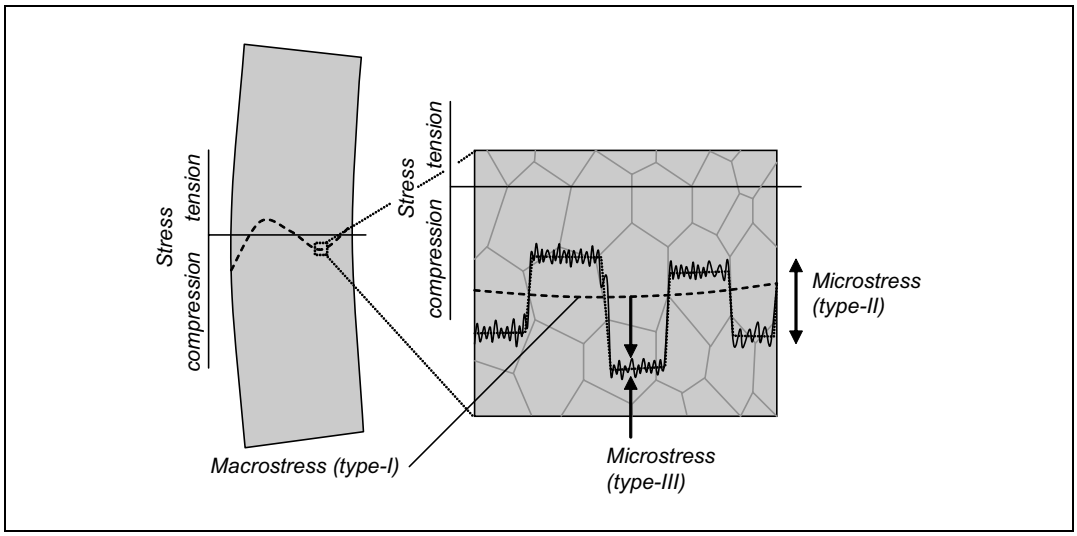

Figure 2-1. Type I, II, and III stresses differ on the length scale over which they self-equilibrate or balance. (courtesy King)

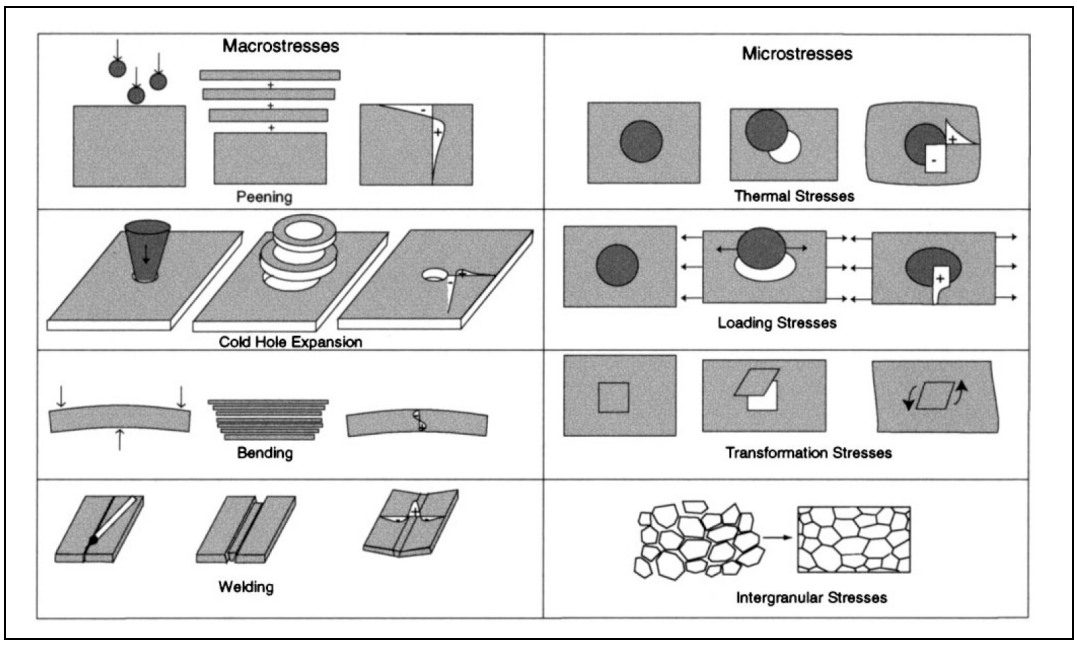

Figure 2-2. All residual stresses, whether macro, micro, or intergranular, are caused by misfits in the material. A number of different misfit-causing processes are shown. (courtesy Withers)

sion and crack propagation in materials (James 1996). Compressive stresses, on the other hand, can have a beneficial effect in these areas, by inhibiting crack nucleation and growth.

Residual stresses are difficult to predict because of their dependence on many manufacturing processes (and previous service life), so characterisation and mea-

surement are important. If unknown, they can cause failure when combined with applied stresses.

There are a large number of experimental methods for determining the residual stresses in an engineering component. These may be divided into destructive and non-destructive techniques, as discussed in the following sections.

2.2 Destructive techniques

In general terms, the destructive techniques operate by perturbing the state of equilibrium that exists in a body by cutting , and measuring the relaxation of stresses that occurs (James 1996). This measurement of strain (or displacement) is uniquely performed at some location remote from that of interest (by virtue of the destruction of that site) and then the stresses are back-calculated by some sort of inversion process, either numerical or analytical.

2.2.1 Hole drilling

The basic principle of this method is that by drilling a small hole in a sample the removal of material will permit stress relaxation around the hole. Measuring these lateral strains with a specially designed triple strain gauge rosette (Figure 2-3) per-

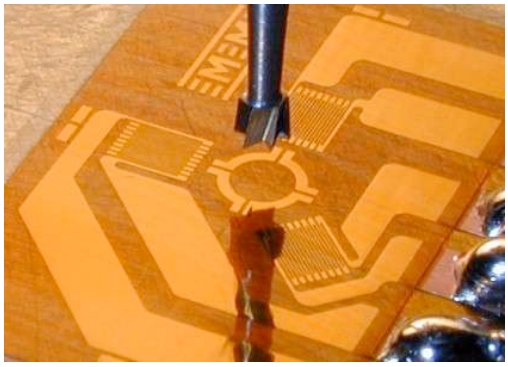

Figure 2-3. A typical strain gauge rosette as used in the hole drilling technique (courtesy Stresscraft)

mits an estimation of the in-plane stresses that were present in the drilled material from the measured strain relaxations (ε_1,ε_2,ε_3), using the formula:

$$\sigma_{\max},\ \sigma_{\min} = -\frac{E}{2}\left(\frac{\varepsilon_3+\varepsilon_1}{(1+\nu)\bar{a}} \mp \frac{\sqrt{(\varepsilon_3-\varepsilon_1)^2+(\varepsilon_3+\varepsilon_1-2\varepsilon_2)^2}}{\bar{b}}\right)$$

The values of $\bar{a}$ and $\bar{b}$ are geometrically determined and are tabulated for a number of different setups (Schajer 1988). This approach is used when the stress field is expected to be uniform with depth (ASTM E837 1999), but this is often not the case, particularly when surface treatments have been used. There are a number of non-uniform calculations available for these problems where the hole is drilled incrementally, and strains measured for each depth (Schajer 1988).

The method is considered as a 'semi-destructive' test, for although material is removed from the sample, the quantity is quite small, and repairs may be made to many samples without compromising their integrity.

As one would expect from a technique that is over 70 years old (described first by Mathar in 1934 (Mathar 1934)), there are a multiplicity of approaches, including different drilling techniques, calibration routines, and analysis tools. It is probably the most widely used residual stress determination method today (Schajer 1996), and has an ASTM standard in which are published the standard coefficients and parameters needed for calculations (ASTM E837 1999).

In a round-robin study (Grant 2002) eight UK laboratories performed hole drilling measurements and the results were compared. Each lab chose their preferred approach, which differed primarily in the analysis algorithm used (while there is a single approach for uniform stress measurements, there are a number of algorithms available when non-uniform stress fields are expected). The results, shown in Figure 2-4, show a variation of over 1100MPa. Clearly, a significant problem existed, and the authors of the study identified two key areas: experimental technique, and algorithm choice. Hole drilling can be quite sensitive to any eccentricity in the drilled hole (relative to the strain gauge rosette), and difficulties in alignment

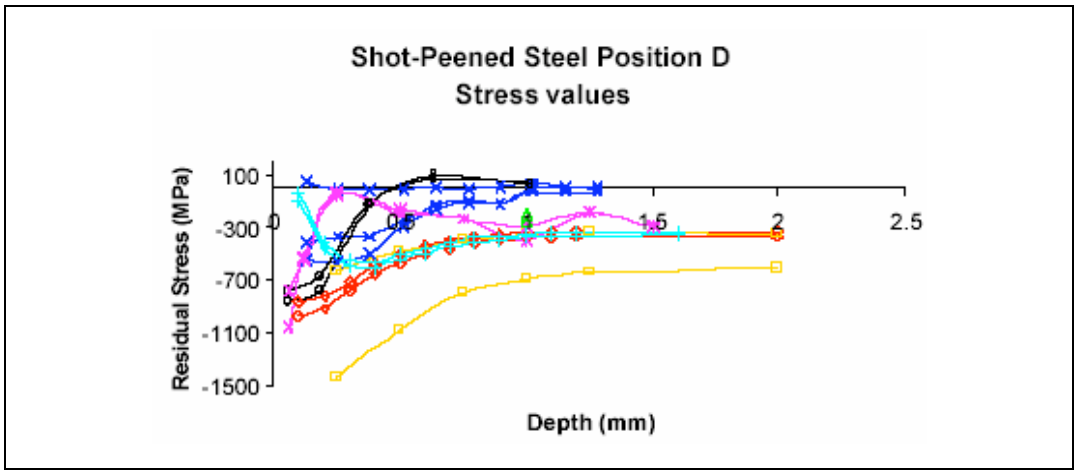

Figure 2-4. Results measured with the hole drilling technique for identical shot peened steel samples from eight UK laboratories. The results show considerable variation between different practitioners (courtesy NPL).

were responsible for some of the variation. However, the choice of algorithms poorly suited to non-uniform residual stress fields (the sample was a shot peened steel plate) also caused errors. A second stage of the round-robin prescribed some of the operator procedures and algorithm choices, and the results were significantly improved.

The strengths of this technique are its simplicity, common usage, and ability to be used in the field with standard equipment. However, it has a number of weaknesses: as seen in the round-robin results, the experience of the practitioner can have a large effect on the accuracy of the results. In addition, the hole itself causes a stress concentration that limits the stresses that can be measured to ~50% of the yield stress before plastic deformation occurs (Fathallah 1994). Hole drilling is also somewhat depth limited - it is a common rule of thumb that the diameter of the hole is equal to the maximum depth over which reliable results may be attained. This is due to the decreased sensitivity of the strain gauges mounted on the surface to stress relief at increasing depths.

Developments are continuing, and while most operators still use strain gauge rosettes to measure the strains around the hole, there is considerable interest in full field measurements, such as laser speckle interferometry (Li 1997) and moiré fringe techniques (Makino 1997),(Yin 2000). These lessen the requirements for

drilling accuracy, but due to the stability requirements are not suitable for measurements in the field.

2.2.2 Ring coring

A variation of the hole drilling technique is ring coring, where instead of strain gauges surrounding a centre hole, gauges are attached to the sample and a pedestal is created by trepanning around them (see Figure 2-5). While this is experimentally

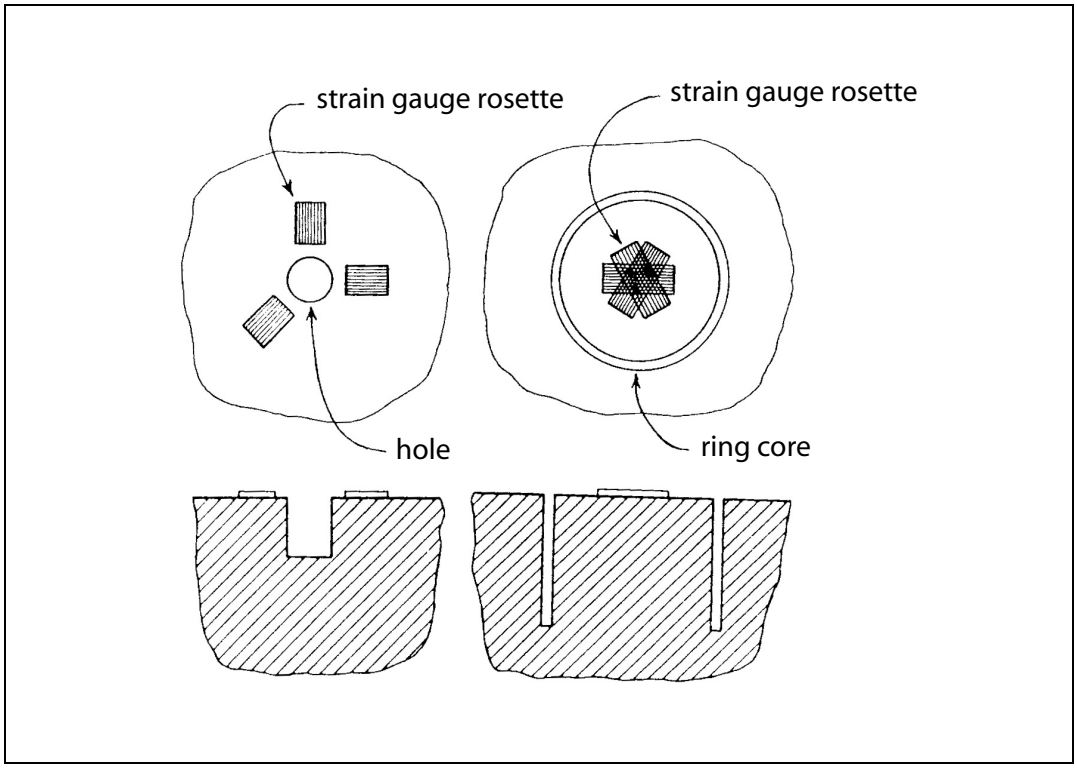

Figure 2-5. Schematic comparing hole drilling (left) and ring-coring (right). Stress relief in ring coring is complete and thus it can resolve stresses at greater depths than hole drilling. (courtesy Schajer1996)

much more difficult to perform successfully, the stress relief in the pedestal is complete and the depth limit is much larger than for hole drilling. There is a certain degree of experimental difficulty, however, as the strain gauges must be detached and reattached for every drilling increment (Schajer 1996).

2.2.3 Deep hole drilling

Deep hole drilling is a recent extension of the hole drilling principle, which permits the through-thickness measurement of stresses. First, a reference hole is drilled through the sample under examination. The diameter of this hole is then measured, both as a function of angular position, and of depth, using an air probe. Then a cylindrical core, coaxial to the hole, is trepanned, during which any axial extension of the central hole may be measured. After the core has been cut, the reference hole is measured again, and distortion radial to the hole is recorded. This permits the determination of residual stresses in a plane normal to the axis of the hole using elasticity solutions (Stefanescu 2004). The process is shown schematically in Figure 2-6.

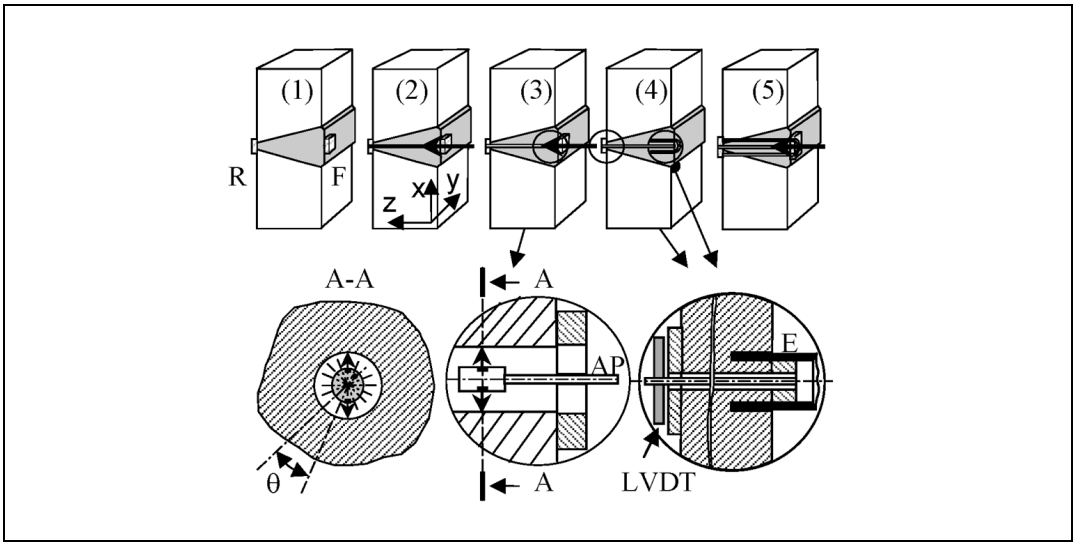

Figure 2-6. Schematic diagram of the DHD technique:(1) attach front (F) and rear (R) bushes; (2) gun drill a reference hole; (3) measure the reference hole diameter using an air probe (AP); (4) trepan a coaxial core around the reference hole using an EDM tubular electrode (E) and measure core length change using a linear variable-differential transducer (LVDT); (5) re-measure the reference hole diameter using an air probe (AP) (courtesy Stefanescu2004)

Although work on deep hole drilling (DHD) is fairly recent (the majority of which has been carried out in the last ten years), a number of important developments have occurred. The technique for trepanning has migrated from electro-chemical cutting (Bonner 1996) to electro-discharge machining (EDM) (Smith 2000) which has increased the coaxiality of the central hole with the core. The number of angu-

lar steps has also increased, from 3 to 8 and beyond ((Smith 1994), (Leggatt 1996), (Bonner 1996)).

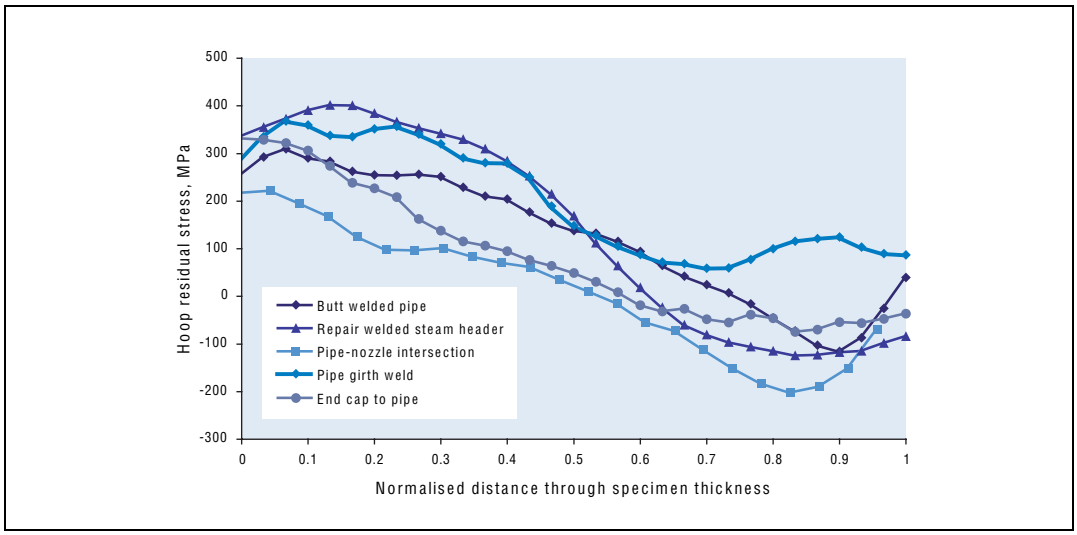

Figure 2-7. Example results for the deep hole drilling technique (courtesy Veqter Ltd.)

DHD is a complement to normal hole drilling. The latter is limited in depth (as mentioned in Section 2.2.1), whereas DHD is best suited to measurements through the bulk of the sample. Like normal hole drilling, DHD requires excellent operator skills to obtain satisfactory results. DHD provides much deeper access into samples than neutron diffraction without the expense, and for single line measurements is an option, but is thus far only available at one laboratory (the University of Bristol).

2.2.4 Crack compliance

The crack compliance method is based on the strain relief that occurs around the location of a small slit (hence the alternate name of 'slitting') (Cheng & Finnie 1986). As the slit is deepened, strain gauges mounted on each side of the long axis of the slit are measured, which permits the back-calculation of the residual stresses orignally present. The geometry of the slit makes the technique sensitive to stresses perpendicular to the cutting direction - and make the implicit assumption that the stress field is uniform along the length of the crack. The calculations used to invert the measured strains and produce stresses are very similar to those of ring coring, crack compliance being effectively a one-dimensional version of that technique.

The strains measured in crack compliance are distant from the relieved stress as is common for relaxation techniques. Crack compliance is more flexible than hole-drilling or ring-coring, because the geometric constraints are much less rigorous. However, there is no standard (as there is for hole-drilling, for instance) over the relative location of slit and gauge, which results in considerable effort being needed to calculate the coefficients needed for inverting the strains. While resolution, accuracy, and depth limits for this method are interlinked in a non-trivial fashion, it would not be unreasonable to expect a stress resolution of 0.01% of the elastic modulus of the material and a depth resolution of 3-4% (of sample thickness) when measuring in aluminium (Prime 2005b). An excellent review of these issues and general progress regarding this technique is to be found in (Prime 1999).

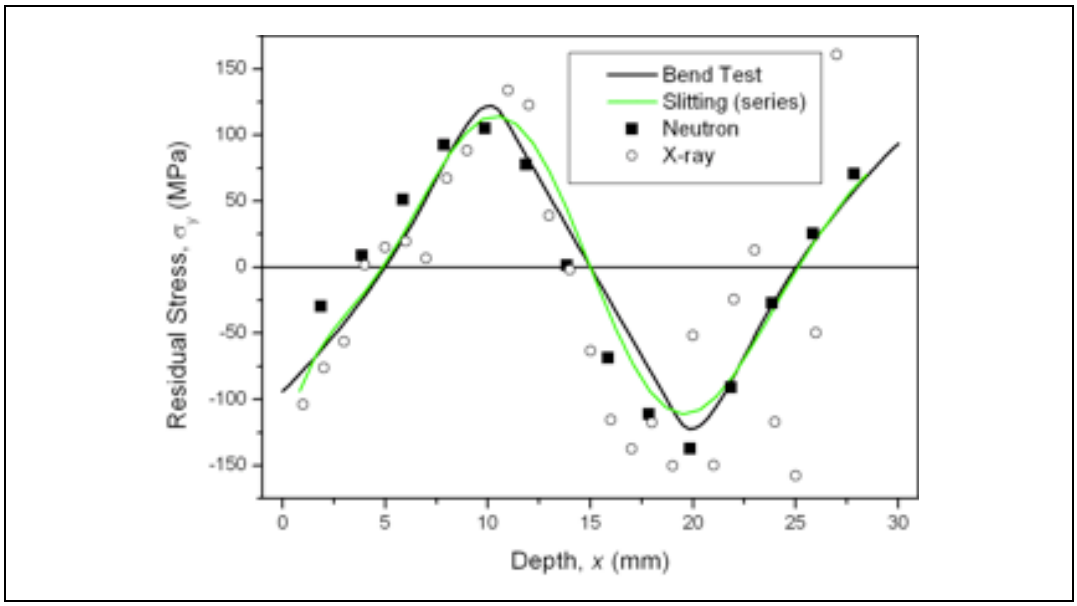

Figure 2-8. Residual stress measured in a bent bar comparing the crack compliance (slitting) method to neutron and synchrotron x-ray diffraction techniques. (courtesy Prime)

2.2.5 Sectioning

Sectioning is the name given to a family of completely destructive residual stress measurement techniques, starting with studies of longitudinal stresses in bars and rods in 1911 (Heyn 1911), with the developments of Sachs in 1927 (Sachs 1927) through straight beams and biaxial stresses in plates and on to thick walled pipes (Ueda 1980) and welds (Ritchie 1987). Like the other destructive techniques, it is

based on stress relaxation as material is removed and residual stresses in a body self-equilibrate in accordance with the new boundary conditions. The relaxed strains are measured on the surfaces of the sample (most often with strain gauges) as the piece is repeatedly sectioned, until the point that no further strains are relaxed. This assumes that it is possible to repeatedly section the object and that the relaxed strains are observable. Like the other techniques, it is also presupposed that the method of sectioning introduces no new plastic strains. As the technique is customised to each geometry, the inversion from measured strains to estimated stresses must be done on a case by case basis, and can be quite time consuming (Ueda 1996).

2.3 Non-destructive techniques

Destructive techniques typically use a strain gauge or some other device to measure the relaxation of the material upon cutting. Non-destructive techniques measure some instrinsic physical property of the sample in order to determine the stress state. There are a number of observable properties which are commonly used, such as polarisation (photoelastic measurements), magnetostriction and Barkhausen noise (magnetic methods), or the speed of sound (ultrasound) (Tiitto 1996). However, in this dissertation, comparisons are made with measurements that use the changes in the spacing of the crystal lattice as an atomic strain gauge. Diffraction is at the heart of these techniques.

Diffraction occurs when a wave impinges upon a regular array of scattering objects, providing that the distance between the objects is of the same order of magnitude as the length of the incoming wave (Cullity 1978). The scattering of the incident wave by this array results in many of the scattered waves being out of phase with each other, leading to destructive interference. However, when the waves are in-phase, constructive interference leads to a distinct outgoing wave. This behaviour is described by Bragg's Law, which relates the wavelength of the incoming wave (and its multiples) $n\lambda$, the spacing of the planes in the scattering array d, and the angle of incidence and diffraction θ.

$$n\lambda = 2\,d\sin(\theta)$$

Equation 2-1. Bragg's law

By varying either the incident wavelength of the radiation, or by observing the intensity of diffracted photons from different angles of θ, it is possible to determine the spacing of the lattice planes of a crystal. This is shown schematically in Figure 2-9.

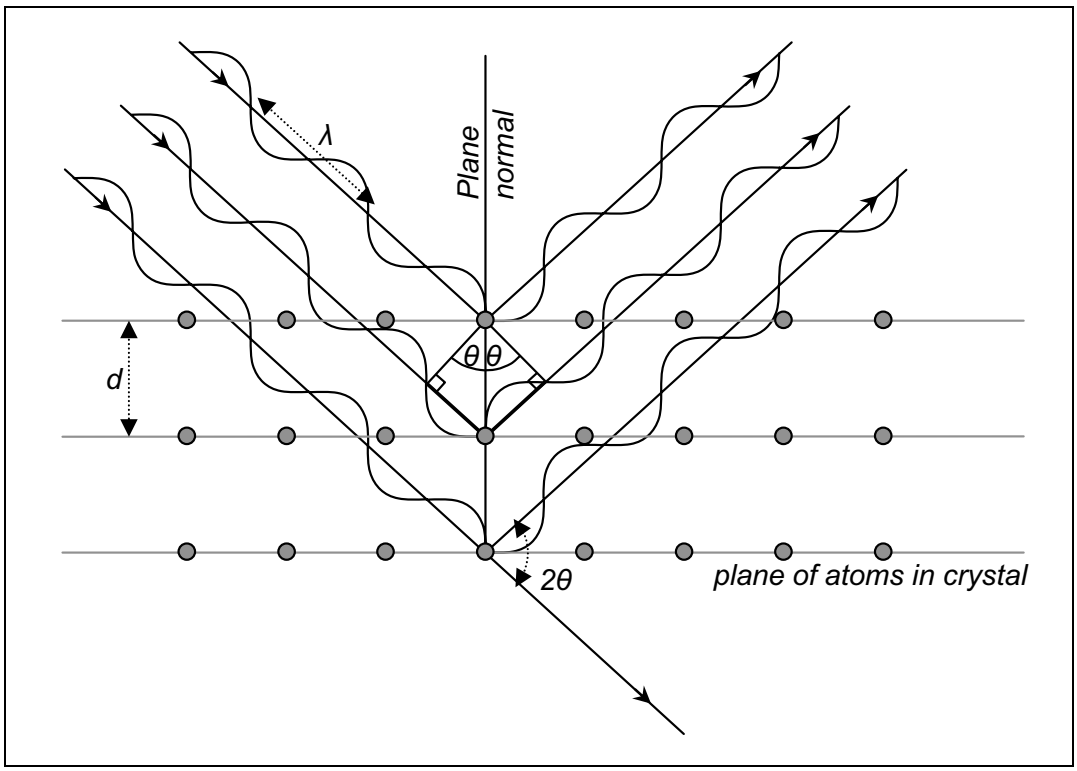

Figure 2-9. Bragg's law represented schematically. (courtesy King)

Elastic strains in the sample (which must have a crystalline material, and usually a polycrystalline microstructure with suitable grain size and texture (King 2008)), whether due to residual stresses or applied loads, result in a change in the spacing of the crystal planes, so by measuring the change in theta (Δθ) for the position of the Bragg peaks, the strain may be calculated using Equation 2-2 where d_o is the lattice spacing for the material under no stress. Estimating the value of d_o can be done in a number of ways (Withers & Webster 2001):

$$\varepsilon=\frac{d-d_0}{d_0}=-\cot(\theta)\,\Delta\theta$$

Equation 2-2. Strain derived from Bragg's law

- measure in a section of the same sample that is assumed to be stress free (for instance, far from the weld line in a welded plate).
- measure a powder from the sample material (relieving the stresses).
- cut a comb-like structure out the material, again relieving the stresses for each tine in the comb. For samples where material properties vary spatially (across a weldline, for instance) the comb can be cut from the same area and each tine can be used as a d_0 correction for the respective part of the sample (Figure 2-10 shows a photograph of a comb structure).
- with measurements made through the depth of a sample, it is sometime appropriate to assume stress and moment balance, and use this to correct the data. However, sometimes the stresses balance over an area, not a line, and insufficient measurements will prevent this method from being useful.

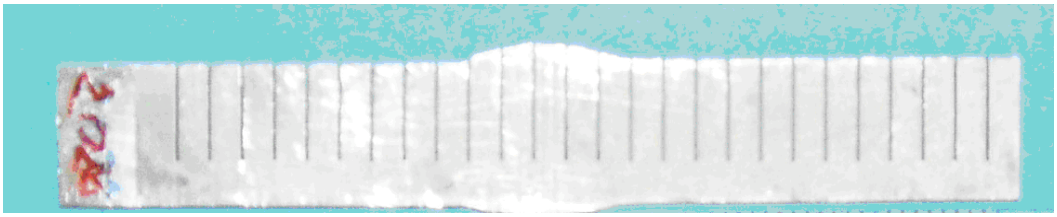

Figure 2-10. Photograph of a aluminium weld comb structure for d_0 measurements (courtesy Ganguly 2004).

2.3.1 Laboratory X-ray diffraction

In X-ray diffraction instruments used in the laboratory, the X-rays are usually generated by colliding a stream of energetic electrons with a metal target. The electrons are generated by a heated filament within an evacuated chamber and are accelerated by a strong electric field. Upon impacting the target (which is usually water cooled) the resulting x-rays are emitted through a thin x-ray transparent window (such as beryllium). The spectrum of the emitted x-rays encompasses the range of energies up to that of the accelerated electrons (termed *Brehmsstrahlung*), with several sharp intense peaks that are characteristic of the target material , which if combined with suitable filters, can produce an approximately monochromatic beam). As seen in Table 2-2, the attenuation of x-rays from typical target

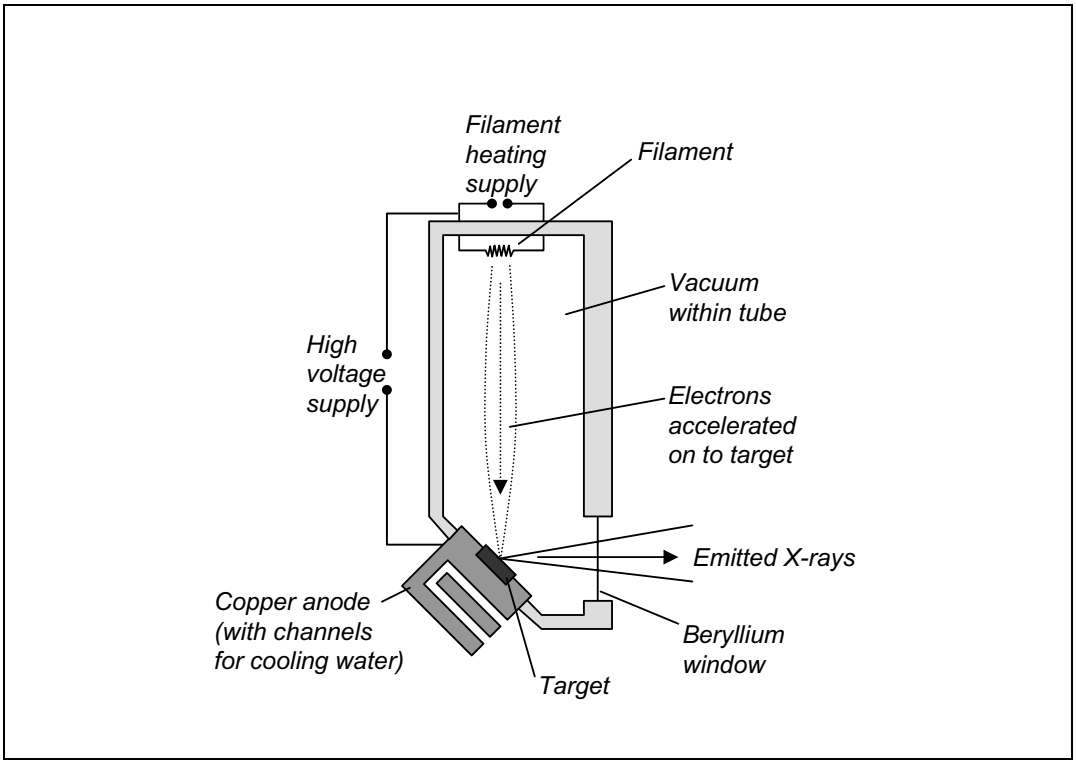

Figure 2-11. Schematic of a lab x-ray source (courtesy King)

materials is very high in the common engineering metals. The x-ray photons thus only penetrate very slightly into the sample, on the order of tens of microns, but if the assumption of plane stress is made (as is reasonable this close to the surface), by varying the angle at which the sample is presented to the instrument in two orthogonal directions, measurements of the in-plane strains are possible. This is termed the $\sin^2\psi$ method (Cullity 1978). One of the main advantages of this method is that there is no need for a stress-free reference d_o.

In order to extend the depth at which measurements may be made, removal of a thin layer of material may be performed between each set of x-ray measurements - this gives access to one millimetre of sub-surface measurements, but this is experimentally very slow as it is usually performed using electropolishing, to reduce introducing additional residual stresses.

Radiation	Penetration length in Ti	Typical feasible path length
lab x-ray (Cu K_α)	10micron	reflection only
synchrotron x-ray (40keV)	1mm	7mm
synchrotron x-ray (60keV)	2.9mm	20mm
synchrotron x-ray (150keV)	13mm	30mm
thermal neutrons	17mm	40mm

Table 2-1. Penetration length (decrease to 1/e of original intensity) in titanium for common diffraction sources (after King, Withers).

2.3.2 Synchrotron X-ray diffraction

Synchrotron radiation was discovered by accident in 1947 by researchers from General Electric (Baldwin 1975). Whilst using a particle accelerator, it was noticed that at each corner in the polygon where magnetic fields were used to steer the particles, a thin beam of light was emitted tangential to the corner. Originally considered a loss in efficiency of the accelerator, synchrotrons are now purpose built to 'leak' as much light (or 'synchrotron radiation') at each bend as possible (XDB2001). In addition to the 'bending magnets' at the vertices, insertion devices are used in the straight sections to obtain x-rays with very high flux and energy. Instead of simply accelerating the electrons radially, the strong spatially alternating magnetic fields of 'undulators' and 'wigglers' that are perpendicular to the electron trajectory impart very high changes in velocity to the accelerated electrons, and the subsequent radiation can be several hundred kilo electron volts. In general, a modern synchrotron, such as the ESRF in Grenoble, is capable of producing very intense coherent beams of radiation, ranging from ultra-violet to hard x-ray (100s of keV).

These beams have very low angular divergence, and the wavelengths can be selected with a narrow bandwidth ($\Delta E/E = 1 \times 10^{-6}$ using a silicon 111 monochromator). The flux of x-ray photons produces at a synchrotron facility are over a million times higher than lab sources, and in combination with the high energies available, this permits measurements at considerable depths with reasonable counting times for

each measurement point. Table 2-2 shows the attenuation coefficients for a

Material	Z	Density (gcm^{-3})	Cr K_α (λ=0.229)	Mn K_α (λ=0.210)	Fe K_α (λ=0.194)	Co K_α (λ=0.179)	Cu K_α (λ=0.154)	Mo K_α (λ=0.071)	Synchrotron (λ=0.015)
Al	13	2.7	402.3	315.9	250.6	198.2	131.5	14.3	0.53
Ti	22	4.51	2719	2142	1700	1371	920	106.9	1.68
Fe	26	7.87	905.1	715.46	572.9	468.2	2549.9	301.4	4.26
Ni	28	8.90	1290	1032	828.6	668.4	438.8	421.9	5.90

Table 2-2. Attenuation coefficients (μ) in cm^{-1} for different characteristic x-ray radiations - wavelengths in nm (courtesy Withers).

number of common engineering materials when illuminated with the characteristic x-ray radiation from different sources. Path lengths in aluminium alloys, for example, can be many centimetres in the 40-80keV range (~0.04-0.015nm). (Withers 2001).

Three methods have been used for measuring engineering samples as illustrated in Figure 2-12. The paradigm for measuring strain varies in each case:

1. As shown in Figure 2-12a, the first approach is to measure the location of a single Bragg peak as a function of 2θ. While this could be performed either in reflection or transmission, the low scattering angles for synchrotron diffraction often make transmission preferable. However, the gauge volume (the geometric volume within the sample that is measured) has a very high aspect ratio for the same reason.
2. Instead of moving a zero-dimensional detector in combination with exit slits to resolve the peak, the second approach uses a 1- (or 2-) D detector (Figure 2-12b). The many peaks from the different crystal planes illuminated within the sample are projected onto the plane of the detector. The gauge volume is effectively the projection of a rectangle (defined by the entrance slits) so that while the lateral dimensions may be very small (20 x 20μm), any variation over the depth of the sample is averaged into a single measurement.
3. Instead of detectors which are purely sensitive to intensity of impinging radiation, the third approach uses an energy-sensitive detector (Figure 2-12c). The combination of this with the entrance and exit slits of the first approach and a white (polychromatic) illuminating beam enables a large diffraction spectrum to be obtained in a single measurement.

The main strengths of using synchrotron radiation for diffraction measurements are the high intensities (and thus low count times) and the possibility of very small

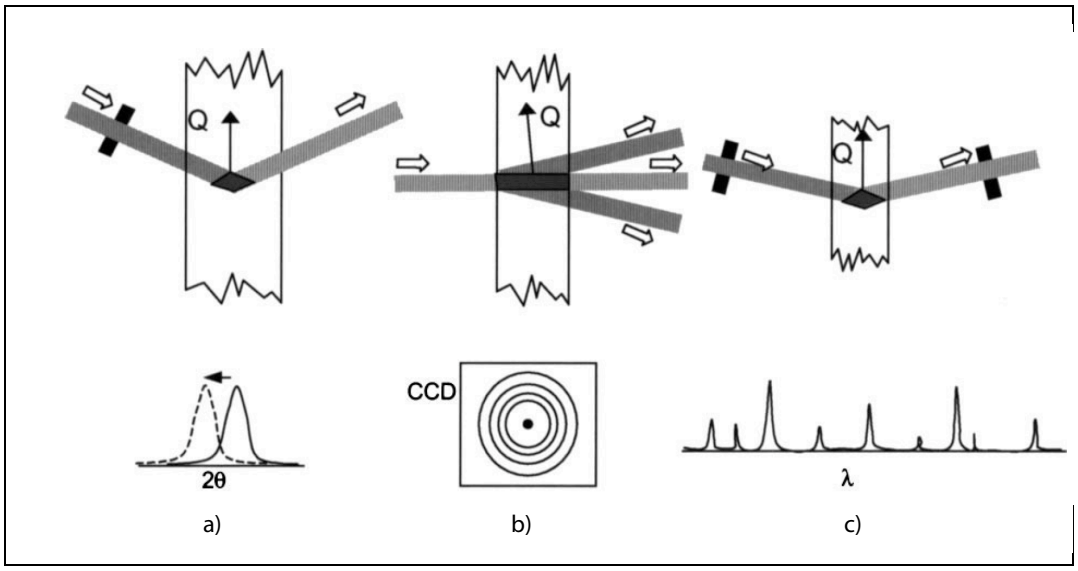

Figure 2-12. Synchrotron measurement geometries: a) 2θ scanning b) low angle transmission c) energy dispersive. Q indicates the scattering vector, the direction of measured strain (courtesy Withers).

gauge volumes (in at least two dimensions). It does not perform well, however, with high degrees of texture or large grain sizes, as the small gauge volume gives a poor statistical measure of the type I stresses.

2.3.3 Neutron diffraction

The penetration of neutrons into engineering materials is far greater than that of x-rays (Withers & Bhadeisia 2001). This penetration is the primary advantage of neutron diffraction for strain measurement, as it permits measurements to be made deep within the bulk of a sample, enabling complete stress fields to be calculated for comparison with finite element models (Londini 2001). The wavelength of thermal neutrons is similar to the d-spacing of most materials, which results in a diffraction angle of ~90° rather than the ~6° of synchrotron x-rays. Due to the cot(θ) term in Equation 2-2, this produces better strain resolution, and the differing measurement geometry can be advantageous for certain samples.

Neutron beams are produced either by spallation (where a proton beam collides with a heavy metal target) or from a nuclear reactor. In the latter case, strain scanning may be performed as in the first approach described for synchrotron radiation, θ/2θ. With a spallation source, packets of neutrons leave the target at the same time, but arrive at the detector at different times corresponding to their energy.

Resolving a diffraction profile in a short time period is thus possible . Reactor neutrons are more intense as the spallation source is pulsed (~50Hz) but only measure a single peak at a time. Spallation sources are less intense (because monochromatic beams are typically needed), but measure a complete profile at once. While the depth of penetration is better for neutrons than x-rays, the counting times are longer - two orders of magnitude is not unusual. As a function of this low flux (and requirements for the geometry of efficient detectors), the lateral resolution of neutron measurements is also typically lower than synchrotron diffraction data, ~1mm at the minimum.

2.4 Summary

This chapter surveys a number of the principal techniques used for residual stress measurement. Some of the features of those techniques are summarised in Table 2-3.

Method	Penetration	Spatial resolution	Accuracy	Comments
hole drilling	~1.2x hole diameter	50μm depth	±50MPa at best	Measures in-plane type I stresses; semi destructive
deep hole drilling	through-sample (<200mm)	<1mm	±30MPa	semi-destructive,
crack compliance	95% of sample depth	4% or 0.1mm, whichever is larger	2MPa or 0.001% E, whichever is larger	1-D profiles
lab x-ray	50μm (Al) - 5μm (Ti)	1mm laterally, 20μm depth	±20MPa	sensitive to surface preparation; measures type I,II, and III stresses (peak position and breadth)
synchrotron	50-150mm (Al) (depends of energy)	20μm lateral to beam, 1mm parallel to beam	$\pm 10 \times 10^{-6}$ strain, limited by grain sampling statistics	small gauge volume can make diffraction patterns spotty; measures type I,II, and III stresses (peak position and breadth)
neutron	200mm (Al) - 4mm (Ti)	500μm	$\pm 50 \times 10^{-6}$	acquisition rates slow; measures type I and II (averaged over gauge volume)

Table 2-3. Comparison of technique attributes (after Withers)

Of these methods, it may be noted that:

- None of the destructive methods is capable of making full-field measurements.
- Neutron methods are limited to ~10mm depths for common engineering steels.
- Diffraction methods, particularly synchrotron and neutron, are difficult to gain access to, as they are only available at large national or international facilities.
- Diffraction methods do not directly give macrostress measurements - the lattice spacing is measured, from which strain and then stress must be calculated.

As a result, there is a space for a technique such as the contour method that would permit full field, easily obtainable measurements through a wide variety of sample geometries with little or no sensitivity to type II or III microstresses.

These points will be explored further in the next chapter, which introduces the reader to the contour method.

3 Introduction to the contour method

The aim of this chapter is to introduce the principle of the contour method as a technique for measuring residual stresses in engineering parts and components. This will include explanations of the method itself, how it is applied in practise, and elements that need to be taken into consideration when employing the method experimentally. A review of previous work carried out using the technique will then be given. The reader is referred to Appendix A for an overview of surface metrology techniques.

3.1 Principle of the contour method

The contour method was first proposed and developed by Prime in 2001 (Prime 2001a). It is an application of Bueckner's principle (Bueckner 1958). This states that:

> "If a cracked body subject to external loading or prescribed displacements at the boundary has forces applied to the crack surfaces to close the crack together, these forces must be equivalent to the stress distribution in an uncracked body of the same geometry subject to the same external loading."

This is derived from superposition, and is typically associated with a schematic such as Figure 3-1. Bueckner is demonstrating the equivalence of stress intensity factors resulting from external loading on a body with those resulting from tractions on the crack face (Aliabadi 1992).

In the contour method, the 'cracked body' is the sample under test, cut by means as similar as possible to brittle fracture. There is no external load, but if the dis-

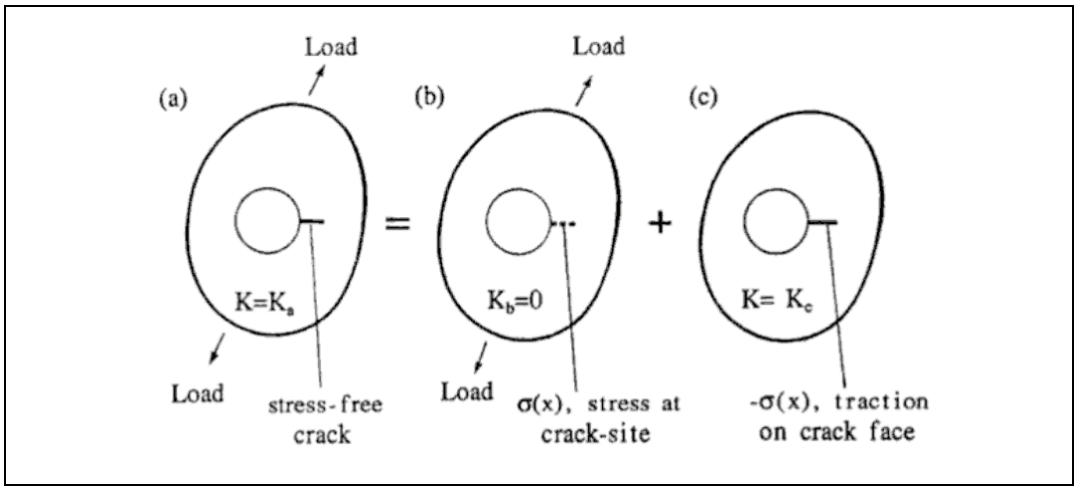

Figure 3-1. A typical schematic illustration of Bueckner's principle (courtesy Aliabadi 1992).

placements at the 'crack surface' can be measured, and the stresses required to negate those displacements calculated, these are equivalent to those present prior to 'cracking' - the residual stresses in the original sample.

As shown in Figure 3-2, part containing residual stress (a) is cut (assuming a planar separation of the two equal halves of the sample in the diagram), relieving the normal (σ_{zz}) and shear (σ_{zx}, σ_{zy}) stresses over the cut surface. This stress relief causes distortion on the surfaces (b) that have been cut. The relaxed surface is then analytically forced back to its original shape (c). The original stress state is the superposition of those at b) and c).

There are three main assumptions to be satisfied for this principle to apply (Prime 2001):

- Any stress relief after cutting is purely elastic.
- The cutting process does not introduce stresses sufficient to significantly affect the measured displacements.
- The original cut plane was flat.

The relaxation of the surface is due to the superposition of two components, the normal and the shear stresses. Whilst in principle all components could be deduced if the complete deformation of the cut surface was measurable, experimentally it is only possible to measure the deformation normal to the surface.

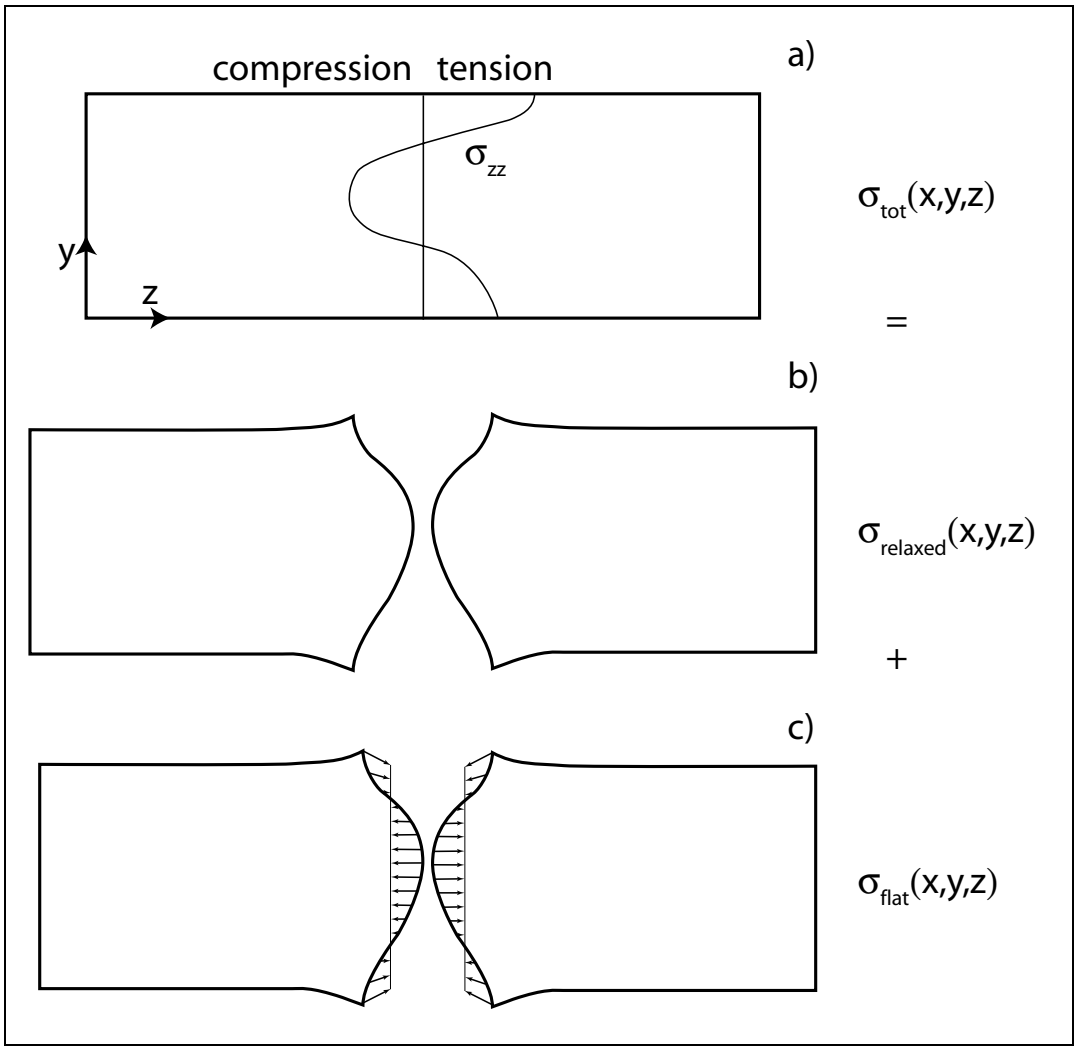

Figure 3-2. Schematic of the contour method (after Prime 2001)

However, by taking an average of the displacements of both sides of the cut, the shear stress relaxation (which is anti-symmetric) is removed and the normal stress relaxation (which is symmetric) preserved. Thus to determine uniquely the normal stresses at the cut plane, the measurement of normal deformation is sufficient - as demonstrated by multiple authors analytically and through numerical simulation (Prime 2001, Zhang 2004).

As the relaxation of stresses is proportional, instead of modelling the deformed body and restoring the distorted surface to planarity, it is possible to start with an undistorted body, and distort the cut surface to the *negative* of that measured. The

stresses induced in the modelled body by this displaced surface are then indicative of those present in the physical sample prior to cutting. This is purely done as a convenience for modelling.

3.2 Experimental application

The steps involved in the experimental application of the contour method are as follows:

1. Make a flat cut through the sample, normal to the stress component of interest.
2. Measure the surface contours on the pair of cut surfaces.
3. Average these two sets of contours.
4. Fit a surface to the dataset so that the contours can be evaluated at an arbitrary location.
5. Build a finite element (FE) model that represents the cut sample.
6. Evaluate the surface at the locations of the nodes on the 'cut surface' of the FE model. Apply the negative of this displacement as a boundary condition normal to the model surface.
7. Execute the FE model, and record the stress that occurs when displacing the cut surface from flat to distorted. These are the stresses that were present in the sample prior to cutting.

The steps involved in the technique, and the complete toolchain developed by the author to accomplish these, are described in comprehensive detail in Chapter 4.

3.2.1 Cutting

The contour method has three criteria for a suitable cutting technique: it must make a flat cut, it should remove as little (and as constant) an amount of material as possible from the sample, and should cause a minimum of plastic deformation (Prime 2001). The only technique available at present that satisfies these requirements is wire electro discharge machining (wire EDM, or WEDM).

Wire EDM cutting is a erosion process induced by electrical breakdown between a continuously travelling wire electrode and the work piece. Unlike sink EDM, which uses oil as a dielectric fluid, the dielectric medium in wire EDM is deionised water, which has a much lower viscosity - causing smaller mechanical deviation of the cut

(Benedict 1987) - and higher thermal conductivity - providing more effective cooling (Jameson 2001). The plasma channel created vaporises material from both the machine electrode and the work piece at a temperature of 8000-12000°C (Boothroyd 1989). The use of a pulsed power generator permits the flushing of the debris in between successive spark events (Huntress 1978). Additionally, the kerf generated is usually only 110-120% of wire diameter (Rotadata 2005) and so a 100μm cutting wire removes only ~120μm. The requirement for electrical conductivity in the part is an acceptable restriction for many engineering materials.

In general application, wire EDM is used to machine parts with complex shapes, and this is performed first with a 'roughing cut' where high voltage permit rapid cutting of the approximate shape required. A 'skim' cut is then used to produce a high quality surface finish. However, for the purposed of the contour method, this double cutting would cause two problems. Firstly, the roughing cut has a large recast layer which is the solidification of the molten area at the spark front (Shobert 1983). This introduces stresses and may reshape the surface. In addition, the second cut would remove whatever surface profile that had been left by the first cut, and no useful measurements could be made. For this reason, the usual EDM practise must be modified to make only a single 'skim' cut through the sample. This slows the process considerably, as the cutting rate is much reduced with the skim settings. Pinching of the wire may also occur because of the (desirable) smaller overcut in this mode. In the event of a wire breakage, the cut must be restarted from the same location, not recut from the exterior of the sample (again, the common practise for an EDM operator) as this would remove the surface distortions that have been manifest (Prime 2001a).

A further modification to the normal EDM cutting practise is necessary when restraining the sample. Normally, the part is clamped only at one side and the waste material is left free to be detached. However, the application of the contour method is based on the relief of stresses normal to the cutting plane, and any movement of the sample due to stress relief may change this plane to some other shape. In certain cases (cf. Chapter 6) it is possible to correct for sample movement/cut-

ting non-planarity afterwards, but this should be considered a remedial solution to an undesired problem. Thus the sample is always clamped on both sides, preferably symmetrically, as close to the cutting head as is practicable.

Reducing the off-axis motion of the wire during EDM cutting is very important for the contour method because of the possibility of deviation from planarity. As represented schematically in Figure 3-3, the cutting wire is moved axially through the

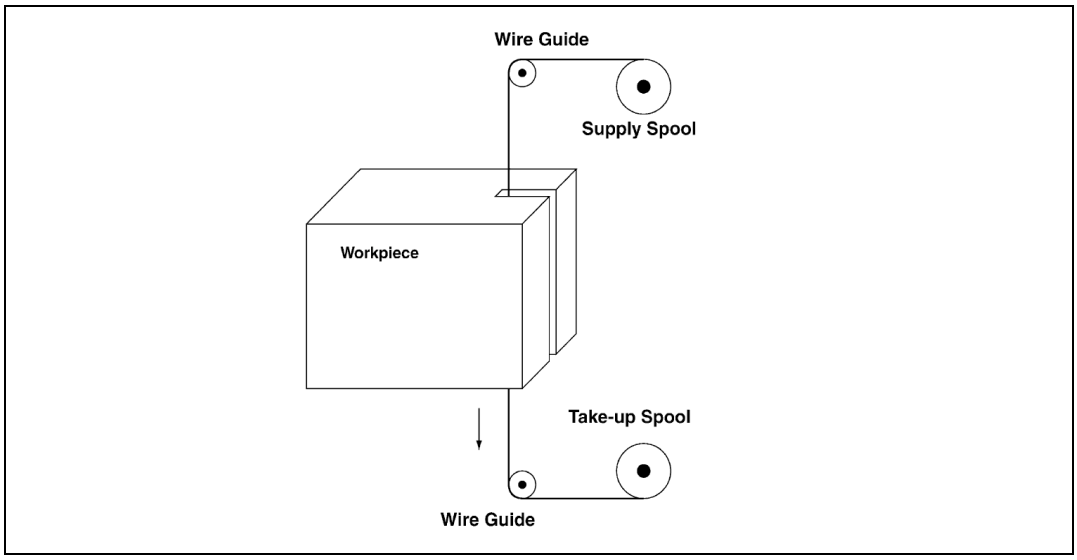

Figure 3-3. A schematic of wire EDM - the moving cutting wire is charged relative to the workpiece, and the spark breakdown causes erosion of the part. (courtesy Lambert)

part and the speed of this movement can promote modal vibrations (particularly in the presence of high pressure flushing jets) or thermal instabilities (prevalent at low speeds due to the increased residency time within the kerf) (Lambert 2002). During this work possible evidence of these problems has been seen (Chapter 6), but as the cutting facilities were not available locally, this has not been investigated further.

Many samples under investigation are prismatic (that is, being geometrically primitive, cuboid etc.) and there are at least two directions in which they may be mounted for cutting. Figure 3-4 shows this for a simple cuboid sample. If the cutting line were in the region of the red line, the length of the cutting wire would be short and the clamping of the sample would be straightforward. Parallel to the

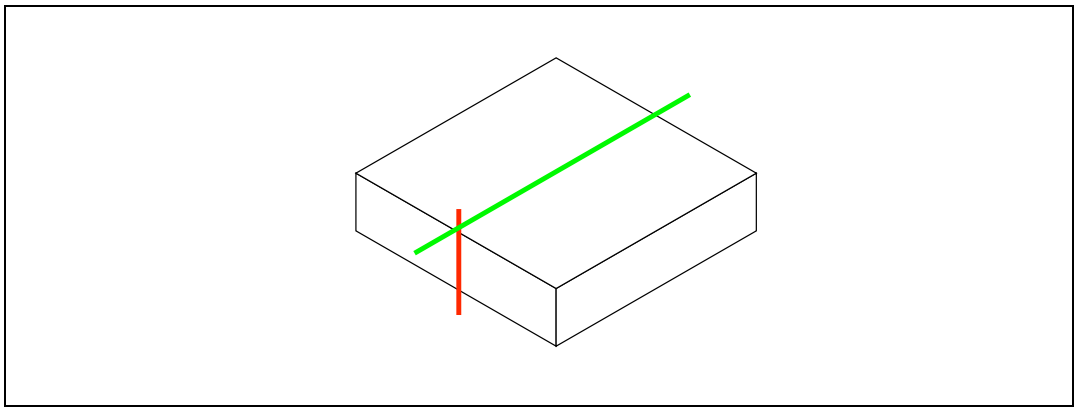

Figure 3-4. For many samples, two choices of cutting direction are possible to give the same result. For this sample, the cutting wire would be either parallel to the red or green lines.

green line, the cutting wire would be longer (and the flushing that occurs from both ends less effective) and the clamping would be more difficult to setup. However, if the stress field were known *a priori* to be largely univariate (for instance, a strong tensile region parallel to the red line) then cutting in the direction parallel to the green line would relieve a more balanced stress profile along the wire length, reducing the likelihood of pinching or wire breakage.

As it is not possible, in general, to discriminate between normal stress relief and cutting artifacts as causes of displacement of a surface, both surfaces from the cut sample are used together. By averaging the displacements from the two sides any anti-symmetric deviations are removed, while symmetric effects (the stress relief) are reinforced. This also reduces measurement noise by a small amount. The other effect of the averaging of the two sides is to remove the effects of shear stresses, which are also anti-symmetric, thus the averaged displacement contours show only the effects of the stresses normal to the cutting plane.

The contour method's use of skim cutting without any prior roughing cut places it outside the realms of most previous EDM characterisation. This is an area that would be very fruitful to study in greater detail.

3.2.2 Surface metrology

The results obtained by the contour method are only as good as the degree to which one can measure deviation from planarity of the cut surface. Measurements of sur-

face height (sometimes referred to as surface profiles or contours) can be undertaken with a vast array of technologies and instruments. For metals having stresses of hundreds of megapascals, the variation of the surfaces can typically be measured in tens of microns across tens of millimeters laterally, so a great number of techniques are either too limited in working volume (atomic force microscopy) or not sufficiently accurate (structured light scanners). The measurements need to be accurate in both lateral location and height. Represented as a dataset, the measurements are always discrete, and it is important to recognise that while the measurement may have been made in a continuous, or analog fashion, it will be stored and processed as a series of discrete points. The final density of these points is one of the critical features in determining the spatial resolution of the contour method.

Instruments that are useful for surface measurement fall into three broad categories: tactile, optical, and electromagnetic. The tactile domain is that of the coordinate measurement machine, or CMM, an instrument in widespread use for quality assurance of fabricated parts. Much of the first work on the contour method used CMMs as they are readily available in many machine shops, operate over large working volumes whilst maintaining precision at the micron level. The optical category contains devices such as triangulating laser probes, confocal microscopes, and interferometers. In particular, the triangulating laser probe is capable of measurements that, on a per-point basis are less accurate than a CMM, but when coupled with the prodigious rate of measurement leads to very large datasets with accuracy that (by virtue of increased counts/unit area) is equivalant to that of the tactile probe. Dealing with these very large datasets can pose problems further in the processing chain, however. The electromagnetic domain is typified by the atomic force microscope. The AFM is not suitable for the application of the contour method to engineering samples due to the very limited working volume and slow speed. It might yet be applied to novel work measuring stresses in micro-machined

parts. All three of these modalities are covered in Appendix A. A summary and comparison of these measurement options is to be found in Table 3-1.

Type	Accuracy	Range	Working area	Speed	Surface finish
Tactile probe	~5μm	100s of mm	100s of mm	1pt/3s	hard surfaces
Triangulating laser	~15μm	100s of mm	100s of mm	20kpts/s	diffuse reflection
Confocal laser	~1μm	1mm	100s of mm	1kpts/s	any
AFM	~100nm	8μm	100μm	2kpts/s	depends on mode

Table 3-1. Comparison of different measurement techniques.

Much of the early contour method work reported used CMMs for surface measurements due to their availability at machine shops and metrology labs (Prime 2001, Dewald 2001, Zhang 2004). However the increased throughput and ease-of-use of laser scanners (where precise path planning is not required for autonomous scanning of large surfaces) has led to their growing usage. Both triangulating probes and confocal laser probes have been used. For instance, Prime published a detailed technique paper in *Experimental Mechanics* (Prime 2004), using a confocal laser probe for the metrology of the VAMAS TWA-20 welded steel plate. This custom device had been developed for use in fusion experients (Sebring 2001) and was well suited to large area measurements.

The increased point density of the laser scanner also enables the measurement of relatively small samples, as shown in this thesis (Chapter 8, on the laser shock peened plate) and previously by Prime and collaborators in measuring a 316-SS rod weld. Low stress measurements (±50MPa in total) were demonstrated in the latter case (Prime 2002a).

3.2.3 Dataset processing and fitting

The measured data from the cut surfaces are very often acquired on a grid dictated, to some degree, by the algorithms and procedure of the measuring device. These discrete locations are rarely those of the nodes in the subsequent finite element model that is used. This is one of the two primary reasons that an analytic or parametric surface must be fit to the measured data - to provide an interpolant that can

then estimate the location of that fit surface at the nodal points of the model. The second reason for fitting is to remove, or at least reduce, the noise inherent in the physical process of measurement.

Initial work on the contour method used 2-D Fourier surfaces for fitting, sometimes extending to the 9th order (Dewald 2001). These have an intrinsic physical meaning to them, as the components of the Fourier series directly correspond to the frequency components present in the cut surface. However, this is not of any benefit, and Fourier methods are not able to cope well with the exptrapolation of the dataset outside the measured area - and with tactile probes, there may be a considerable margin around the possible measurement area that extends to the perimeter of the sample itself. Chapter 4 in this work deals with some of the techniques developed to accomodate this difficulty.

Given that the physical meaning of the Fourier fit was not beneficial, almost all work has now migrated to using splines (Prime 2004, see also Section 4.4.3). Most practioners have used bivariate splines with uniform knot spacing (Prime 2004, Frankel 2007) but extensions to non-unform knot spacing have been developed in this thesis and are of considerable interest in stress fields with strongly varying gradients (Chapter 7, Chapter 8).

3.2.4 Modeling

Due to the impracticality of evaluating an analytic model for any but the simplest of sample geometries, finite element modelling is used to evaluate the normal stresses required to restore the deformed surface to planarity. However, the use of FEM for the contour method is straightforward, and the reader is referred to Chapter 4 and Appendix B for further information. It is notable that when measuring the surface contours, there is no datum point to which the heights are referenced. This results in an arbitrary displacement of the entire analytical model. In addition, there are two arbitrary rotations. All of these unconstrained degrees of freedom are determined by force and moment balancing which occurs naturally in the model. The other two displacements and the final rotation (within the six

degrees of freedom in a 3-D rigid body) are constrained to prevent any numerical errors in the model from causing infinite movements.

In co-ordination with the CM modelling, additional FE work has been carried out. Projectile damage has been explored in a paper co-authored by Prime and Martineau and presented in Portugal in July 2002 (Prime 2002b). A series of tungsten carbide spheres were projected at speeds up to 2km/s into a plate of HSLA (high strength low alloy) steel. In addition to the conventional FE work done in the contour method, a special kinematic simulation was carried out to estimate the stresses induced by the impacts of the spheres. The agreement between the modelled results and the contour method measurements was to the author's satisfaction, particularly given the high degree of non-linearity in the simulation of impact.

Along with partners from Los Alamos and Boeing, Prime presented some novel work in 2004 at the Congress of Experimental and Applied Mechanics (Prime 2004b) where stresses in the parent part of a dissimilar aluminium alloy (7050-2024) friction stir weld were estimated from a small sample that had been parted out. Pre-relaxation stresses in the parent part were estimated using an iterative process.

3.2.5 Validation against complementary techniques

Hughes and Webster (Salford University) collaborated with Prime on a paper comparing contour method results with neutron measurements on a weld sample (Prime 2001b) made for the VAMAS TWA20 program (Vamas). They demonstrated excellent agreement between the two techniques, and also showed that the contour method worked in regions where the yield stress had been exceeded.

DeWald has recently published a paper using both crack compliance and the contour method to assess laser shock peening efficacy in reducing tensile stresses found in welds - with particular regard to containment vessels for nuclear waste (Dewald 2005). He uses an interesting technique for edge determination (necessary when using a continuous tactile probe) involving first order Fourier fits (this problem is discussed in Chapter 5). His results showed a lack of susceptibility to the large grain sizes (50-150μm) in the Alloy 22 material studied. It was found that

multiple pass laser shock peening was able to introduce deep compressive residual stresses - 7.7mm deep in a 33m thick weld.

Prime *et al* produced an internal report early in 2003, followed by a more detailed publication in the Journal of Neutron Research by Kelleher *et al.* (Kelleher 2003) later that year concerning in-service railway rails. Kelleher compared these contour method results with synchrotron, lab x-ray, and a magnetic stress measurement technique. This work highlighted the deficiencies of synchrotron methods for measuring strain in highly plastically deformed regions, and combined the longitudinal contour method data with in-plane x-ray data on thin slices of the rail.

Recently, the Open University in the UK has begun using the contour method. Zhang has applied it to a VPPA (variable polarity plasma arc) weld of 2024-T351 aluminium alloy (Zhang 2004). Although some cutting problems occurred, the extracted results showed good agreement with both neutron and synchrotron results.

3.3 Summary

A number of important factors need to be taken into consideration when preparing a sample for measurement, such as the sample restraint and the surface fitting procedures used. It is important that the position of the sample is suitably aligned such that the cut gives accurate surfaces representing the residual stress distribution under measurement. Studies have shown the technique to compare well with the conventional and more established methods of neutron and synchrotron x-ray diffraction.

This chapter has introduced the basics of the contour method, detailed some of the features involved in the measurement process, and reviewed the work that has been done in this field. The next chapter explores in much greater detail the techniques and processes this author has developed in order to perform contour method measurements.

4 Technical aspects of the contour method

The concept of the contour method is simple, yet it has not gained widespread adoption since its conception. The reasons for this centre around the four technical challenges of measurement, data handling, modelling, and validation. In this chapter, each of the first three is examined in depth: a brief survey of the possible solutions for each problem, followed by an in-depth examination of the approach taken by this author, justifying the route followed. Validation is examined via case studies in subsequent chapters.

Throughout the analysis described in this chapter, a simple well-characterised case study has been examined, namely the case of a four point bent bar. In this way, it has been possible to illustrate the features of the approach adopted.

4.1 Residual stresses introduced by four point bending

The residual stresses introduced by bending a bar under four point loading are well known and can be derived by elementary analysis (Boresi 2003). For this reason, a bent bar was chosen as a simple test case to develop and refine the contour method[1].

The following process was used to calculate the loading force required to produce plastic deformation for the bending of the square cross-section bar as shown in Figure 4-1. As shown in full in Appendix B, the bending moment and shear stresses as a function of z along the bar are plotted in Figure 4-2. From the flexure formula

1. As a historical footnote, a bent bar was one of the first components to be examined by neutron diffraction residual stress measurement (Pintchovius, 1982)

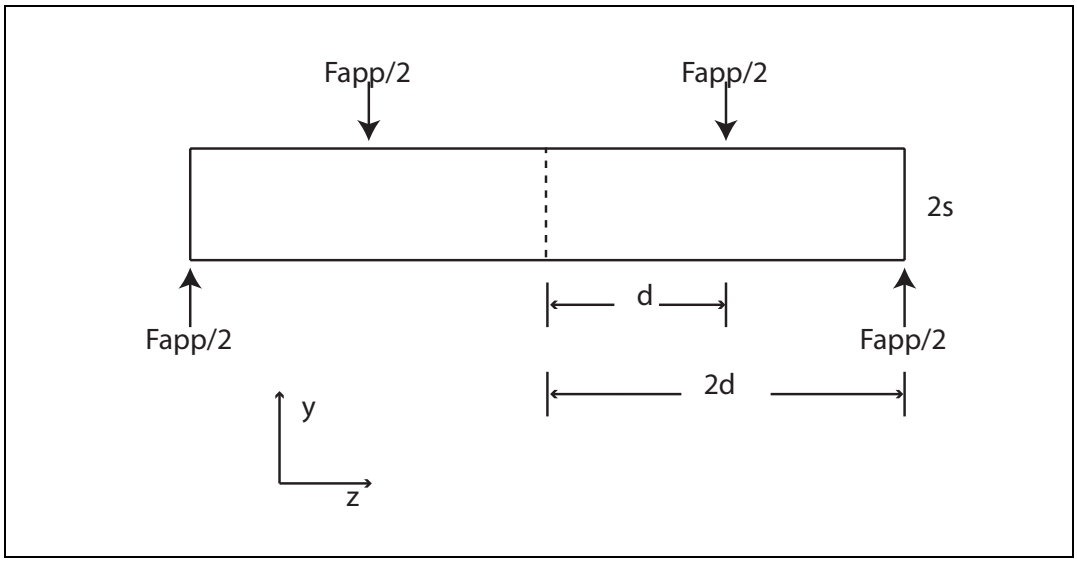

Figure 4-1. Schematic of bar with dimensions and loading locations, with loading points at +-d and +-2d, the bar having a square cross section 2s x 2s in size.

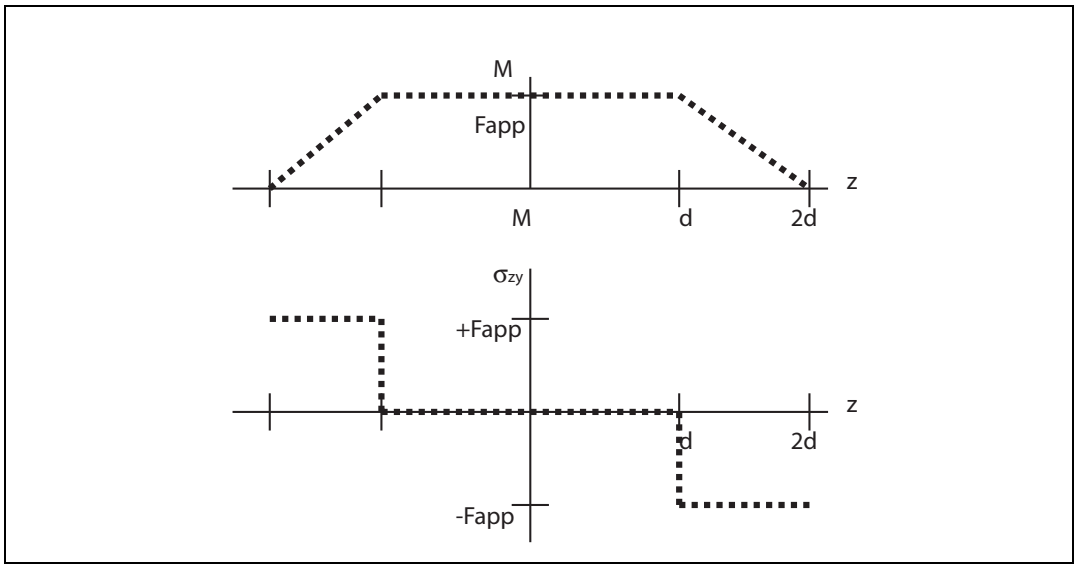

Figure 4-2. Bending moments and shear stresses for the bent bar

(Equation 4-1), using the second moment of area (I_A)for a square cross-section

$$\sigma_{zz} = \frac{M \cdot y}{I_A}$$

Equation 4-1. Flexure formula

beam of width and depth *2s* (Equation 4-2) we can deduce the maximum stress

$$I_A = \frac{4}{3} \cdot s^4$$

Equation 4-2. Second moment of area for a square sectioned beam, side length=2s

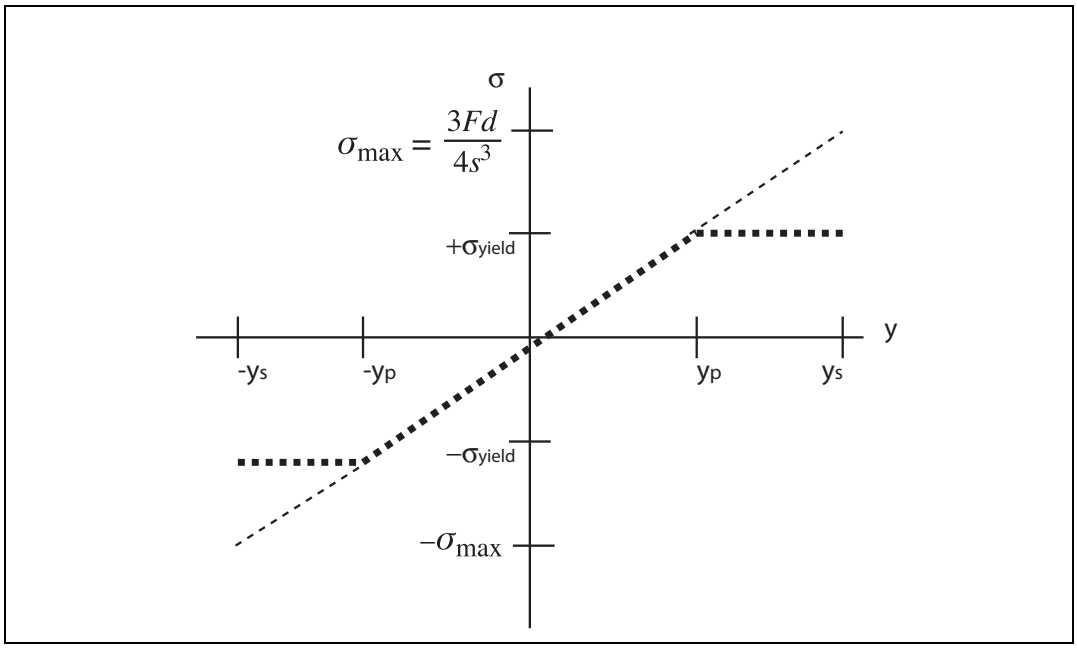

Figure 4-3. Elastic-purely plastic behaviour as a function of distance from the neutral axis

magnitude at both outer and inner surfaces of the beam when bent elastically. With an elastic-purely plastic model for the material, Figure 4-3 shows the resultant stress profile as a function of distance from the neutral axis. This is shown in terms of y_p, which denotes the location of the plastic/elastic interface, and y_s.

The residual stress is best considered by superposing the elastic-plastic loading with elastic unloading. The total bending moment for the plastically loaded bar is given by Equation 4-3.

$$M_{loaded} = 2s\sigma_{yield}\left(s^2 - \frac{p^2}{3}\right)$$

Equation 4-3. Bending moment for the loaded bar

When unloaded, the forces and moments must balance, as in Equation 4-4.

$$M_{loaded} = -M_{unloaded}$$

Equation 4-4. Moment balance

The stress profile after the load has been removed (Figure 4-4) has a unknown

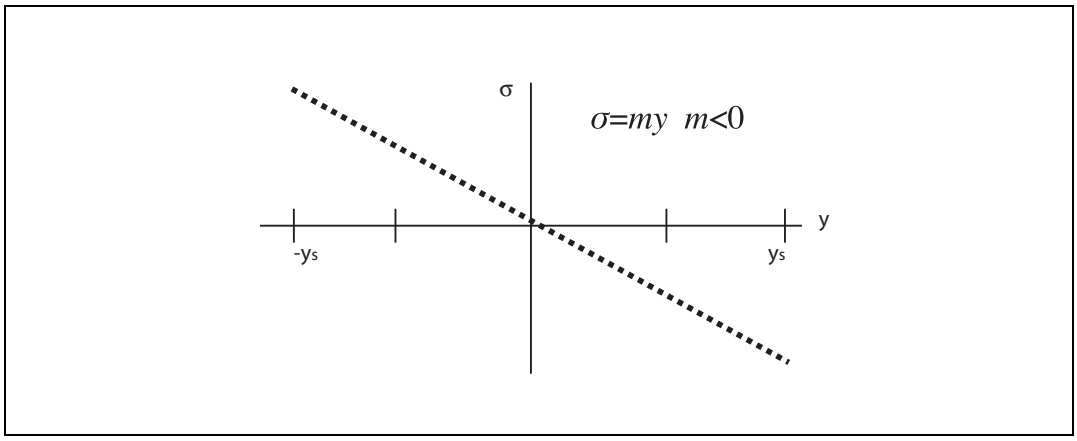

Figure 4-4. Change in stress upon elastic unloading

slope which may be calculated according to Equation 4-5.

$$\sigma_{unload}(y) = \frac{-3 \cdot \sigma_{yield}}{2 \cdot s^3} \cdot \left(s^2 - \frac{p^3}{3} \right) \cdot y$$

Equation 4-5. Stress profile across bar after load has been removed, obtained by moment balance with the loading moment

The loading force required to induce a chosen depth of plasticity (y_p) is obtained by simple rearrangement of these equations. This requires the knowledge of the material properties of the real material, as obtained in the next section.

4.2 Material preparation and characterisation

4.2.1 Material

The four point bent bar specimen was cut from EN3B/080A15 designated steel stock (see Table 4-1 for composition) .

C	Mn	Si	S	P
0.25 max	1.00 max	0.35 max	0.06 max	0.06 max

Table 4-1. Composition by % weight of EN3B/080A15 mild steel, the balance being Fe.

The samples, 20 x 20 x 300mm bars, were stress relief annealed (heated to 650°C, maintained for 90 minutes, then air cooled) to relieve any residual stresses present from manufacturing (Honeycomb 1995).

4.2.2 Tensile testing

In order to assess the mechanical properties of the bars, some material was cut into standard Hounsfield extended style tensile test samples (see Figure 4-5), and

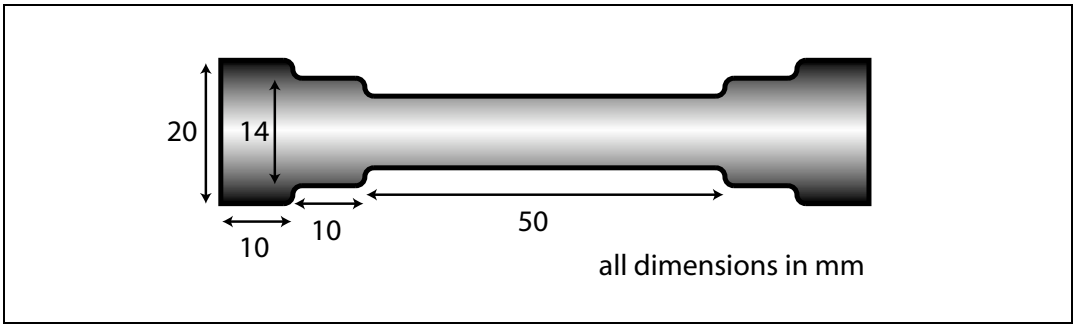

Figure 4-5. Hounsfield extended style cylindrical tensile test specimen

tested using an Instron 5569 Universal testing machine (equipped with a 50kN load cell). The stress-strain curve (strain measured using an extensometer) for both the nominal and true stress is shown in Figure 4-6. The value of Young's modulus was taken as the slope of the elastic region, and the yield stress was taken after 0.2% plastic strain (208GPa and 450MPa, respectively).

Using these material properties, and the dimensions of the bar introduced, it was decided to bend the bars such that a plastic zone of 6mm in depth be formed on both the inner and outer diameters. Solving for the applied load in the equations

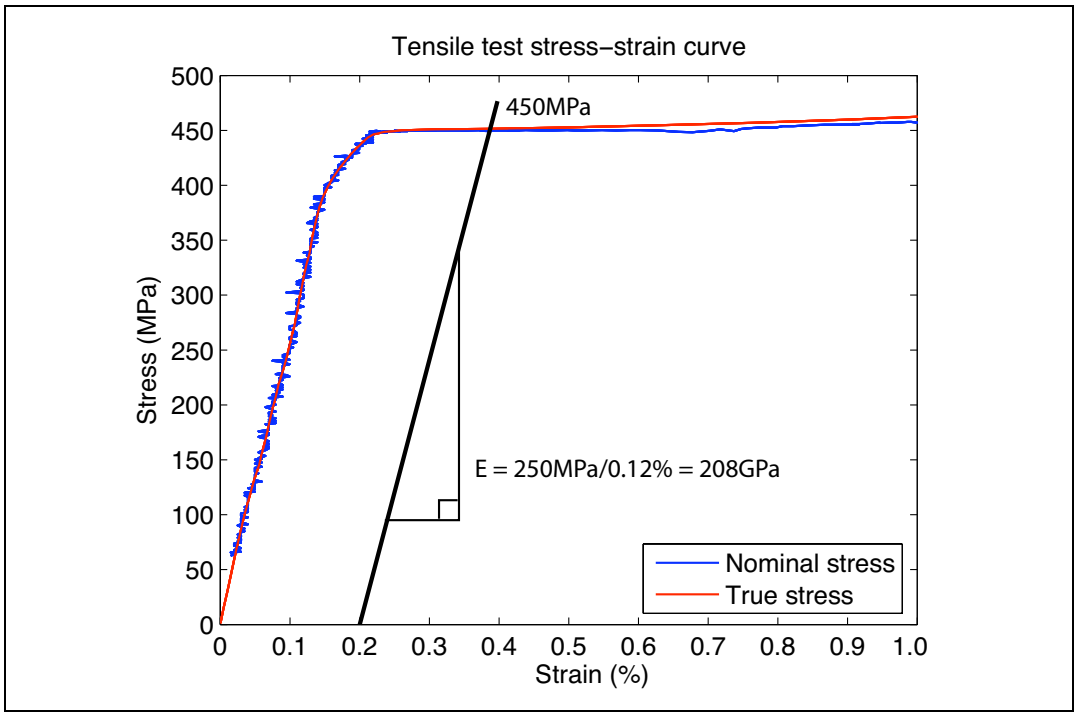

Figure 4-6. Tensile test curve for EN3B steel. True stress has been smoothed (50 sample average) for clarity. The Young's modulus was estimated to be 208GPa and the yield stress to be 450MPa.

presented in the previous section gave a value of 38.5kN. The loading and unloading curves, and the superposition of the two (giving the predicted residual stress profile for this sample) are shown in Figure 4-7.

4.2.3 FEM prediction of residual stresses

The analytical section assumed an elastic-perfectly plastic model. To produce a more realistic estimation of the stresses expected on the cut plane of the bent bar, a full three-dimensional finite element model was made. The four point bend procedure was simulated, in conjunction with the complete measured stress-strain curve as measured for the material. The model was built using ABAQUS 6.4 (Abaqus 2004), and full details are in Appendix B.

The complete half-model in Figure 4-8 shows the bar and the upper and lower rollers from the right hand side of the model at the end of the loading step, with the ensuing (exaggerated for clarity) deformation of the bar.

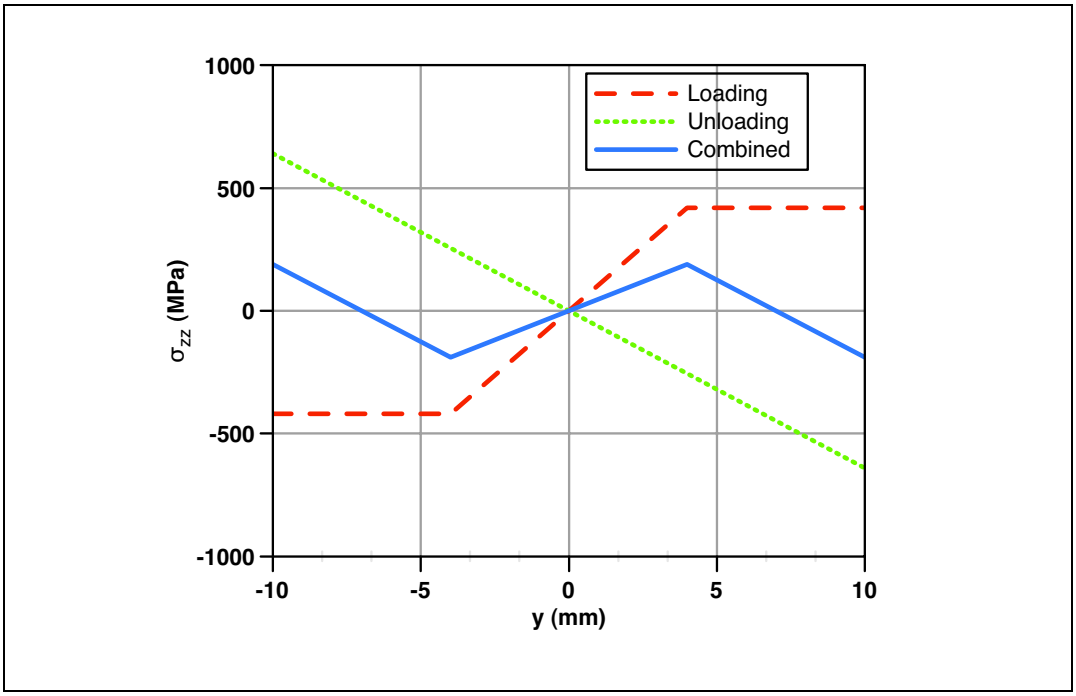

Figure 4-7. The two components of residual stress typical of a bent bar: the elastic-perfectly plastic loading (green) and the elastic unloading (red), with the superposition of the two showing the total stress after unloading.(blue) The plastic region is 6mm deep. A yield stress of 450MPa and Young's modulus of 208GPa was used. Stresses at the surface of the bar are +-188MPa and the interface between the plastic and elastic zone is at -+193MPa

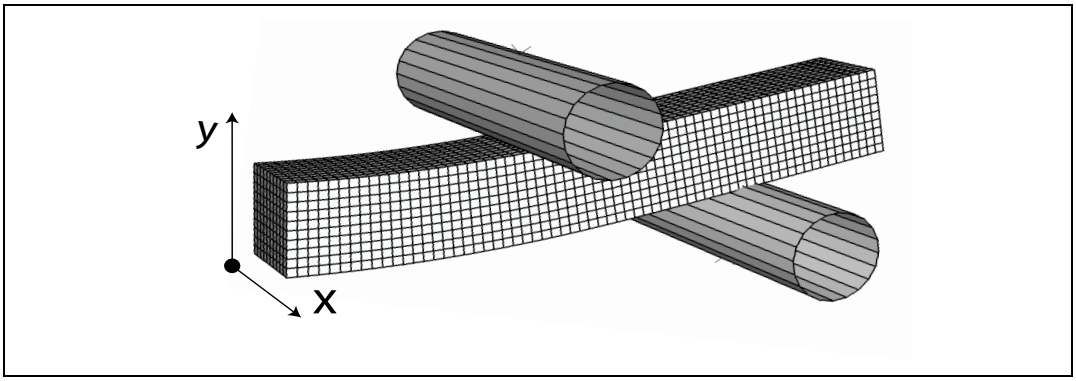

Figure 4-8. The finite element half-model (Section 4.5) used to simulate the four point bending process. Shown in the fully loaded condition, the left hand side (the cutting plane) is constrained to remain on the centre line, equivalent to the elements at that location in the complete bar. The x- and y-axes are shown. (Exaggerated 3x for clarity)

The ABAQUS input deck for this is shown as fourpointbend.inp in Appendix 2.2.

Results are shown in Figure 4-39.

4.2.4 Bending

Two identical samples were bent using the same Instron machine with a four point mechanism, as indicated schematically in Figure 4-9. An applied load of 38.5kN

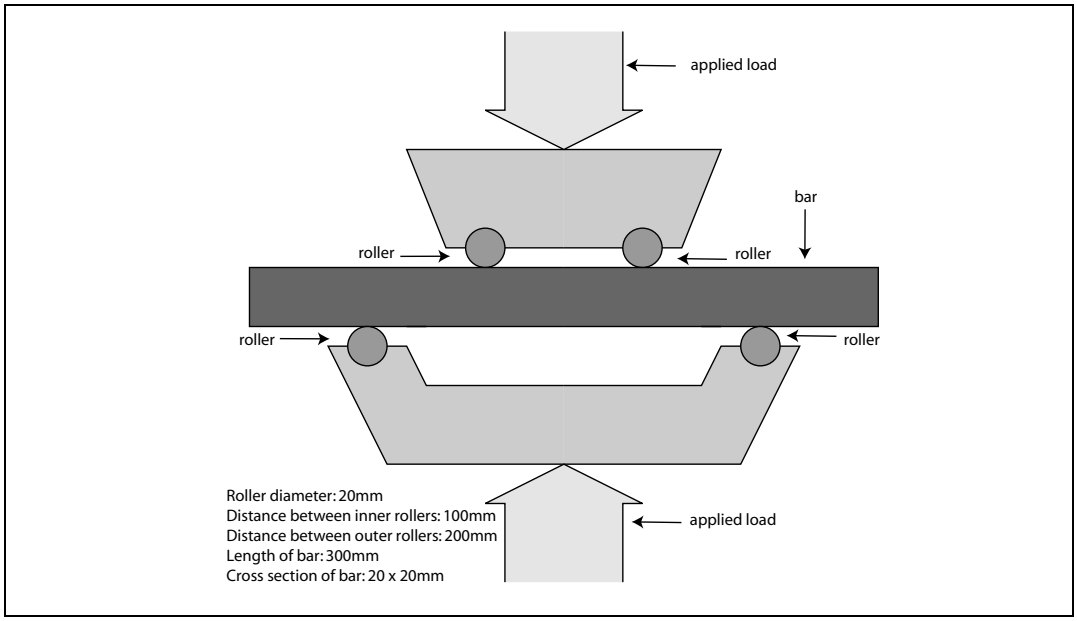

Figure 4-9. Schematic of a four point bend test rig. The load is applied vertically to the pair of jigs, in which the cylinders are free to roll as the bending occurs.

was used, inducing a region of plastic deformation predicted to be 6mm deep in the upper and lower portions of the bars where they lay between the inner rollers.

4.2.5 Cutting

To compare and contrast the cutting results for two different EDM machines, one of the bars was cut at a local machinists, Parkside, and the other was cut at the Department of Materials at the Open University.

The cut made at Parkside (sample 'PK') was done with a 0.25mm wire and a cutting speed of 2mm/hour. The other sample ('OU') was cut using a Fanuc Robocut with a 0.1mm wire and a speed of 6mm/hour. These parameters were chosen by the operators as best suited to achieving a skim cut finish with low likelihood of wire failure.

The two 'side' surfaces of the samples - that is those which were parallel to the plane of bending, were used to clamp the samples for cutting. The EDM wire was parallel to the bent surfaces (see Figure 4-10). This was done to facilitate restraint of the bars, but it is not ideal because of the increased bending moment that occurs as stresses are relieved in the tensile portion of the bar before the compressive section is cut. Any cutting artifacts are also made at the most important area of the sample, so if possible with uniaxial strain components, future cutting should be done at right angles to the variation of interest.

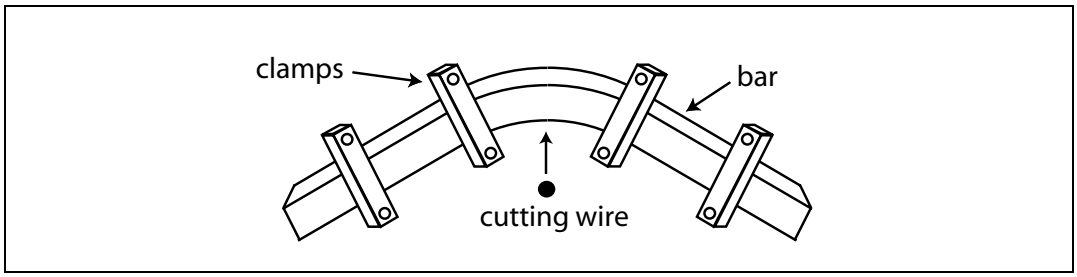

Figure 4-10. Plan view schematic showing bent bar (clamped), EDM cutting wire and cutting direction with respect to bent bar

4.3 Surface measurement

The contour method requires very accurate measurement of the profile of the cut surface. Prior to this project, no equipment capabale of performing this task was available, thus one of the first tasks of the author was to procure a suitable coordinate measurement machine for installation at Manchester. Although to be used primarily for the contour method, it was also to be a general purpose metrology tool, so a compromise of working volume, accuracy, speed, and ease-of-use was made. Most of the measurements reported in this document were made with this machine, and use was made of other facilities (Los Alamos, UC Davis) when high accuracy optical scanning was required. This section details a number of tests made and procedures developed by the author during this project to ensure a reliable measurement of the surface profile.

4.3.1 Modes of measurement

After evaluating a number of different instruments, a Mitutoyo CMM (model Euro-C-Apex (Mitutoyo 2001), working volume of 700 x 700 x 600mm) was procured. It

was equipped with the Renishaw SP600; a probe capable of both discrete ('hen-peck') and continuous ('scanning') measurements (Figure 4-11).

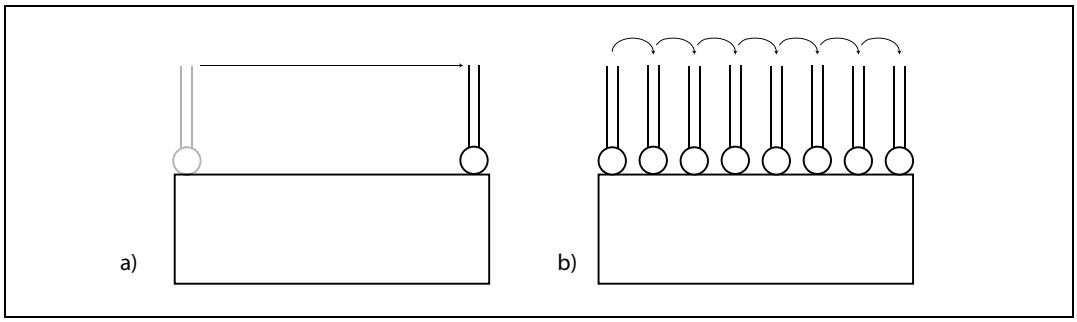

Figure 4-11. a) 'Continuous' probe movement, where the probe is brought into contact with the surface, then dragged over it. Surface features cause movement in the probe tip out of the plane of movement. Measurement speed is much higher than for the 'hen-peck' mode, but less accurate. Surface tracking (keeping the probe in contact with the surface using a constant force) complicates the controller design, particularly for surfaces with large perturbations. b) 'Hen-peck' probe movement, where the probe makes intermittent contact with the sample. This obtains the highest possible accuracy from the probe, because of the very controlled approach trajectory of the stylus.

The advantage of the scanning mode is vastly reduced measurement times -- the probe may move at 10mm/s without any difficulty over a nominally flat surface, whereas the henpeck mode requires about 3s/point.

A simple test to compare the quality of henpeck and continuous measurements was made using a small bar of titanium alloy (Ti-6Al-4V). The measurements (Figure 4-12) have been corrected for linear trending (that is to say, the removal of any background slope). The henpeck data was taken at a 200μm pitch, while the SP600 internally filtered a large (unknown) number of points, and recorded points at 100μm spacing. The standard deviation of the scanning measurement is 1.6μm whereas the henpeck mode is only 0.9μm.

In addition to the choice between scanning and hen-peck measurements, the motion of the probe head can also make a difference in certain situations. Uni-directional motion (Figure 4-13) has a considerable dead time at the end of each scanline, while the probe head is lifted from the sample surface and returned to a start position laterally displaced from the previous one.

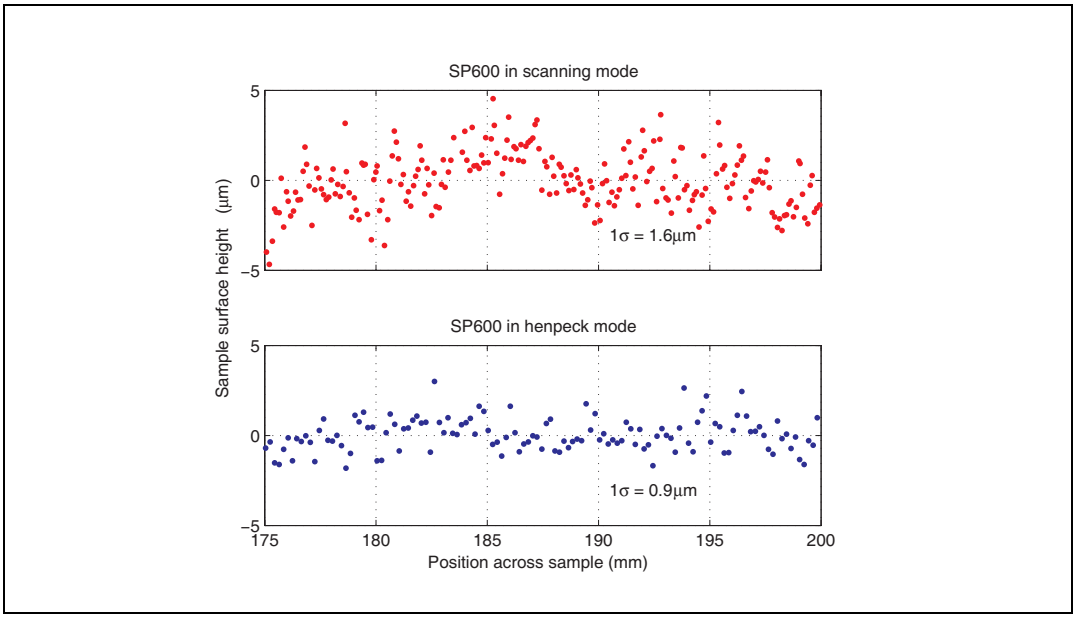

Figure 4-12. Two scans over the same Ti-6Al-4V surface made with the SP600 probe. The standard deviation for the scanning (upper plot) mode of operation is 1.6µm, whereas that of the henpeck (lower plot) mode is only 0.9µm.

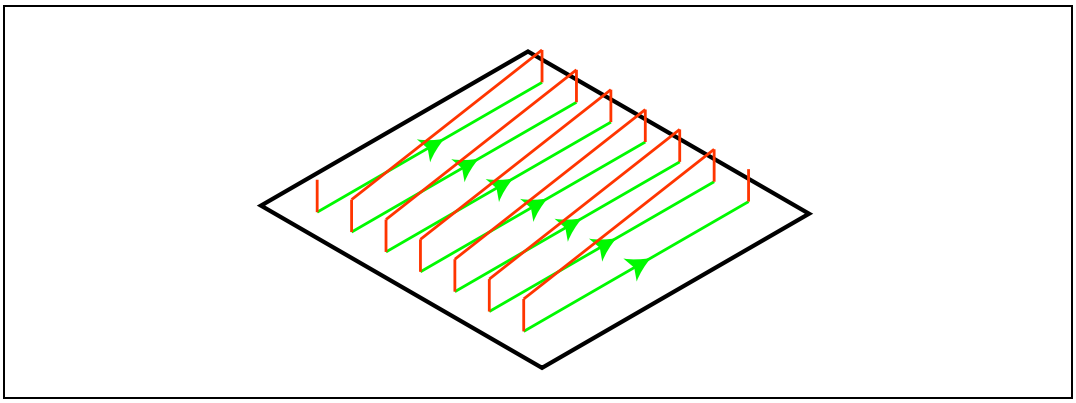

Figure 4-13. Schematic of uni-directional scanning. Green indicates the path of the probe when measuring, red when moving off-sample. Note that the probe must move the full length of the sample between each scanline

Bi-directional scanning (Figure 4-14) eliminates the dead time at the end of each scan line (which can be many seconds) and is therefore much faster over large scans.

Apart from speed, the other advantage of using the scanning mode is that continuous digitisation of the surface may be used to determine the location of the edges of the sample. To do this, the probe starts below the surface to be measured, ascends the side, measures the top surface and then descends on the other side, as

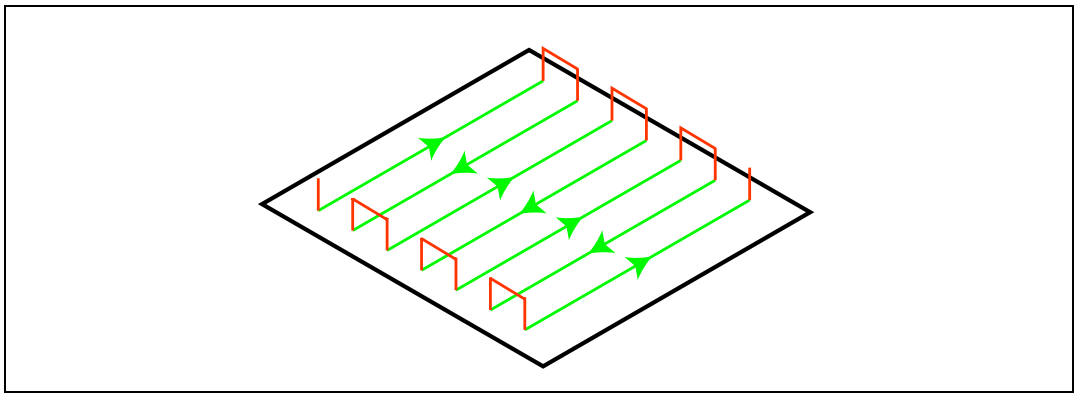

Figure 4-14. Schematic of bi-directional scanning. This mode minimises dead-time (red) between scan lines (green) but hysteresis problems in the implementation of the filtering in the SP600 made this difficult to use for high-precision measurements

shown in Figure 4-15. The full procedure to estimate the boundaries of the top sur-

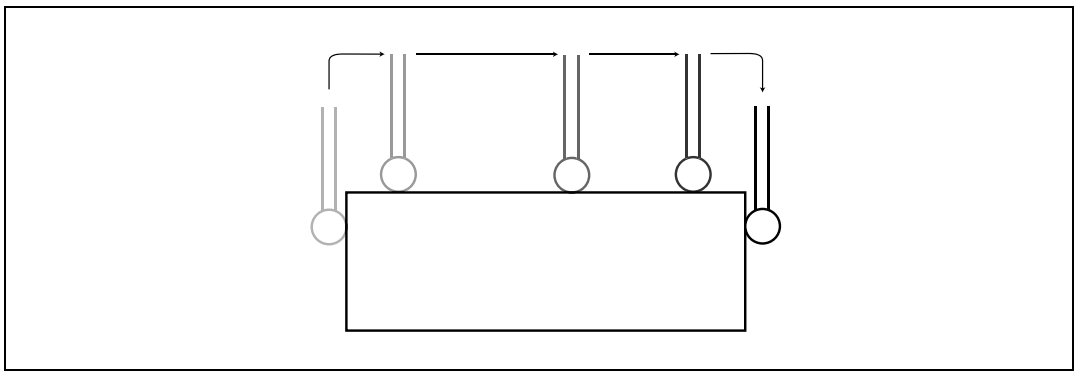

Figure 4-15. Probe path when attempting edge detection in continuous scan mode

face is explained in Chapter 5.

If the henpeck mode is used, then the measurements might be no closer to the edge of the sample than a complete pitch, leaving important data undetected. In samples where the stresses of interest are in the interior of the sample, this is less important, but very often the desire is to look at samples very close to the surface of the original sample. This is another point in favour of moving to non-contact measurement technology, where the transition region around the edge is much easier to distinguish.

4.3.2 Scanning artefacts: Wear

As mentioned previously, while the probing force may be quite small, the vanishingly small contact area of the probe sphere causes a large pressure to be applied to the surface of the sample. The Renishaw SP600 probe has a spring constant of 1.2N/mm in all directions, and the displacement condition that causes a trigger can be set in the software. Thus the pressure applied can be reduced by increasing the sensitivity of the probe. This has to be balanced against the likelihood of 'air triggers', where false measurements are made.

In order to evaluate the depth of excavation that can be caused by the scanning probe, three consecutive scans over the same path were made on an steel sample. Figure 4-16 shows the surface height for each of the three scans. Table 4-2 summarises the average value for each scan - on average, each pass reduced the mea-

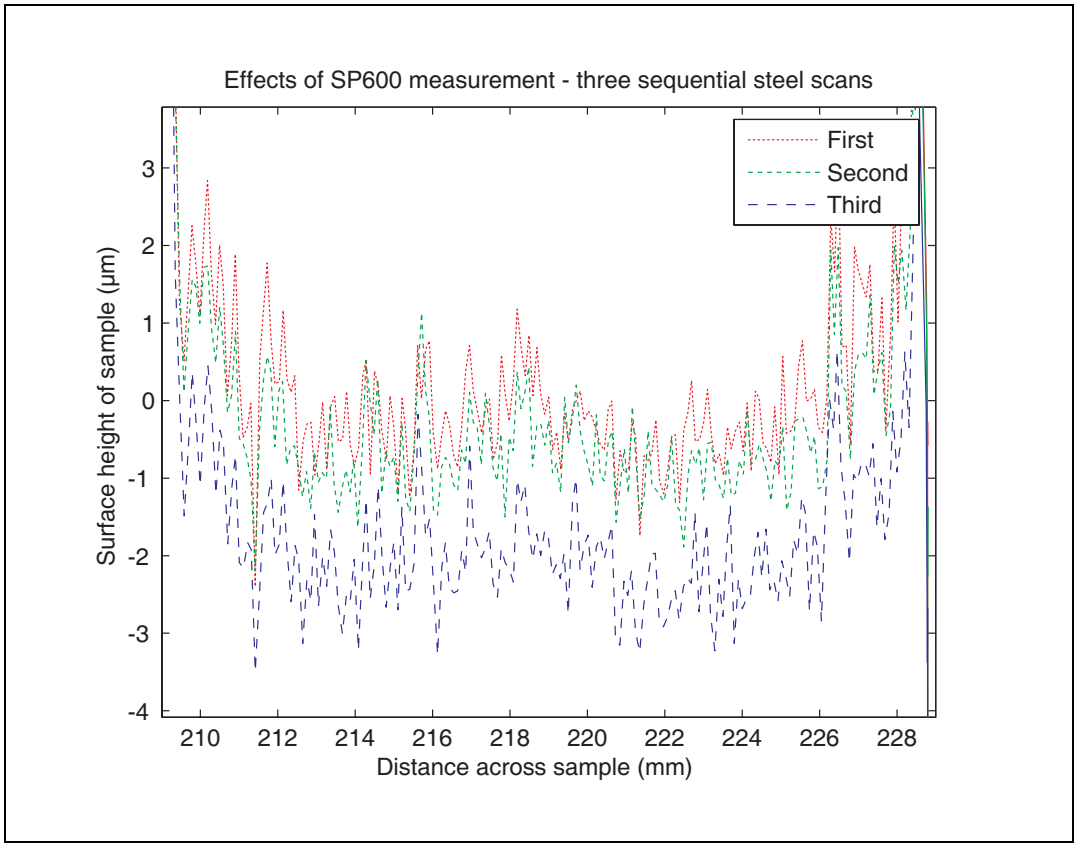

Figure 4-16. Surface height after multiple coincident scans across steel showing surface wear - see Table 4-2 for average heights.

surement value by just over 0.5um. While this is an observable effect, it is very small in comparison to other errors possible in the contour method (particularly as the likelihood of traversing the same path multiple times is very small) and it is thus left unaccounted for.

Scan number	Average surface height
One	0.2μm
Two	0μm
Three	-1.4μm

Table 4-2. Average surface height of consecutive scans covering the same path on an aluminium sample

4.3.3 Scanning artefacts: Collisions

Of course, when the CMM is moving rapidly within the working volume, undesired collisions sometimes occur. These can cause significant damage to both the part and the machine itself. There is some degree of protection in the SP600 probe head - if the collision is perpendicular to the *z*-axis of the probe, then the kinematic mount will release. Likewise, the articulating joint on which the SP600 is mounted (Renishaw PH10MQ) will disengage under stress, preventing further damage. Figure 4-17 shows the effect on a steel sample when neither of these protection mechanisms worked. A full recalibration of the probe tip is essential after any unintentional contact to ensure that the accuracy of the machine is maintained, and after serious collision, requalification by the manufacturer is recommended.

4.3.4 Continuous CMM measurements of both samples

These contour measurements were made using the SP600 probe, a tactile probe that is kept in contact with the surface as it is dragged from one side to the other. The position of the probe centre was recorded at 100μm intervals. This was done at a pitch of 1mm across the width of the bar, to produce 18 scanlines. Figure 4-18 shows these measurement locations. Appendix H contains the full listing of the gen_cmmscan script that automatically generates the scanning instructions.

4.3.5 Henpeck measurement of the PK1 sample

It was clear from the continuous measurements results (shown later in Figure 4-29 and Figure 4-30) that PK1 was the best cut sample, but the noise of the measure-

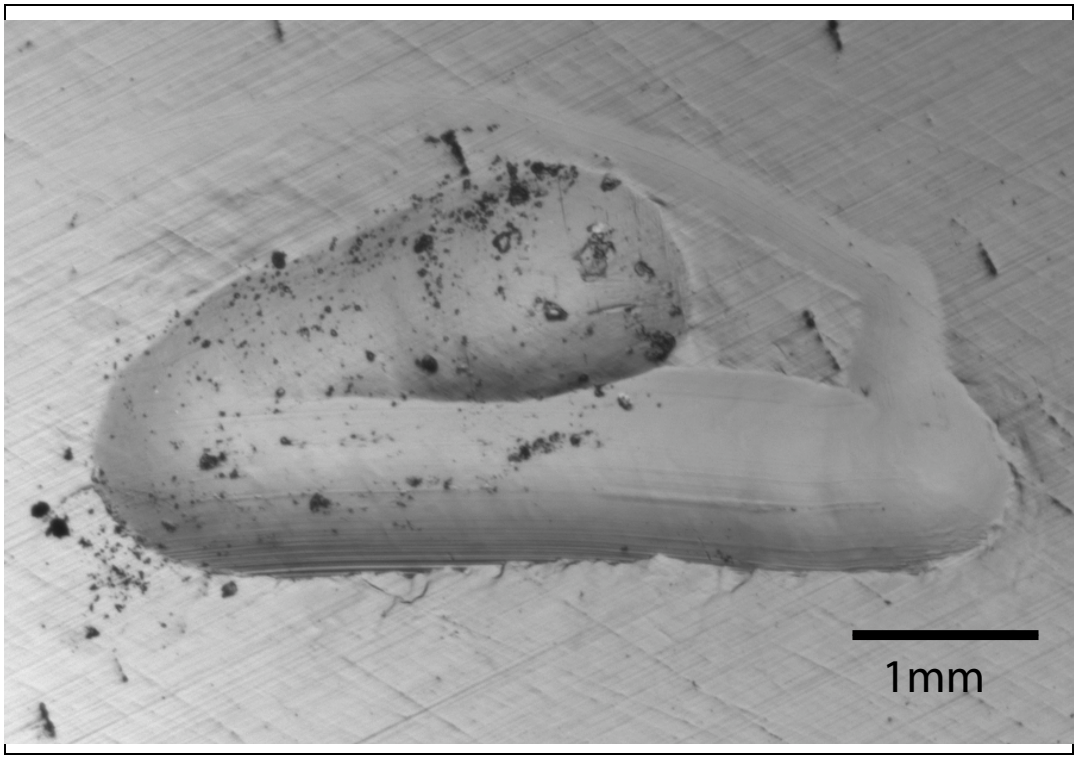

Figure 4-17. Optical micrograph of a steel sample after high speed impact by a 8mmϕ ruby probe.

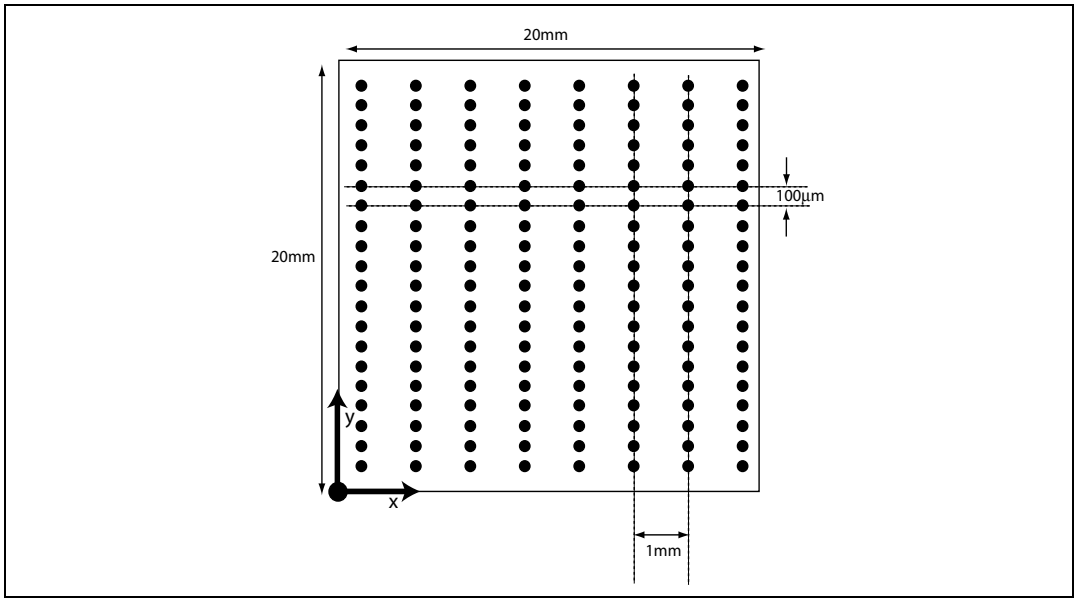

Figure 4-18. Measurement locations on the 20mm x 20mm bent bar cut surface. An individual scanline (continuous contact) results in points at a 100μm pitch. Each scanline is 1mm apart.

ments in combination with the practical difficulties of fitting non-uniformly pitched data led to PK1 being remeasured using a 200μm pitch in *both* directions -

at right angles to each other - in the henpeck mode, and then reprocessed. The contour map of the averaged data for PK1 (henpeck), is shown in Figure 4-19.

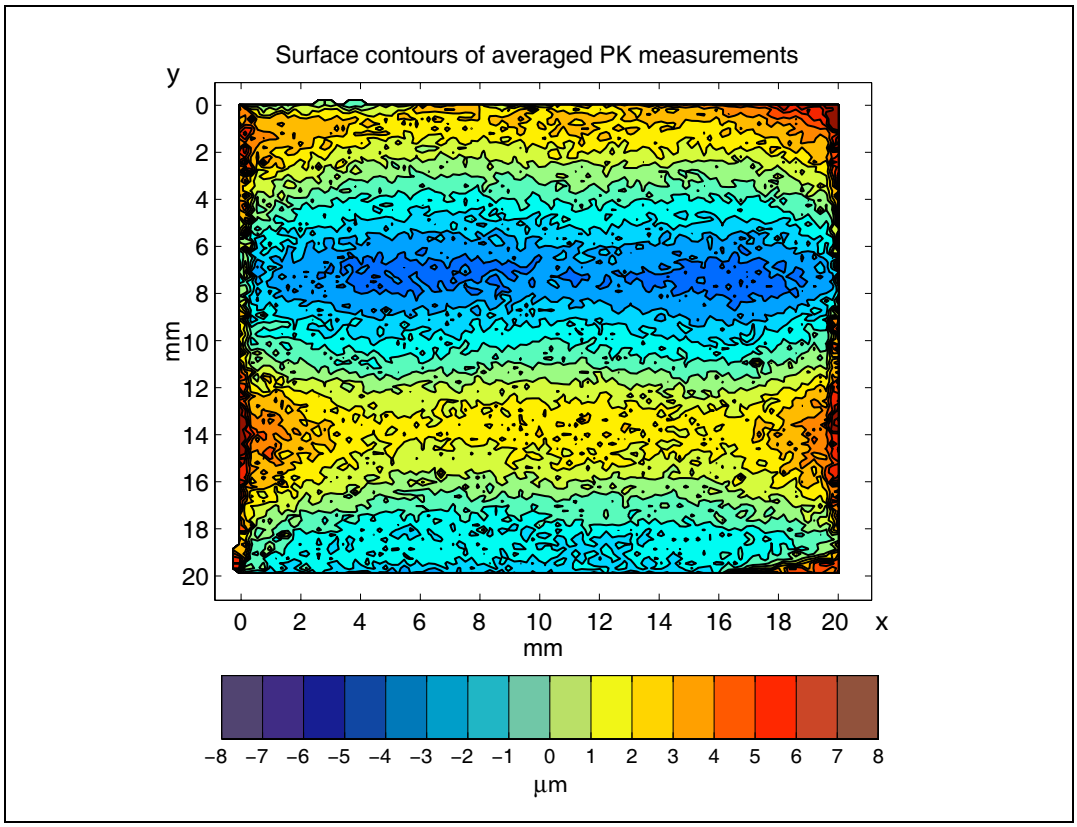

Figure 4-19. The contour map of the averaged displacement data measured from the EDM cut surface of PK. The majority of the sample (1σ) lies within a range of ±2.3µm. Measurement made in the henpeck mode.

4.4 Surface data processing

The previous section covers the measurement of the surface data. However, before measurements can be used to derive stresses they must be processed. Any measured dataset, from any source, is a combination of signal and noise. Noise may be described as anything that obscures the interpretation of the data, and it comes from a number of different sources in surface measurement. It can be divided into two separate categories: system noise, and outliers. System noise is generated by both mechanical and electrical sources in the measurement instrument: backlash, vibration, thermal distortion, digitisation noise and others. This noise is often statistical in nature, and repeated measurements (or longer measurements at the

same location) can increase the ratio of signal to noise. However, there are also very often completely spurious data points which appear to have no explanation for their existence which adorn the dataset. Outliers must be removed, and system noise should either be removed or at least accounted for. Section 4.4.1 deals with noise and the removal of unwanted points.

In the contour method, there are always two surfaces which are measured, one for each half of the cut side (see Section 3.2). At some point in the process these surfaces must be averaged and to do that they must be in alignment with each other. Section 4.4.2 examines a number of ways of achieving this.

The two aligned datasets must then be combined and represented as a surface (that is, a form from which heights may be extracted at arbitrary locations). Surface fitting is a vast area of interest across disciplines - a brief overview is presented in Section 4.4.3 where the approach taken by this author is described in more detail.

4.4.1 Noise reduction

Depending on the measurement technology, the noise present in the data can vary considerably. Tactile CMM measurements do not generally suffer from large quantities of background noise but do encounter problems close to sample edges and may also record false points ('air-trigger') when the force threshold is set too low. Optical measurements are often very noisy throughout, but as the sampling density is much higher (and quicker) measurement statistics can be used to improve the ratio between signal and noise. Contamination of the sample surface also occurs, and any scratches or defect in the surface can cause unwanted points to be recorded. In principle, the removal of these is straightforward, but trying to identify them amongst several thousand points can be difficult. The measurements made for this project were primarily done with a tactile probe. As shown in Figure 4-20, the probe tip, having a finite radius, may sometimes when descending vertically make contact with some part of the sphere other than the bottom. As the probe tip position is measured to the centre of the probe tip, then the probe radius is added in with the direction of approach, this leads to measured points which are considerably below the level of the surface. Likewise, if the probe is used in a con-

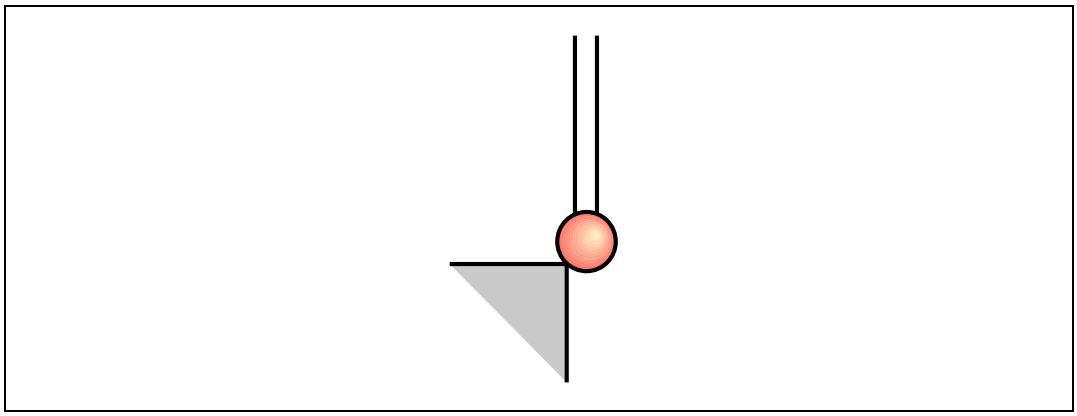

Figure 4-20. A tactile probe may register a point that is not actually on the top surface. This needs to be removed manually before further processing of the data

tinuous fashion, being dragged across the surface, a large number of points will be measured as the probe is ascending or descending the 'walls' on either side of the surface of interest. A number of possibilities for automatic removal of these points have been considered.

Although it was attempted to try and identify these points automatically by looking at the gradients in the point cloud, it proved to be simpler and faster for the operator to remove these points by eye. To do this, the author has written a small program for noise removal, called `cmm_clean`. Implemented in Matlab, it is fast and efficient, permits the user to remove unwanted data points and also subtract planar components from the dataset. By way of an example, a screenshot of the program viewing a pointcloud of a railway rail is shown in Figure 4-21.

The point cloud may be seen from four directions: the three orthogonal axes, and an isometric view (as seen in Figure 4-21). The colour of each point corresponds to its height in z, as detailed by the colour bar. On the left hand side of the frame, there are a series of buttons (which are also accessible with keyboard shortcuts). Full instructions forthe usage of cmm_clean are in Appendix D.

4.4.2 Surface alignment

The straightforward approach to alignment of the two cut surfaces would be to measure them with reference to a common coordinate system. Whilst optical scanners generally work in a fixed frame of reference (relative to the machine move-

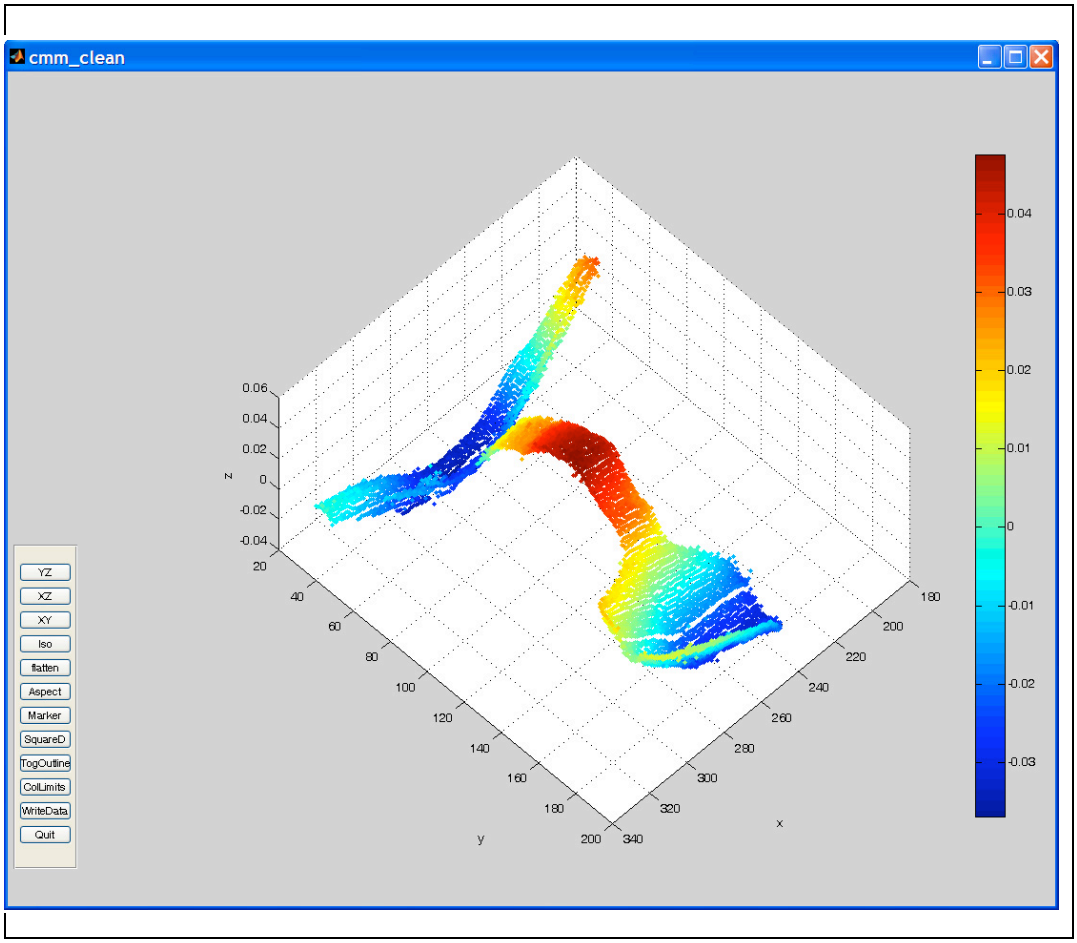

Figure 4-21. The author's program `cmm_clean` being used to remove noise from the measurement of a railway rail. In this case, all units are millimetres, but the data is treated as unitless. The buttons on the left side of the frame control the various aspects of the software.

ment axes) most CMMs have the capability to change their frame of reference relative to geometric features on a part. While it is possible in some cases to make measurements of the two halves of the cut by aligning the CMM axes to certain features present on the sample boundary, it is not always the case. Particularly with samples that do not have strong geometrically primitive shapes, ascertaining where the exact location of a radiused corner is can be quite challenging (for instance, the rail shown in Figure 4-21). For this reason, the author felt a better approach to be that of using the whole perimeter of each half of the sample as an alignment guide. By matching the whole outline at once, it is seen to achieve excellent results. This removes the need for time consuming and error prone procedures

on behalf of the operator, who need only lay down the samples approximately (within 10°) aligned to the machine axes.

The script that performs the alignment, `cmm_align`, takes as input the outline files (measured at the very beginning of the sequence) and the two corresponding data files. By arbitrary convention, the files from the sample on the left side of the CMM are termed the 'reference' files, and are static, while those from the right side are termed 'floating' and are moved to lie coincident with the first. The first action is to mirror the second surface, as shown in Figure 4-22. This can either be done across

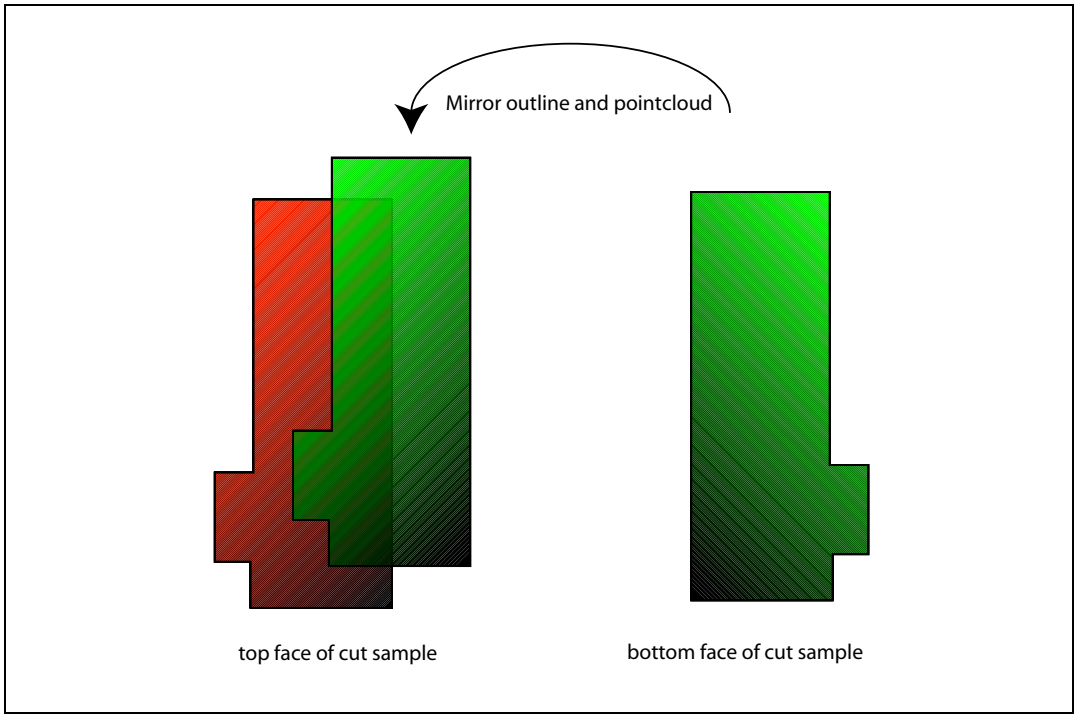

Figure 4-22. Schematic of mirroring of second dataset onto first. Axis across which to mirror can be selected.

the *y*-*z* (default) or *x*-*z* planes. If the data are badly out of alignment, the `square-data` routine is used, as shown in Figure 4-23.

After squaring off the datasets, both are translated to a common origin, using the mean values of the *x* and *y* coordinates in the pointclouds. If the samples boundaries have very complex sections (such as weld flash (cf. Chapter 7), with very small details that would take considerable time to measure without aiding the results)

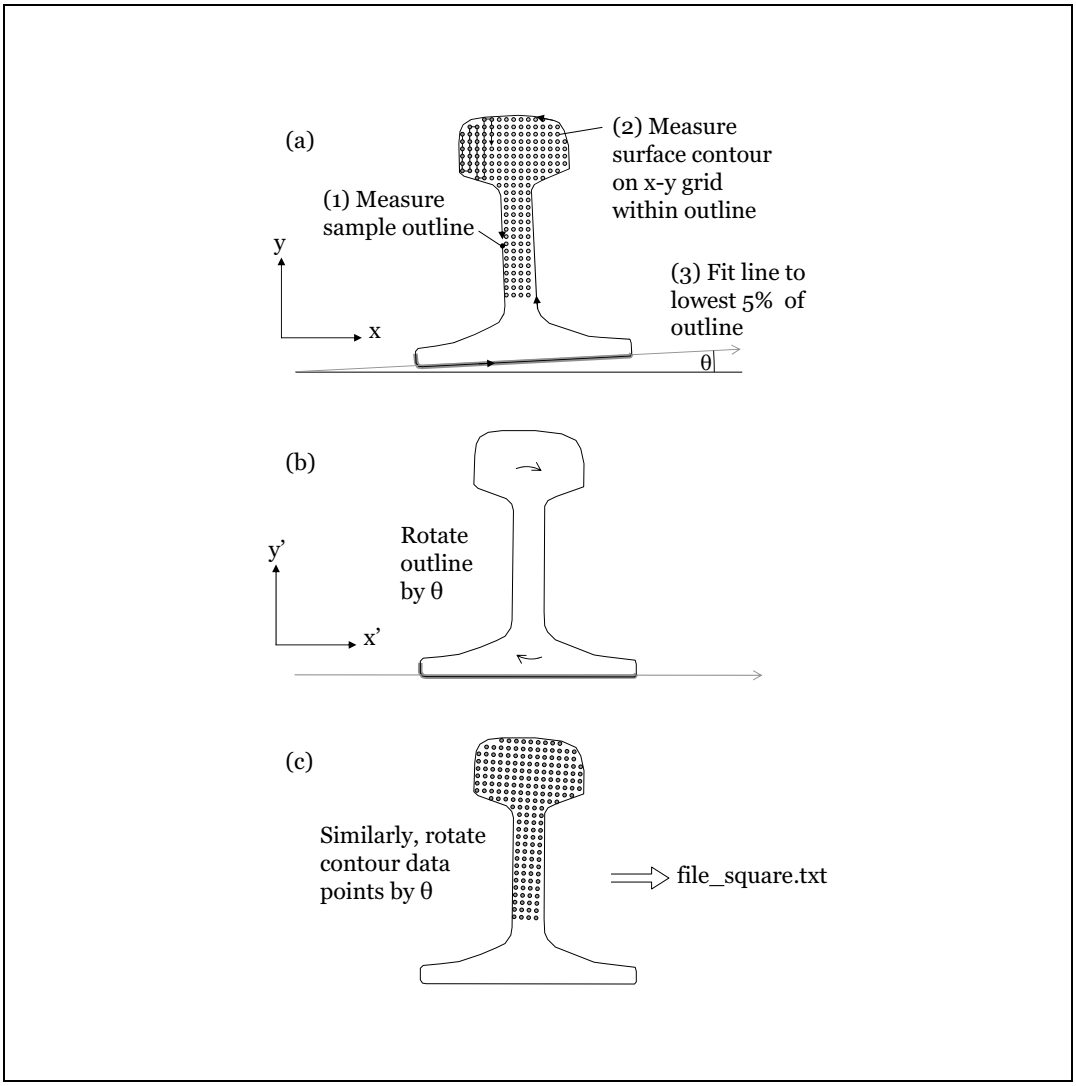

Figure 4-23. The procedure for squaring off a dataset works on the assumption that the sample was measured with a nominally flat edge closest to the user (minimum y values for the CMM). a) the bottom 5% of the points are selected, and a straight line fitted to them. b) the boundary is rotated so that the straight line runs parallel to the x-axis. c) the dataset is rotated by the same amount, and both the outline and the dataset are written to disk with the "_square" suffix appended.

then these can also be removed from the outlines, so as not to affect the subsequent steps.

As the two outline files, while representing the same shape, do not actually contain coincident points, it is not possible simply to perform a one-to-one matching of points from one outline with the other. The alignment is done using an iterative closest point (ICP) (Besl 1992) procedure, which involves calculating the distance from every given point on the 'reference' outline to all possible points on the 'float-

ing' outline. The minimisation of the global sum of these distances is done by rigid body translations and rotations (in two dimensions) of the floating outline file, either until a distance criteria is reached, or an iteration threshold is exceeded. In most cases, the distance criteria used is 50μm, and the number of iterations limited to 25. More details on the iterative closest point transform can be found in Besl's paper, or (Fisher 2005).

Finally, the transformation matrix that represents the best alignment of the floating outline is applied also to the floating pointcloud. A single outline file is written to disk, along with the two aligned datasets.

4.4.3 Surface fitting and combining profiles from the two halves

Measurement and cutting artifacts contribute noise to the displacement data. In addition, the measurement locations are unlikely to be those of the nodes in the finite element model, so it is necessary to fit a surface to the points that can be evaluated at arbitrary locations. Additionally, as there are initially two datasets, one from each half of the cut sample, these need to be combined, either pre- or post-surface fitting. It is not immediately clear in which order these two tasks should be performed. The datasets from the two cut surfaces are aligned in the same coordinate system, but the points from one side may or may not line up with those from the other. This means that performing point by point averaging is not possible. On the other hand, fitting two surfaces to the datasets, then evaluating them at coincident locations and averaging those results could, depending on the surface fitting parameters, lead to the incorporation of cutting artifacts or other defects that should be averaged out immediately.

The sequence adopted by this author is to take the dataset for each side and linearly interpolate this onto a common grid, after which the two sets may be averaged.

There are many ways to create and describe surfaces deriving from points, each having it's own merits. For the contour method, there are two main reasons for fitting a surface:

- To be able to smooth the surface a known amount, removing any noise still present in the dataset while preserving the relaxed strain contours.

- To permit the evaluation of the boundary conditions at the node locations determined by the FE mesh. These are unknown at the time of measurement.

The simplest way of fitting data (whether in one dimension or two) is with a polynomial. For surfaces, the simplest ('zero-th order') fit is the surface which has as its height the average value of the data points. The first order is a linear plane, the second a paraboloid, and so on. However, a surface which needs a 3rd order curve to capture it's shape in one dimension may only need a 1st order curve for the other direction. Further more, polynomials assume that the variation of the surface is constant from one boundary to another - and this is most certainly not the case when examining the residual stresses in a sample. Most often there are large areas of low stress with a smaller section where the stress magnitude is very high. Polynomials are unable to represent these types of functions adequately.

Initial work by Prime et al. (Prime 2001) used Fourier surfaces. Described more fully in many texts, (*cf.* Pain 1993), these describe the surface as a tensor product of transcendental function series. The higher the order of the fit, the greater the frequency component that is represented in the signal. Even a square wave can be fit with an infinitely high order Fourier series, but anything less than infinite representation leads to a oscillating effect at the edges (known as Gibb's phenomenon). If it were important to characterise the frequency spectra of the surface, Fourier surfaces might be more desirable, but this is not necessary for the contour method.

Polynomials can actually be very accurate representations for small areas of smooth data. If one were to subdivide the data that were being represented into small smooth areas, and use a low order polynomial for each, one could represent very accurately large complicated datasets with a simple set of parameters. The American mathematician, Schoenberg, coined the phrase 'spline' to describe this curve (Schoenberg 1946). Figure 4-24 shows how a number of different simple polynomials are used to composite a single more complex curve. A spline is described by the coefficients of the polynomial used in each section and the break locations, (often called 'knots') which specify the domain on which each polynomial is to be used. The actual fitting of the spline is usually accomplished by mini-

mising the error between the data points and the fit in a least-squares sense. In the work done by this author, two dimensional ('bivariate') cubic smoothing splines have been used to fit the surface data with varying break locations assessed on a case by case basis.

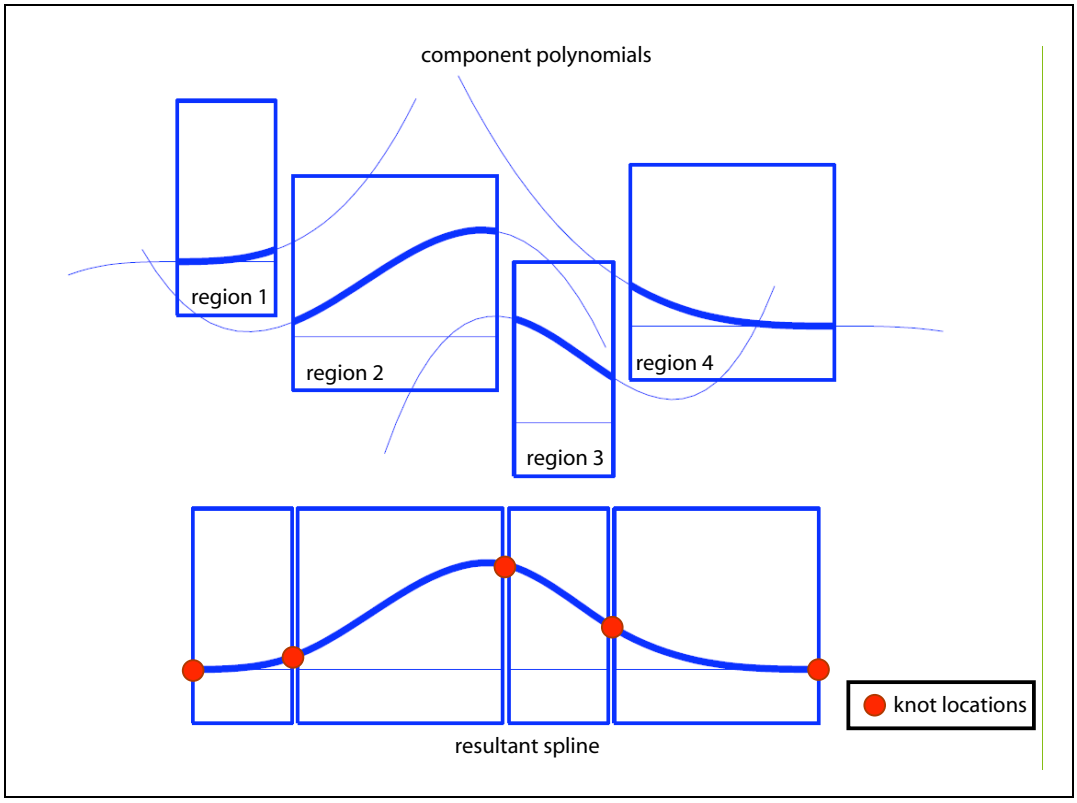

Figure 4-24. Construction of a spline - piecewise smooth combinations of polynomirals

The validity of a surface fit may be estimated in many different ways, but doing so without any characterisation of the measurement device is difficult. This is because there is no underlying model of what the data should look like to be able to compare the measurements with. At one extreme, that of underfitting (over smoothing), the fit obscures all legitimate detail that was measured, whils at the other, of overfitting, the fit can become an interpolant, connected the noisy values together.

Surface fitting may be characterised by a goodness-of-fit indicator. For normally distributed data (which it may be assumed that that produced by a coordinate measurement machine is), the standard deviation of the errors between fit and raw

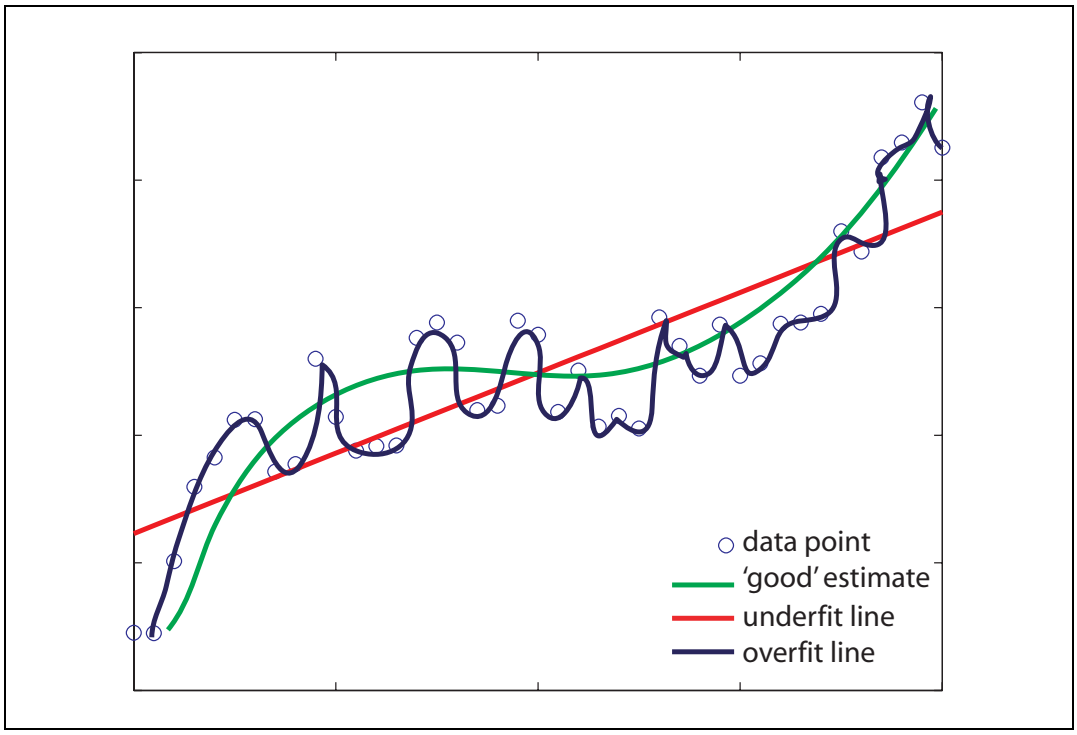

Figure 4-25. With noisy data and no *a priori* model of the underlying surface, both underfitting and overfitting are possible errors.

data describe this. However, with any smoothing fit, the error falls as the smoothing becomes closer and closer to interpolation, and there is no minimum after which the goodness-of-fit indicator starts to rise. For the case of the bent bar, a purely visual estimate is used as a sufficient good indicator of fit. The plot of residuals for an overly smooth fit has gross trends visible, while the residuals for an interpolation are zero. Given a range of splines, the fit chosen is the *first* one for which the residuals do no exhibit any trends as one moves from high to low degrees of smoothness. This is demonstrated in Section 4.4.6 concerning the bent bar specimen.

This preliminary method of fit determination is clearly subjective, and in Chapter 5 is replaced with a robust and objective error measurement. However, both techniques, while adequate for simpler samples do not work well in cases where the displacement data has varying gradients: a uniform fit across the entire sample leads to overfitting in some areas and underfitting in others. Advanced non-uniform fit-

ting techniques are developed in Chapter 7 and Chapter 8 where they are applied to a linear friction weld and a laser shock peened plate, respectively.

The `fit_spline` script has been developed by the author to facilitate the surface fitting of contour data. Taking as input an outline and the two aligned data files, it interpolates the two datasets onto a common grid, the pitch of which matches the pitch of the original data. The average surface can then be produced point-by-point. The user is asked what knot densities should be used, and the script generates a bivariate cubic spline for each knot spacing. Each spline is evaluated and compared against the original data set to produce a set of residuals. These are then shown to the user from graphical evaluation, and the splines saved to disk for evaluation later in the modelling stage.

4.4.4 Sample perimeter determination

The alignment of the samples was done manually, so the cut surface is not necessarily exactly square to the machine axes. A planar surface was fit to the data, permitting the correction to a truly horizontal surface.

One of the difficulties with the contour method is the determination of the edges of samples. In this case, the probe was started from the side of the sample, allowed to climb up to and traverse the cut surface, then descend slightly on the far side.

The probe was a 2mm diameter synthetic ruby sphere, and the correction for the probe radius was performed after measurement. For this geometry (the sides being at right angles to the cut surface) the following procedure was used (see also Figure 4-26):

1. Fit a vertical line to the vertical portion of the data (z-axis)
2. Fit a horizontal line to some of the top surface data
3. Offset the vertical line towards the sample by the probe radius (a)
4. Offset the horizontal line downwards by the probe radius (b)
5. Find the intersection point of the two lines. (c)
6. Denote this as the 'real' corner of the sample

7. Project this corner point vertically onto the data, and accept only data points between this point and the matching point for the other corner as valid for analysis. (d)

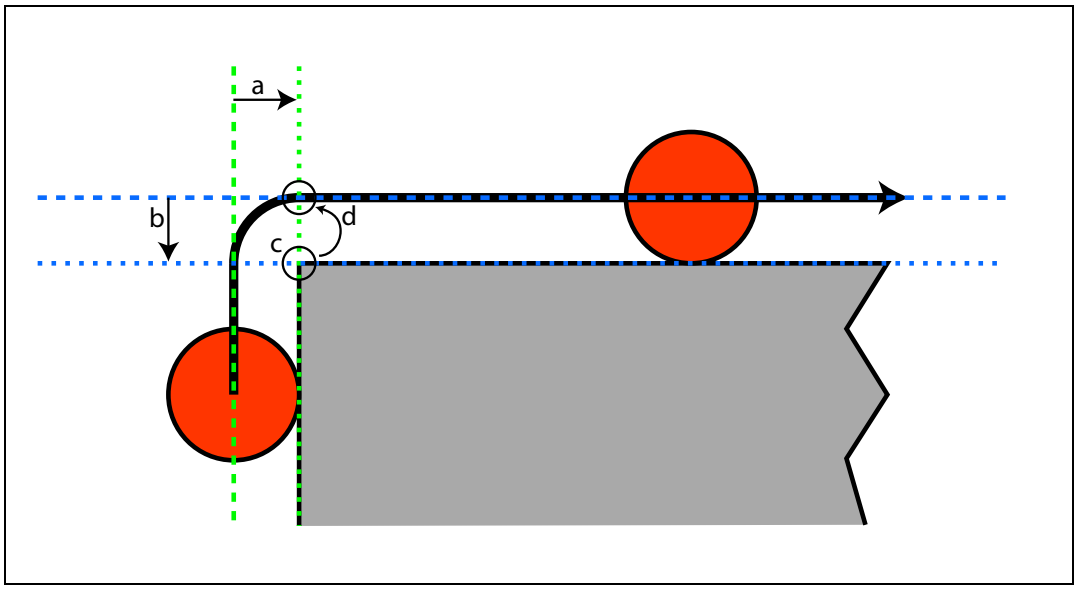

Figure 4-26. A schematic of the edge detection process used with data measured with a continuous tactile probe. The probe (red circle) is programmed to travel up a small part of the *side* of the sample before traversing the top surface. A linear fit is made to the data from the vertical section, then displaced laterally by a probe radius (a). Likewise, the bulk of the data from the top surface is linearly fit and shifted vertically (b). The point of intersection (c) is computed. This point is the estimated corner point of the sample. Point (d) is a single probe radius vertically above (c). The same process is performed at the other edge of the sample, and the data is considered to be valid between the two (d) points.

Corresponding scanlines from each of the two cut surfaces (two halves of the sample) are then paired and overlaid on one another. The method devised for cropping the lines can be adversely affected by a number of factors (non-right angled corners, noise in data used for linear fits), and each half of the pair may not be the same length. Each scanline is compared with the adjacent pair, and any difference in endpoints that exists is reduced by sliding the scanlines back and forward until the profile of the scan itself is a best fit match. An example of this is seen in Figure 4-27.

Once matched, the two surfaces are averaged together. Figure 4-28 shows the averaged data for a single scanline, both without (top) and with (bottom) correlation.

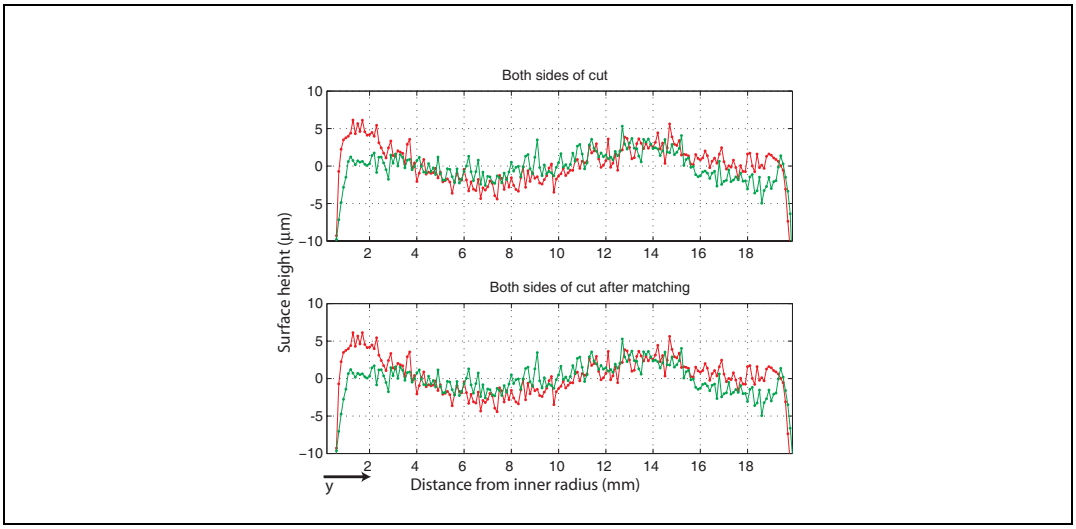

Figure 4-27. Line profiles across the two (red=left, green=right) cut surfaces of OU3, showing the raw overlay (top) and the correlated overlay (bottom)

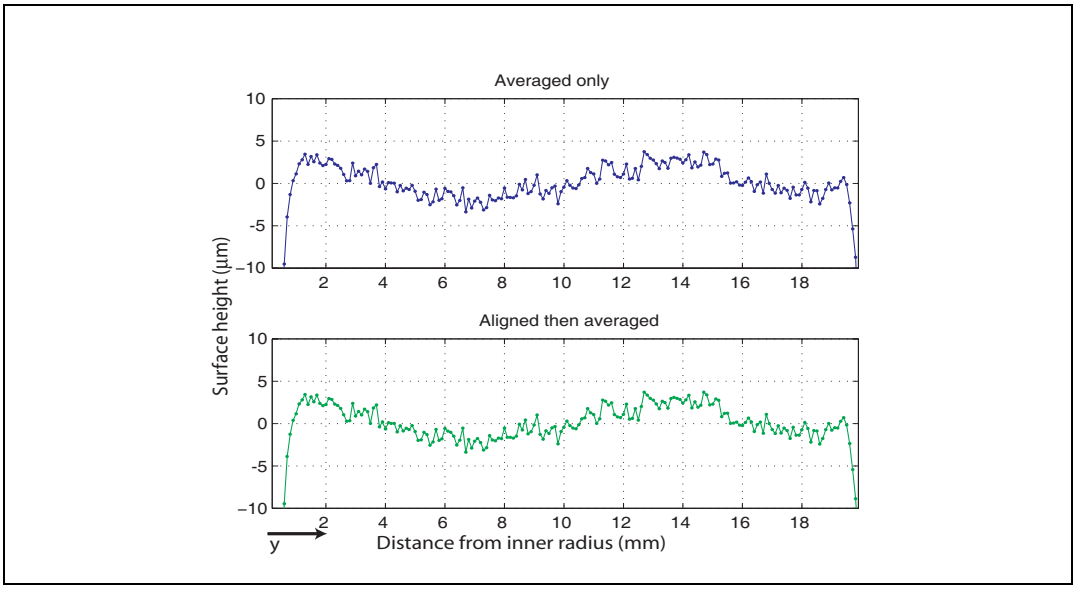

Figure 4-28. Averaged data from the two halves of the cut OU3 bar, showing that in this case the correlation is not necessary as the equivalent sections of the data have been extracted from both sides (top - raw average, bottom - average of correlated scanline)

All 18 scanlines, made at 1mm intervals, are overlaid - this should produce a series of coincident lines if the profile of the surface truly varies in only the direction measured. The next two figures (Figure 4-29, Figure 4-30) show the results for the OU and PK samples.

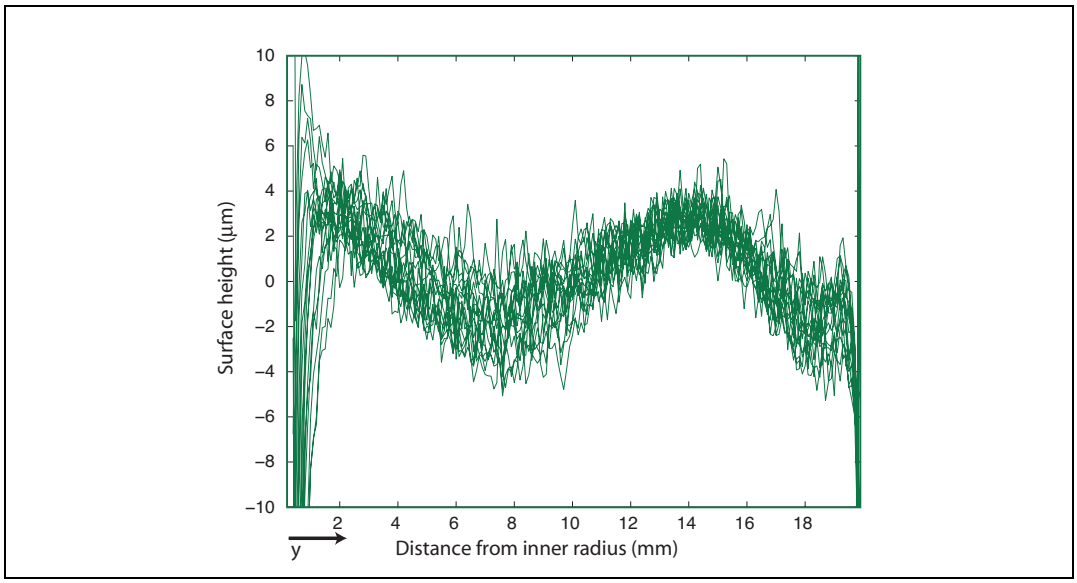

Figure 4-29. All averaged scanlines for the OU3 bar, overlaid on top of each other, showing variation across the sample

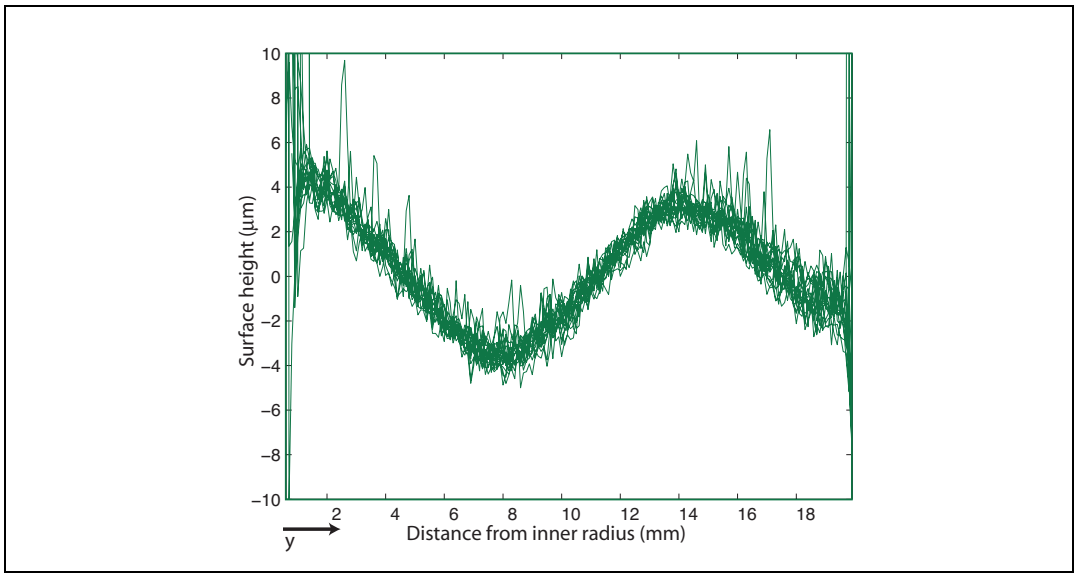

Figure 4-30. Overlay of all averaged scanlines for the PK1 bar showing much more consistency across the 18 lines

It is clear that the surface roughness of the two cuts differs by some qualitative amount. Because of the smoother cut of the PK1 bar, only these data are processed further. All 18 scanlines across the sample are averaged, as shown in Figure 4-31.

Aberrations within 1mm of the edges are primarily due to cutting artifacts, which occur as the wire finally separates the part into two pieces and the electric field

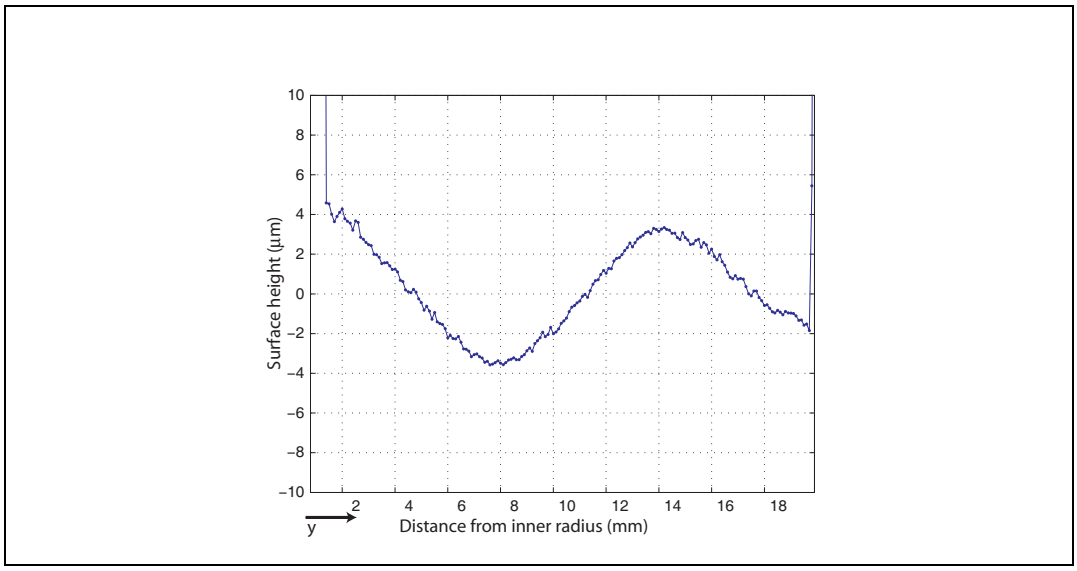

Figure 4-31. The final average across the PK1 bar of all 18 scans, showing the averaged cut height from the entire width of the bar

changes rapidly. A lip at the exit is often seen, and if not removed (as was done for later samples) can lead to this effect.

4.4.5 Fitting continuous data

A series of preliminary spline fits were made for the PK data. While the actual pitch of the raw data is 1mm laterally (between scanlines), the pitch *along* the scanlines is 100µm. Figure 4-32 shows six different spline fits, ranging from knot spacings of 10mm down to 0.3mm. It is seen, particularly in the finer pitched splines (0.625mm and 0.3125mm) that considerable periodicity appears. The spline is uniformly pitched in both x and y axes, so while the y knot spacing is still above the data density (100µm), the x knot spacing is less than the data density in that direction (1mm). This causes overfitting and hence the visible rippling in the surface. To avoid this, one should either make measurements at the same pitch in both x and y or extend the spline fitting to permit different knot spacings in the two axes.

4.4.6 Fitting results

The henpeck measured data of both halves of the cut were processed using the method described in Section 4.4: manual removal of outlying points, flat plane removal, dataset alignment, and meshing onto a single grid.

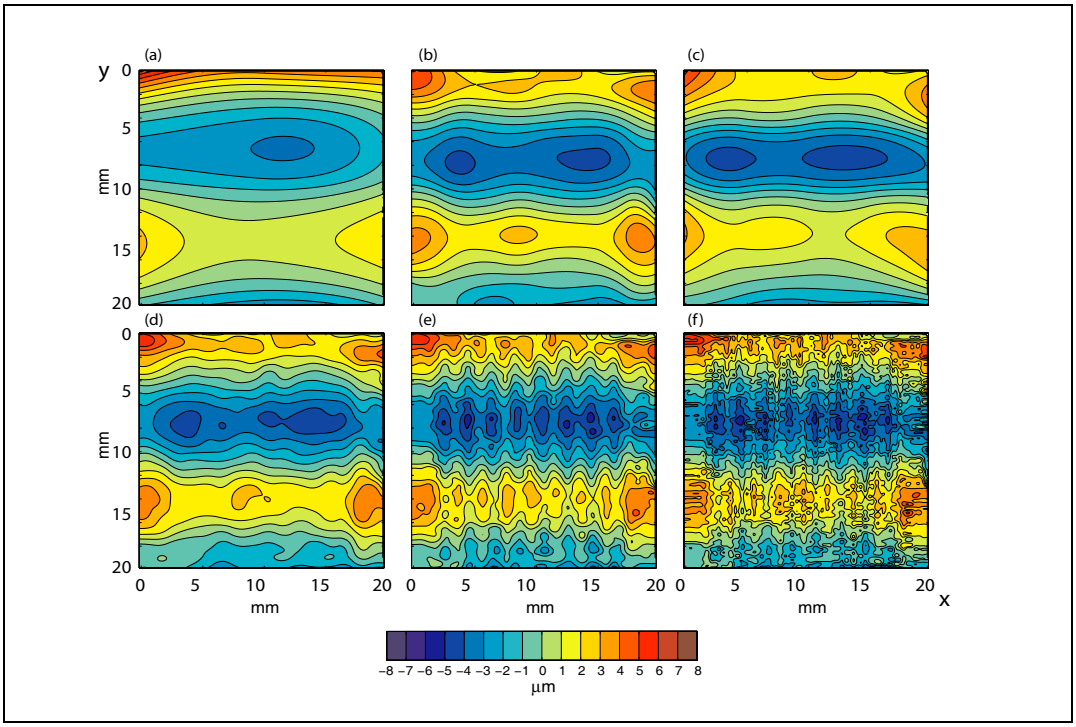

Figure 4-32. Six spline fits to non-uniformly pitched continuous data, showing periodic artifacts as the data is overfit in one dimension. Artifacts such as these could lead to misinterpretation of the results. Knot densities: (a) 10mm (b) 5mm (c) 2.5mm (d) 1.25mm (e) 0.625mm (f) 0.3125mm

A number of bivariate splines are fit to the averaged dataset with increasing knot densities. Starting with three knots, one at each edge and one in the centre of the sample (in both x and y), this density is increased by a factor of two for each fit. Figure 4-33 shows the series of spline fits for a range of knot densities.

In order to assess which of the spline fits best represents the data, the simple but often sufficient technique of graphical analysis of residuals was used (Section 4.4). The residuals from the entire 2-D surface are graphed as a single line. Trends seen at this level are representative of underfitting across the width (x axis in the schematic) of the sample. If a small section of the vector is viewed, then the residuals show only trends along the length (y axis) of a particular section. Figure 4-34 and Figure 4-35 show these two aspects. This technique while conveniently simple to apply is, of course, highly subjective and prone to bias. A robust technique using the power spectral density of the measured data is presented in Chapter 8.

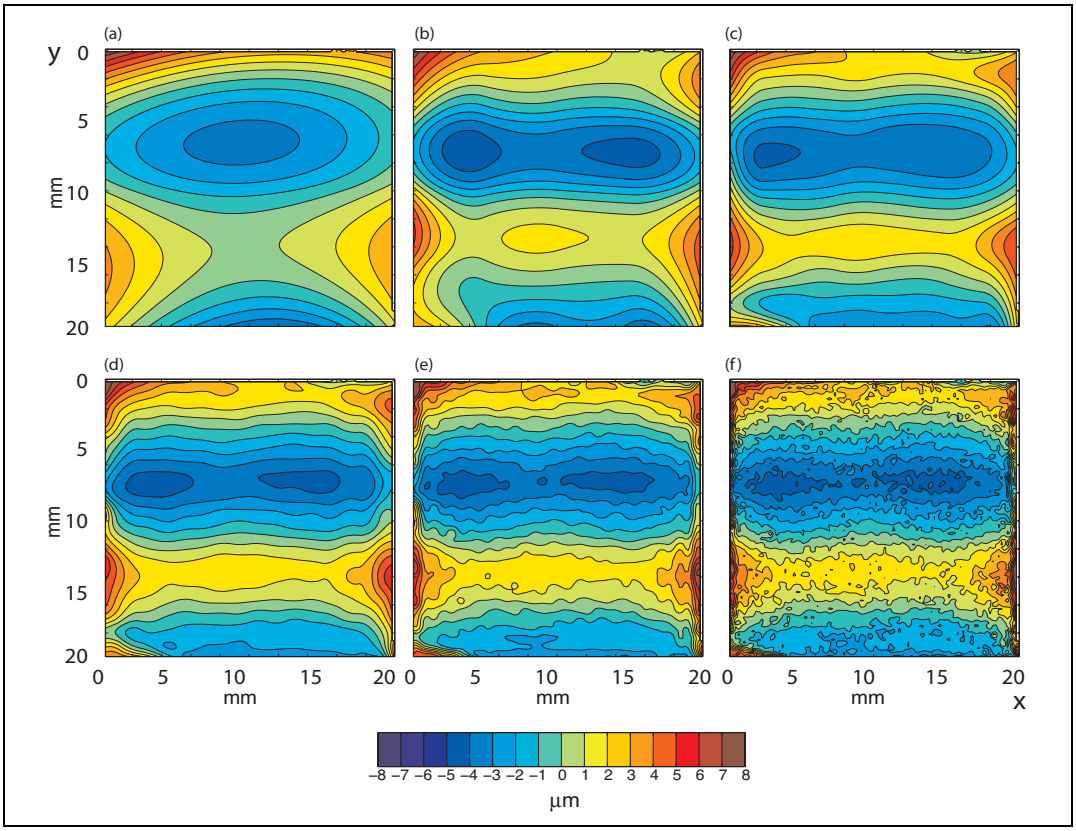

Figure 4-33. A series of six bi-variate spline fits to the same underlying data (measured at a 0.2mm pitch) of the PK1 bent bar. Knot spacing: a) 10mm b) 5mm c) 1.25 mm d) 0.625mm e) 0.3125mm . Measured in the henpeck mode.

By examining both of these figures, the knot spacing at 1.25mm was chosen by eye as being the smoothest spline that did not show any significant trending across the width or the length of the sample.

4.5 Modelling

As explained in Section 3.2, the final step in the contour method is the inversion of measured displacements to calculate residual stresses. For very simple geometries, it is possible to do this analytically as shown in Chapter 5 with the four point bending of a square bar. However, for anything other than prismatic geometries with homogenous material properties, a numerical technique is required.

Finite element modelling has become the prevalent way of solving large stress-displacement problems by utilising the vast increase in computer power that has become available over the last three decades. For situations where analytic solu-

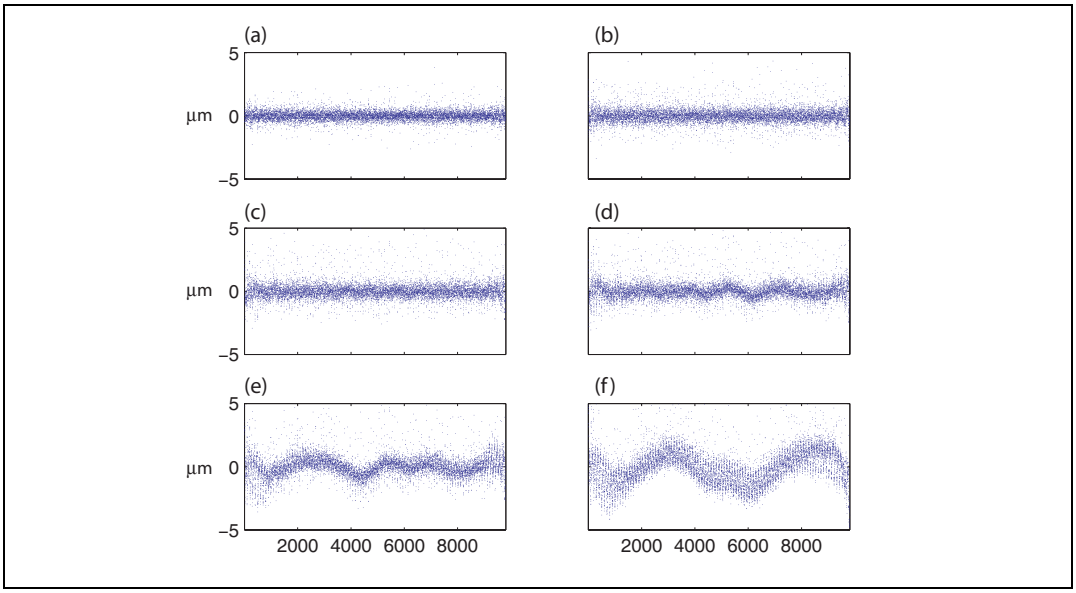

Figure 4-34. The residuals of the entire fit (10000 points) to PK1 for each spline of Figure 4-33. Trends seen in each figure are representative of underfitting across the width of the sample. Knot spacing a) 0.3125mm b) 0.625mm c) 1.25mm d) 2.5mm e) 5mm f) 10mm.

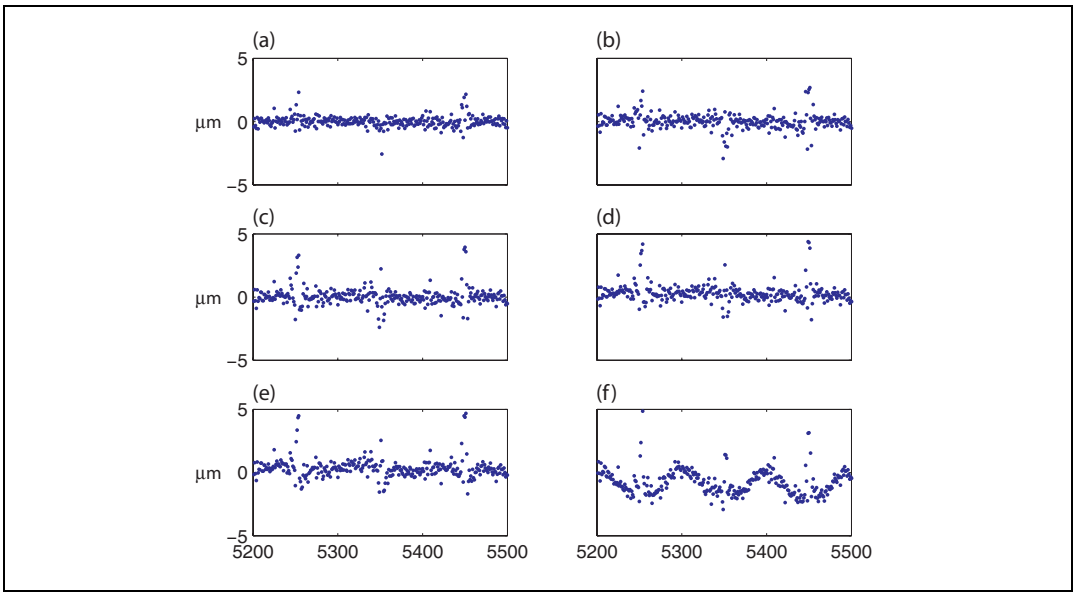

Figure 4-35. The residuals of cropped section (each 300 points long) of the entire fits to PK1 for each spline. Trends seen in each figure are representative of underfitting along the length of the sample. Knot spacing: a) 0.3125mm b) 0.625mm c) 1.25mm d) 2.5mm e) 5mm f) 10mm.

tions do not exist, the partitioning of models into small but finite sized elements and treating each independently except at the boundaries with adjacent elements permits the solution of previously intractable problems. The use of finite element modelling (FEM) in the contour method is of the pure elastic variety. As discussed

in Chapter 3, the main use of the modelling step in the contour method is to invert the contours measured on the cut surface of the sample to estimate the stresses present when the sample was whole. The steps involved in this are detailed here:

- Model the undeformed geometry of half of the cut sample.
- Establish constraint nodes to prevent rigid body motion.
- Apply the boundary conditions for a given spline to the cut surface of the model.
- Repeat the previous step for any other splines. Each is performed as a linear perturbation about the equilibrium point.
- Extract the data at each node for analysis and visualisation.

4.5.1 Details of modelling

The modelling procedures developed in this dissertation are based on a combination of ABAQUS functionality and custom Matlab scripts.

4.5.1.1 Geometry generation

The geometry of all the samples examined in this work may be adequately modeled as the extrusion of a cross section. This assumption is examined for the cylindrical Inertia Friction Welds - Chapter 6 - but is strictly true for all other cases. The cross section of the sample is measured on the CMM as part of the contour measurement procedure, and this is converted to a file that ABAQUS can use (the Autocad DXF format) with the `gen_outline` script. The parameters to this script specify the spacing of the points in the outline - either as a function of distance (a point every N mm, for instance) or curvature (a point whenever the outline changes direction more than M degrees). While it is possible to use the measured outline without reduction, ABAQUS uses each point in the outline as a mesh seed. This means that the outline pitch will determine the pitch of the ensuing mesh.

Once the DXF outline file has been imported into ABAQUS CAE, it is then used as the basis for a part. The part is extruded to correspond with the length of the cut sample.

4.5.1.2 Meshing

Prior to meshing, mesh seeds must be established on the model to give ABAQUS an initial guideline as to mesh density. Each node in the outline is used as a seed, and along the extruded length a number of seeds are also set. The top surface of the model is region of interest, so a biased set of seeds in used along the extrusion to give a finer pitch near the top and coarser pitch in less important areas. This reduces the computational time require to evaluate the model. As an example, the inertia friction weld of Chapter 6 is seen in Figure 4-36, where mesh seeds have been drawn as magenta boxes.

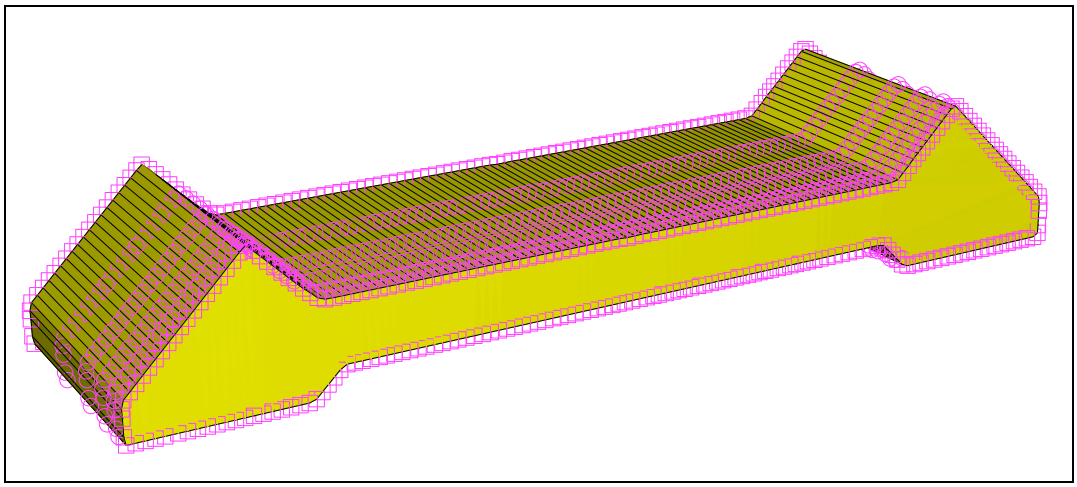

Figure 4-36. The model of the inertia friction weld (Chapter 6) with mesh seeds shown as magenta boxes. The perimeter of the cut surface (closest to viewer) is seeded uniformly, while biased seeds are used in depth as less detail is required.

The part is meshed using 20 noded hexahedral elements with reduced integration (C3D20R). Element choice for modelling is a complex subject, and ABAQUS offers many different types to choose from, with comprehensive advice on how to make that decision (see the Analysis User's Manual Chapter IV (Abaqus 2004)). The choice of these elements was made for several reasons:

- hexahedral elements (cuboid) match the geometry of most extruded parts without requiring very fine meshes to generate adequate detail.
- quadratic elements (having 20 nodes rather than 8) provide higher accuracy than linear elements for problems that are 'smooth' - not involving impact, complex contact conditions, or severe element discontinuities.

- reduced integration saves a great deal of computational time. Instead of 27 integration points, as in the C3D20 full integration element, the C3D20R reduced integration element only has 9.

Most parts may be meshed automatically, but some require partitioning of complex shapes to give ABAQUS further hints for its initial efforts.

4.5.1.3 Skeleton input deck creation

The FE problem is described entirely by an "input deck" - an ASCII file that contains the entire specification of the problem. At this stage, the problem has not been entirely defined, so a skeleton input deck is written to disk for further modification by Matlab scripts. This permits the manipulation of problem parameters in a way not possible from within the ABAQUS CAE environment.

4.5.1.4 Material properties

The skeleton input deck is read by the `create_inp_displacement` script. The user is able to specify both the Poisson ratio and the Young's modulus for the sample. For some samples (e.g. welds of dissimilar materials as seen in Chapter 6) multiple materials may be defined.

4.5.1.5 Boundary conditions

The splines created by the `fit_spline` tool are read by `create_inp_displacement` and applied to the nodes in the top surface of the sample. Each spline creates a set of boundary conditions, and is modelled as a separate step. These steps are implemented as linear perturbations and are named according to the spline knot density.

4.5.1.6 Creation of input deck

As the mesh is often quite large, the complete input deck is split into two parts by the script. For a job named abc, there are two files: abcmesh.inp and abcABQ.inp. The mesh file contains only the nodes and elements, while the ABQ file contains the material properties and the boundary conditions for each step.

4.5.1.7 Execution of job

The job is run by executing the abcABQ input deck (which includes a reference to the mesh file). Progress of the job may be monitored by examining the .dat and .msg files.

4.5.1.8 Extraction, visualisation, and analysis of results

The results from the job are kept in the output database (an .odb file). This may be viewed from ABAQUS CAE and reports may be extracted. In general, the out-of-plane stresses are those of main interested (S_{33}) and these may be exported to an ASCII file. If other stress measurements of the data are available, these may be compared with contour method data.

The script `show_results` is used to visualise the top surface of data from ABAQUS. The data must be exported as 'Unique nodal' values from within CAE to an ASCII .rpt file. The script reads both the results (which simply correlate node indices with stresses) and also the mesh file. It then selects the top surface of the mesh, and draws each element, together with the stresses values for each corner. As the elements are 20 noded, each face has four corner nodes, and four mid-edge nodes. These latter are discarded for the sake of rapid viewing. Output from the `show_results` script can be seen in later chapters.

4.6 Results

The finite element model was generated by taking the CMM measured outline of the bar cross section, then extruding it 130mm. The mesh was seeded at ~1mm intervals around the perimeter, and biased with a 1:5 ratio away from the cut surface. The 1.25mm spline was applied as the boundary condition on the cut face. The mesh had approximately 50000 nodes in total, across approximately 11000 hexahedral quadratic elements (C3D20R in ABAQUS) and is shown in Figure 4-37. As described in Section 4.5, the displacements from the spline were evaluated at the nodal locations and applied as boundary conditions to the cut surface.

After the model had run, the σ_{zz} results were extracted at each node, and meshed again onto a rectilinear grid for visualisation, as seen in Figure 4-38.

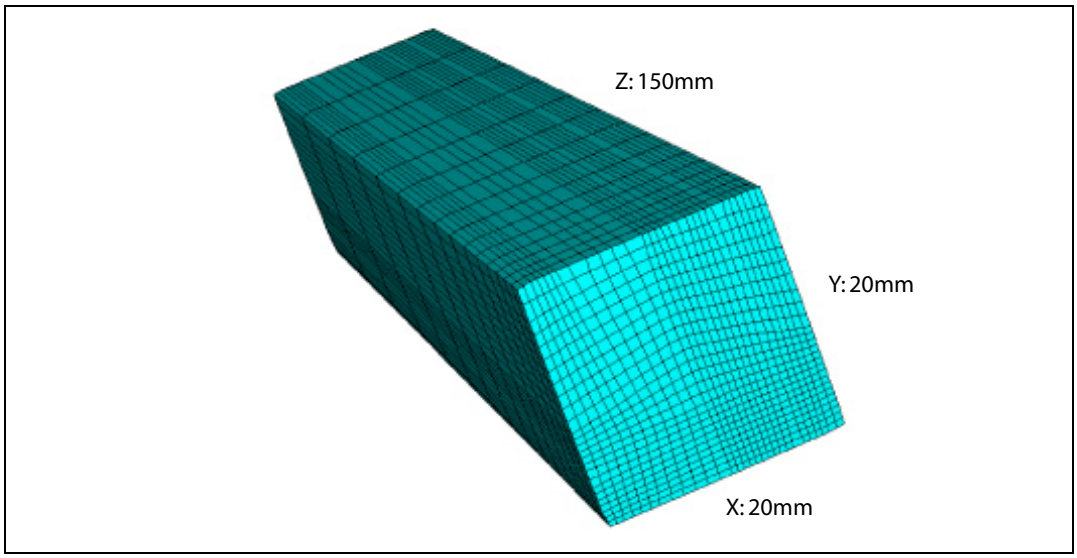

Figure 4-37. The FE model used for the bent bar evaluation. Seeded at approximately 1mm intervals around the 20mm x 20mm EDM perimeter and with a 1:5 biased mesh along the 130mm length of the sample.

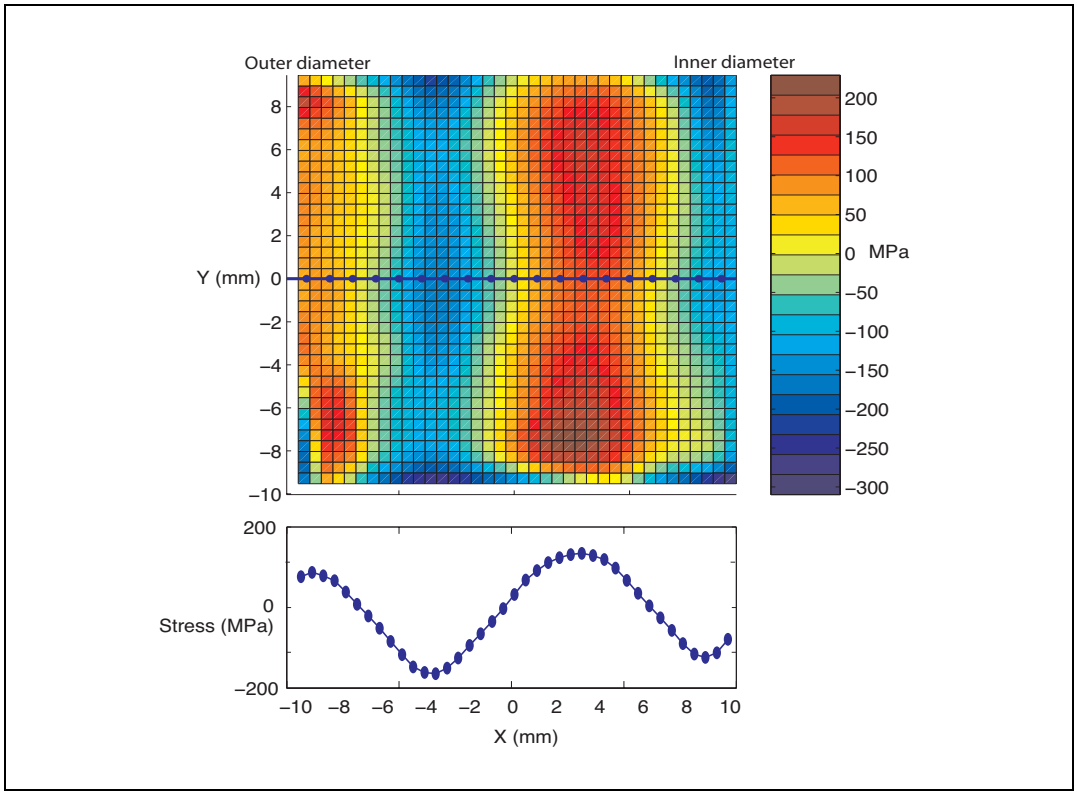

Figure 4-38. The cut surface of the PK1 bar, showing the σ_{33} results from the contour method. The centre line is extracted and shown in the subplot at the bottom. Maximum compressive stresses across the midline are 164MPa, and maximum tensile stresses are 134MPa

The processing steps outlined in Section 4.5 were applied to the measured surface data, and the results from the contour method are show in Figure 4-39, overlaid with both the analytical and finite element predictions - the former using elastic-perfectly plastic behaviour, and the latter incorporating the mechanical properties that were measured.

It is clear that there is, in general, very good agreement in the form of the stress profile between the CM and the FE results. The compressive peaks are both at the same location, though the magnitudes differ by 40MPa. An increasing spatial discrepancy between the two occurs as the cutting depth increases (the cutting started at y=-10, proceeding to y=+10), and the tensile peaks, though having the same magnitude, differ in location by ~1mm. There is an upturn, in the range 8<y<10, that is only apparent in the CM data. The reasons for this were not understood at the time of measurement, but the issue, concerning spline extrapolation, is discussed in Chapter 5 and some possible explanations and remedies are offered.

4.7 Discussion

The lateral discrepancy between the CM and the FE results appears to increase with cutting distance (from negative to positive y). One likely source of error is the mechanical properties used for the FE model. These were obtained from a single uniaxial tensile test, but the actual sample has undergone both compressive and cylic loading. More complete characterisation of the material properties would be valuable. There is also a possibility that this may be partially due to insufficient clamping while cutting. If the material was stress-free at the time of cutting, the kerf (width of removed material) would be constant through the cut. However, as shown in Figure 4-40 for the example of a tensile stress field, the kerf may vary. While the cut does occur on a plane fixed with reference to the machine, the material ahead of the cut is deforming due to the stress release that has occurred. This results in a kerf that is not constant with depth, but varies according to some function of depth and the released stresses, and limited by the proximity of the clamping mechanism. The assumption of the contour method, that the cut surface can be forced flat in the model to obtain the original spatial state of the model, is thus not

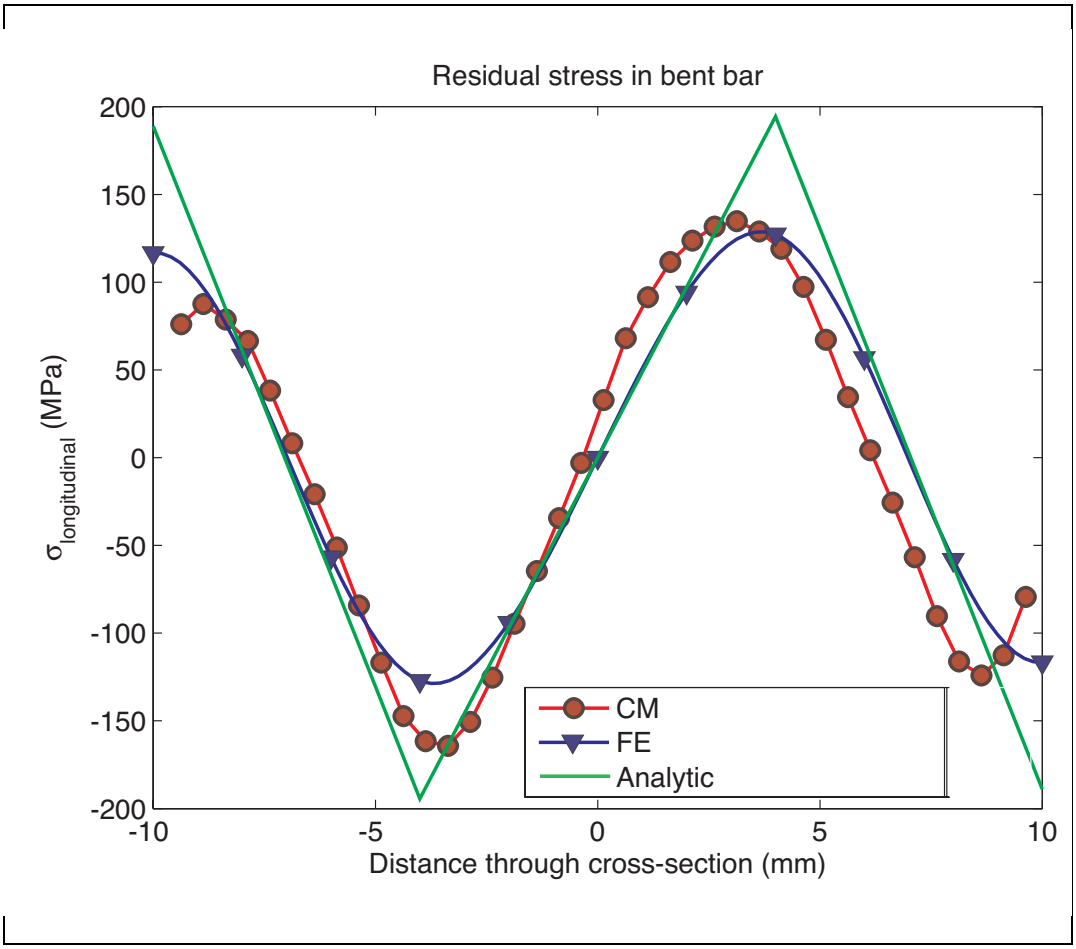

Figure 4-39. Comparison of contour method data (for central profile) with FE model and analytical calculation for the four point bending mechanism

not completely true - and consequently, the error in the obtained stresses increases. The reduction of the average kerf width (by using a smaller diameter cutting wire) reduces this artifact, as does constraining the sample more completely in close proximity to the cut, both solutions that are experimentally difficult to achieve. Recent work by Prime and subsequently Frankel (Prime 2008, Frankel 2008) has highlighted this so-called 'bulge effect'. This could be a very profitable area of further work that would require modelling of the cutting process and an estimation of the over(under) kerf width. Removing this from the measured displacement data would be a valuable improvement.

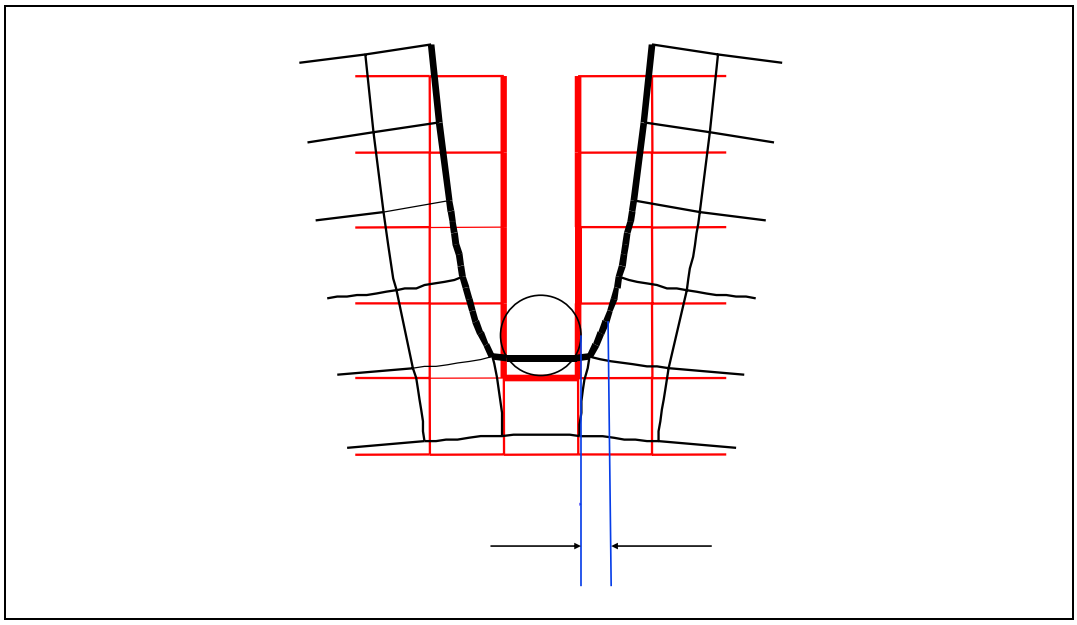

Figure 4-40. The non-uniform kerf around a cutting wire in tensile stress field (courtesy Prime).

4.8 Summary

It is possible to draw a number of conclusions from this study of the bent bar.

Firstly, that the cutting of the sample plays an important part in the process. While not examined in this dissertation, economic access to an EDM machine would permit useful research into the optimal cutting parameters for the contour method. EDM cutting has been characterised in some detail (Ramasawmy 2004, Petropolous 2004) but the use of 'skim' cut settings for a first cut is highly unusual and consequently has not been examined in great depth.

Secondly, the measurement technique needs to be well suited to the application. Using the continuous mode of the SP600 probe greatly reduces measurement times, but the noise levels rise. For samples with small displacements, using the hen-peck mode gives better quality data. In addition, careful attention needs to be paid to the measurement pitch - if the data is not uniformly spaced (in the two in-plane axes) then artefacts can occur in fitting. Coordinating the spline knot spacing with the measurement spacing would ameliorate this effect.

Thirdly, certain measurement methods (continuous tactile contact as discussed in this chapter, laser scanning as discussed in Chapter 7 and Chapter 8) have special

requirements for edge detection. The extrapolation method used here is effective, but of more interest in the techniques for dealing with the optical data because of the advantages of that modality: high speed, sensitivity, and measurement density. This is discussed in Chapter 8.

Fourthly, assessing what spline parameters give the best fit is currently done by looking at the residuals in a qualitative fashion. More advanced methods are developed in Chapter 7 and Chapter 8.

The primary aim, of validating the principles of the contour method by their application a classical bent bar has been achieved. Good results have been achieved for the bent bar, and the errors that have arisen would be a suitable target for further work. In the process, the chapter has broadly outlined the substantial suite of tools that have been developed by the author to handle surface measurement, noise reduction, sample alignment, surface fitting, FE model generation, and the application of boundary conditions.

Having started by examining a classical mechanical testing sample, the next chapter is concerned with applying the contour method to another straightforward stress profile, that of the quenched bar. The motivation for this is to critically examine the claims of a company specialising in cyrongenic stress relief to see if the method is successful.

The contour method requires the measurement, processing, and evaluation of large quantities of data. At each stage, critical decisions have to be made: how best to measure the raw data, how to clean and fit surfaces, how best to define and model the geometry of the sample. Each of these decisions can have a large bearing on the usefulness of the results. This chapter has outlined each of these steps in detail and described the comprehensive toolkit of processing routines that have been built. The subsequent chapters investigate a number of case studies, examining the applicability of the contour method to a range of problems.

5 Cryogenic 'stress-relief' of aluminium plate

For some time there has been a popular interest in relieving residual stresses in metallic parts by cryogenic cooling. A number of companies (Three 2005, TechSpec 2005, OneCryo 2005), mostly in North America, offer this service for metallic items ranging from automotive components to musical instruments. The process is reputed to both relieve type I stresses (described in Chapter 2) and to strengthen the material. In particular, it is said that

> "This one-time process tightens grain structure creating a denser microstructure while increasing surface area. This improves the path of energy and provides increased stress relief and dimensional stability. The bottom line — components last longer and perform better." (Nycro 2005)

In order to assess whether these unscientific and unsubstantiated claims have any basis in fact, it was decided to use the contour method (see Chapter 3) to measure residual stress pre- and post-cryogenic treatment.

5.1 Cryogenic treatment process

The 'cryogenic stress relief' process is one propounded by a number of companies, primarily in the USA and the UK, as a method for achieving improvements in material properties. These properties are diverse, ranging from "increasing abrasive wear resistance", "increasing tensile strength, toughness, and stability coupled with the release of residual stresses", and "decreasing brittleness" (Dynat 2005) for mechanical parts to the more unusual "restores intonation and pitch resonance" for musical instruments. The process appears to be straightforward: cool the

sample in question to the temperature of liquid nitrogen (-197.8°C) and maintain this temperature for some hours, perhaps up to 24. Then slowly warm the object to room temperature.

The suggested reasons for believing this to be an effective residual stress relief process are as diverse as the properties it is purported to improve. Many of them use language unfamiliar to the material scientist, as seen in the quotation in the introductory paragraph.

To evaluate scientifically the performance of this cryogenic process, a number of bars of aluminium alloy were used. The first was examined as received from the manufacturer, the second was quenched from elevated temperature in order to introduce residual stresses and used as a control sample, and the third was quenched and then cryogenically treated by a specialist company. The contour method was then applied to all three samples to compare the stresses and assess what difference the cryogenic treatment had made to the quenching thermal residual stresses.

5.2 Sample provenance

Aluminium 7075 (composition given in Table 5-1) is a high strength aluminium alloy used in highly stressed structural parts, such as aircraft fittings, gears, shafts, and valve elements. A plate of Al-7075 T7451, 60mm thick, was supplied by Alcoa International. T7451 is a thermo-mechanical treatment combining solution treatment at 465°C followed by quenching to room temperature in water and then application of a 1.5-3% uniform plastic strain in the rolling direction to relieve the quenching stresses.

Four samples were cut from the plate using a vertical bandsaw, all 60mm wide,

Alloying element	% wt.
Al	90
Cr	0.18-0.28
Cu	1.2-2
Fe	max 0.5
Mg	2.1-2.9
Mn	max 0.3
Si	max 0.4
Ti	max 0.2
Zn	5.1-6.1
Zr+Ti	max 0.25

Table 5-1. Elemental composition of Aluminium 7075 (Polmear 1995)

producing final dimensions of 60 x 60 x 200mm. The long direction was parallel to the rolling direction in the original plate. Elastic properties for this alloy were determined by tensile testing to be a Young's modulus of 72GPa and a Poisson ratio of 0.33. Figure 5-1 shows how the samples were cut from the supplied plate.

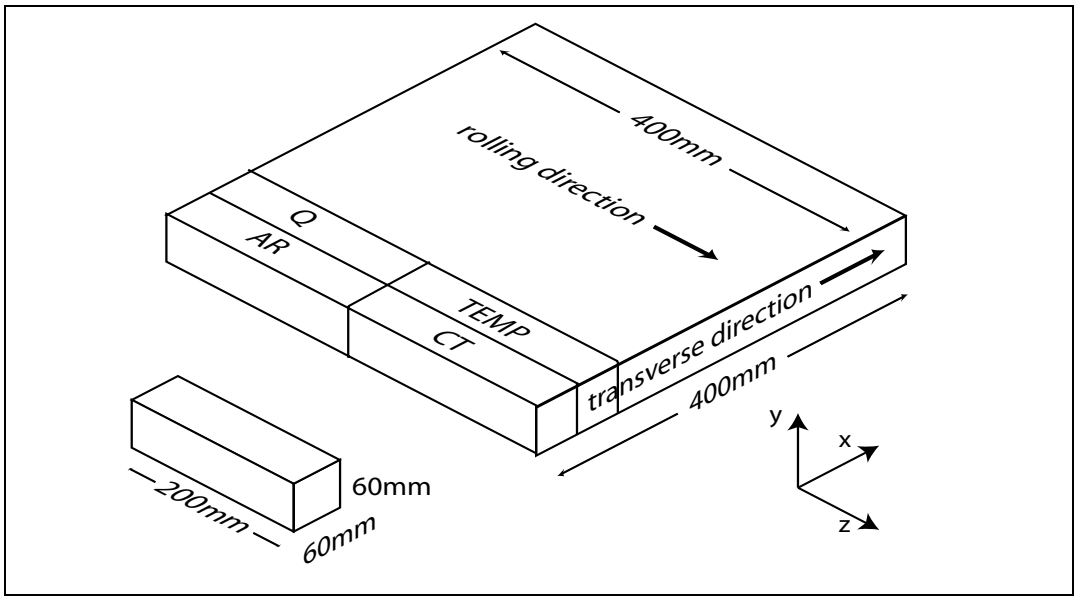

Figure 5-1. From the supplied plate, four samples were cut, each 200 x 60 x 60 mm (as shown inset). One was used without further treatment (AR), Q and CT were both quenched, and CT was further subjected to the cryogenic stress relief process. TEMP was used as a temperature monitor in the quenching process.

One of the samples was used without further treatment (AR), while two were heat treated/annealed and quenched (Q and CT), and one of the pair further subjected to the 'cryogenic stress relief' process (CT). The remaining sample (TEMP) was used as a temperature monitor for the quenching process then discarded.

The heat treatment consisted of the standard solution annealing (470°C for 120 minutes) then rapidly quenched to 20°C using a large water bath (after Polmear 1995). This was done to induce a residual stress profile across the sample. Cryogenic treatment would then be used to investigate its capacity to relieve this stress.

5.3 Cryogenic treatment

The company that performed the cryogenic treatment is called Cryogenics International[1], and is a subsidiary of the American company Deep Cryogenics Ltd. It has been in business for at least a decade, and treats a wide range of samples with the objective of "reducing residual stresses, increasing wear resistance, and producing a harmonic dampening effect" (Deepcryogenics 2005). There appear to be no studies in the scientific literature supporting these claims, however a considerable amount of anecdotal evidence is quoted by the company and others in the same business.

The process of treatment involves cooling the sample over a period of six hours to -196°C (the boiling point of liquid nitrogen, which is used as the coolant), a soak period of approximately 24 hours, and then a warming period of another six hours. Further heating to 50°C is performed over two hours, then the sample is permitted to air-cool. This process was applied by Cryogenics Intl.

5.4 Measurements

Each of the three samples (as received, quenched, and cryotreated) was EDM cut at Parkside Tool & Die[2] using a 150μm zinc coated brass wire. The cut surfaces were measured using the CMM in Manchester with a 1mm diameter ruby probe. The

1. www.cryogenicsinternational.com
2. Parkside Tool & Die: www.parksidetool.co.uk

measurement pitch was 1.5mm in both lateral directions (details on measurement procedures described in Section 3.2).

The quality of the raw data is excellent, with very few points needing removal. As an example, the displacements for the Q (quenched) sample are shown in Figure 5-2.

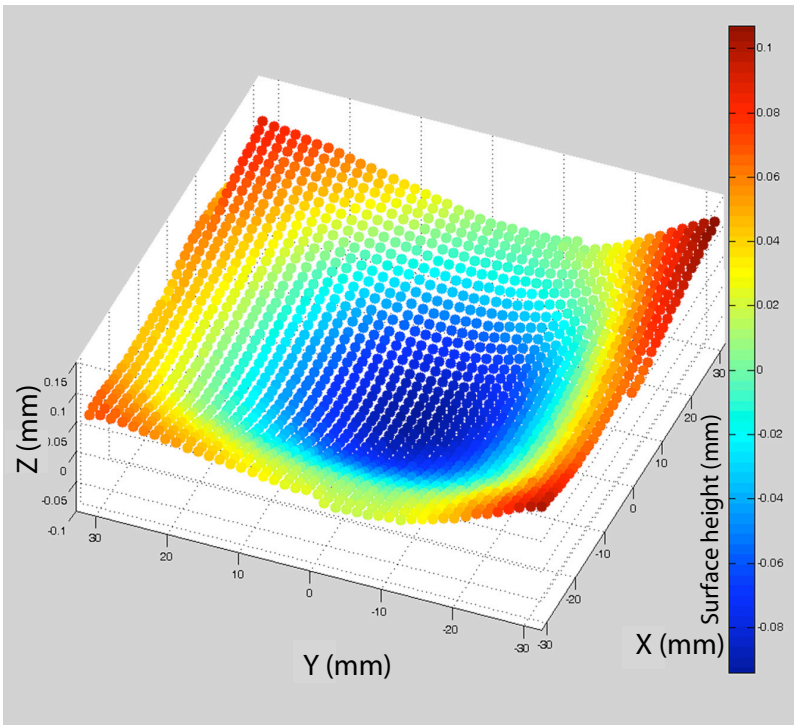

Figure 5-2. Displacement data for the quenched sample (Q). The range of displacement is between +100µm and -90µm.

The finite element model was built in the usual manner (cf. Chapter 4), using 1.5x1.5mm quadratic reduced integration elements (C3D20R). As the meshes were constructed using the outline file that `gen_outline` (Appendix G) automatically generated, they are not as uniform as would be the case if made manually. As the displacement does not vary from node to node with elements of this size, this irregular spacing of the nodes does not affect the results.

5.5 Surface data fitting

As described in Section 4.4.3, once the profile has been measured, it needs to be fit to a surface. Whilst the best fit surface of very simple samples can be evlauated visually, this clearly is neither a robust nor objective technqiue for deciding upon a suitable knot spacing for the surface fitting spline. Simple error measurements (comparing the fit surface to the values of the measured data) have no minima with increased over-fitting (Section 4.4.4), so are unhelpful. In addition, no adequate model of the measurement instrument characteristics exist, so a deconvolution technique is not trivial to apply.

However, by dividing the dataset randomly into *N* sub-datasets (useful values of N being 10-20, dependent on computing resources available), and using the *k*th set to verify the fit generated against the set made from the remaining *N-1* sets, a error measure with a global minima can be estimated. This is called cross-validation, or the *hold-out method* and is a common method used in Bayesian analysis to avoid under- and over-fitting (Bishop 1995, Haykin 1999)

The pseudo-code for this process is described in Figure 5-3. The evaluation of the

```
given three 2D matrices, xTot, yTot, zTot:
zTot(m,n) is the measured value at the location (xTot(m,n),yTot(m,n))

Divide the dataset into k=1:N random pieces x{k},y{k},z{k}
iterate over entire knot range
  iterate over all k
    regroup all pieces _except_ the kth for fitting into xfit,yfit,zfit
    rename the kth piece xtest, ytest, ztest
    create spline for this knot choice against xfit,yfit,zfit
    measure RMS error of spline against xtest,ytest,ztest
  end k iteration
end knot iteration

take mean of errors over all k subdatasets as function of knot spacing

display error against knotspacing (in both x and y)
```

Figure 5-3. Pseudo-code of generalisation error calculation

error requires substantial amounts of computing power to perform over a wide range of knot spacings in both *x* and *y* directions, and consumed 250 hours of CPU

time to produce each error map. Figure 5-4 shows the three error maps for the as-received, quenched, and cryo-treated samples. As expected, the condition corre-

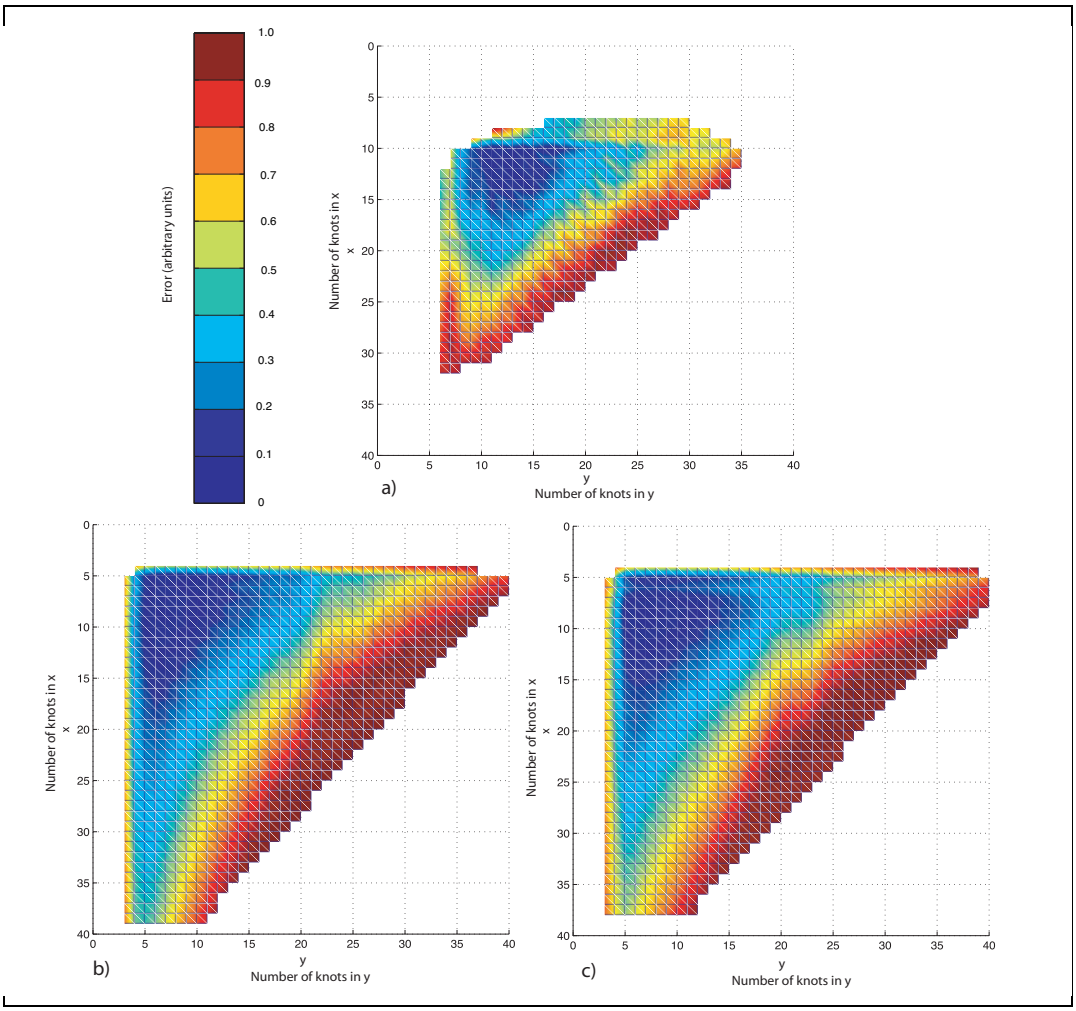

Figure 5-4. Normalised error as a function of the number of knots for a) as-received sample (minima at12 knots = 5mm pitch) b) quenched sample (minima at 8 knots = 7.5mm) and c) cryo-treated (minima at 8 knots = 7.5mm)

sponding to the lowest error (coloured blue) in the maps is the same in both axes, and for the AR sample corresponds to ~12 knots across the sample (5mm pitch) and for Q and CT samples is at ~8 knots across the sample (7.5mm pitch). It is also apparent that the minima is quite broad, so the error is not sensitive to small variations from these values. A knot spacing of 5mm was used for all three samples as a result.

5.6 Results

The results for the as-received (AR) sample are shown in Figure 5-5. As the source plate was stretched as part of the T7451 treatment after fabrication (Section 5.2), low stresses were measured. Maximum and minimum residual stress values are +32MPa and -28MPa respectively, but there is no significant trend across the sample. Two line plots are shown below in Figure 5-5. These are the X and Y cross sections extracted through the centre of the sample.

The results for the quenched (Q) sample are qualitatively what would be expected - an essentially parabolic distribution of stresses with a peak tensile stress of 300MPa in the centre of the sample and compressive stresses around the outer edges (Figure 5-6). However, when the line plots are extracted for the X and Y directions, it becomes clear that the stress distribution differs from what might be expected over the outer 5mm of the plots. Instead of a monotonically decreasing stress value (increasing compression), a 'kickback' occurs, and the inferred stresses become less compressive in magnitude. The peak compressive stresses observed are also different in each slice: X cross section -150MPa, Y cross section -250MPa, both located ~5mm beneath the surface of the sample.

The corresponding cryogenically treated (CT) sample results are shown in Figure 5-7. There is very little difference to be seen between the CT results and the Q results, and the line profiles bear this out. Again, the peak tensile stresses are ~300 MPa, and the unusual stress turnover (kickback) behaviour near the edges of the sample is again observed in almost identical detail. There is a slight shape difference of the stress distribution when looking at the 2D map, but it is hard to quantify.

For easier comparison of the effects of the cryo treatment, Figure 5-8 shows the quenched and cryotreated profiles overlaid for X and Y directions.

No significant difference is to be seen between the two samples - the profiles are shifted laterally slightly because of the differing FE meshes, and on the left hand side of the transverse cross section, the cryo treated sample is ~40 MPa greater in

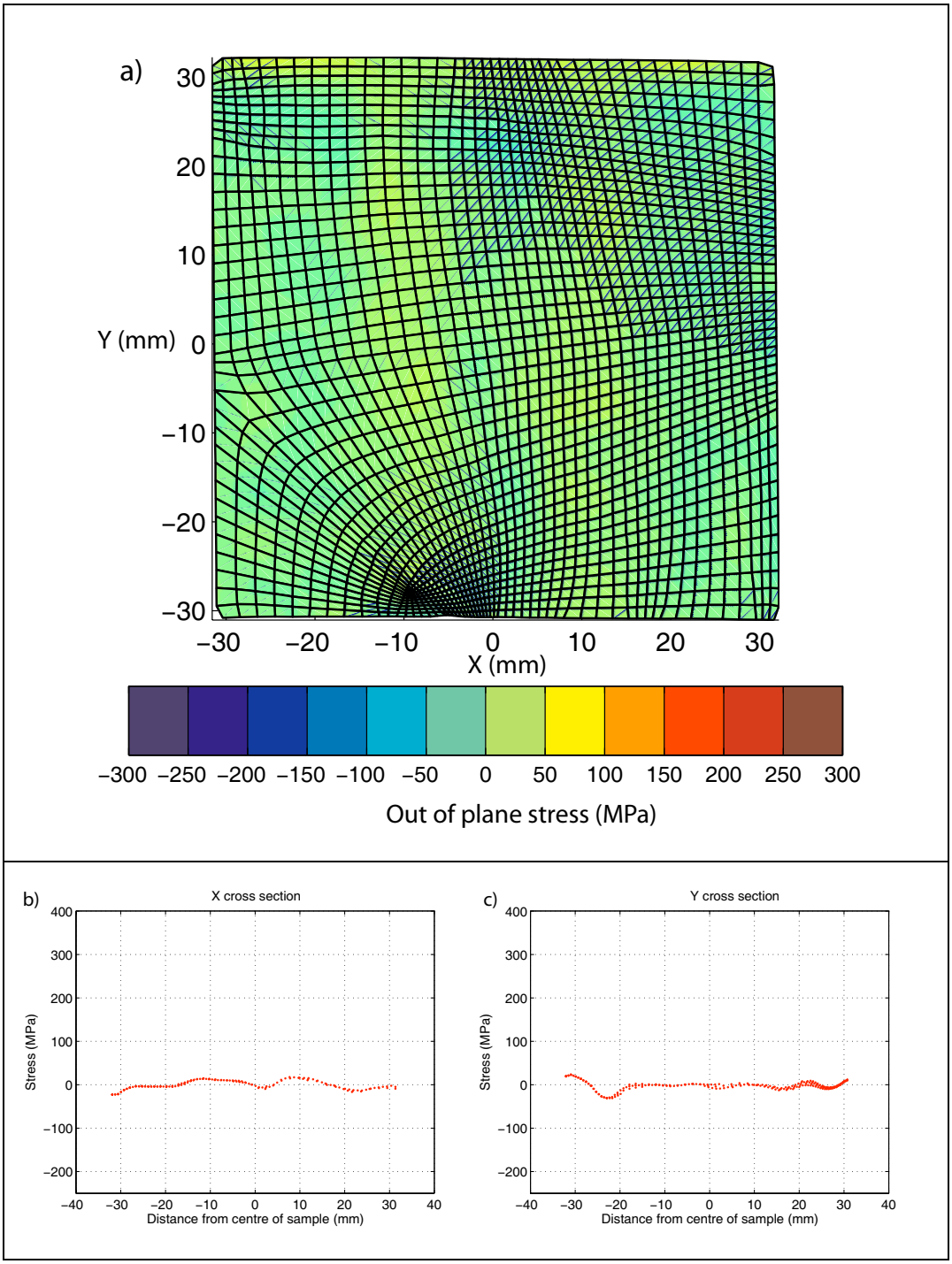

Figure 5-5. a) Contour method results for the as-received (AR) sample showing out of plane stresses. Essentially flat, all stresses are within ±32MPa. Line plots extracted from the AR sample, showing b) X (y=0) and c) Y (x=0) line profiles. No trends are observable in the data.

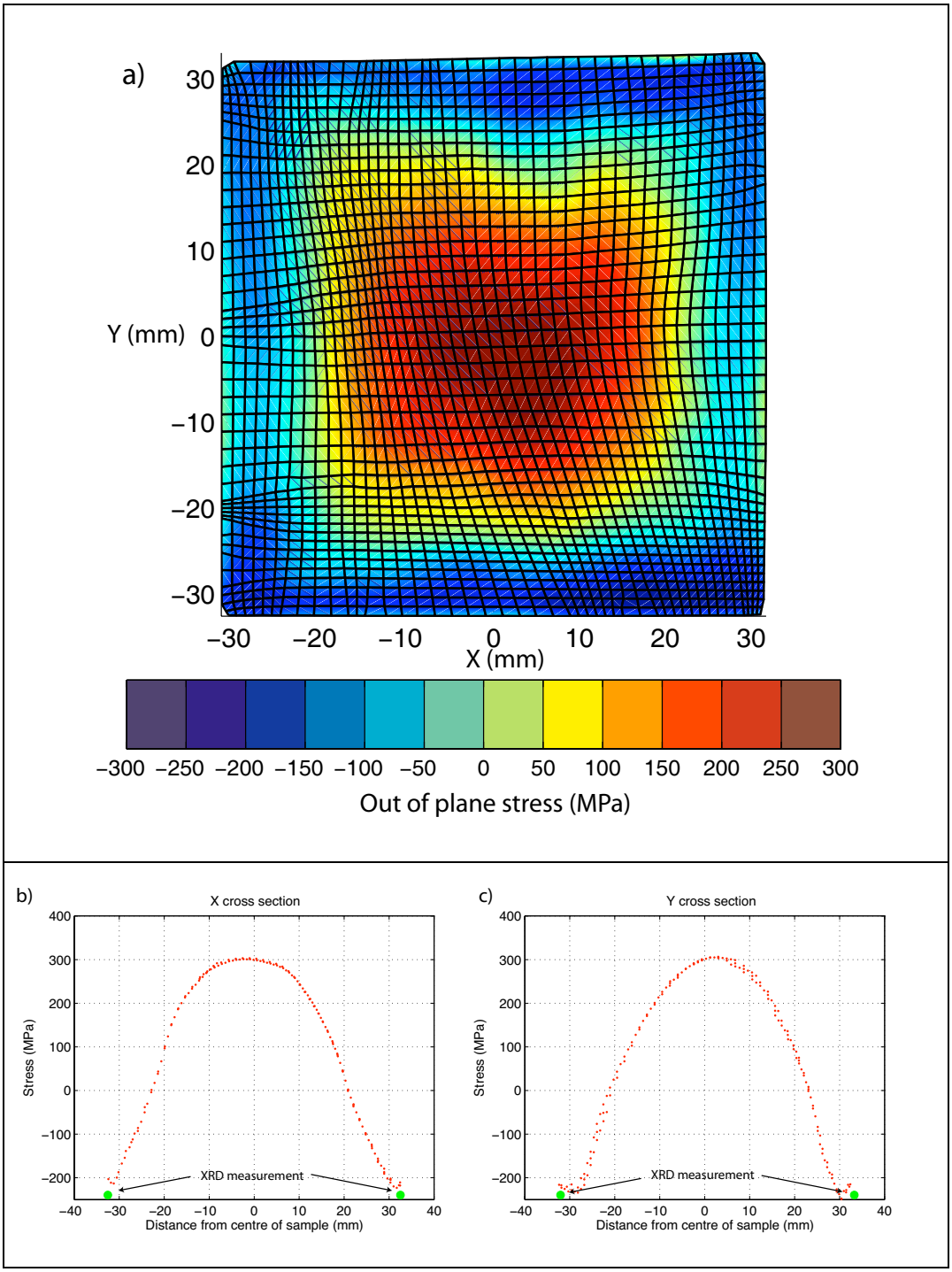

Figure 5-6. a) The contour method results for the quenched (Q) sample showing out of plane stresses. The peak tensile stresses are found in the centre of the sample, about 300MPa. b) X(y=0) and c) Y (x=0) line profiles extracted from the Q sample. Notice the asymmetry in the compressive peaks, 100-150MPa for the X, but 250MPa for the Y cross section. The magnitude is of surface stresses measured by XRD is -244MPa (solid green circles).

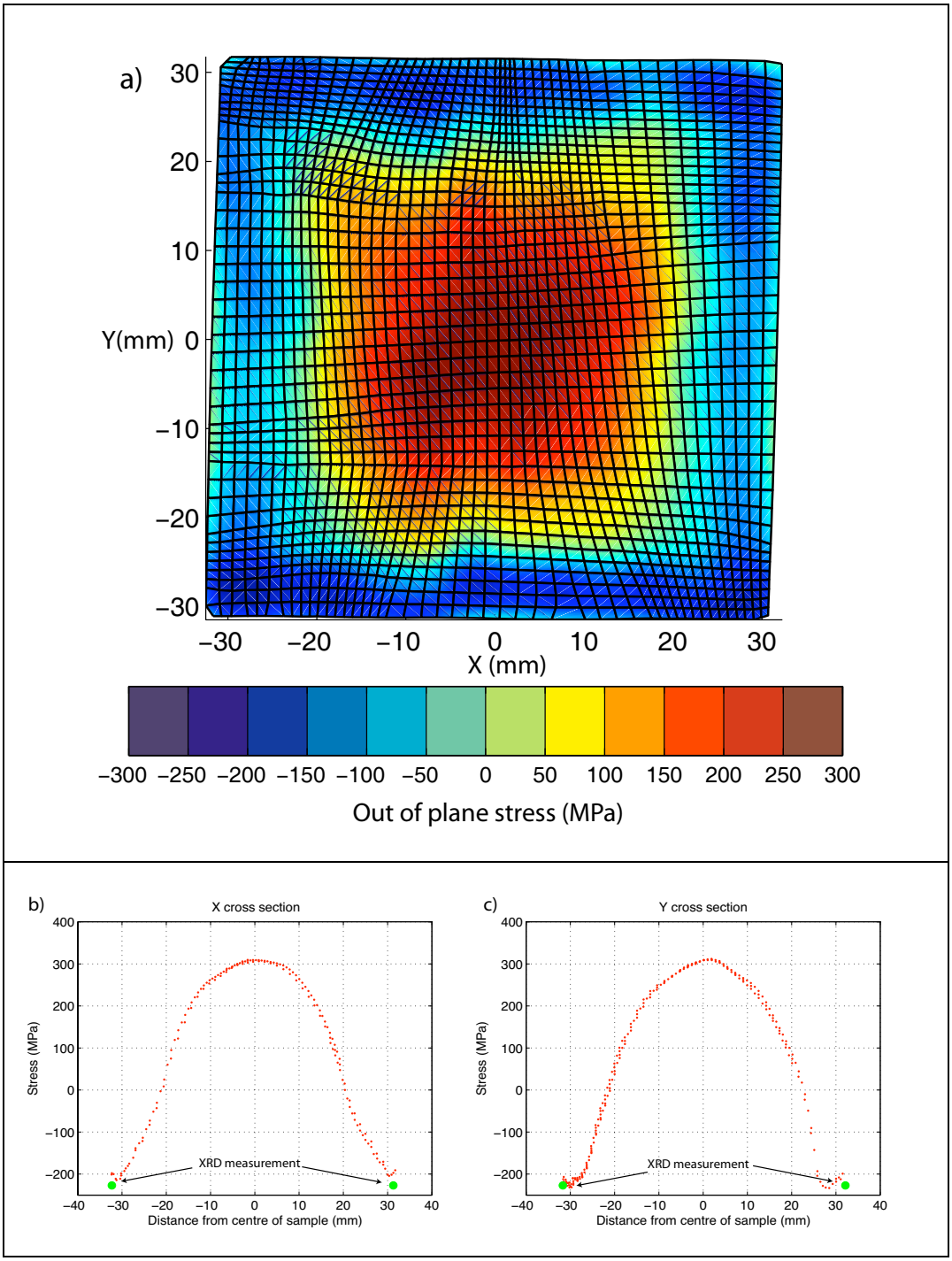

Figure 5-7. a) The contour method results for the cryogenically treated (CT) sample. No significant difference between the quenched and the 'stress relieved' sample is evident. The extracted line profiles for b) X and c) Yshow the same form and magnitudes as those for the quenched sample. The magnitude of surface stress measured by XRD is -228MPa (solid green circles).

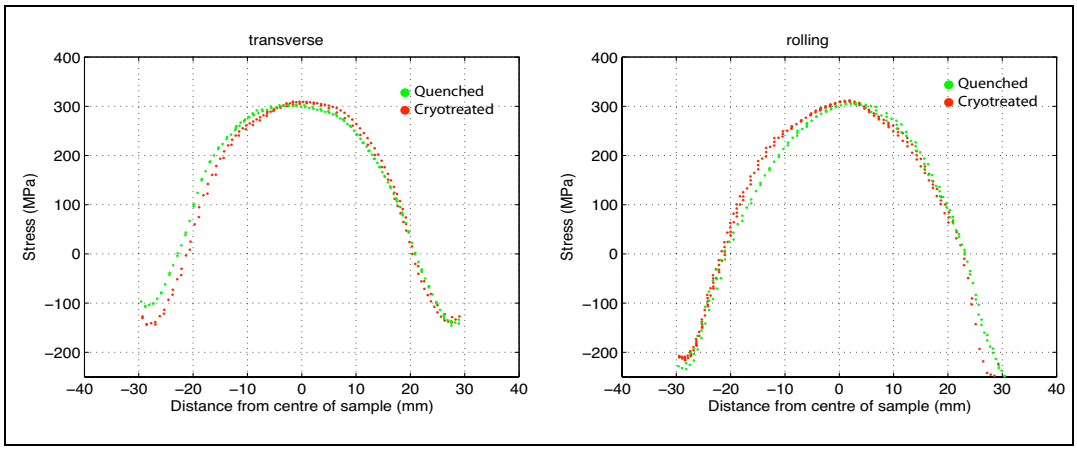

Figure 5-8. X (left) and Y (right) line profilesof both the quenched (green) and cryotreated (red) samples. Significant differences are not seen between the two samples.

compression than the untreated - the 'stress relief' appears to have increased the stresses slightly.

A single XRD measurement was made for each sample (using the $\sin^2\psi$ technique on the Proto iXRD instrument[1] as described in Section 2.3.1) by Russell for both the quenched and the cryo-treated samples. The voltage applied between the cathode and the copper anode was 25kV, and the current was 5mA. A 2mm collimator was used.

Unfortunately, no record was kept of which of the four sides was measured, so the green dot (Figure 5-6a,b and Figure 5-7a,b) which represents this value has been plotted in the figures as if the measurement were symmetric. However, it is apparent to the eye that the XRD measurements are approximately in line with the extrapolation of the contour method results, until the upturn is encountered. In both the transverse and rolling cross sections, this upturn is 2-3mm from the surface of the sample.

This feature would not be expected for a homogenous material. However, the assumption that the samples are homogenous may not be correct. In other studies of 7000 series alloys, through-thickness inhomogeneity in mechanical properties and toughness has been reported ((Brown 1983),(Dejong 1980)). This was

1. Proto X-Ray Diffraction: www.protoxrd.com

observed in work also carried out on 7050-T74 using crack compliance (Prime 2002) - the results are shown in Figure 5-9. These also show peak compressive stresses occurring below the surface, and Prime correlates this with variations in through-thickness strength.

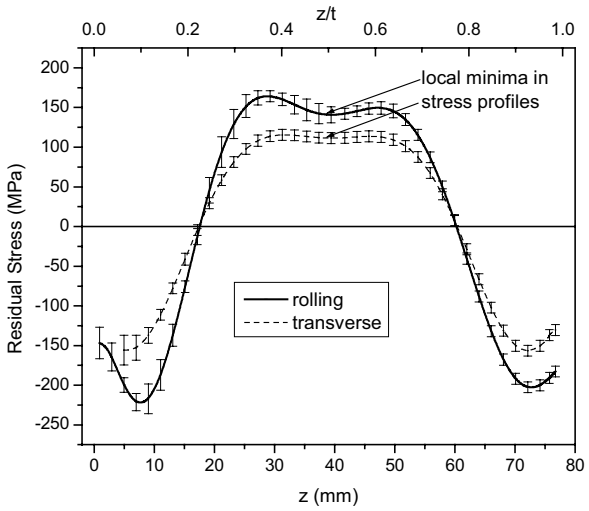

Figure 5-9. Crack compliance ('slitting') stress results measured by Prime (Prime2002) on the same alloy as considered in this chapter.

The preliminary results showed a much larger stress turnover, and one aspect of the data treatment that contributes to this effect is the surface analysis and fitting. Consequently, the code the author wrote to fit the splines (`fit_spline.m`, Appendix C) was re-examined, and a factor that contributes to this issue of stress turnover (also seen in Chapter 5) was discovered. The results shown here include this correction, as described below.

When the data from the two halves of the cut surface are averaged, they are first meshed onto a single grid. This grid, which must be rectangular, is the size of the bounding box that contains the entire sample. If the sample is a) not rectangular or b) not aligned to the axes of the bounding box, then there is some empty space outside the sample (see Figure 5-10). The extrapolation of the surface measurements into this region had been done with a nearest-neighbour scheme, which meant that the data points outside the sample were maintained at the value seen on the outline

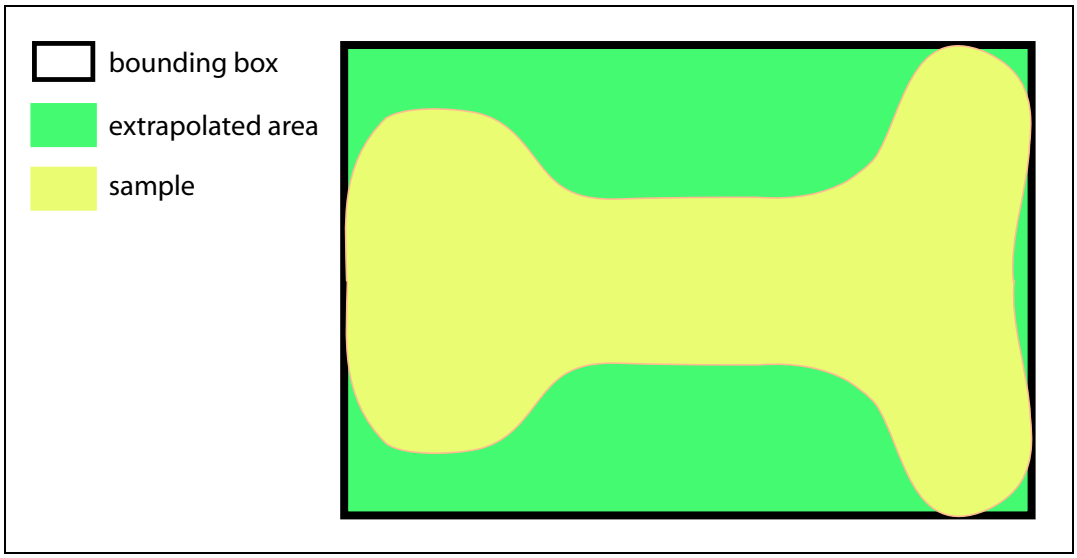

Figure 5-10. The single rectangular grid (the bounding box) contains the sample (yellow) but also an area outside the sample which must contain extrapolated points.

of the sample. It was thought at the time of creation of the algorithm that as the boundary conditions for the FE model only come from inside the sample outline, this would not be a problem. However, the spline fit trys to accommodate *all* the data inside the bounding-box, not only that of the sample but also the boundary region. As shown in Figure 5-11 this can lead to a spline fit inside the sample outline

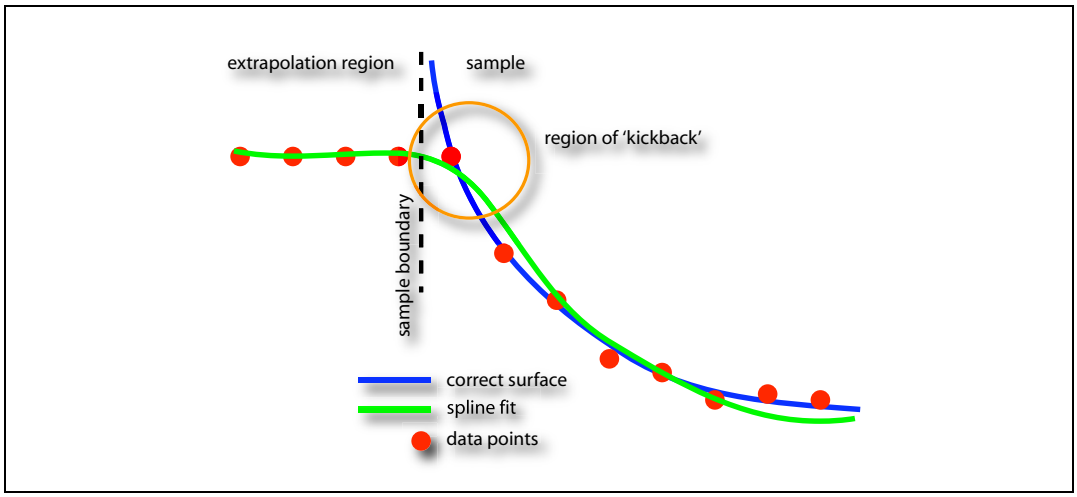

Figure 5-11. 'Plateau' extrapolation of measured data points. While the extrapolated points are outside the sample, the spline fit accommodates them also, and causes a decrease in the slope (green line) rather than preserving the gradient of the sample close to the edge (blue line)

that is in error. This does not occur in every situation, but is controlled by the following issues:

- the larger the area of the boundary region, the more significant the induced error in the spline fit
- the steeper the gradient of the data just inside the sample outline, the more severe the misfit of the spline.

In consequence, the algorithm was subsequently replaced with an extrapolation that maintains the gradient (not the value) of the data at the sample outline, and the model was rerun. It is possible to see in Figure 5-12 the difference between the

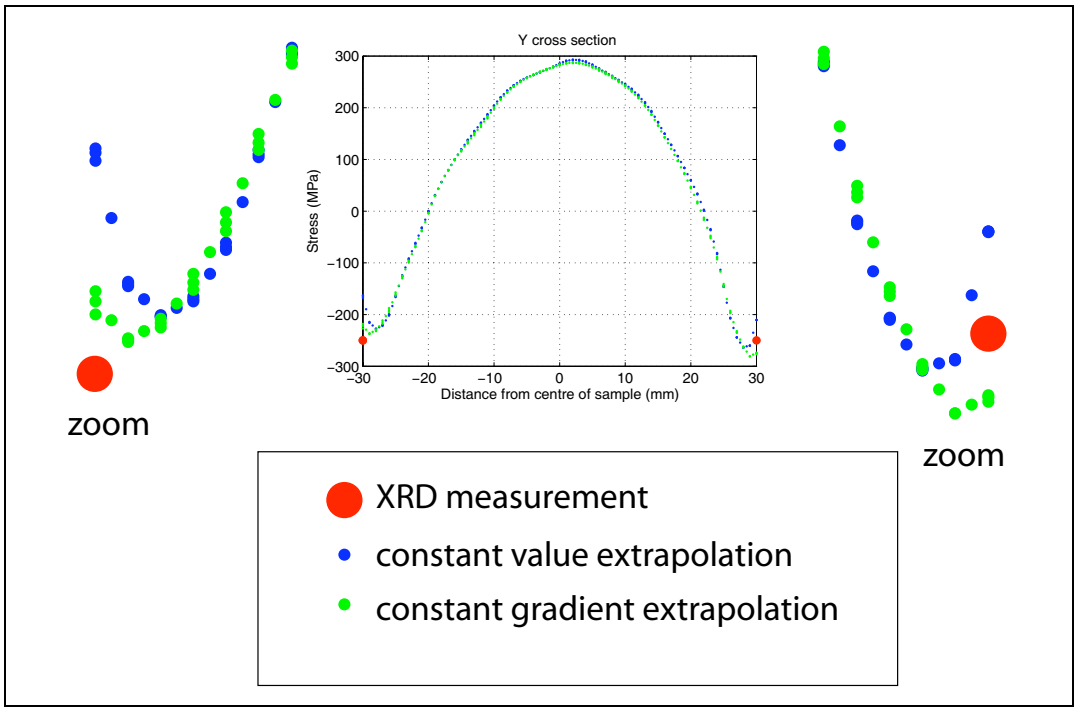

Figure 5-12. Comparison of constant value and constant gradient extrapolation, showing the reduction but not elimination of the stress turnover. The detail at the sample edge is shown magnified on the left and right sides of the overall plot

initial results and the refined algorithm used in this chapter. It also shows that while this has made some improvement in bringing the contour method stress profile closer to the surface x-ray results, there is still a significant 'kickback' that occurs, strongly suggesting that the turnover in stress observed here and also reported by Prime is a real effect.

5.7 Conclusions

The contour method has achieved very consistent results across the quenched samples. This demonstrates clearly that for aluminium 7075 the cryogenic treatment had essentially no effect in reducing the residual stresses introduced by quenching.

However, the results are not as were initially expected for a quenched sample, with a simple variation from tensile stresses in the centre to compressive stresses at the surface. This turnover in the stress profile near surface has been observed by other authors, so the contour method results are believed to be indicative of a real trend. However, this work highlighted a problem with the data treatment algorithms, which was subsequently corrected. Further work should include measuring the other three surfaces with XRD and also the assessment of material inhomogeneity.

From the point of view of contour method development, the sample highlights the problems that can occur in close proximity to the edge of the sample when the stress is significant.

In this chapter, a rigorous method has been applied to evaluate the surface fitting errors. This is a valuable addition to the CM tool chain. It provides the practioner with a high degree of confidence and a semi-automatic manner for choosing knots spacings when using a uniform spline fit.

Moving on from samples with nigh analytical stress profiles, the next chapter is the first of two to use the contour method to assess stresses in welds. The next chapter examines inertia friction welds made using two high performance steels, these involve much larger samples with a more complex geometry. These contain signficant areas of low stress areas combined with a small weld region of very high stresses. The results are compared to neutron diffraction measurements and then extended to samples that neutron diffraction cannot measure.

6 Inertia Friction Welds

Inertia friction welding is a process able to join metal alloys in a solid state fashion that would not otherwise be possible using conventional fusion techniques. The aeroengine industry in particular has driven development of this welding technique for use in both nickel based superalloys and dissimilar steel assemblies. The shaft of a modern jet engine requires substantially different material properties along its length, ranging from high temperature creep resistance in the compressor, to high cycle fatigue and toughnesss in the fan, thus the use of suitable alloys in a joined assembly is highly desirable.

Residual stresses across the inertia friction weld (IFW) boundary are of crucial importance in assessing the efficacy of any post-weld heat treatment (PWHT) process from a structural integrity viewpoint, but very few measurement techniques exists that are able to make a representative number of measurements in such materials within feasible budgetary and timing constraints. Neutron diffraction is reasonably well suited to IFW studies, but is limited in the size of samples that can be measured and real problems of accessibility.

In this chapter, the hoop stresses in two dissimilar steel shaft IFWs are examined. The first weldment, IFW1, was specially prepared for neutron diffraction measurements by wall-thinning. This sample is also measured using the contour method, to compare the two techniques. The second weld, IFW2, is a full wall-thickness shaft that is not measurable with neutrons, but the contour method was used to study it and compare with the results obtained for IFW1.

6.1 The inertia friction welding process

Friction welding is fundamentally a solid state process of using the heat generated by kinetic friction to join two parts. While friction welding has been in use since the late 19th century (Britannica 2001), inertia welding, using axi-symmetric parts, was invented at Caterpillar in the 1960s, and commercial welding machines have been available since that time (Johnson 1966).

In this process (see Figure 6-1), one of the parts to be welded is attached to a large rotating flywheel whilst the second part is forced against it. The kinetic energy in the flywheel is dissipated in the form of heat through the friction and plasticity at the contacting surfaces, raising the temperature to just under the melting point of the material. Any material that does melt at the interface is expelled due to the axial pressure. Additionally, some energy is expended in creating local plasticity at the boundary. The flywheel having come to a halt, the axial pressure applied to the parts may be increased, and the weld formed by forging (Wang 1975).

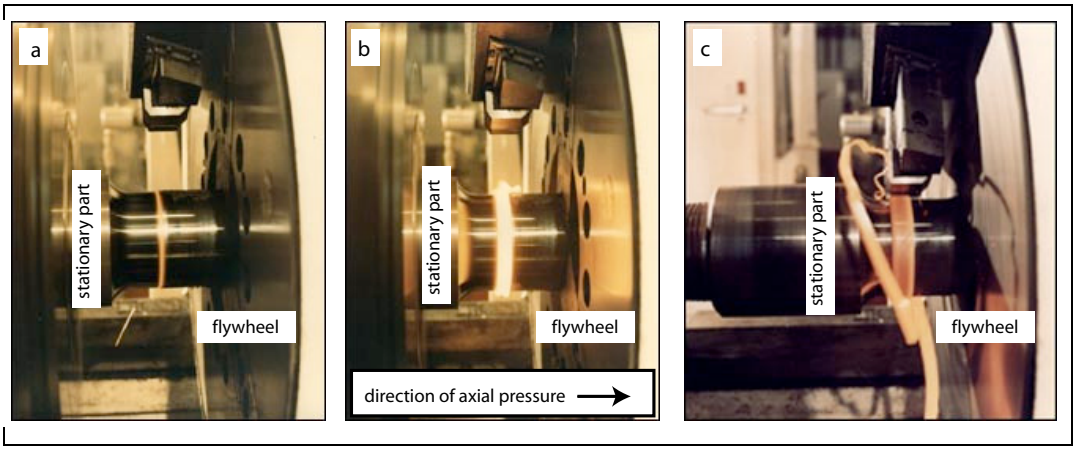

Figure 6-1. Three stages in inertia friction welding. a) Initial contact between the two parts b) application of axial pressure causing heating and local plasticity c) just before cessation of rotation, flash is removed. Forging pressure may subsequently be applied. (courtesy NCT Welding)

A limited number of reports have been published on IFWs, distributed between work on Cr-Mo steels (Sudha 2002), dissimilar stainless steels (Lee 2004), stainless steel and titanium (Kim 1995), and the alloys studied here, Aermet and SCMV (Bennett 2007, Robotham 2005, Moat 2008). Most of the work concerning residual stresses has been on nickel based superalloys (Pang 2002, Preuss 2003), using

neutron diffraction. As discussed in Section 2.3.3, this technique is able to rasterise through a material to generate a 3D map, but is expensive, time consuming, and limited in the size of sample that can be accommodated.

All of the results published have shown there to be a region of large tensile stresses around the weld line, comparatively low stresses radially, and a long range bending stress axially, attributed to the machine clamping forces (Pang 2002).

6.2 Sample provenance

The most common material used in the shaft of an aeroengine is steel. In modern jet engines, the performance requirements of these shafts are very high, with working temperatures ranging from ambient air at the fan through to 450°C within the compressor. In order to accommodate these stringent working conditions whilst maintaining an economical materials cost, two different steels are used in the shaft of the Rolls-RoyceTrent 300 engine. The material used in the compressor end of the shaft is SCMV (Super Chromium Molybdenum pressure Vessel steel) which has good creep resistance at the high temperatures experienced, combined with high strength and toughness at lower temperatures. For the fan end of the shaft, Aermet 100 is used, an expensive ultra high strength and highly alloyed steel. Its mechanical properties are excellent at lower temperatures (Karadge 2005).

Material	Elastic modulus	Poisson's ratio
SCMV	208GPa	0.278
Aermet 100	187GPa	0.280

Table 6-1. Elastic properties of SCMV and Aermet

	C	Cr	Ni	Co	Mo	Va	Si	Nb	Mn	Fe
SCMV	0.3	3.15	-	-	1.6	0.1	0.6	-	-	Ba
Aermet 100	0.2	2.5	10.1	12.7	1.37	-	-	3.26	0.01	Ba

Table 6-2. Composition of SCMV and Aermet 100 Element wt%)

Two IFW weld samples were examined. The first, IFW1, (Figure 6-2) was made suitable for neutron measurements by removal of material from inner and outer diameters, reducing the wall thickness from 36mm to 15mm. A neutron access port (20mm x 40mm, required to reduce the overall neutron path length and obtain

adequate counting statistics) was also machined on the far side of the shaft (Figure 6-5). The second, IFW2, shown in Figure 6-3, was full thickness (36mm).

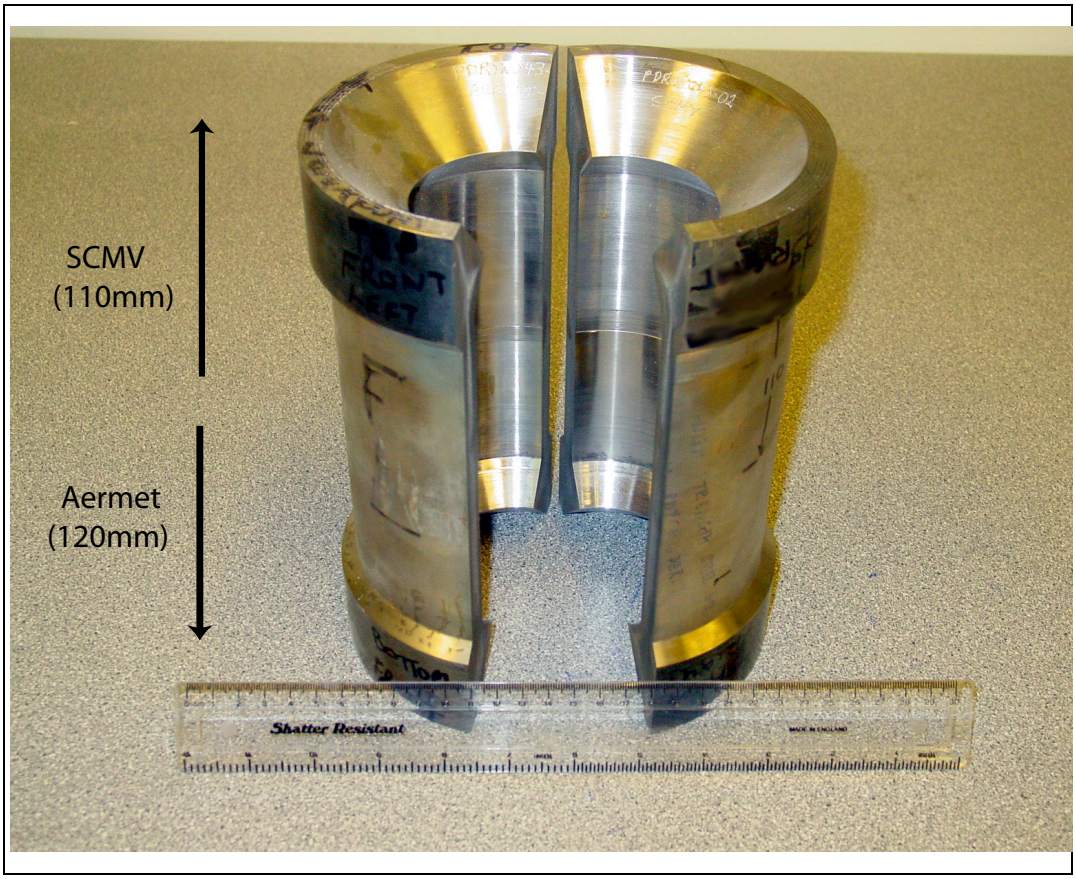

Figure 6-2. IFW1, shortly after cutting. A vertical wire passing from front to back was used to separate the halves. There is 120mm of Aermet on the bottom, with 110mm of SCMV above it.

Both components had been post-weld heat treated (PWHT) by heating at 482°C for five hours.

6.3 Neutron measurements

The neutron measurements of IFW1 were made by Karadge at the Paul Scherrer Institute (PSI) using the POLDI instrument (Karadge 2005). The wall of the sample was machined to 15mm prior to making the measurements, as shown approximately in Figure 6-4 but more precisely in the mesh in Figure 6-8, in order to decrease counting times to a feasible period. Even so, Figure 6-5 shows that the

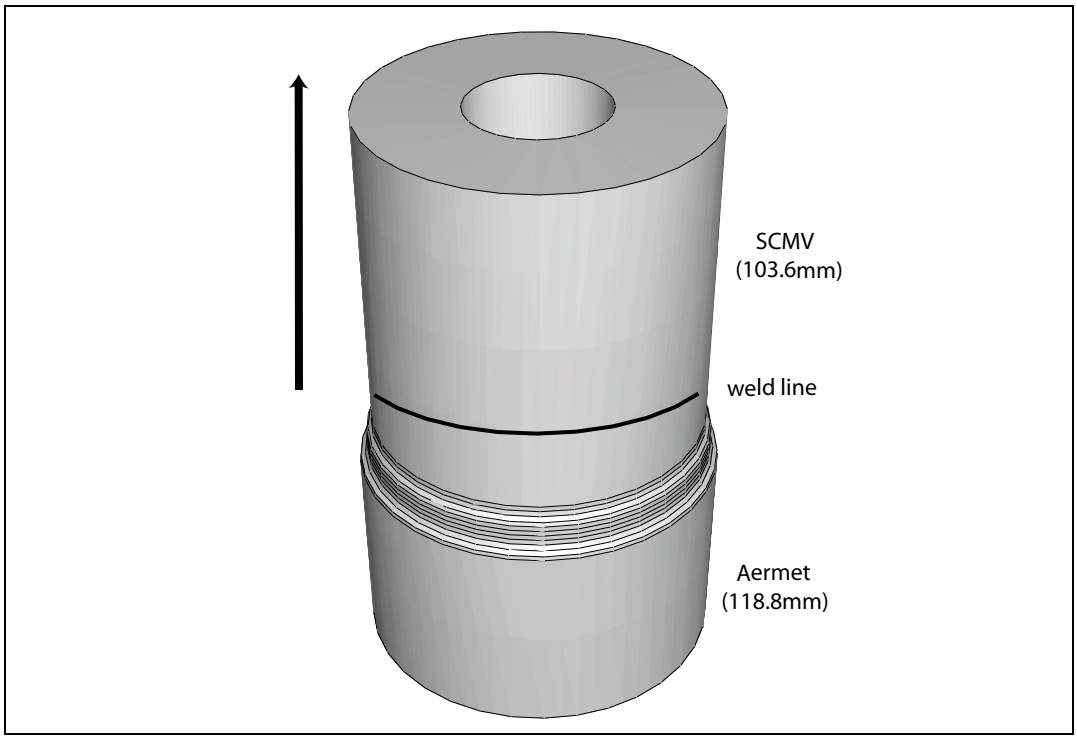

Figure 6-3. A model of IFW2, a full weld with no wall-thinning. It was cut in the same manner as IFW1.There is 118.8mm of Aermet with 103.6mm of SCMV above.

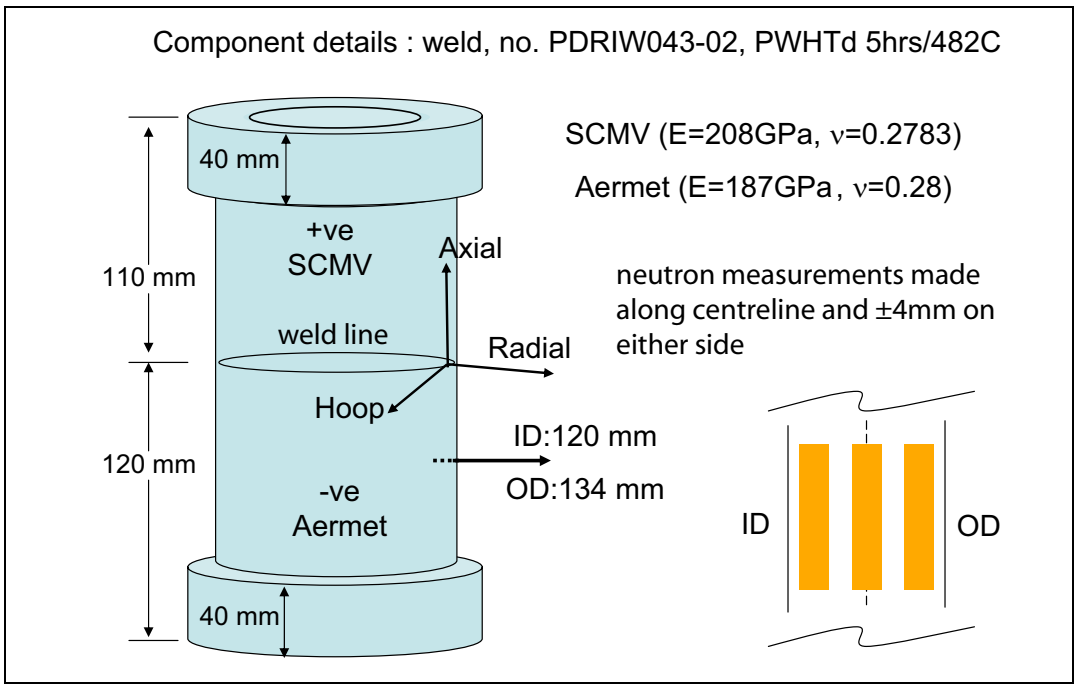

Figure 6-4. Schematic of IFW1 with dimensions, the location of the two materials, and measurement positions used in the POLDI neutron measurements (courtesy Karadge).

hoop strain measurements require a very long path length, so a window was cut in the sample to reduce this.

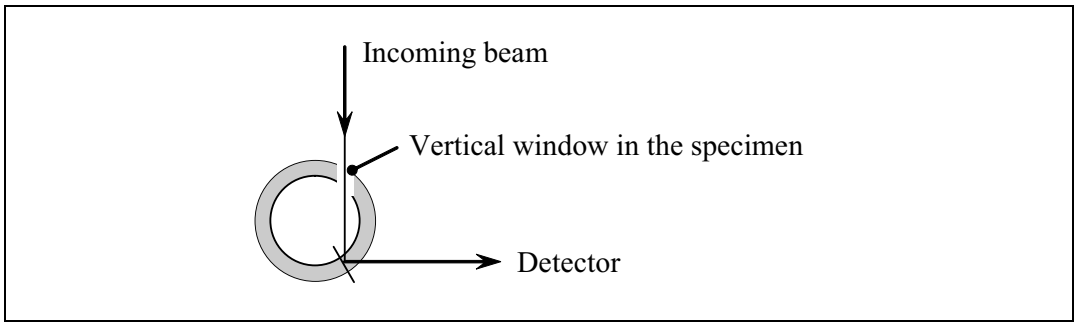

Figure 6-5. For hoop strain measurements on IFW1, a window was cut in the sample to reduce the path length of the neutrons through the sample.

As POLDI is a reactor source(see Section 2.3.3), entire diffraction spectra were gathered and the data were analysed using routines developed at PSI. The stress-free lattice parameter (d_0) was calculated using the stress balance method as it was not possible to measure the d_0 variation across the same by, for example, making biaxial $\sin^2\psi$ measurements (Preuss 2002). This provides a major uncertainty for the neutron method.

The results of the hoop stresses are compared with contour method measurements in Section 6.7.

The neutron measurements were made along the centre line of the wall, and also ±4mm from this line. The gauge volume used was approximately 1.25 x 1.25 x 1.25 mm within 5mm of the weldline, and 1.5 x 1.5 x 1.5 outside this region.

The counting times and gauge volumes are displayed in Table 6-3.

Strain component	Material	Gauge volume (distance from weldline)		Counting time (distance from weld line)	
		<10mm	>10mm	<10mm	>10mm
Hoop	SCMV	1.25x1.25x1.5	1.5x1.5x1.5	45 minutes	60 minutes
	Aermet	1.25x1.25x1.5	2x2x1.5	90 minutes	120 minutes
Axial	SCMV	1.25x1.25x1.5	1.25x1.25x1.5	40 minutes	50 minutes
	Aermet	1.25x1.25x1.5	1.5x1.5x1.5	60 minutes	90 minutes

Table 6-3. Counting times and gauge volumes for the neutron measurements. (courtesy Karadge)

Strain component	Material	Gauge volume (distance from weldline)		Counting time (distance from weld line)	
		<10mm	>10mm	<10mm	>10mm
Radial	SCMV	1.25x1.25x1.5	1.25x1.25x1.5	20 minutes	20 minutes
	Aermet	1.25x1.25x1.5	1.5x1.5x.15	30 minutes	45 minutes

Table 6-3. Counting times and gauge volumes for the neutron measurements. (courtesy Karadge)

6.4 Cutting

Cutting a large cylindrical inertia friction weld with the quality of surface required for the contour method is challenging. In order to measure hoop stresses, the cut must be made in the axial-radial plane: either with the cutting wire parallel to the diameter, or with it parallel to the z-axis of the sample.

In order to make the highest quality cut possible (that is, the flattest and smoothest, with the thinnest recast layer), the cutting wire length should be minimised so that the flushing jets are able to remove all debris during the cut (Vaughan2005). However, if this is done with the IFW, the wire will pass initially through one side of the weld, then the weld (and HAZ) and then finally the other side of the weld. Any region of compression (which is likely to occur to balance a tensile region at the weld line) will act on the entire cutting wire at once, and may cause pinching. Wire breakages (and subsequent restarts) are detrimental to the cut quality. In addition, a custom jig would be required to hold the cylindrical sample and provide sufficient clamping force. These concerns are sufficient to merit cutting in the other direction, even though it involves a much longer cutting wire. However, with the wire parallel to the z-axis of the sample, not only will the cutting debris be removed less effectively, but it is not known what will happen once the first cut through the cylinder wall is completed, and the effect this will have on the rear wall.

The two samples were cut at Rotadata, Derby, using a 300μm brass wire. Figure 6-2 is a photograph of IFW1, shortly after cutting. The sample has been cut with a long wire parallel to the z axis. It was originally assessed that balance of compressive and tensile stresses over the length of the weld would help to prevent pinching of the wire, a phenomena that had been observed on other cuts by the EDM operator (Vaughan 2005). The weld was clamped from above onto the EDM table after

it had been permitted to come to thermal equilibrium in the water bath. When the water had been drained from the machine after the second cut, it was observed that the sample had shifted slightly (though clamped) and had opened up a few millimetres (in the same fashion as the photograph, though not to so great a degree). At this point it was not known whether this had happened during the first or the second cut surface, nor what effect might be had on the surface measurements. Certainly, a relieved bending moment after the cut of the front wall would be very difficult to constrain, and the result noted is consistent with this notion. IFW2 was cut in the same direction as IFW1.

6.5 Contour measurement and data processing

6.5.1 IFW1 processing

The surface contours of both the front and the back cut surfaces were measured with the CMM at Manchester (Section 4.3.1), using a 2mm probe and a measurement pitch of 0.5mm, producing four point clouds with approximately 16,000 points each.

Each cloud was processed using `cmm_clean`, as described in Section 4.4.1, to remove outliers. The cutting wire did not always pass through the entire sample at once, as the sample is not rectangular. Because of this, the wire (and cut plane) appears to jump considerably (about 20μm) at the point where the effective cutting length changes. This is shown in Figure 6-6. One of the primary assumptions of the contour method is that the cut is truly flat, and the effect of these step changes, if they remained, would be the generation of very large stresses along the boundary of the plateaus. In order to get a stress balance over the sample, the overall level of the data would be shifted. This was noticed in the initial processing of this data. A 'nudge' function (Section 4.4) was added to `cmm_clean` at this point to facilitate the shifting of certain areas by a few microns up or down, until the step change between areas is removed.

It would also be useful to make the equivalent to the stress-free comb used in neutron and synchrotron measurements - a second cut made in close proximity to the

first. This would be nominally stress-free and thus any measured displacements would be indicative of cutting effects. The removal of cutting induced artifacts would be helpful in removing smooth but erroneous displacement profiles.

The effect of a unknown bending moment relieved upon cutting is impossible to quantify. An device that was able to cut both the front and the rear wall simulataneously would be helpful in alleviating any effect (though impractical).Instrumenting the rear wall with a strain gauge during the cutting of the front wall would sufficient information to indicate whether a bending moment had, in fact, been relieved - and also correct for it. Figure 6-6 shows both surfaces with respect to the same datum, and no overall variation between the two is noted.

The variation in the back face does reveal, however, that the clamping failure that had been observed after cutting probably occurred when the wire was halfway through the second cut, with the result that the entire part moved slightly. There is a significant, but non-uniform, shift in the point cloud of about 15µm, and this prevents the data from the second face being used further.

The data was then fit to splines with knot pitches ranging from 1.5mm to 4mm as discussed previously (Section 4.4). The residuals for each fit were assessed graphically, and the 2mm spline chosen as the most representative of the underlying data.

6.5.2 IFW2 processing

The same process was used for IFW2 as for IFW1, but the dataset is considerably larger due to the greater surface area of the cut. The data from the front and rear cuts are shown after minor noise removal in Figure 6-7 below.

It is clear that the quality of this cut was far inferior to that obtained on IFW1. There are a number of possible reasons for this. Firstly, the flushing of the cut was inadequate. As the cutting wire length was the entire length of the sample (over 230mm) and the high pressure jets designed to clear the cut slot of debris during the erosion process are at the far ends of the slot, it is possible that the debris was not being adequately removed. However, this had not occurred on IFW1, even at

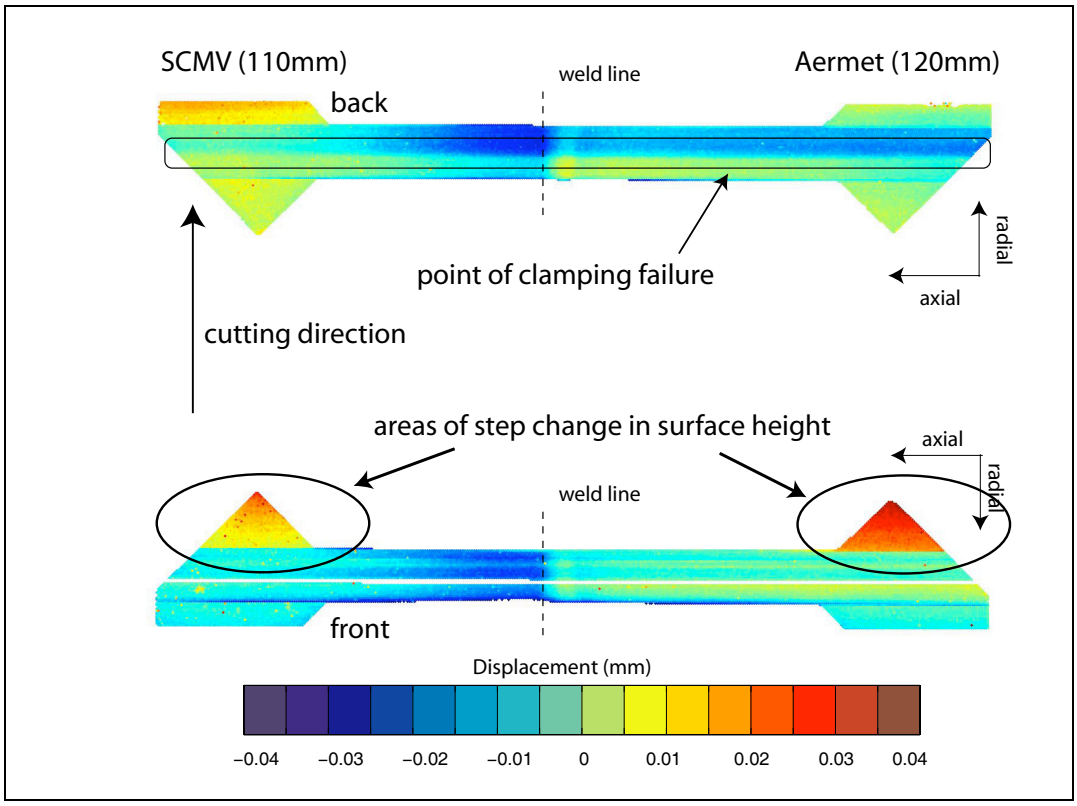

Figure 6-6. Initial measurements of a cut surface (IFW1) showing the step changes that occur where the effective length of the cutting wire has changed dramatically as it moved through the sample. This figure shows that the clamping failed halfway through the back edge (top of figure) of the cylinder.

the back edge of a cut, where 20mm of slot lay behind the wire. On IFW2, this cutting problem was occurring long before the slot had been cut to these depths. Secondly, the thinning of IFW1 had relieved stresses that were still present in IFW2 and these caused the slot to pinch the wire.

Although it was not initially clear why, the striations on the surface of both the front and the back cuts indicated that the wire had stalled numerous times during the cut, leaving a terraced appearance. The EDM operator believed that deterioration in the bearings on the wire feed of the EDM (cf. Figure 3-2) may have caused this problem (Vaughan 2005).

6.6 Finite element model

The outline from both IFW1 and IFW2 was extruded 600mm, and then seeded every 2mm around the perimeter. Biased seeds (1:5 ratio) were used along the

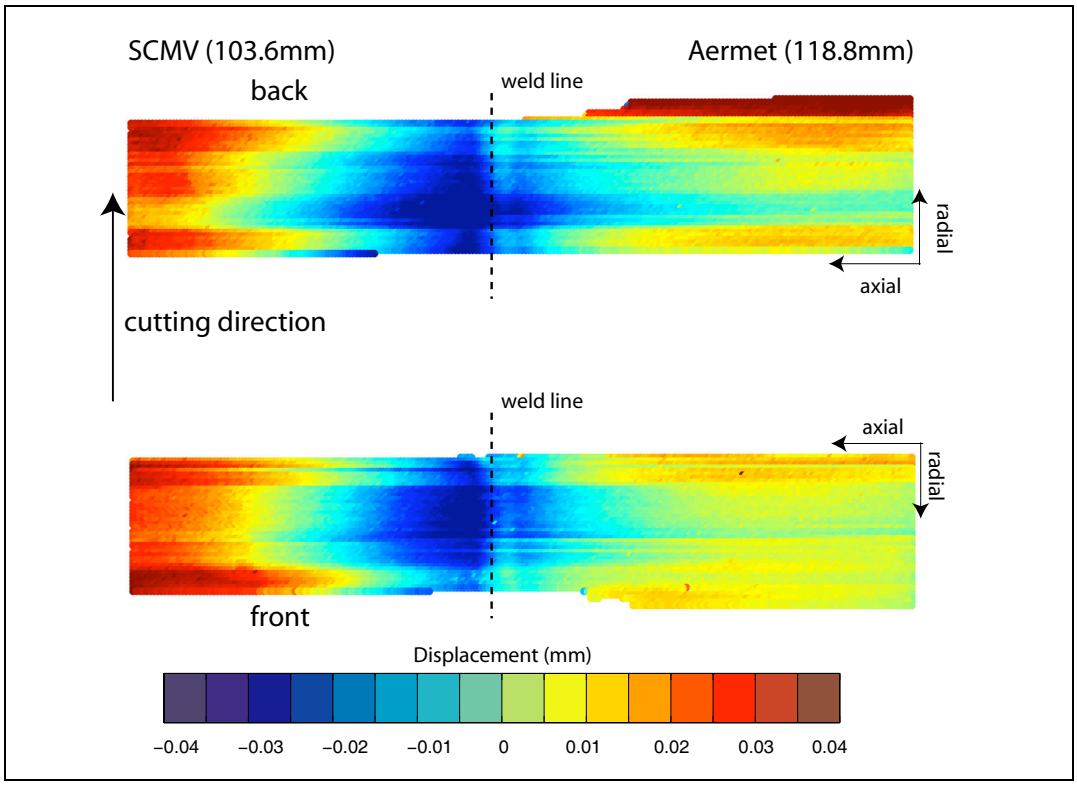

Figure 6-7. Front and rear cut surfaces from IFW2. Cutting problems (the horizontal striations) affect the measurements.

length of the extrusion. The meshing element, as usual, was the ABAQUS C3D20R (20-noded hexahedral quadratic, with reduced integration). Figure 6-8 shows the mesh used for IFW1, and Figure 6-9 shows the mesh used for IFW2.

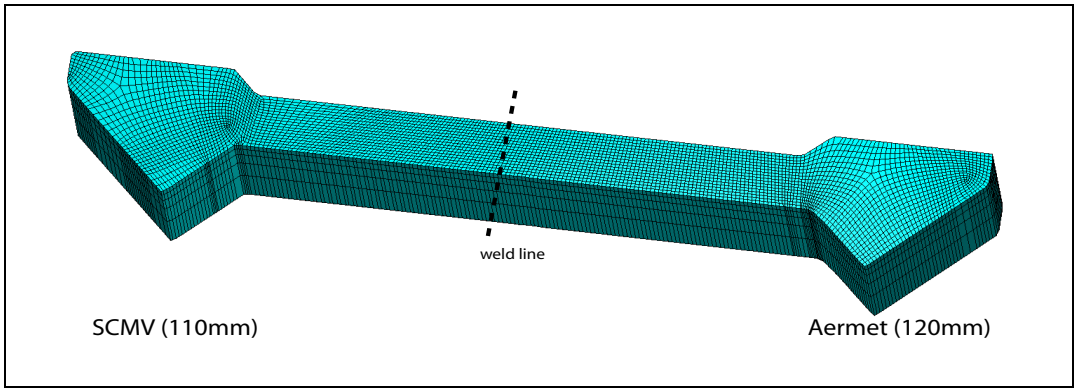

Figure 6-8. Model of IFW1. Initial seeds were placed at 2mm along the outline, and biased seeds were used in the extrusion. There are 9k elements and 45k nodes in total.

The front and back models of IFW1 each contained 9k elements with 45k nodes, while IFW2 used 11k elements with 55k nodes.

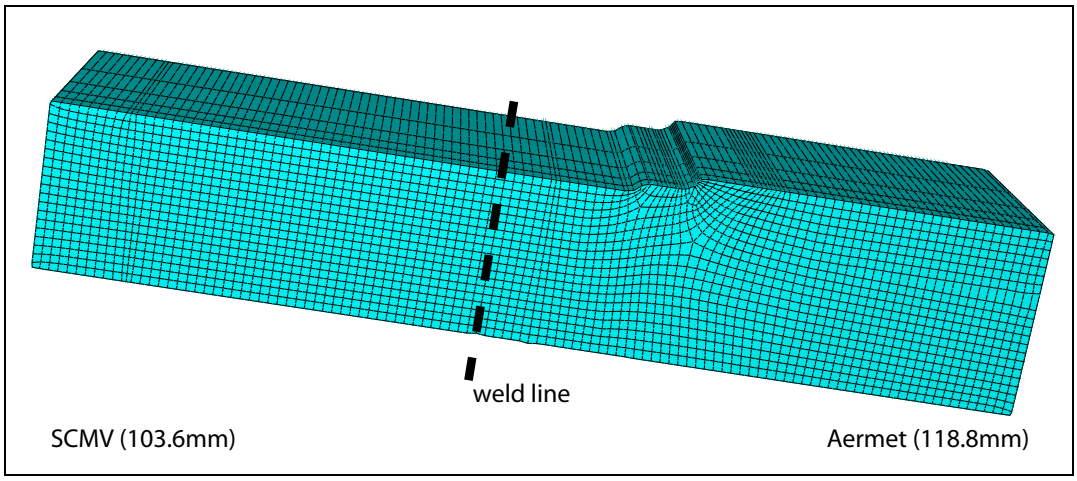

Figure 6-9. Model of IFW2, created in the same manner as IFW1. It contains 11k C3D20R quadratic hexahedral elements, with 55k nodes in total.

Unlike the other samples that have been discussed, the inertia friction weld is a combination of two dissimilar materials. This is taken into account in the model (created with a special version of the `create_inp_displacement` script) which creates two element sets with different material properties for each (Table 6-1). No special consideration is taken of the welding dynamics (and any gradual variation of elastic properties close to the weld line) due to the results from Moat and Karadge that report distinct separation of the parent parts at the weld line (Moat 2007).

The use of a linear, rather than cylindrical, extrusion to model the sample was intended only as a first approximation during this work. The scripts developed as part of this project to automate the creation of models only handled linear extrusions, and it was planned to extend this to accommodate arbitrary geometries. This would be a useful addition to the toolchain developed by the author. However, results comparing the contour method results with neutron diffraction measurements show very good agreement, as shown in Section 6.7.

6.7 Results

6.7.1 IFW1 front wall

The contour method gives a full two-dimensional map of normal stress across the section, and the results for the front surface of IFW1 are presented in Figure 6-10.

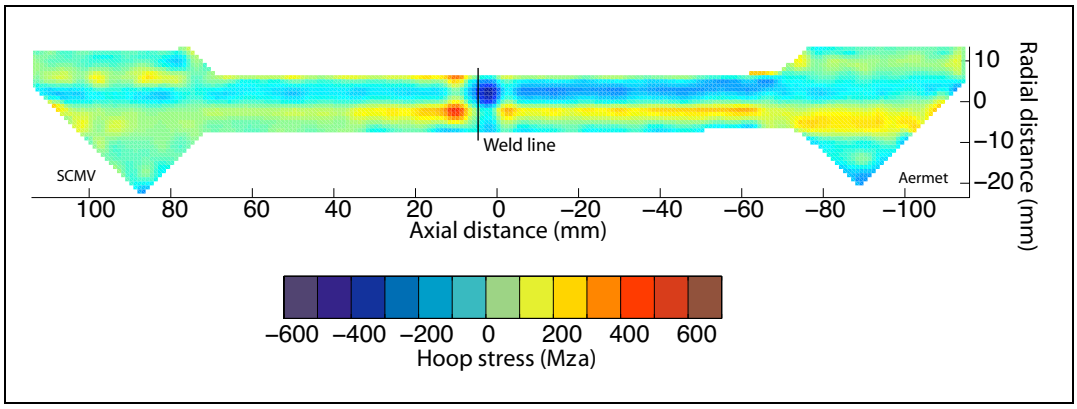

Figure 6-10. Hoop stresses in IFW1 (front cut) measured with the contour method.

Two dimensional maps are somewhat difficult to interpret quantitatively, but is it to be noted that there appear to be some axially oriented band-like structures that run through both materials in the weld - a broadly compressive area near the outer wall (top of plot) and less clearly a tensile area near the inner wall (bottom of plot). Both of these are interrupted by the weld line. Unlike the contour method, the neutron method is effectively a point measurement technique (although they actually average strain over a gauge volume, cf. Table 6-3). Stress maps are assembled from neutron data by interpolating between a small number of points, but these can be misleading because of the sparsity of the data points - a consequence of the time required for each measured point. In the case of the measurements made at POLDI, they should be considered as three line scans, and no attempt has been made to estimate the variation over the whole 2-D area due to the sparsity of the data. With this in mind, the three lines scans, labelled as 'inner' (4mm inside the centre line over the weld), 'centre' (the centre line), and 'outer' (4mm outside the centre line) are presented individually in the figure below (Figure 6-11). Overlaid on top of the neutron results are lines extracted from 2-D the contour map.

There is good agreement between the contour method data and the neutron measurements from POLDI. Particularly over the weld line, the shapes are very similar and the magnitudes also match well. Upon initial observation, the occurrence of a compressive hoop stress at the weld line is unusual, as hydrostatic tensile residual stresses are the norm as a result of welding processes. However, work by Bhadeshia regarding martensitic transformations of steel and the consequent volume increase

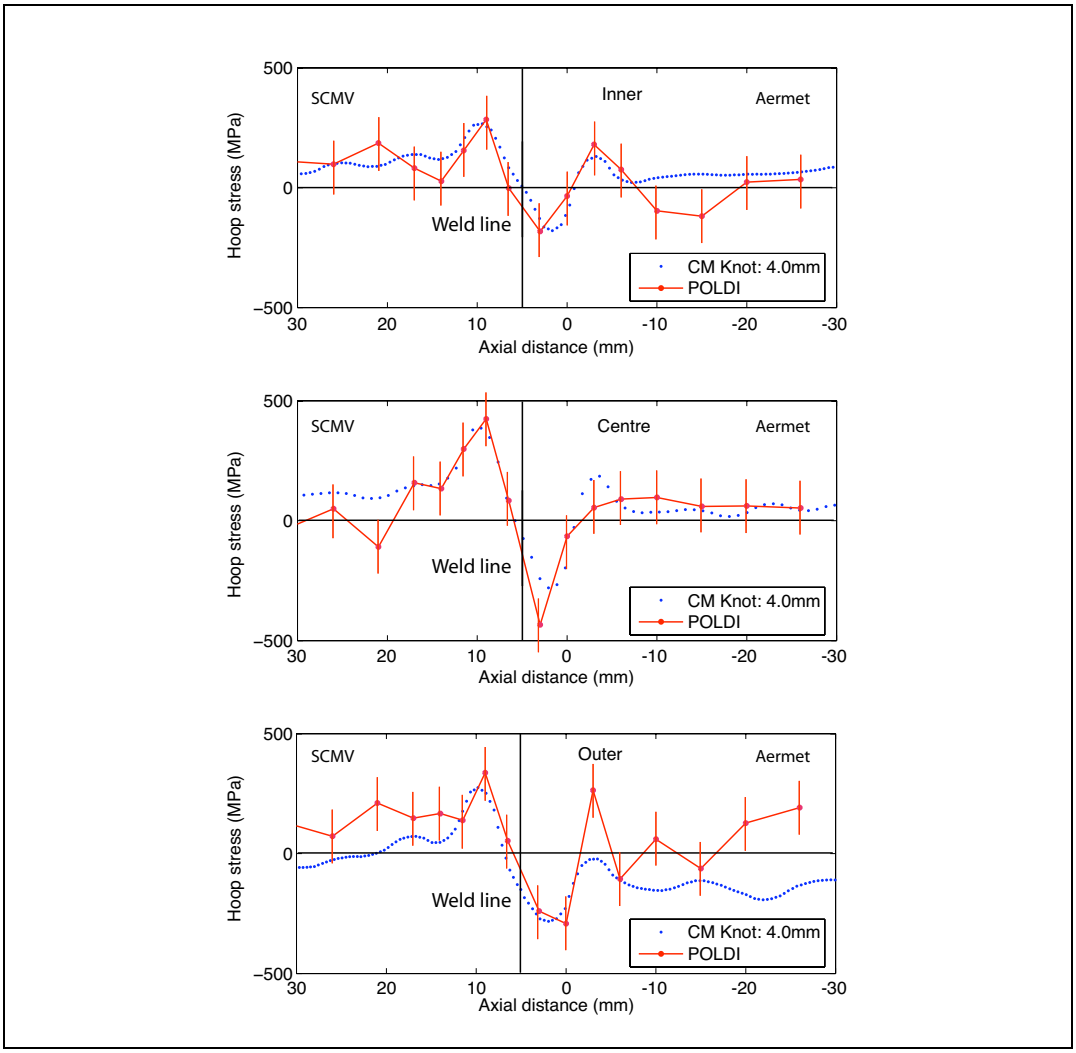

Figure 6-11. Contour method results for a 2mm pitched spline fit, compared with the neutron data measured at POLDI by Karadge. Not only is shape agreement good, but magnitudes also match well over the weld line.

that occurs under certain conditions, suggests that it may be this process that would counteract the shrinkage and tensile residual stresses that would normally occur in cooling material.

In terms of the CM measurement, Figure 6-12 illustrates the result of neglecting to correct for the cutting faults. The step change in the dataset is not removed, and in this case, the contour method results still give the correct trends but there is a base-line shift - caused by a bending moment. In order to accommodate the large

stresses caused by the wire 'steps', the rest of the model must be shifted very slightly to preserve equilibrium.

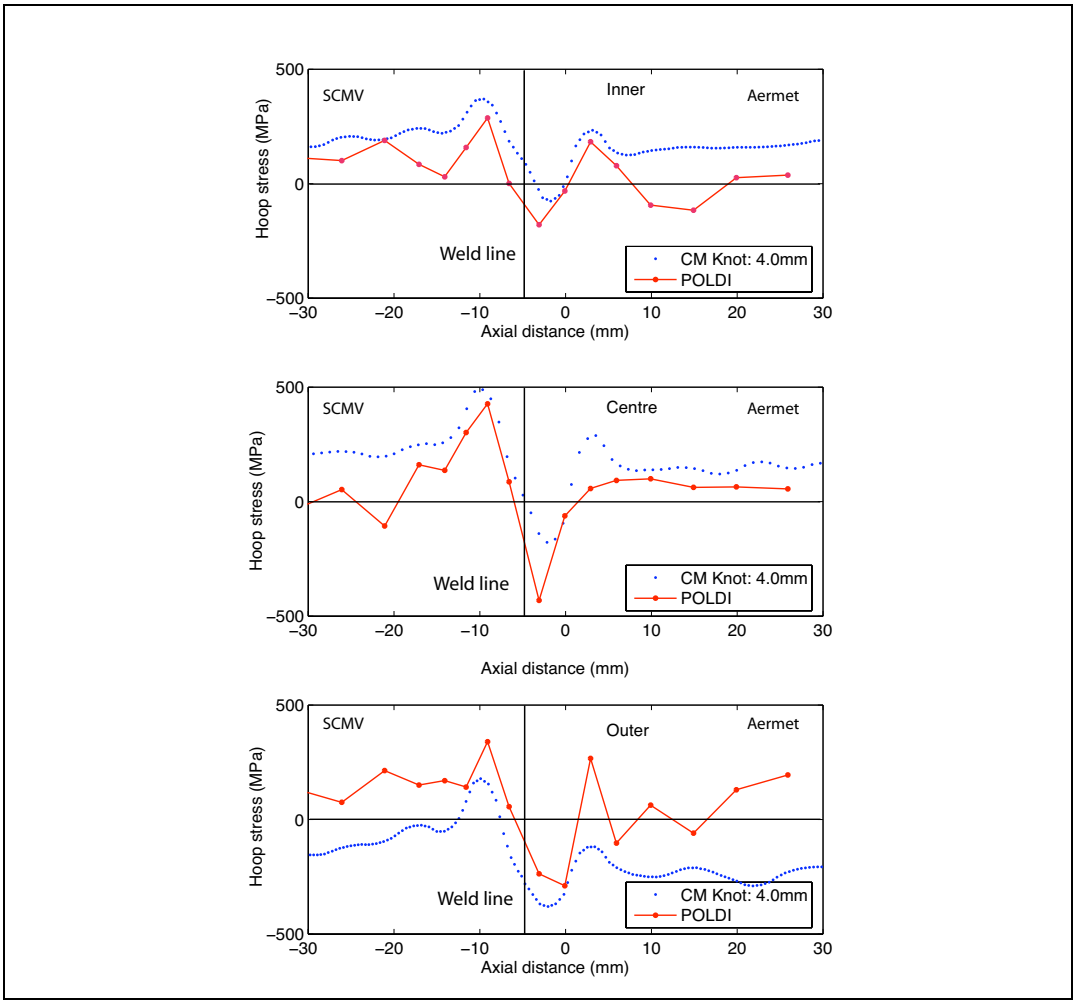

Figure 6-12. Results of contour method if wire artifacts are not removed - errors are manifest as a base-line shift. Large compressive and tensile stresses are apparent in the far-field region - a clear indicator of incorrect results.

Interestingly, despite the agreement between the neutron measurements and the contour method data extracted at the same locations, it is clear from the 2-D contour map that the stress profiles change quite quickly as one moves radially from outer to inner wall of the weld. Neutron measurements give no indication of this, but arbitrarily extracting a single line from the contour map would be imprudent without a fuller understanding of the context. This highlights an advantage of the

contour method over selected neutron point measurements, since the entire map can be viewed at once.

6.7.2 IFW2 front wall

Whilst the initial measurements of the surface of IFW2 look poor, showing large cutting striations, the surface fitting acts as a smoothing filter. The results therefore still show some axial banding (Figure 6-13), but not significantly more so than

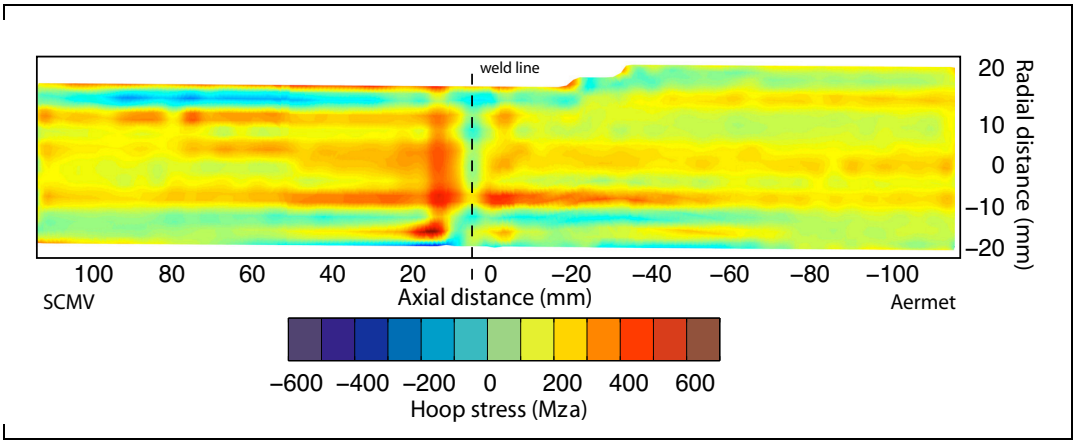

Figure 6-13. Contour method results for IFW2 front cut.

those from IFW1. As the welds were performed at different times, and the wall-thinning was done without records being kept, it is not possible to align the final dataset from IFW2 over IFW1. Some general observations are possible however:

1. While axial variations are seen in both welds, the strong compressive band (highlighted in Section 6.7.1) seen in IFW1 does not appear in IFW2. This band is confirmed by the neutron measurements. This may indicate that the wall-thinning process causes the creation of this region. It would be interesting to simulate the machining process in an FE model in order to verify this.
2. EDM cutting with long wires (300mm) is very difficult to control and results in poor quality surfaces that are not easily corrected. Cutting with a shorter wire in the perpendicular direction would improve the surface finish, but would require the cutting wire to pass entirely through the weld line at one time. Clamping of a cylindrical sample is much more difficult in this attitude.
3. A considerable amount of smoothing is possible with poor quality surface data, but differing knot pitch in the lateral directions would permit greater smoothing in one axis while retaining high spatial frequency information in the other.

6.8 Conclusions

The examination of a sample well suited to both measurement techniques has validated the contour method against the widely-accepted neutron diffraction technique. The results in the region of the weld line show good agreement, and they highlight the role of martensitic transformation in the residual stress maps of this dissimilar steels weld.

The success of the contour method is strongly determined by the ability to make a defect-free planar cut through the sample, and this is clearly a weakness when attempting to measure such large samples. Despite this, small post-measurement adjustments can be made in certain cases to enable results to be extracted. Further work in optimising both the cutting parameters and the clamping mechanisms would be valuable.

Whilst the wall-thinning procedure had previously been accepted as a reasonable manner of permitting neutron measurements of these weldments, the CM results for IFW2 clearly reveal substantial differences from those of IFW1. In the light of this, some reassessment of this procedure for practitioners may be necessary.

The next chapter examines a second friction weld, and develops the spline to better accomodate the characteristic strong variations across the weldline whilst not over fitting the low stress parent materials.

7 Stresses present in linear friction welds

Friction welds, whether linear or inertia (Chapter 6), contain high stress gradients and magnitudes at the weld line, which can typically be difficult to measure accurately with diffraction methods. In this chapter, titanium alloy linear friction welds are examined in the as-welded and post-weld-heat-treated states using the contour method. These samples provide a good testbed to develop the ability of the CM to capture strong localised gradients using non-uniform spline fitting. To this end, I have developed a procedure for identifying non-uniform knot spacings for better fitting of sharply varying displacement fields giving better estimates of the underlying stress fields. In addition, comparitive synchrotron data also exists to verify the results.

7.1 Background

While conventional fusion welding is effective for joining many metals, it is less than optimal when used with titanium alloys, as the material is highly reactive at elevated temperatures. Localised inert gas environments are used to ameliorate this problem, such as TIG (tungsten inert gas), EBW (electron beam welding) and PAW (plasma arc welding), but any lack of weld control is manifest as weld defects: pinholes, shrinkage cracks, pores, grain coarsening and embrittlement (Daymond 2003). The melting and re-solidication of the weld line also results in high residual stresses with a signficant hydrostatic tensile component and a heterogeneous microstructure (Preuss 2004).

Linear friction welding (LFW) is a technique developed over the last three decades that involves the reciprocating motion of one part against the other to the point of

plasticity while under an axial loading force. Figure 7-1 is a schematic of this process. As pointed out by both Daymond (Daymond 2003) and Threadgill (Threadgill

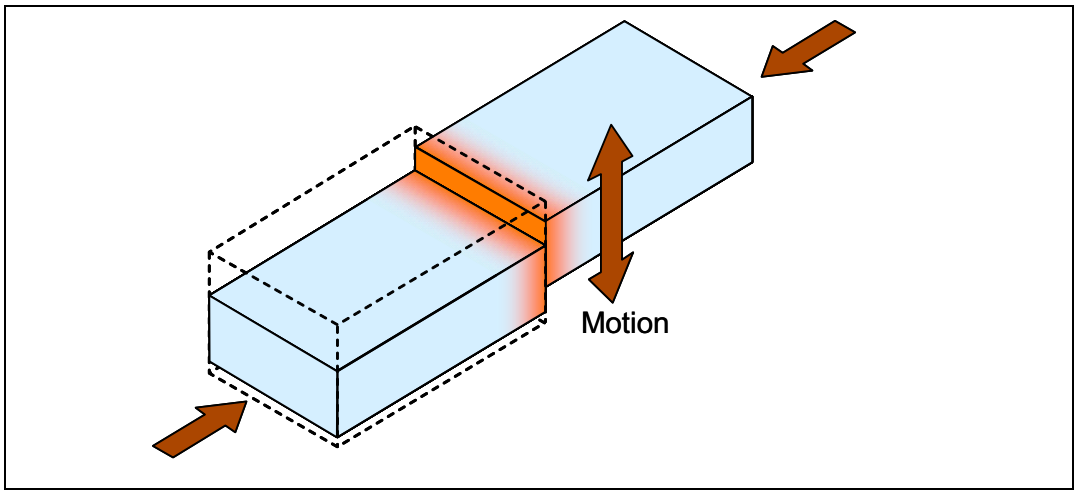

Figure 7-1. Schematic of the linear friction welding process (courtesy King).

2001), the benefits of linear friction welding are that:

- it is a solid state process (no melting) which gives reproducible, high-quality welds
- no filler wire or shielding gas is required
- no fume or spatter is produced
- less material is lost than with fusion welding

In the aero industry it has garnered a great deal of interest, particularly for joining high temperature components used in jet engines. The traditional method of assembling turbine blades and the central ring or disk, for instance, is either to machine the components from a single billet or to use a central ring with slots into which each blade is inserted. Machining the whole assembly from a single billet is complex and expensive, produces large amounts of waste, and the material for disk and blade must be the same. 'Fir tree' roots from joining blades to a central ring - producing a 'bling' permit the combined usage of suitable materials, but are heavy and have problems with fretting damage which can lead to failure. Linear friction welding permits the joining of dissimilar materials for blade and ring that have each been optimised for the environment they operate in, can create a joint with

excellent aerodynamic properties, and may be performed in the physically contstrained space of the turbine ring assemblys.

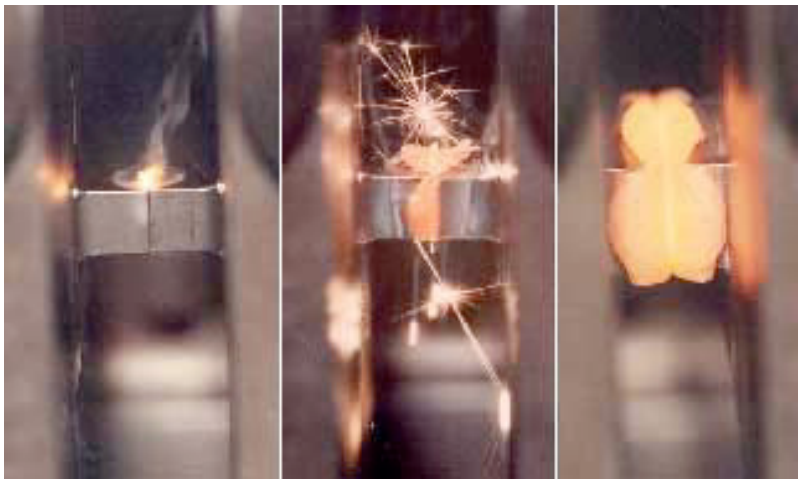

Figure 7-2. Three of the stages in the LFW process: a) Initial b) Equilibrium c) Forging (courtesy Rolls-Royce)

There are four distinct stages to the LFW process (Vairis 1998):

1. Initial phase. The two parts are brought together and while the contact surface is not complete (due to imperfect surface finishes on the samples) the frictional heating causes softening. This in turn increase the contact area.
2. Transition phase. The contact surface between the parts is 100% of the area, and a plasticised layer forms between the samples. Under axial load, deformation starts to occur. Large wear particles are being expelled, but no axial shortening has happened. Any material that does melt is also expelled.
3. Equilibrium phase. The plastic contact layer is now expelled from around the parts, forming flash on all sides. The axial shortening (upset) rate is linear with respect to time.
4. Forging (or deceleration) phase. Once the required amount of axial shortening has occurred, the parts are held stationary in their final position, and the axial pressure is increased to the forging level. Once cooled, the weld is complete.

Unlike many other welding processes where heat is applied to the external surface of the materials, the heat flow in LFW is from the interface boundary outwards (Mary & Jahazi 2006). Materials like titanium are well suited to this process, as their lower thermal conductivity results in more uniform temperature distribu-

tions across the weld during the equilibrium phase. While the temperature of the heat affected zone is uniform at the start of the declaration phase, the outside surface of the sample cools much quicker than the inner core resulting in tensile residual stresses due to the local yielding of the part. LFW can produce joints of very high quality, but the stresses that remain after welding mandate some form of stress relief (Frankel 2008), usually in the form of post-weld heat treatment (PWHT). Evaluating the efficacy of different PWHT parameters is of great interest, and requires the accurate measurement of the effect they have on the residual stresses. In this chapter contour method measurements are undertaken and compared with synchrotron measurements made at the ESRF by Frankel et al. (Frankel 2005).

7.2 Provenance of the samples

The three Ti-6Al-4V LFW samples that were studied are process development samples, rather than in-service components (see Figure 7-3), provided by Rolls Royce plc. The welding parameters are not available in the public domain, but the first sample was in the as-welded condition (AW), the second was heat treated for one hour at 500°C (PWHT500), and the third was heat-treated for one hour at 600°C (PWHT600).

The coordinate system for these samples has been adopted from that of the engineering components, as seen in Figure 7-4. The contour method is only able to measure stresses on a single plane at a time, and in this chapter the axial stresses were those of concern.

In order to characterise the residual stress distribution across the weld, high energy synchrotron x-ray diffraction measurements were carried out on the ID15A beamline at the ESRF, France (Frankel et al.). The measurements were undertaken using white beam (polychromatic) x-rays and a measurement gauge volume of 0.25 x 0.25 x 2mm. Strain measurements were made in the three principal directions (radial, hoop, and axial) in order to be able to calculate stresses. The strain scans were carried out at mid-wall thickness.

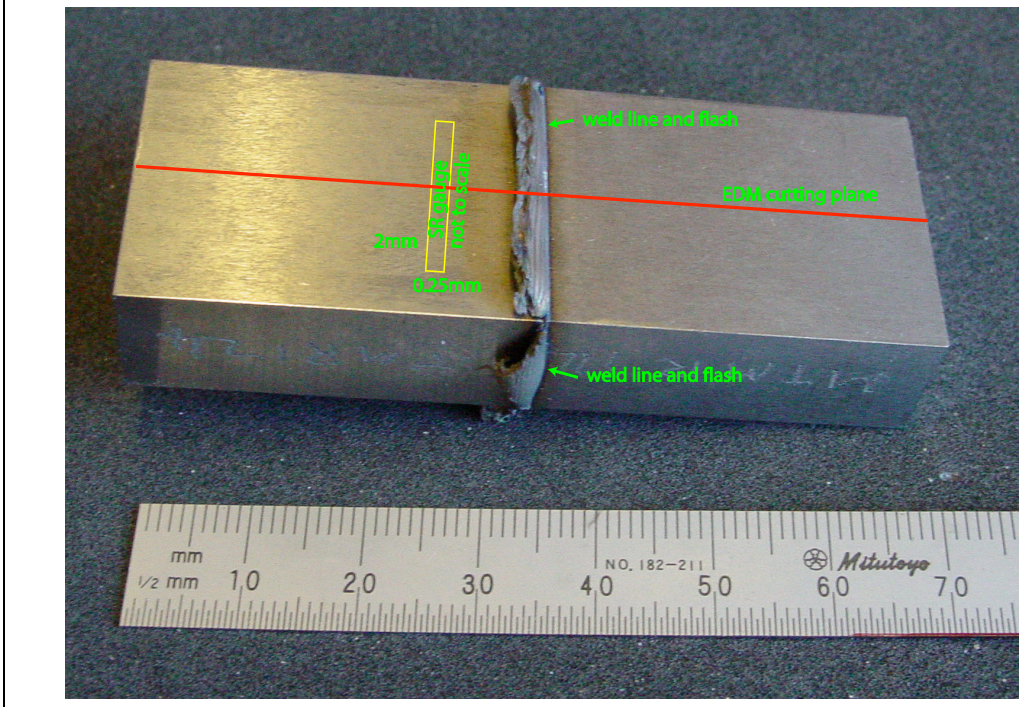

Figure 7-3. One of the samples after welding, overlaid with gauge shape (not to scale) used in synchrotron measurements.

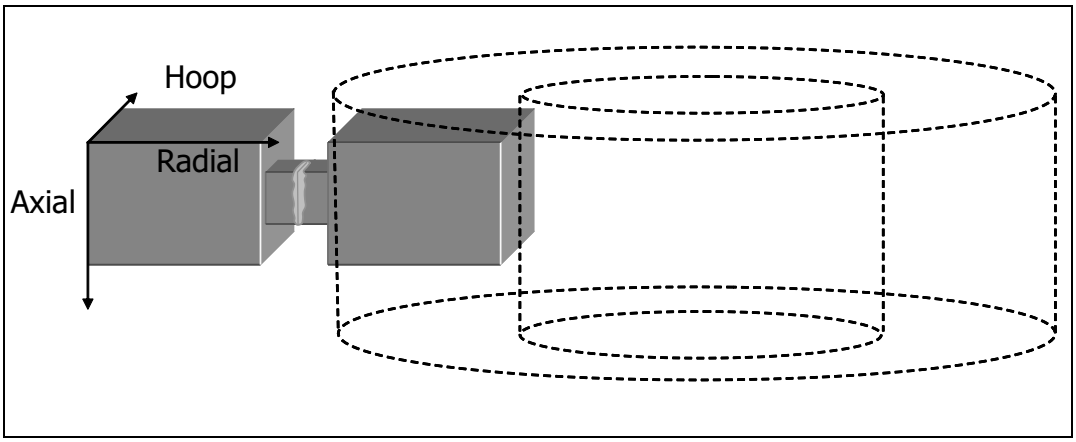

Figure 7-4. Schematic of blade-disk assembly for a linear friction weld. The cylindrical nature of the part influences the axes naming convention; radial, hoop, and axial. The measurements in this chapter concern the stresses in the axial direction. (courtesy Frankel)

An optical micrograph (Figure 7-5) reveals a relatively fine microstructure that is well suited to synchrotron diffraction based measurements, as the sampling volume includes a large enough number of grains to give good measurement statis-

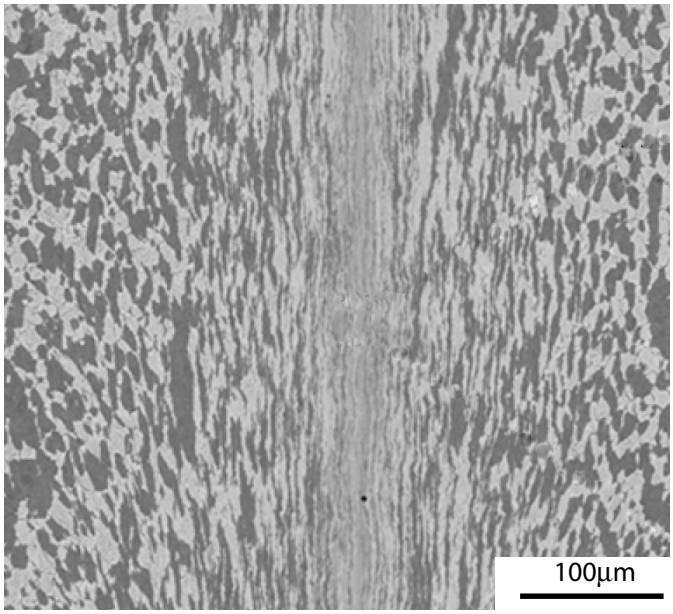

Figure 7-5. Micrograph of a typical Ti-6-4 LFW, showing microstructural changes across the weld line (courtesy Karadge).

tics of the macrostrain (type I stresses) but reduced sensitivity to intergranular strains (type II stresses).

As described in Section 2.3.2 the strain-free lattice spacing, d_o, is used to determine the measured lattice strains. The synchrotron measurements in this case were made using a global d_o value. This is outside recommended practice because lattice spacing might be expected to change considerably across the plastically affected zone (PAZ). However, no d_o measurements were available so the reported values must be treated with caution, and the values around the weld line are not shown in the figures.

7.3 Cutting and measuring

For the contour method studies, samples were cut by Parkside Tool & Die, using a Charmilles Robofill 2020 (Charmilles 2020) with a 250µm zinc coated brass wire. The as-welded samples had flash on both sides of the welding plane, but one side had been removed prior to examination. The cutting plane was mid-thickness, perpendicular to the axial direction, resulting in samples as shown in Figure 7-6. The sample was clamped close to the cutting line on both sides, and cut from left to

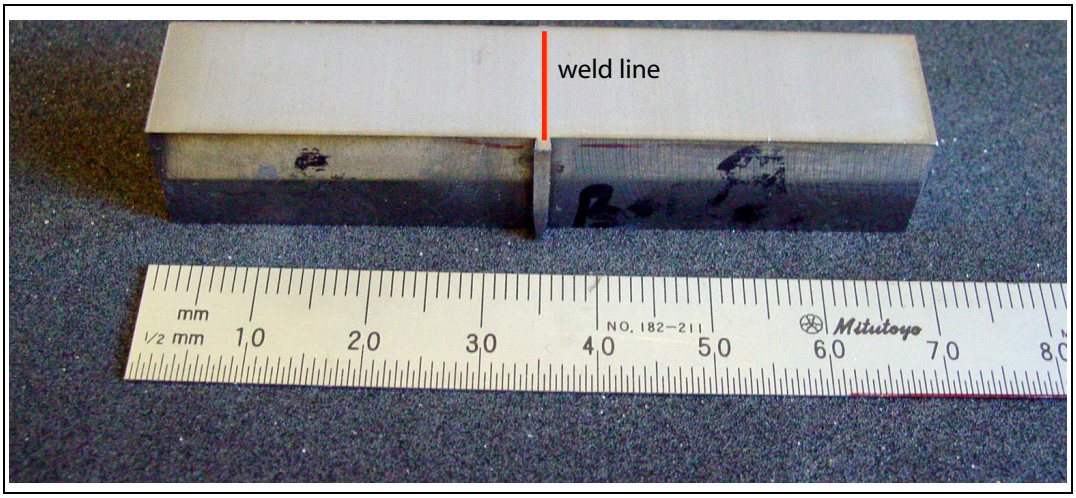

Figure 7-6. Ti LFW after cutting. Most of the flash has been trimmed or machined away entirely. Cut was made from left to right with respect to the camera.

right (with respect to the photograph). The operator chose the EDM parameters, using a preset on the Charmilles machine for 'skim' cuts. This would normally only be used as a secondary finishing cut but uses a much lower cutting voltage, causing a smaller recast layer to be formed.

The two halves were measured with the CMM in the periodic measurement ('hen-peck') mode using the SP600 with an 8mm diameter ruby probe (see Section 3.2.2). The data from the linear friction welds, taken at a 200μm pitch in both lateral directions, are shown in Figure 7-7. The tensile region around the weld line is visible in the displacement data as a valley, where upon release after cutting the material retracts.

7.3.1 Surface data processing

The process of minimisation of noise was performed manually for gross outliers by removing the points, then the two surfaces were aligned with the iterative closest point routine detailed in Section 4.4.2. Best fit planes were also removed (according to the procedure defined in Section 4.4.1). The two surfaces were averaged together and then a spline was fit to the mean surface. The surface fitting in this example was quite difficult, because, as seen from the projection view of the point cloud, most of the surface has a very low gradient, with high gradients only present 5mm on either side of the weld line. Two different fitting procedures were used

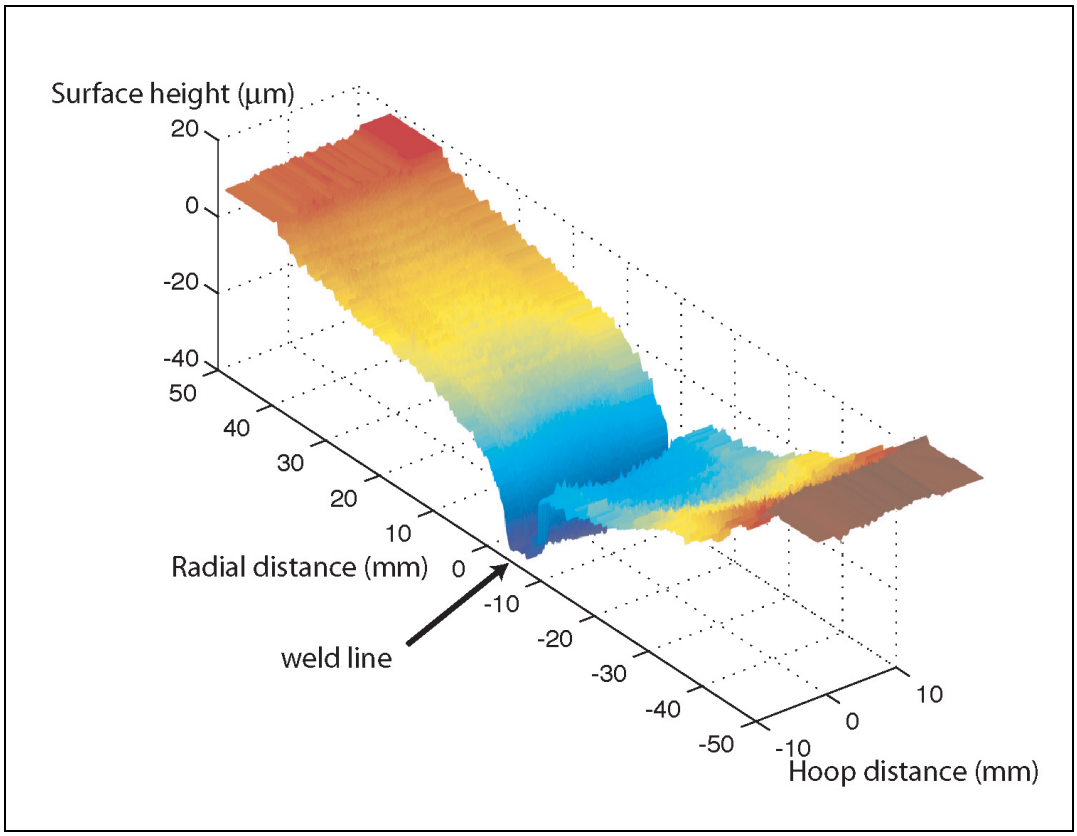

Figure 7-7. Averaged displacement (surface height) data for the as-welded Ti LFW. The measured point density is 200µm using the henpeck mode.

with these samples. This first, as had been used previously in this thesis, was a uniformly knotted bivariate spline, (explained in Chapter 4) with knots placed every 2mm, and third order (cubic) polynomials used for each segment. This process, and the reasons for the spline parameter choices, are explained more fully in Section 4.4.3. Figure 7-8 shows the results of the 2mm spline of the averaged surfaces.

However, as shown in the initial results (Figure 7-12), this fit highlights the inadequacy of choosing the spline parameters visually. Using a uniform knot spacing to represent a surface that is non-uniform in gradient leads to compromised stress estimations - in this case a periodicity having a square form.

The difficulty with the uniform spline fitting technique used up to this point is two fold. Firstly, the spacing of the knots should be sufficient to fit only the measured data (but not fit the intrinsic noise of the measurement instrument). Secondly, the

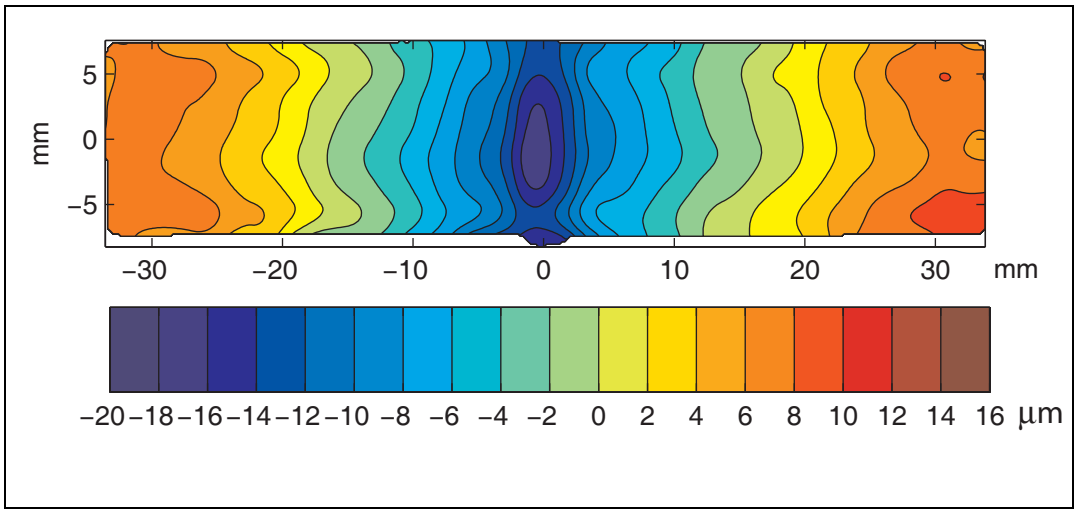

Figure 7-8. Averaged surface displacement plot of as-welded Ti LFW.

regular spacing of those knots does not take into account variations in the frequency content of the displacement data. The LFW samples are particularly strongly affected by this problem as displacement variations are largely one-dimensional (in the radial direction). The next section develops the original techniques of uniform knot spacing to accomodate this sample.

7.4 Non-uniform spline fitting

Given some one-dimensional data that has a distinct region of high gradient com-

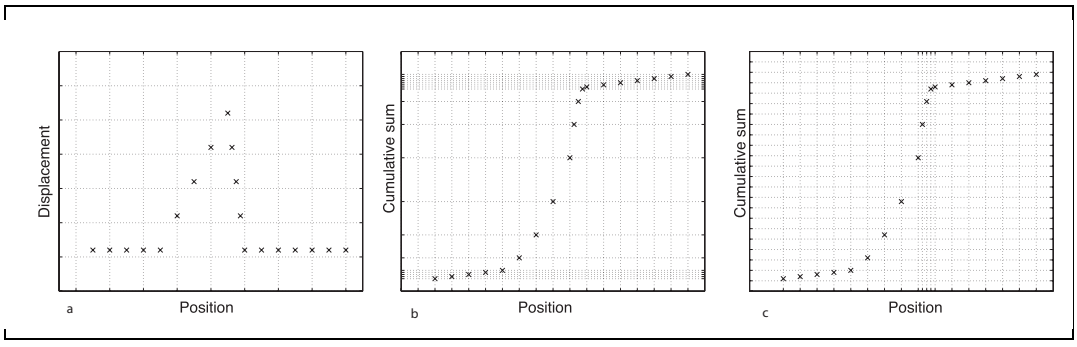

Figure 7-9. Process for generating non-uniform knot spacing as a function of the gradient content of the measured displacement dataset.

bined with a low gradient background (Figure 7-9a, shown with uniformly spaced knot locations underneath), one would like to generate a knot spacing that was denser in the region of the peak, and more widely pitched in the non-varying

region. The original data are offset to ensure positive values, then the cumulative sum is taken. The offset ensures that the summed data (Figure 7-9b) is monotonically increasing. The vertical axis is then rescaled to the value of the position axis (from 0 to *max position*). These data are a one-to-one mapping for the x coordinate, but a many-to-one mapping for the y coordinate. A linear interpolation is performed against the y-axis, resulting in a vector of data containing the knot spacing now weighted towards the regions with larger slopes (Figure 7-9c).

This process was applied to the LFW sample, and the resulting non-uniform knot locations are shown in Figure 7-10.

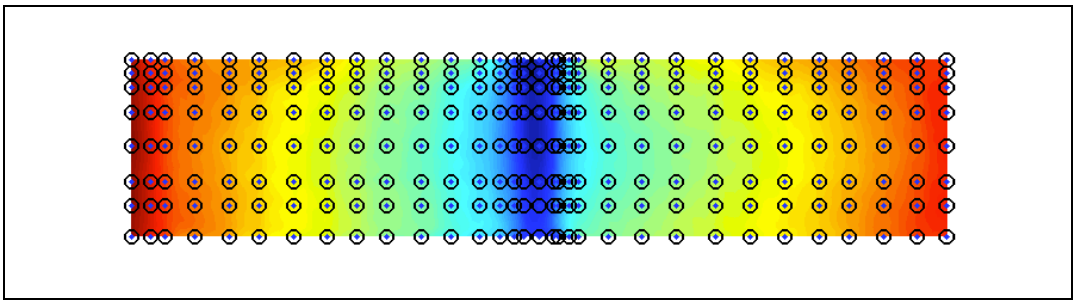

Figure 7-10. Non-uniform knot spacing for the as-weld sample (AWnu) The density of knots is highest around the weldline.

7.5 Modelling

A simple homogenous model was used (assuming that all parts of the sample, including the heat affected zone (HAZ) around the weld had identical elastic properties). The mesh (Figure 7-11) was built using 20-noded hexahedral elements (8160 in total) with 1mm^2 dimensions in the contour plane, and a biased mesh seed (5:1 ratio) to reduce unnecessary computational load towards the bottom face of the sample. The elastic properties were taken to be those customary for Ti-6Al-4V: 113GPa for Young's modulus, and 0.3 for Poisson's ratio. The entire sample was restrained with two corner nodes to prevent rigid body motion.

The measured displacements were applied to the model as boundary conditions, the fitted spline being evaluated at the location of each node on the top surface. After equilibrium, the boundary conditions were applied, and the resultant stresses

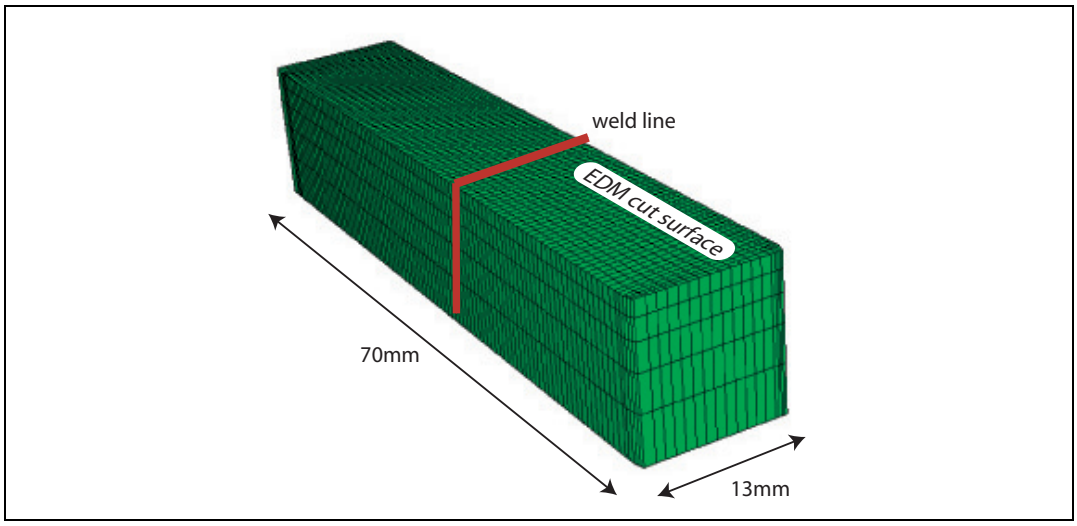

Figure 7-11. Finite element mesh of Ti LFW, showing biasing in mesh density away from top surface

recorded. The LFW samples are of a very simple geometry, and meshing them in ABAQUS was straightforward.

7.6 Results

The contour method produces a full 2-D stress map in a single process, unlike many other residual stress measurement techniques. Figure 7-12 demonstrates the problems that can be caused by using an inappropriate knot spacing. The uniformly pitched spline knots (applied to the AW sample), have a clear periodic patterning in the parent materials, caused by overfitting. With samples that contain

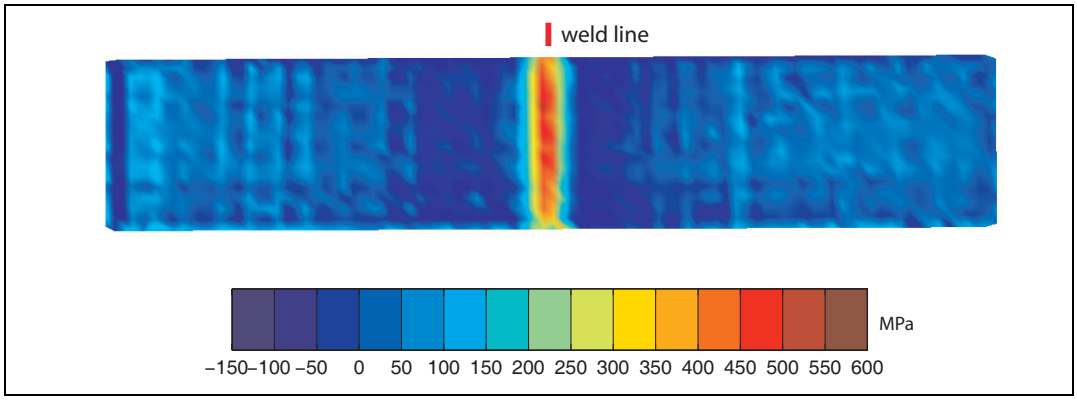

Figure 7-12. Contour method results for as welded Ti LFW using a uniform pitched spline (AWu). The patterning that appears in the parent material is as a result of overfitting in this area.

such variability in the displacements fields, a non-uniform knot spacing provides smoothing that is adapted to the underlying displacement gradients.

The much improved results for the non-uniform knot spacing are shown in Figure 7-13 (AW, PWHT500 and PWHT600).

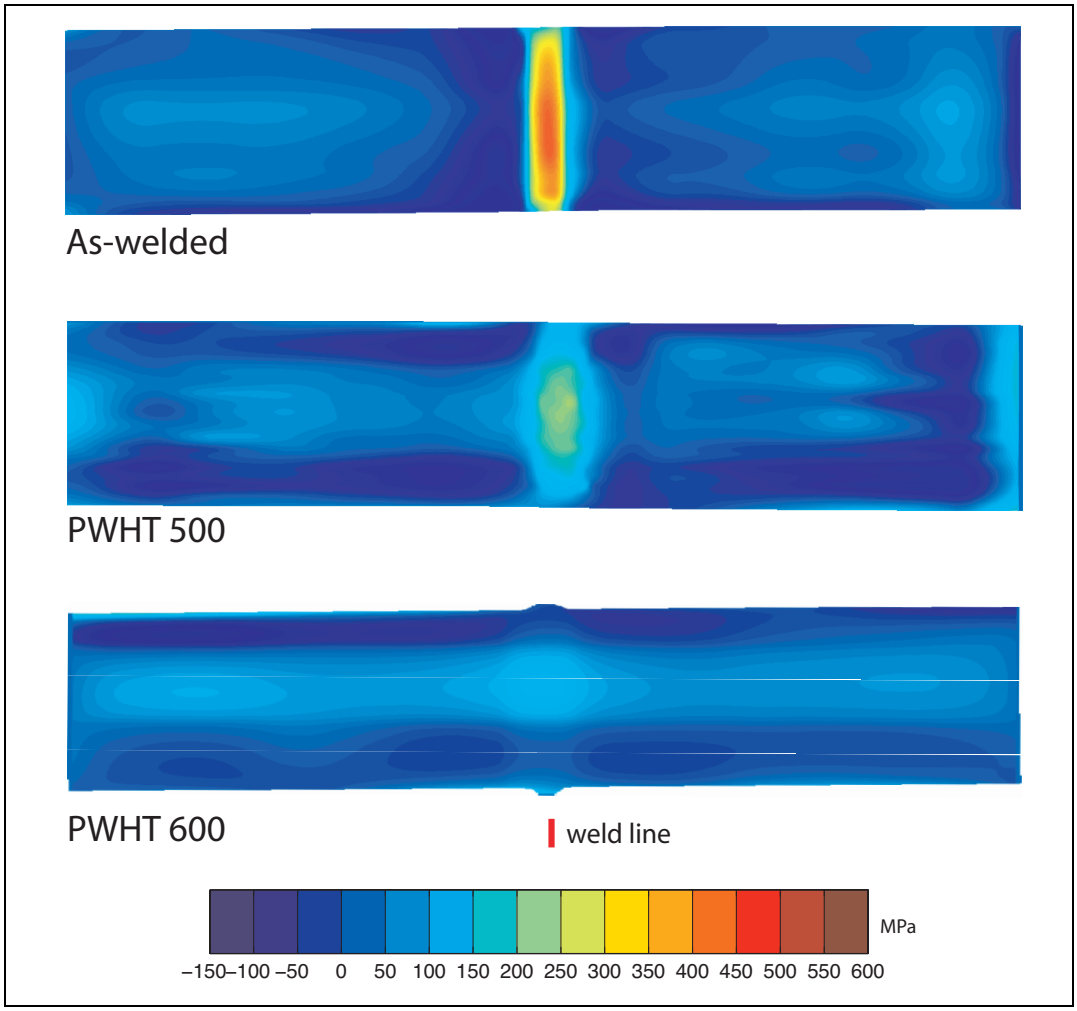

Figure 7-13. Full CM maps showing the AWnu, PWHT500nu and PWHT600nus samples

Qualitatively, the PWHT500 sample exhibits a significant reduction in the tensile stresses present at the weld line in the AW sample, but it is only with the elevated temperatures used for PWHT600 that the stress relief is essentially complete.

In order to quantitatively compare the axial stresses in the three welds, a single line was extracted from the centre of the three maps (shown in Figure 7-14).

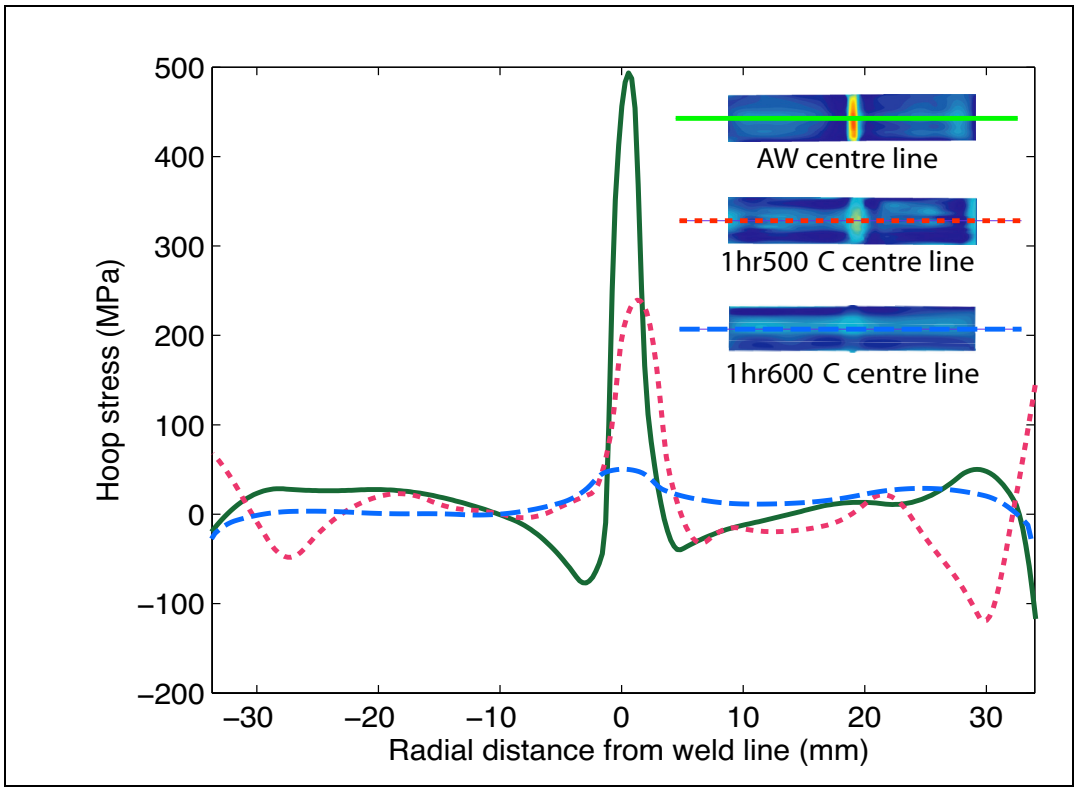

Figure 7-14. Overlay of as-welded (green) and PWHT-1hr500 (red) Ti LFW using non-uniform spline knot spacing. Insets showing centre line used to extract line plots from 2D contour maps.

This confirms the initial observations made using the 2-D map that the high tensile stresses at the weld line (almost 500MPa in the as-weld condition) have been reduced significantly (but not fully relieved) to just over 200MPa after 1 hour of heat treatment at 500°C. The 600°C treatment reduced the stresses to around 90MPa at the weld. In the as-weld condition, there appears to be a small degree of balancing compression present on either side of the weld line, which is not apparent in the PWHT samples.

These data were then compared with synchrotron diffraction results (measured by Frankel et al. 2008). Figure 7-15, Figure 7-16, and Figure 7-17 are comparisons of the contour method and synchrotron measurements for the AW, PTWHT500 and PWHT600 samples, respectively.

The agreement in the case of the as-welded sample is reasonable, with peak positions well matched. The peak magnitude is much smaller in the contour method results,assuming the SR data gradients on either side of the weld line would con-

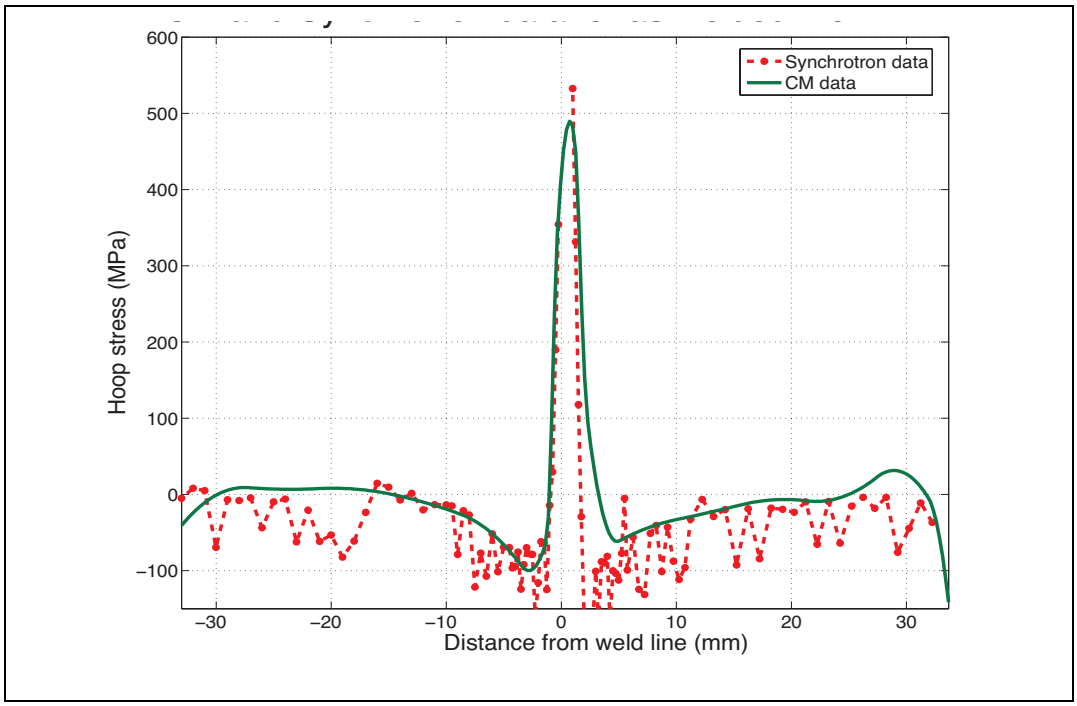

Figure 7-15. Comparison of the CM results with the synchrotron diffraction results for the as-welded sample (SR data courtesy Frankel)

tinue until the lines intersected. However, as noted previously (Section 7.2), the SR results are not valid over the weld line (no stress-free lattice spacing is available in this region), so these data points are not displayed.

The results for the heat-treated samples show good agreement, although without valid synchrotron data at the weld line, the comparison is not complete. There is a signifcant reduction in the area of balancing compression that was visible in the as-welded sample about 3mm on both sides of the weld line, certainly in the contour method results, and mostly so in the synchrotron diffraction results.

While the synchrotron diffraction technique can yield accurate results (±30MPa in the bulk, ±50MPa over the weld line when using an accurate d_o value (Preuss 2005)), it does have some disadvantages when the measurement of type I stresses is intended. The gauge volume often encloses only a small (and variable, depending on local microstructure) number of grains, and thus the macro stresses must be inferred from averaged measurements (Withers 2003).

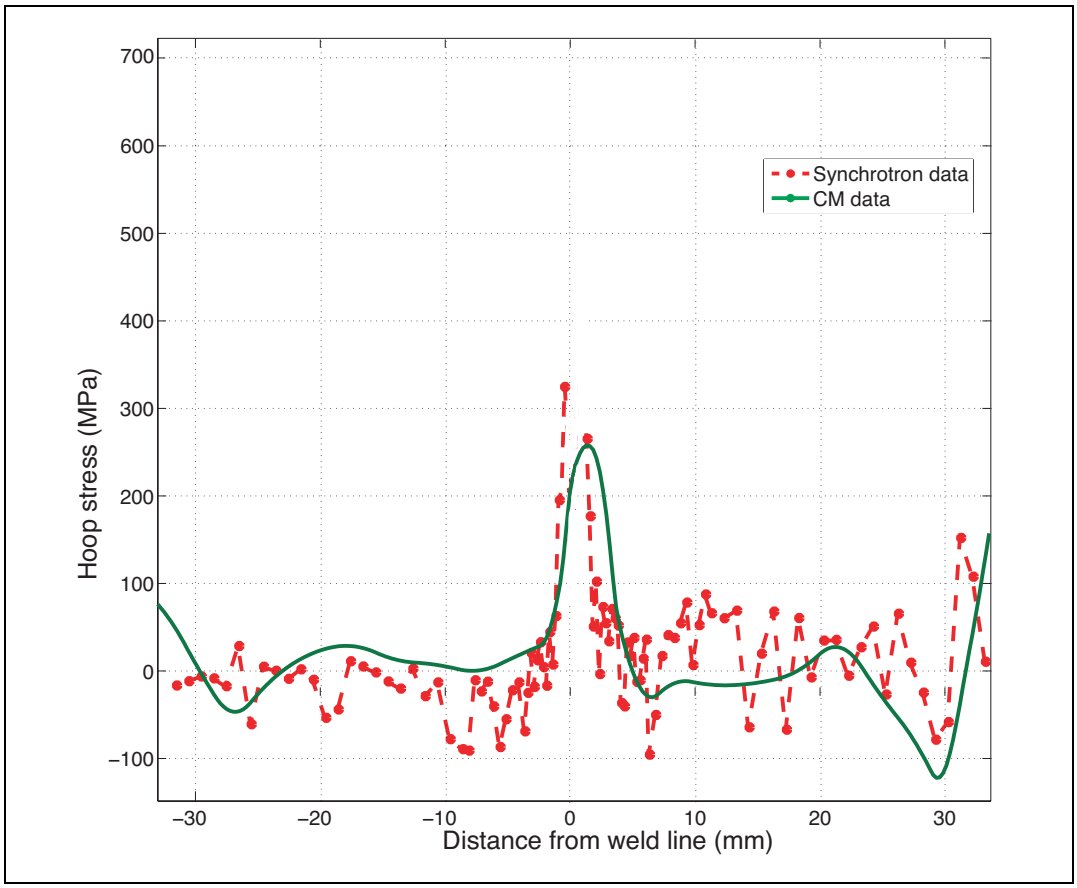

Figure 7-16. Comparison of the CM results with the synchrotron diffraction results for the PWHT500 sample (SR data courtesy Frankel)

The spatial resolution of the contour method is a combination of a number of different parameters. Firstly, the measurement pitch used in recording the displacements. Secondly, the smoothing effect of the surface fitting used. Thirdly, the node density (element size) of the finite element mesh used in modelling. It is difficult to ascertain the relationship between these factors, but certainly the results have no greater spatial accuracy than the lowest resolution used in any of the three stages.

The nearest equivalent to gauge volume (the synchrotron's *de facto* spatial resolution) for the contour method in this case is the mesh of the finite element model. This was 1mm, and as such is acting to average underlying stresses. This results in an inability to represent the very steep stress gradients of the weld region and a reduction in peak magnitudes.

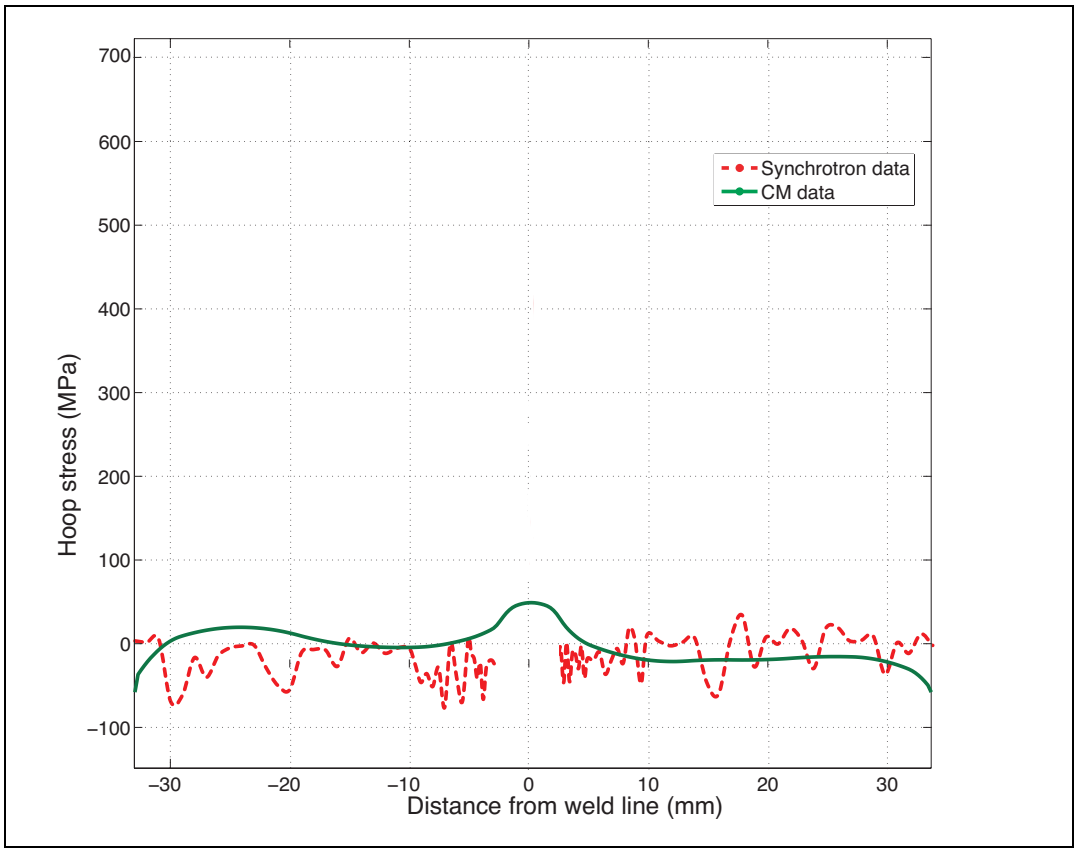

Figure 7-17. Comparison of the CM results with the synchrotron diffraction results for the PWHT600 sample (SR data courtesy Frankel)

7.7 Conclusions

The use of the contour method to measure locally intense stress components has been demonstrated to be promising in resolving the steep stress gradients associated with this type of welding, and verifying the efficacy of post-weld heat treatments. While the CM does not have any sensitivity to local microstructure as the SR results do (preventing the measurement of stresses using X-rays at the most interesting location - the weld line) the CM appears to be somewhat unconservative (under estimating of magnitude).

The steep gradients present in LFW present real problems for traditional fixed knot spacing approaches.The author developed a variable knot spacing approach that concentrates the highest knot densities in the region of sharpest gradient. This improves significantly the estimates of stress that can be achieved, matching well

to synchrotron data. Ideally, methods should be developed that allow variable knot spacing in 2D or, better still, vary the knot locations in an irregular manner to respond to local varations in the stress gradient.

From investigating the applicability of the contour method to large samples, the next chapter moves to using high precision optical measurements to look at very small displacements in laser shock peened plates, extending this work to a bi-directional non-uniform fit, and discussing some of the changes required in modelling that would be need to optimally fit the entire displacement data.

8 Stresses induced by laser shock peening

Laser shock peening is a relatively new technique for inducing near-surface compressive residual stresses. It was developed in a laboratory setting in the 1960s (White 1963), but advances in laser technology only enabled its commercial adoption in the mid-1980s. It is used in industrial settings for a wide range of processing tasks, primarily involved in reducing the propensity of cracks to propagate by creating a compressive region in the surface of the component. As it introduces stresses much deeper (~1-2mm) than conventional shot peening, it is not suited to hole-drilling measurement and x-ray layer removal is very time consuming.

This chapter examines two laser shock peened (LSP) samples. The parts have two different test patterns peened onto them, and the possibility of studying the induced residual stresses with the contour method is examined. This is an excellent test of the ability of the contour method to resolve detail very close to the surface.

8.1 Laser shock peening: history and technique

Shot peening, a mechanical impact process for inducing compressive residual stresses in the surfaces of components, has been in common use for six decades (Montross 2002). Using fairly simple equipment, a stream of hard spheres is projected into the sample, inducing a compressive layer that inhibits crack nucleation and propagation that is up to 250μm thick (Zhuang 2001, Prevey 1996). A large amount (~40%) of work hardening is introduced, and the resulting surface finish is typically poor (Prevey 2000). Laser shock peening is a non-contact extension of

this treatment, but has the advantages of being able to introduce much deeper stress fields with a uniform surface finish (Askar 1963). Developed over thirty years ago (Fairland 1974, Fairland 1976, Fairland 1979), it was hindered by inadequate laser power densities until the 1990s.

LSP induces a compressive residual stress field by shock wave propagation. Figure 8-1 shows a schematic of the three elements required: the sample, a sacrificial layer that is ablated by the laser, and an inertial tamping layer.

The laser beam is directed at the sample, and the absorption of the photons by the

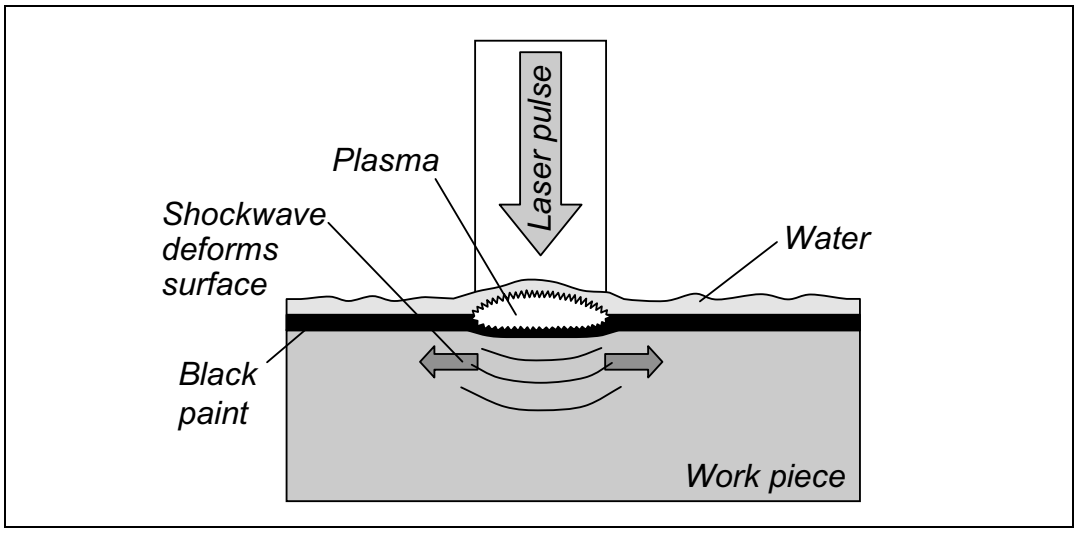

Figure 8-1. Components of laser shock peening: the sample to be treated, a sacrificial layer (paint) which is ablated, and an inertial tamping layer (most commonly water). (courtesy King)

sacrificial layer (most commonly black paint or tape) creates a plasma that expands rapidly. The tamping layer (usually water, but glass and quartz have also been used (Devaux 1993)) constrains the plasma, directing the shockwave into the sample. In order to achieve the plasma creation, very high power densities must be achieved (on the order of 10GW/cm^2). These specifications can only be met for very short durations, so the laser pulse width is typically ~20ns. The repetition rate (limited by the recharging time of the capacitor banks which drive the laser and the heat load on the focusing optics) is presently a few cycles per second (2-5Hz) using a neodium YAG laser (Peyre 1996).

8.2 Sample provenance

In many jet aero engines, the fan blade is attached to the disk with a dovetail joint, as shown in Figure 8-2. Fretting damage has been observed (Fridrici 2001) and in some cases has caused root failure. To prevent the initiation and propagation of

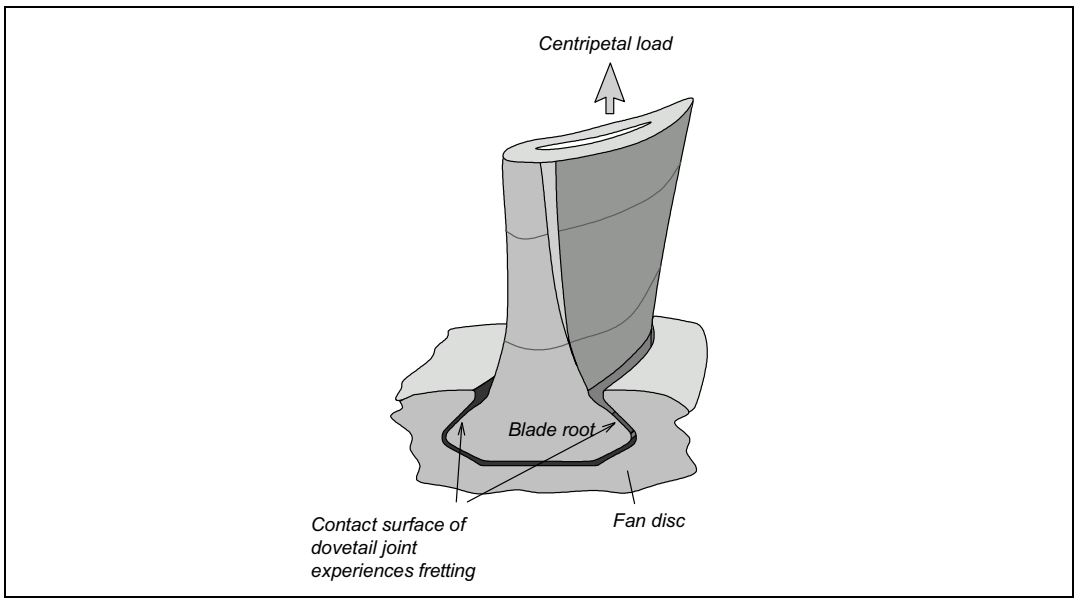

Figure 8-2. Dovetail joint assembly for WCFB (courtesy King)

cracks in this region, some form of mechanical surface treatment is used. Most commonly, shot peening is used (for instance, the Rolls-Royce Trent 800 engine must be thus treated to be certified for flight (King 2005)), but laser peening is also an option.

The Metal Improvement Company[1] (MIC) specialises in treatment services including both shot and laser shock peening. The two samples considered here were both peened by them at their UK plant. Synchrotron diffraction strain measurements have been made on these samples by Evans & King (Evans 2004) at the SRS in Daresbury. Their results are used as a comparison with the contour method measurements.

1. Metal Improvement Company: www.metalimprovement.com

The samples were identical high strength aluminium 7075 T7351 alloy plates (see Table 5-1 for composition), ~6.4mm thick and 45-50mm square. The mechanical properties for this plate were the following (AllMetal 2004):

- Yield stress: 450MPa (0.2%)
- Ultimate tensile stress: 515MPa
- Young's modulus: 69GPa
- Poisson ratio: 0.35

Sample A had been peened in a single location, approximately in the centre of the plate, with a double repetition laser pulse. The fluence of the laser (energy/unit area) was 180J/cm^2, and a square mask of 3x3mm was used. Considerable plastic deformation had occurred, and a square depression with bevelled edges of ~4mm width was visible to the eye (schematic in Figure 8-3).

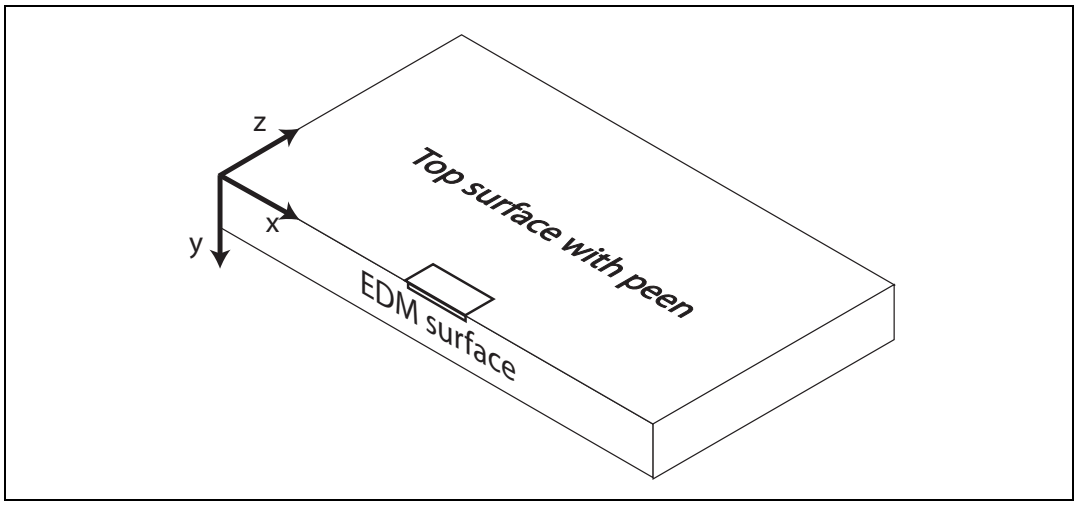

Figure 8-3. Sample A - doubly peened in the centre of the plate. Figure shows view after EDM cutting at z=0.

Sample B had been peened with the same laser parameters, but using a patterned distribution where the impacts were butted up adjacent to each other, and then a second shot was overlaid with an offset of 1.5mm in both lateral directions (shown in Figure 8-4). A section of the top surface, clearly showing the indentation caused by the peening, is shown in Figure 8-5.

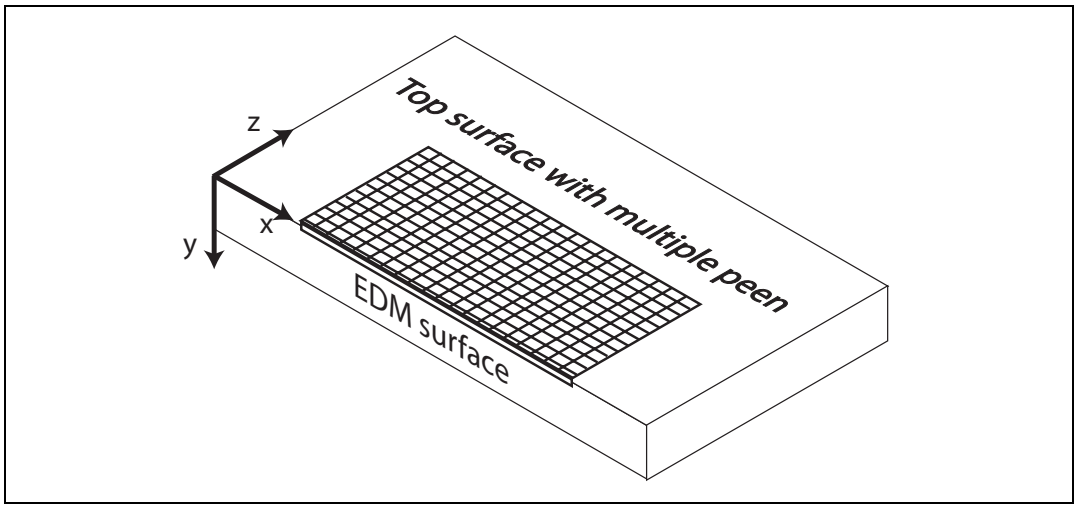

Figure 8-4. Sample B - multiple pattern peened over a large area, with overlapping laser shots. Figure shows view after EDM cutting in half at z=0.

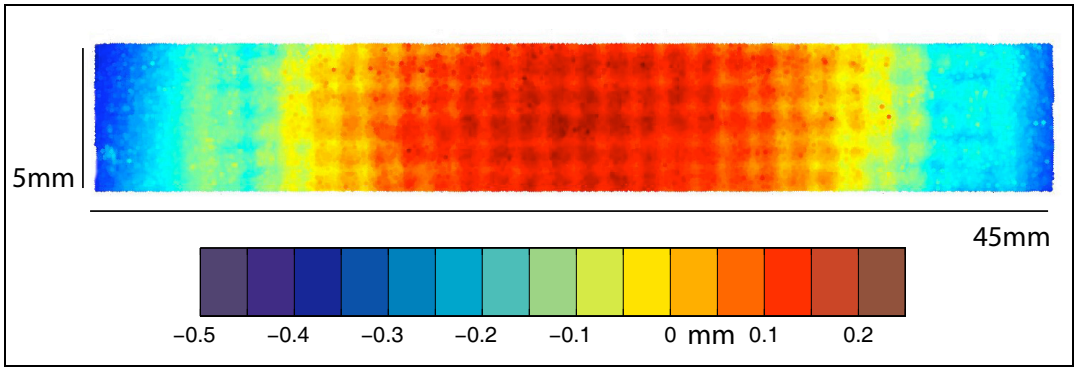

Figure 8-5. The surface profile of a portion of the multiple pattern peened sample - the indentations of the peening are clearly visible.

8.3 Cutting

Both samples were sent to be cut at Parkside Tool & Die[1]. Sample A was successfully cut there, as shown in Figure 8-6, but the spark was unsustainable with sample B, almost exactly at the entry point into the peened area (Figure 8-7). Sample B was then sent to another company (Rotadata[2]) where it was cut successfully. It is not clear why the spark could not be maintained on the mutiple pattern peened sample in the initial attempt - the alloy has no non-metallic component -

1. Parkside Tool & Die Ltd, Water Street, Stockport. 0161 480 7178. http://www.parksidetool.co.uk
2. Rotadata Ltd, Bateman Street, Derby. 01332 614 224. edm@rotadata.com

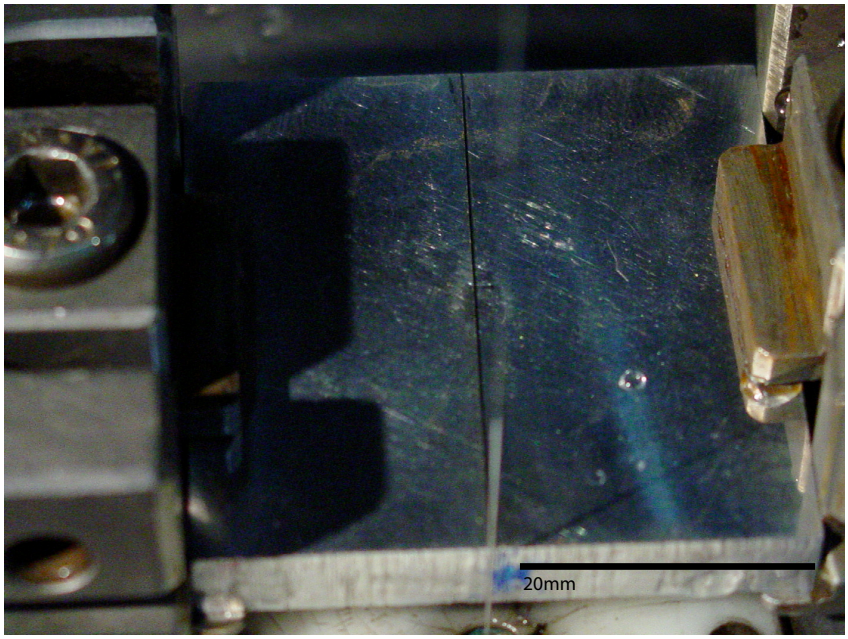

Figure 8-6. Sample A (doubly peened) after cutting. The peen is barely visible in the centre of the plate

but it was conjectured at this stage that a large tensile stress field might cause this. Section 8.6 discusses this further.

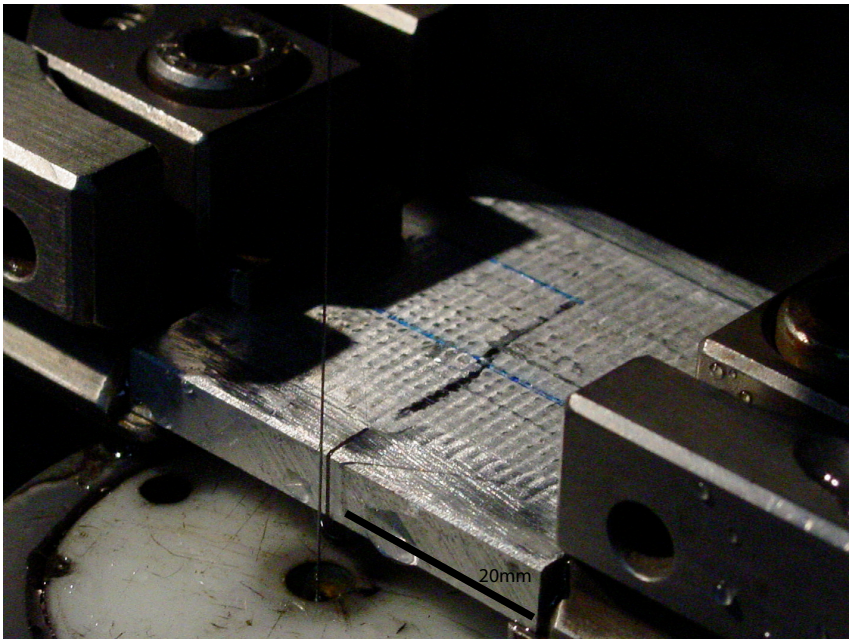

Figure 8-7. Sample B (multiple pattern peen) showing aborted cut due to loss of spark.

8.4 Measurements

With such small samples, (~45 x 6mm cut area), it was decided to use an optical probe to measure the very small surface contours that were expected. While Manchester did not have access to an optical scanner, Robert Sebring *et al.* has built an instrument at Los Alamos National Laboratories (LANL) which was used for precision metrology of components in a high power laser program (Sebring 2001). Using a confocal probe produced by Keyence (model LT-8105) and with air bearings for the lateral motion, it has been used for making a number of other contour method measurements by Prime (Prime 2004). The probe itself has a nominal accuracy of 0.2μm with a spot size of 7μm (Keyence 2005). Dr Prime graciously arranged for the singly peened sample to be measured at LANL for this project. The patterned sample was scanned courtesy of Adrian DeWald at UC Davis (also investigating the combination of the contour method and crack compliance for LSP assessment) using a commercial surface profiler (Taylor Hobson Talyscan 250). It has a quoted accuracy of 0.1μm with a 30μm spot size (Talyscan 2001).

8.4.1 Doubly peened sample

These data were acquired using the LANL instrument at a 30μm pitch. Unlike the measurements made in Manchester using the CMM, the pointcloud had no associated outline file, so this was created manually using the exterior points from the surface data. The density and size of the pointcloud made any appreciation of surface contours that might be present impossible in the raw data - each side contained over 300k points. In addition, the confocal scanner produces data with considerable noise - about ±9μm at 1σ. However, the measurement pitch is sufficiently high that although the raw data appears to lack any signal content, once the two sides are averaged and splined (which effectively acts as a filter of the high-frequency noise component) the contour is revealed.

Figure 8-8 shows the results of the 2mm spline fit to the displacement data (averaged top and bottom surfaces). The peen is clearly visible as the raised area in the centre of the surface. Apart from the peen, there is very little other structure visible.

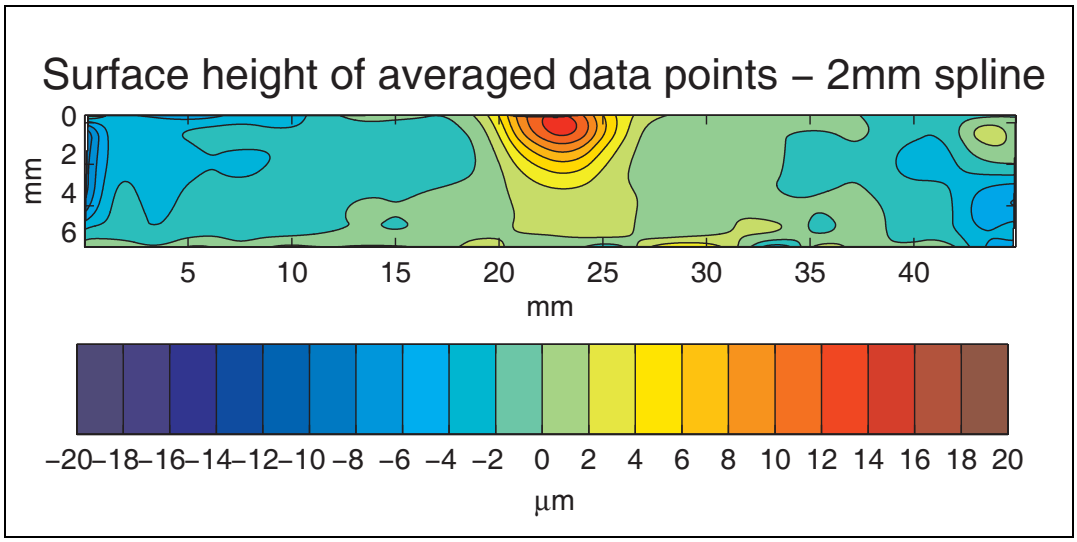

Figure 8-8. Sample A - Single LSP displacement map after averaging of both sides and fitting with a 2mm pitch spline.

8.4.2 Multiple pattern peened sample

The surface measurements of this sample were made by the UC Davis instrument.

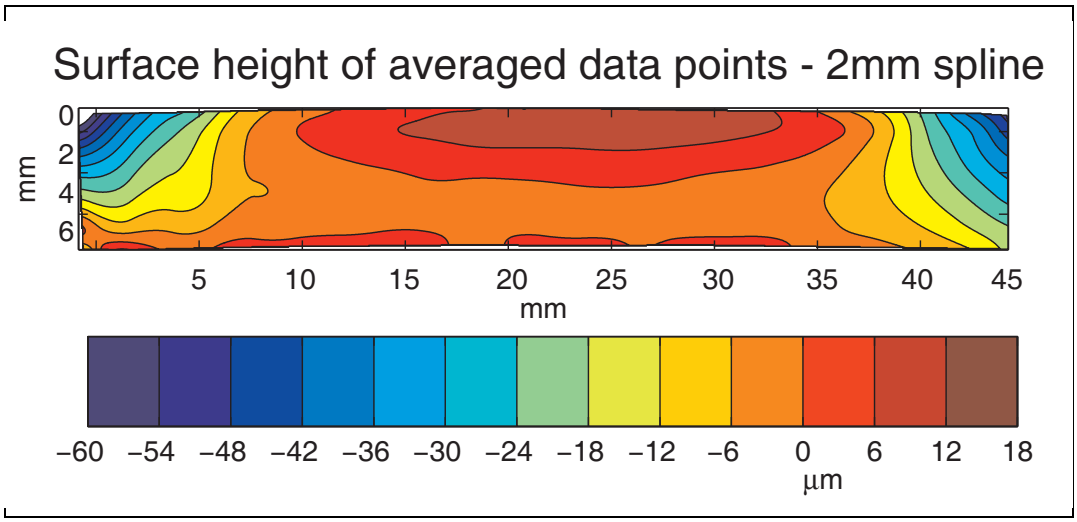

Figure 8-9. Sample B - Multiple pattern peened LSP displacement map after averaging of both sides and fitting with a 2mm pitch spline.

The pitch of the measurements was again 30µm, and Figure 8-9 shows the displacement map for both sides averaged together and fit with a 2mm spline. The zero-point for the displacement map is an arbitrary value, taken as the average of all points within the map. The very strongly depressed upper left and upper right

corners weight this value heavily. It is expected that these corner depressions will propagate through the FE model to become areas of high tension.

8.5 Finite element model

The model for both samples was made as described in Chapter 4, and the mesh is shown in Figure 8-10. The element sizes used were approximately 200 x 200μm in the central 15mm of the sample width and 1 x 1mm elsewhere.

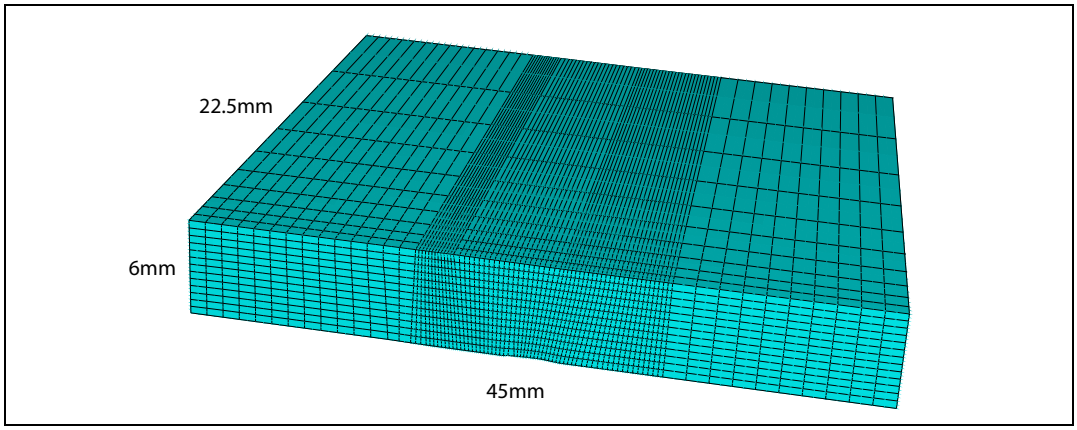

Figure 8-10. Finite element mesh used for the doubly peened sample (A). The mesh used for the multiple pattern peened sample was similar. A denser mesh (~200μm square) was used in the central 15mm of the sample - the rest of the sample used a coarser mesh (~1mm square).

8.6 Results

8.6.1 Sample A (doubly peened)

The first map, shown in Figure 8-11, is of the singly peened sample. It is clear that the peen is in the centre of the sample, with a peak compressive region (~-300MPa) extending down from the surface to a depth of about 3mm. The balancing low-level tension is spread throughout the rest of the sample, with no clear pattern for its distribution.

Figure 8-12 contains a line plot extracted from the centre of the contour map (shown by the blue line in Figure 8-11) overlaid with the synchrotron diffraction data measured at the same location. The diffraction measurements used a gauge volume of 1.4mm (depth) x 3mm (lateral), thus averaging over the area of a single peen. (The peen itself is a square spot, 3x3mm in size.) The agreement between

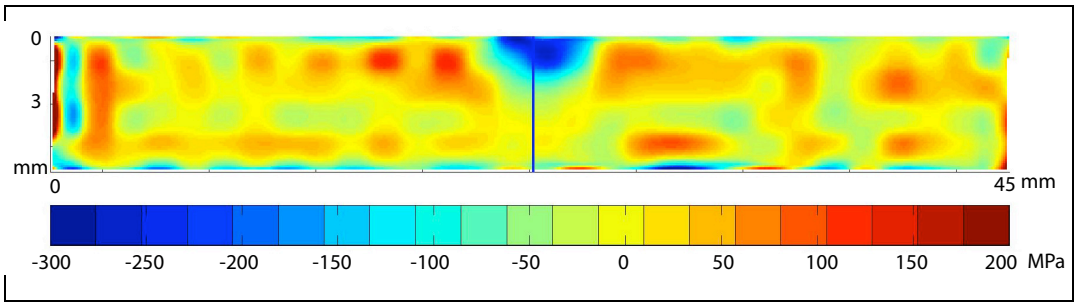

Figure 8-11. Contour method results for singly peened LSP (sample A). Blue line shows location of subsequent line plots

these two measurements is good in both form and magnitude, particularly close to the surface, and while the 0MPa crossing is at the same location, the compressive trough is larger according to the diffraction data.

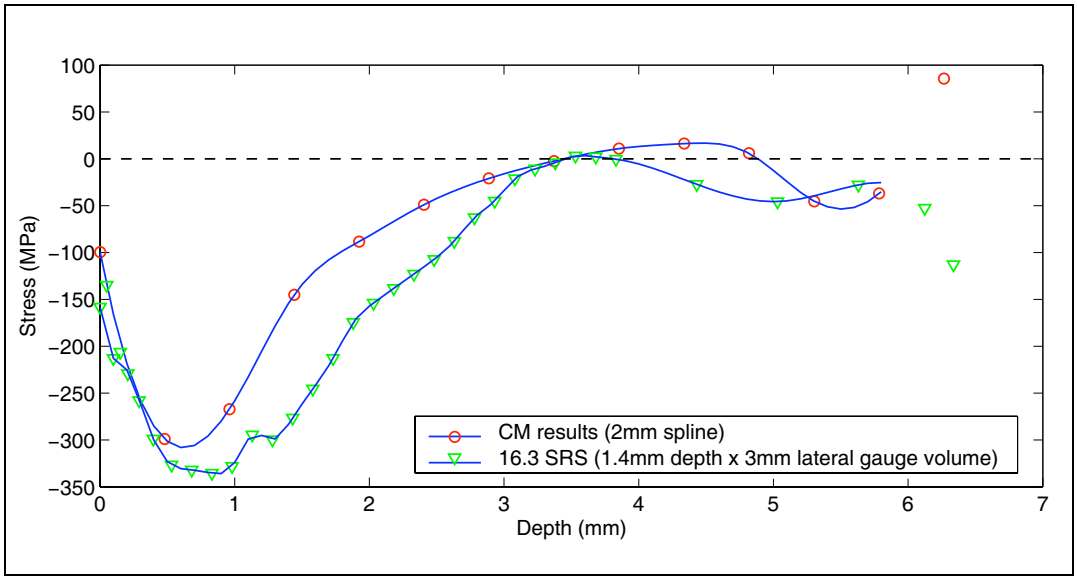

Figure 8-12. Line plots for the doubly peened sample (A) from both contour method results (taken at blue line in Figure 8-11) and synchrotron results, measured at the SRS on station 16.3

8.6.2 Sample B - multiple pattern peened

The second map (Figure 8-13) shows the results for the multiply peened sample. A number of features are immediately apparent:

- The compressive region at the surface of sample B is much larger (~35mm wide) than for the singly peened sample (A), corresponding to the large peened area of this sample.
- The compressive region is not uniform, with five or six local stress maxima distinguishable by eye.

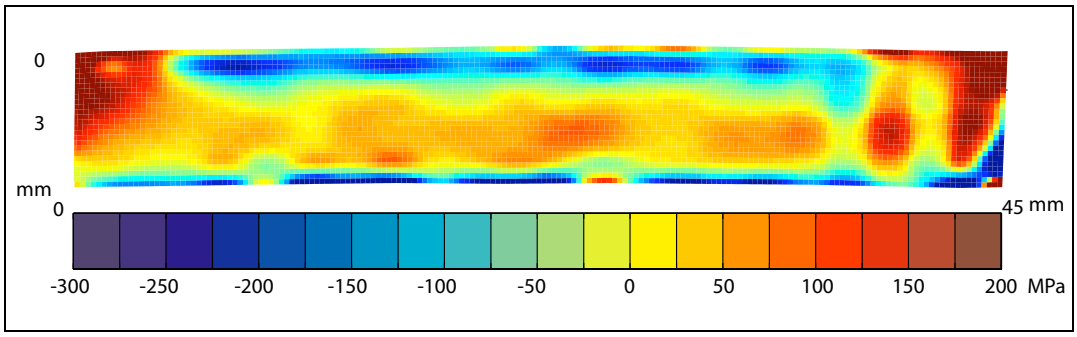

Figure 8-13. Contour method results for multiple pattern peened LSP (sample B). Large balancing tensile regions are apparent at the upper outside corners, while the compressive region is between. Some variation in the compression layer is visible, possibly due to problems that occurred during peening. The sample is curved away from the impact zone. A thin compressive layer is visible on the back surface.

- At the outer edges of the sample (left and right sides) in the border around the peening, there are substantial areas of high tension (~200MPa).
- At the lower edge (the back face) of the sample, there is a thin (~0.4mm) but substantial area of compression (~190MPa).
- The overall section of the sample is no longer rectangular (as it was prior to peening), but has been curved slightly, with the left and right edges lower than the centre.
- While there is a substantial compressive region at the upper surface, there also appears to be a decrease in that, or possibly a tensile region, in the very top nodes. This is difficult to ascertain from a 2D image but is shown in a cross-sectional plot in Figure 8-15.

The regions of higher compressive stress within the peened area do not correspond to the peens themselves. However, it was noted by Evans (Evans 2004) that there were difficulties with the process of peening. A black tape was used as the ablative area, and it apparently lifted from the surface a number of times during treatment. It may be that differing areas of stress correlate to occasions when the tape failed to adhere, but this cannot be verified since the positions were not recorded.

The border surrounding the peened area contains considerable tensile stress. It was shown in a thermal misfit finite element model (Evans 2005) that this was expected (see Figure 8-14), but it would be difficult to locate and quantify without the contour method data unless exhaustive studies had been made with other techniques. The difficulty with the initial cutting of the sample might be attributed to this tensile stress field - if the material pulled away from the cutting wire suffi-

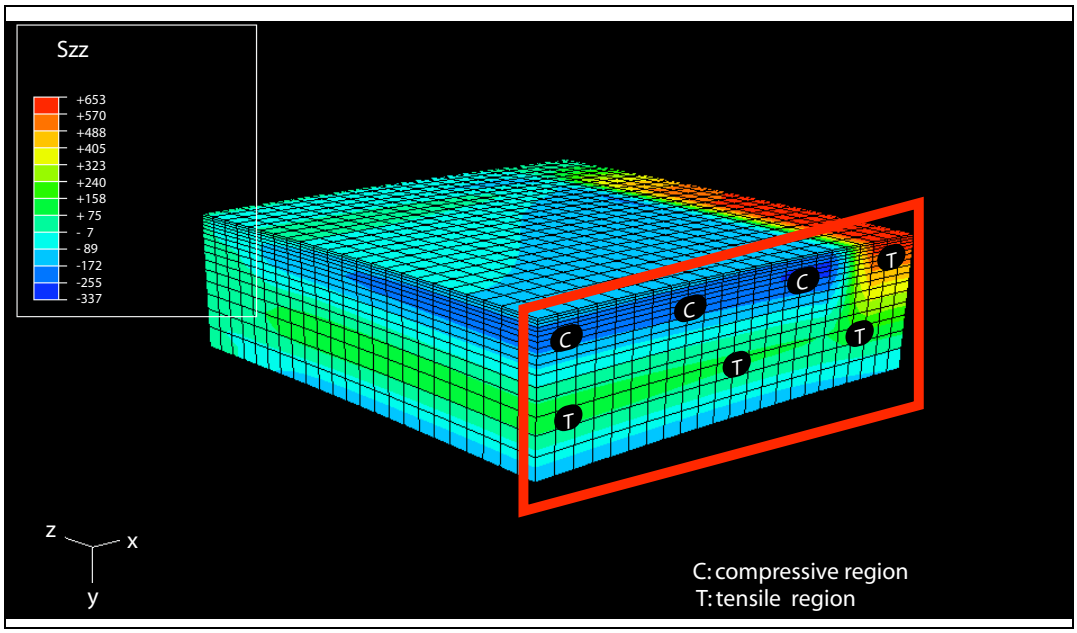

Figure 8-14. Finite element model of multiple pattern peen (thermal misfit model). Volume modeled is one quarter of entire sample. Area inside red rectangle corresponds to right hand side (due to symmetry) of plane on which contour method measurements were made. Area of compression (blue) in centre of sample is balanced by strong tensile area (red) in outside upper edges. (model courtesy Evans (Evans 2005))

ciently, the voltage between the workpiece and the wire might not be large enough to maintain an arc.

The thin area of compression found at the back face of the sample is a result of elastic bending that occurred during peening (Evans 2005). This is not usually a desired outcome of LSP but is a consequence of imparting deep compression on the top surface.

Some of these features may be examined in more detail in Figure 8-15 which overlays the synchrotron diffraction data taken from the centre of the plate with the data taken from a region 3mm wide in the centre of the contour method results. By showing all the nodes within an equivalent region to the gauge volume of the synchrotron diffraction data as individual points rather than a single averaged point, some appreciation is gained of the scatter of the contour method data over a wider area.

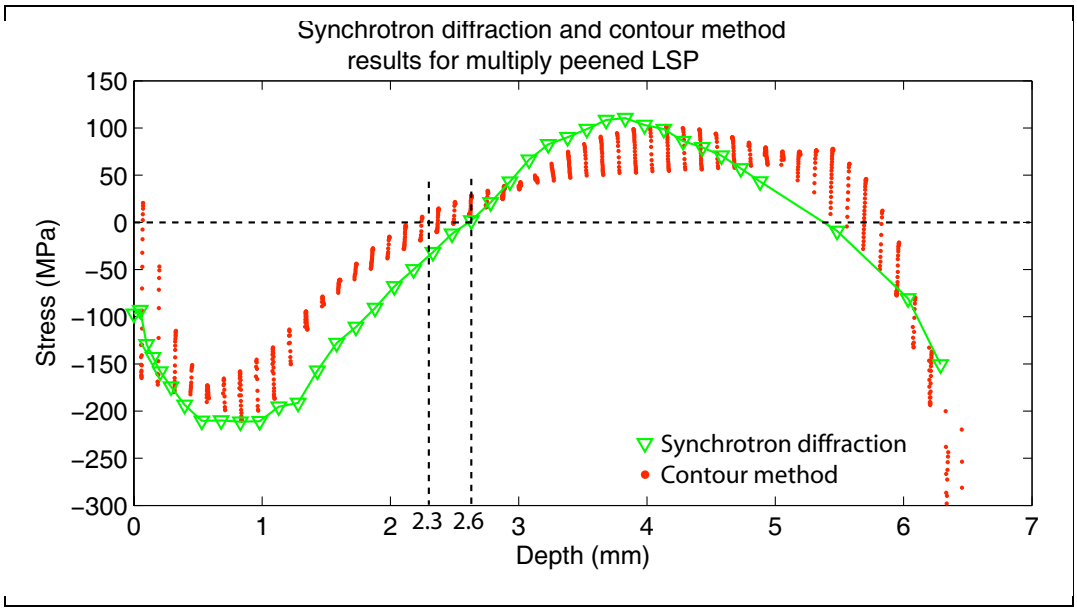

Figure 8-15. Comparison of contour method and synchrotron diffraction data for the multiple pattern peened sample. The gauge size of the synchrotron diffraction data (green triangles) is approximately 3mm wide (in 'x' direction), so the extracted data for the contour method points (red dots) is also from a region 3mm wide within the FE mesh, hence the scatter of points for each depth. The depth of the compression zone predicted by the contour method data is 2.3mm, while the synchrotron diffraction data crossing the axis into tension at 2.6mm.

Again, the agreement between synchrotron diffraction and contour method data is good in both form and magnitude. The compressive area at the bottom face of the sample is clearly visible in this plot.

8.7 Conclusions

The contour method is an excellent tool for these types of samples, where it would be common to make single line profiles with diffraction techniques and thus completely miss the critical areas of high tension that occur around the borders of peening. The agreement with the synchrotron measurements made by King and Evans (Evans 2004) is very good.

In contrast to synchrotron diffraction measurements, where each additional data point requires incremental amounts of time, it is essentially cost-free to make contour method measurements at higher resolutions, particularly when using fast optical scanners. The labour involved in the contour method is almost independent of sample size - measurements are automated, and the finite element models are

restricted only by computing resources. This also means the contour method can be used to make very dense maps of stresses without incurring great expense.

These results have also demonstrated the capability of the contour method to resolve stresses very close to the surface - within 100μm in this example, limited by FE mesh resolution - and still obtain reliable results. It is often noted anecdotally that cutting artefacts occur primarily at the entry and exit points of the cutting path (Prime 2005). To minimise the masking effects that this can have on sub-surface stresses, it is important to cut perpendicularly to the surfaces of interest, as done in this case (the surfaces of interest are at the extremes of the y-axis, so the cutting wire was used parallel to the x-axis). It would be interesting to perform a rigourous comparison of this assertion, and perhaps also explore (with the use of more sophisticated clamping techniques) cutting at an angle to both primary axes of a sample.

The final chapter summarises the work done in this dissertation and make some concluding remarks about both the current strengths and weaknesses of the contour method, and potential areas of interesting future work.

9 Conclusions

9.1 Summary

The contour method is a recent addition to the suite of tools available for residual stress measurement. In comparison to other destructive techniques, full two-dimensional maps of the stresses normal to the plane are produced in a single study. Measuring only type I stresses, it is insensitive to microstructural variation and grain size, unlike X-ray, synchrotron, and neutron diffraction. Not requiring specialised equipment or expensive facilities, it is in theory accessible to a wide range of practitioners.

However, the uptake of the contour method thus far has not been large. Whilst the theoretical framework for the method is simple, the practise of it requires a substantial investment of decision-making, effort, and computing power. The toolkit that has resulted from the work presented in this dissertation will, it is hoped, lower the barrier for subsequent researchers to utilise this useful tool.

The work comparing the four point bend CM results with an FE model showed very good agreement in stress gradient and peak magnitudes. The trivial stress profile brought to the fore an apparent phase-delay which may correspond to the so-called 'bulge effect' recently reported. The work required to correct this (an iterative loop around the modelling stage) might increase the complexity and time required for the CM - a current strength.

The arbitrary choice of knot placement in 2-D uniformly spaced splines has been examined by the use of the cross-validation technique, borrowed from neural network theory. In the case of the aluminium plate with quenching stresses, this showed a broad region with low sensitivity of the CM to knot spacing. However, it is clearly appropriate in many situations to use variably-spaced knot locations. This is a challenging task, particulary concerning bivariate variation, but 1-D

method has been presented here in the case of the linear friction welds, where the dataset contains high stress gradients around around the weld line and lower gradients in the remainder of the material. Whilst synchrotron diffraction had difficulties measuring strains over the weld line due to the lack of a stress-free reference, the CM produced results through the sample, and, where possible, the agreement was very good with the diffraction measurements - both demonstrated the positive effects of the post-weld heat treatments in reducing the tensile stress field due to welding.

When applied to very large engineering parts, such as those commonly joined using inertia friction welding, even typically non-destructive measurement techniques such as neutron diffraction require extensive destructive machining of the samples. After validating the results of the CM against measured neutron results for a wall-thinned weld, the CM has been able to provide stress maps for an unthinned weld, raising questions about the heretofore presumed non-modification of the stress field by the machining process. However, cutting such large samples still remains an error-prone and time-consuming action, to the detriment of the CM.

The final experimental work in this thesis looked at low-magnitude displacement measurements with the contour method, examining thin aluminium plates that had undergone laser shock peening. Through the use of an optical scanner, shallow sub-surface stresses were measured, and indications of peening faults had occurred were observed. Comparisons with synchrotron data indicated good agreement throughout, including only 100μm from the surface.

9.2 Further work

There are a number of avenues of investigation which would lead to interesting further work.

1. The aspect of the contour method not evaluated in this dissertation: cutting effects. With economical access to an EDM machine, considerable observations could be made about the effect of using a non-standard cutting protocol (bulk cutting with ‘skim’ cutting parameters) and artefacts introduced.

2. Further investigations of near-surface measurements. The work on the LSP samples shows that there is no reason in principle why representative values may not be obtained for near-surface stresses. It would be useful to quantify the conditions under which such results may be obtained. It may be interesting to consider oblique cutting paths: sample clamping would be more difficult, but entry and exit artefacts may be reduced, giving better quality results on all sides of the sample.
3. Improvements in surface fitting and error estimations. Variable pitch splining, has been demonstrated here, but the use of radial distance functions for the splines would remove the need for regular grids which currently preclude full 2D variability.
4. Work on estimating the accuracy on a given contour method measurement would be very valuable. Estimates of displacement measurement error do not lead immediately to error estimates in the resultant stresses as it is not clear how these propagate through the intervening steps, but study of this process would be useful.

A Surface metrology

The aim of this chapter is to introduce the principle of the contour method as a technique for measuring residual stresses in engineering parts and components. This will include explanations of the method itself, how it is applied in practise, and elements that need to be taken into consideration when employing the method experimentally. A review of previous work carried out using the technique will then be given.

1.1 Coordinate measurement machines - tactile measurements

1.1.0.1 Mechanical structures

The coordinate measurement machine (CMM) is a mechanical instrument that moves a probe to measure the location of points on the surface of a sample. They have been used in various designs for several decades, and have progressed from manual to semi-automatic to full computer control. The four components of a modern CMM are: the movement system, the probing device, the hardware controller, and the application software.

There are a number of common mechanical structures which suit different purposes (sample sizes, accuracy requirements, flexibility). The bridge machine, an example of which is shown in Figure 1-1, is the most common, with two legs and a cross member which travel over the workspace. The probe system is attached to a vertical quill which is itself mounted on the cross member. The gantry system is similar, only usually on a much larger scale so that the workspace can accept large parts without lifting them on to a specialised table.

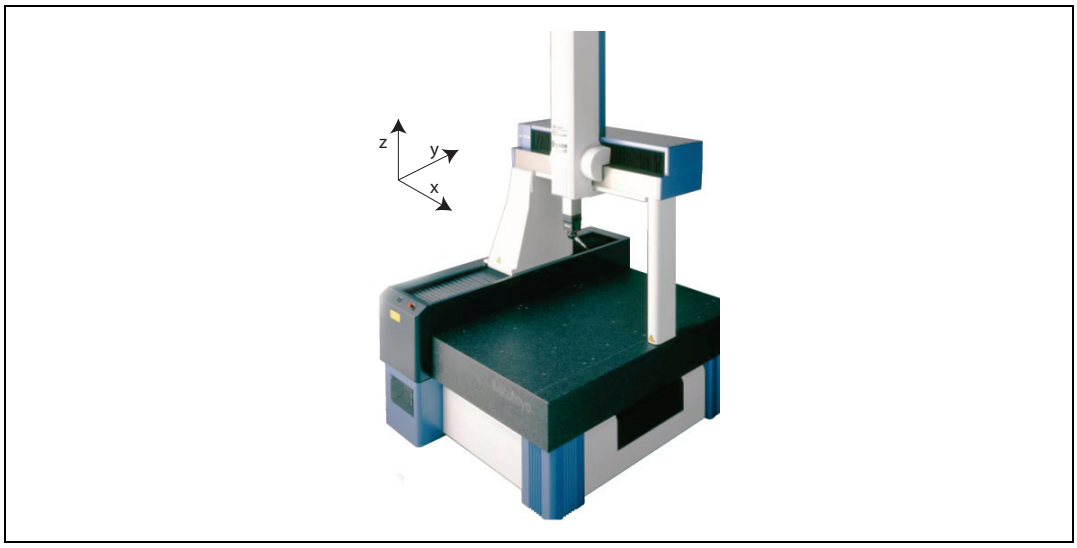

Figure 1-1. The Mitutoyo Crysta CMM, a typical bridge machine

A horizontal arm machine (Figure 1-2) has the probe cantilevered from the side of the workspace on a horizontal quill. This can be very useful in situations where the

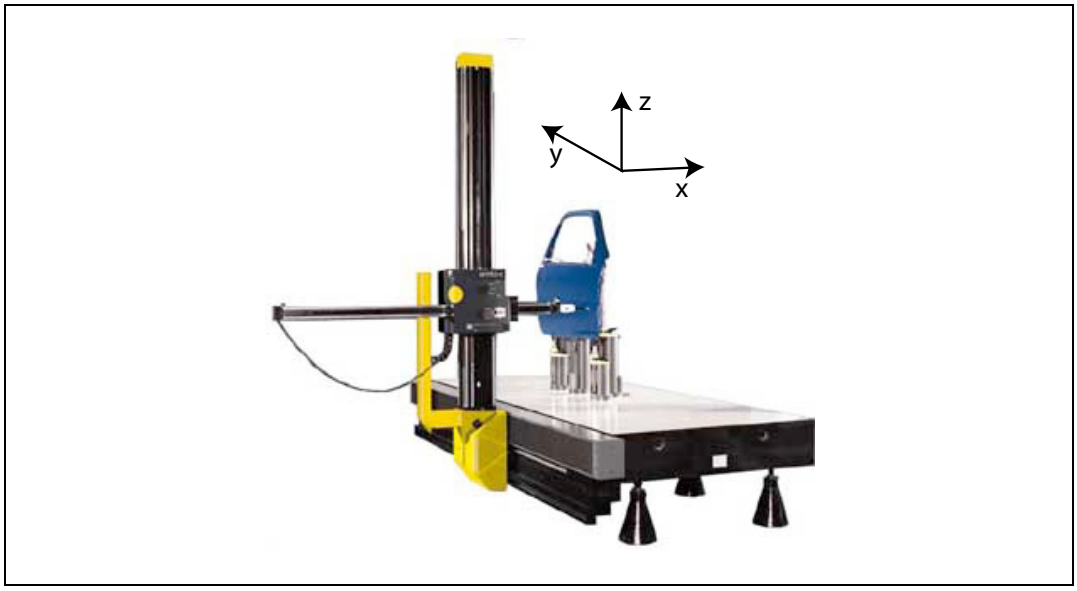

Figure 1-2. The Brown & Sharpe Legos CMM, a typical horizontal arm machine

workpiece is considerably larger than the space available, as it can be brought in from the open side of the machine without constraining it. There have also been a number of articulated arm CMMs, where the probe is mounted on the end of a jointed robot. These are very flexible in terms of probe positioning, but because of

the many joints between the mounting point and the probe the inherent accuracy of the system is not as good as more rigid structures[1].

1.1.0.2 Probing devices

The probe system includes the probe tip (the element that contacts the workpiece), the stylus (a long member which includes the tip and connects it to the probe body, and the body (which houses the electromechanical components that measure the displacement of the probe tip).

The most common probe tip is a ruby sphere. Ruby is an excellent material for this purpose because it is hard, with a Vickers number of 2500-3000, (any deformation of the tip during contact with the sample surface would lessen the accuracy of the measurement) and the balls are easily manufactured to a very high degree of sphericity. The measurement of the probe location is always done to the centre of the tip, and the tip radius added afterwards as a correction. Any non-uniformity in the sphere will cause inaccuracy. Styli, usually ceramic (for high stiffness, low mass, and low coefficient of thermal expansion) are available with probe tips ranging from 200μm to 8mm or greater. Figure 1-3 shows a 8 mm ruby mounted on a 50mm stylus. Further information on other varieties of probe tips is contained below in the paragraphs pertaining to scanning probes.

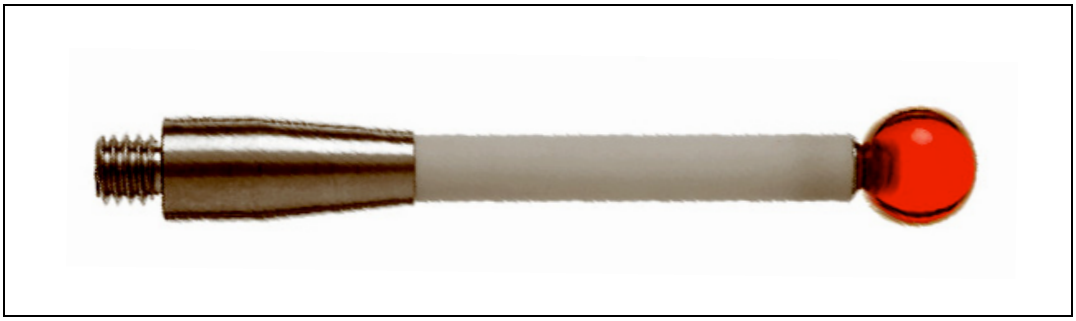

Figure 1-3. A 50mm stylus with 8mm ruby tip. Much longer styli are available, either as extensions or single parts, but accuracy is highest in shorter sizes. (Ceramic in white, ruby in red).

1. For instance, a standard bridge machine (Brown & Sharpe GLOBAL) can obtain an accuracy of ~5μm over 50cm while a 6-axis robot arm with a reach of 60cm (Beckman Coulter ORCA) has an accuracy of only 250μm.

Probe systems are also available in a number of varieties to suit different purposes. Traditionally, CMMs used a simple switched probe, where the displacement of the probe tip as it came into contact with the workpiece would interrupt an electrical circuit in the probe head, causing the sampling of the encoders that indicate the position of the machine to be affected. Indeed, this is still the most common tactile probing type, though the design has become considerably more sophisticated.

Touch-trigger probes are now based on one of three measurement technologies: resistive, strain gauge, and piezo. In all variations, the probe stylus is mounted within the probe head in the same fashion, as seen in Figure 1-4. Typically, three rods support the stylus, each resting in the cradle of two balls. The stylus is held in place by a spring that pushes downwards.

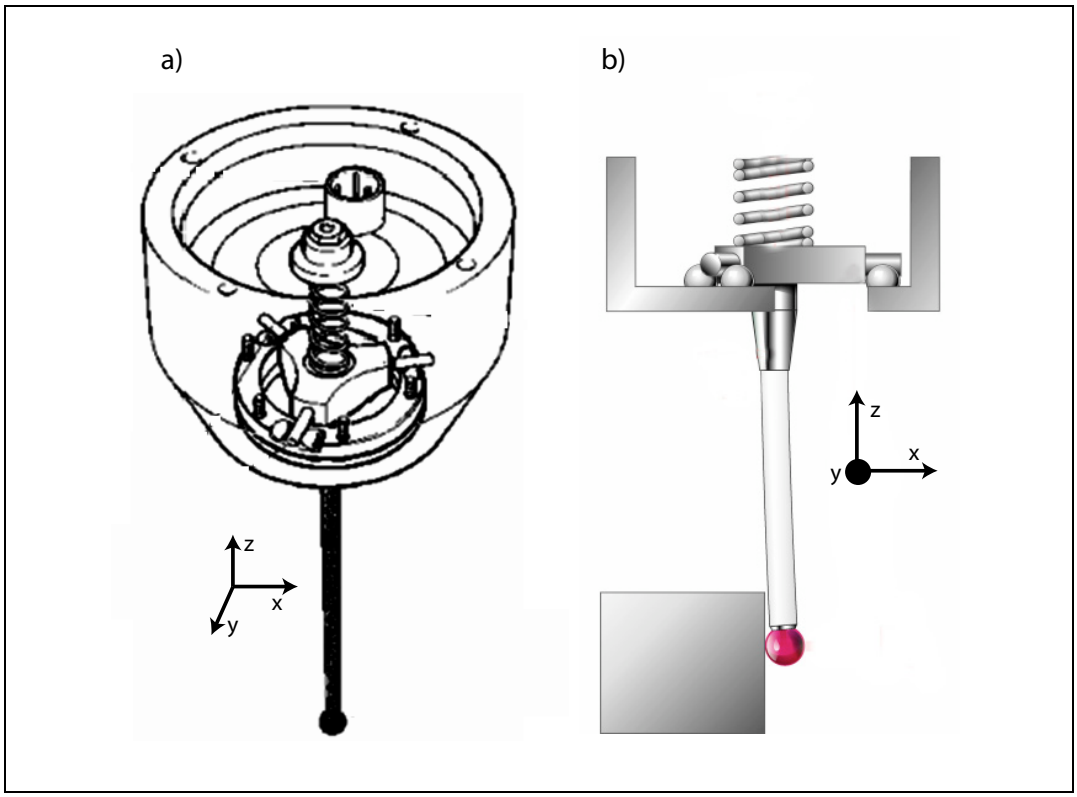

Figure 1-4. a) Isometric and b) cross-sectional views of stylus mounted on kinematics (courtesy Renishaw plc.)

When lateral (X-Y plane) contact is made, the stylus assembly pivots about the kinematic mounts. After contact is released, the spring causes the return of the

stylus to the original position, usually to better than 1μm resolution (Renishaw 2004).

In the resistive touch-trigger probe, (an example of which, the Renishaw TP200, is shown in Figure 1-5), each kinematic mount is an electrical circuit, with a small current passing from one ball, through the stylus rod, and returning through the second ball. The elastic deformation of the materials mean that the contact point between the balls and rod is finite, and reduces as the pressure is reduced. The resistance of the contact is inversely proportional to the contact area, and so increases as the stylus makes contact. This changing resistance triggers the probe, before the contact is actually broken. Because of the inductive load of the probe, the breaking of the contact would lead to arcing, and eventual degradation of the contact surfaces.

Figure 1-5. The TP200, a Renishaw touch-trigger strain gauge probe, fitted with a 40mm ϕ6mm ruby stylus. (courtesy Renishaw plc.)

Ideally, the displacement of the stylus before the probe triggers is constant in all directions. However, this pre-travel varies because of the location of the kinematics. The pre-travel variation (PTV) is an important characteristic of a probe. Figure 1-6 shows the PTV for the TP6, a Renishaw touch-trigger probe[1]. The effect

of the three kinematic mounts is clear, and this pattern is commonly known as 'lobing'.

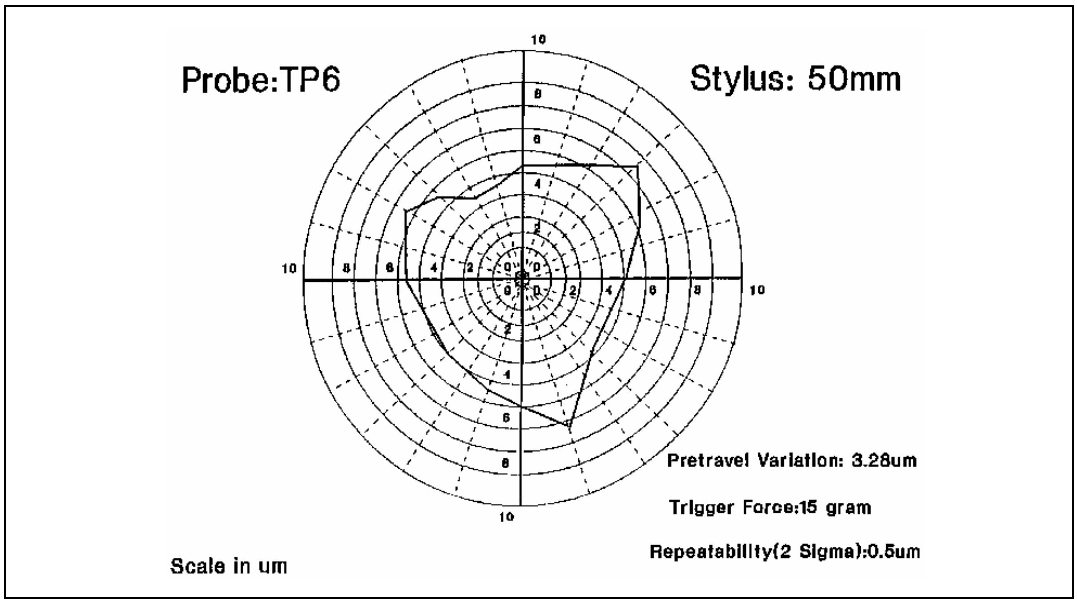

Figure 1-6. Pre-travel variation plot for Renishaw TP6 touch-trigger probe. Three-cornered shape is due to increased force required to pivot stylus at location of kinematics. (courtesy Renishaw plc.)

The PTV in Figure 1-6 shows only the variation in the lateral direction, but there is also a variation in the vertical direction. For small PTV values, the probe may be calibrated in a straightforward fashion, but for probes with large PTV, the probe must be brought into contact with a known feature from all (or at least a representative proportion thereof) directions. This test is standardised as ISO 10360-2 (ISO 2002).

Building on the principles of the kinematic resistive probe, but reducing the problem of PTV, is the strain gauge touch-trigger probe. The stylus is mounted in the same kinematics, but they are no longer used to trigger the probe. Instead, strain gauges are mounted on webs inside the probe body. For very small displacements of the stylus, the forces are transmitted through the kinematic mounts to the probe body and the resulting deformation measured by the gauges. The probe can be triggered before the kinematics are unseated. The advantage of this system is that the

1. Renishaw plc: www.renishaw.com

contact force is now equal in all directions, and the PTV values are much reduced. As an example, the Renishaw TP6 *kinematic resistive* probe has a maximum PTV of 3.28μm, while the TP7M *strain gauge* probe has a maximum PTV of 0.34μm (Renishaw2004).

Finally, the resistive and strain gauge techniques can be complemented by a piezo electric sensor, which detects the high frequencies transmitted through the stylus as the probe tip hits the sample. As these high frequency sound waves travel at 800m/s (Renishaw2004), and the path length is constant regardless of contact direction, the probe can trigger with very small displacements and PTV of the order of the sphericity of the probe tip. However, this technique is affected by surface contaminants (which dampen the contact) and approach speed variations, and so is usually used in conjunction with the kinematic and strain gauge techniques inside a single probe head.

The other variety of tactile measurement is continuous probing, or scanning. Rather than momentary contact of the probe tip with the stylus to make a measurement, scanning probes are dragged across the surface of the sample, and the machine records the path of the probe tip as a series of closely spaced discrete points. An example of this design is shown in Figure 1-7.

The mechanism of the scanning probe is considerably more complex than a touch-trigger probe, and is shown schematically in Figure 1-8. The probing force is controlled by a triple box spring in the probe head, and damped by a ferrofluid chamber (a colloid of magnetite particles in mineral oil) (Raj 1997).

Optical pickups are used to measure the displacement of the upper part of the stylus body, either through triangulation or with position sensitive diodes (PSDs). The probe body movement is controlled in a dynamic fashion as the stylus traverses the surface of the sample by monitoring the change in displacement of the stylus relative to the probe head, and the ability of the controller to track the sur-

Figure 1-7. One of Renishaw's scanning probes, the SP600, with a ϕ4mm ruby tip (courtesy Renishaw plc.)

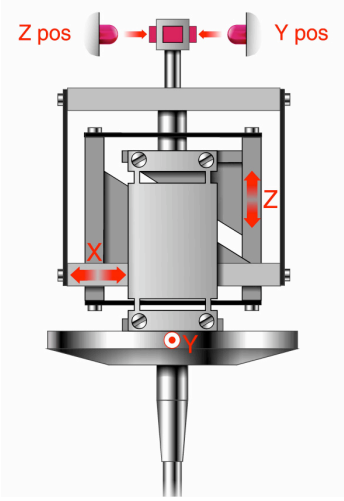

Figure 1-8. Schematic view of the internal structure of a scanning probe. Each axis is a box spring, contained in a parallelogram-shaped structure. Optical readout of position is done at the upper part of the stylus. (courtesy Renishaw plc.)

face determines the performance and usability of the probe. With smooth surfaces, this is a straightforward process, but with larger surface variation, the tracking controller must reduce the speed of the machine to maintain contact with the sur-

face without the stylus exceeding the range of motion available within the probe head (usually ~1mm in each axis).

The surface-probe interaction when using the scanning probe is considerably harder on the probe tip than when using a touch-trigger probe. Probe tips suffer from three problems when scanning. Firstly, debris pickup occurs. Any material that is present on the workpiece may cause small perturbations to the scanning path. Figure 1-9 shows an example of this occurrence.

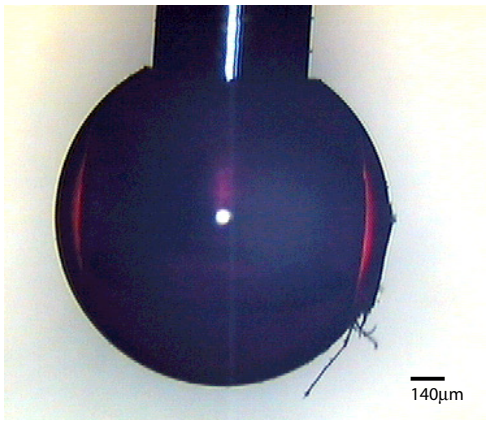

Figure 1-9. Debris buildup is independent of probe or workpiece material, and can be cleaned periodically with a lint-free cloth. (courtesy Renishaw PLC)

The second problem occurs when scanning aluminium surfaces. Ruby, Al_3O_2, binds to the aluminium workpieces, and adhesive wear takes place. Figure 1-10 shows an extreme example of this, where after 350m of scanning with 15g contact force a sizeable amount of aluminium has been picked up and causes a 2µm distortion to the ruby.

Thirdly, the opposite condition occurs when using a ruby probe on steel; Figure 1-11 reveals the extent of the abrasive wear.

The problem with scanning aluminium can be resolved by using silicon nitride balls, but the level of the problem is minimal enough (note the distance travelled to incur a 1µm loss of sphericity) for steel that ruby is still recommended as the best option.

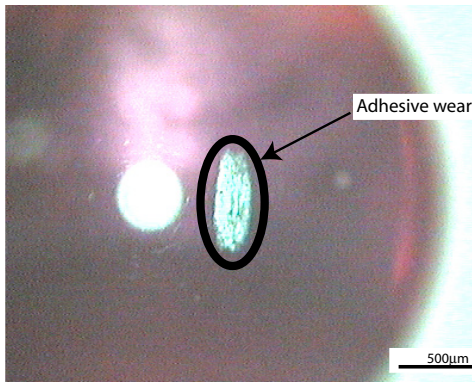

Figure 1-10. After 350m of repeated scanning with a ruby stylus on aluminium, using 15g contact force. The adhesive patch is 200µm x 500µm across and has a 2µm impact on the ball form. (courtesy Renishaw plc)

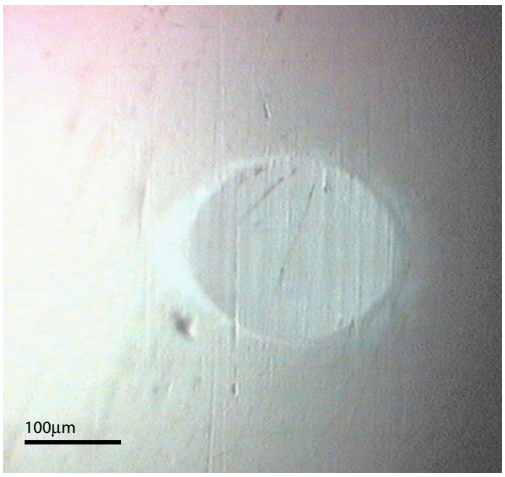

Figure 1-11. After 5600m of scanning with a ruby probe (15g contact force) a flat region on the ball approximately 150 µm in diameter has been formed. 1.5µm of ruby has been removed. (courtesy Renishaw plc)

1.2 Triangulating optical probes

Optical probes are also available for many CMM systems, working on a number of different principles. The most common is that of triangulation, where a light source illuminates the surface of the sample. The diffuse scattering light is imaged and processed to detect the scattering location. Using simple geometry, the distance of the sample from the probe is calculated and recorded. This is shown schematically for a point source in Figure 1-12.

The methodology for optical scanning is quite different from tactile probing. The

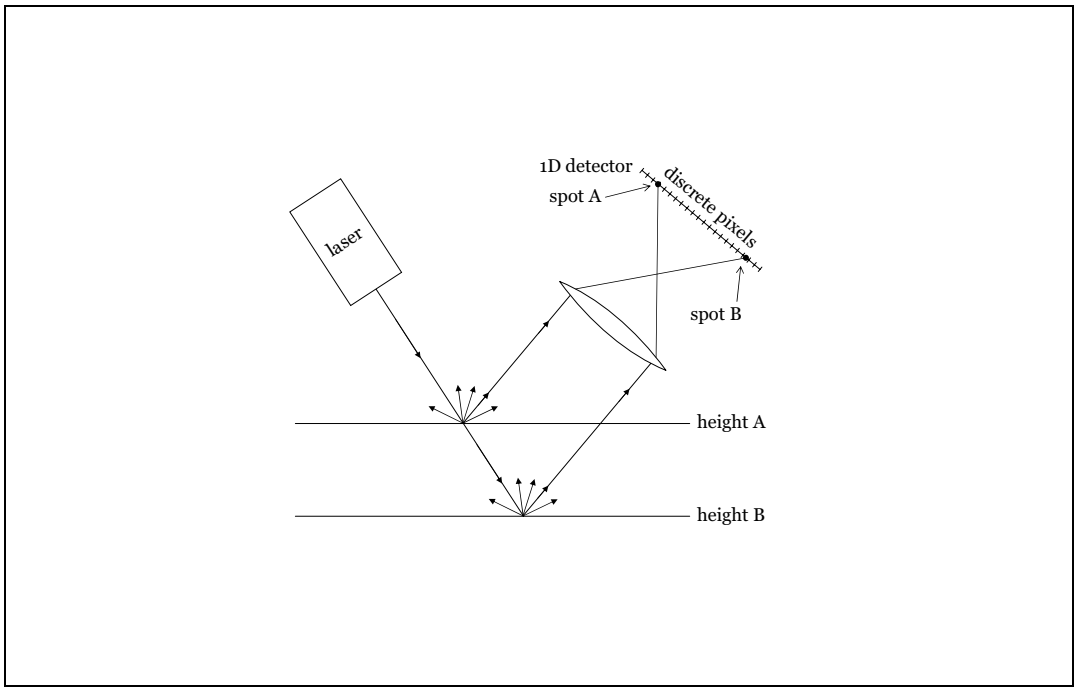

Figure 1-12. The triangulating optical probe is based on straightforward geometry. The distance of the sample from the probe head displaces the location of the image of the spot on the probe detector. Knowing the geometry of the light source and detector, the location of the sample can be calculated. (courtesy Andrew King)

nature of light is such that measurements may only be made where there is a clear line of sight (Figure 1-13). This means that any overhangs, slots, or crevices are usually only partially visible.

To get around this, multiple passes with different viewing angles are usually taken. This fills in the previously obscured area.

The light source usually used is a solid state laser (as on the Metris LC15 probe, for instance, shown in Figure 1-15), which is both small and efficient, with little heat generation - maintaining a constant temperature in the probe reduces sources of error. Focussing optics are used to create a small spot, but as the focussing plane is a fixed distance from the probe, the spot size on the sample will be larger on either side of the focal distance, which will lower the precision of the measurement. The light must scatter diffusely from the sample, so that a sufficient quantity of light returns to the probe. This precludes the use of both mirror or very dark finishes.

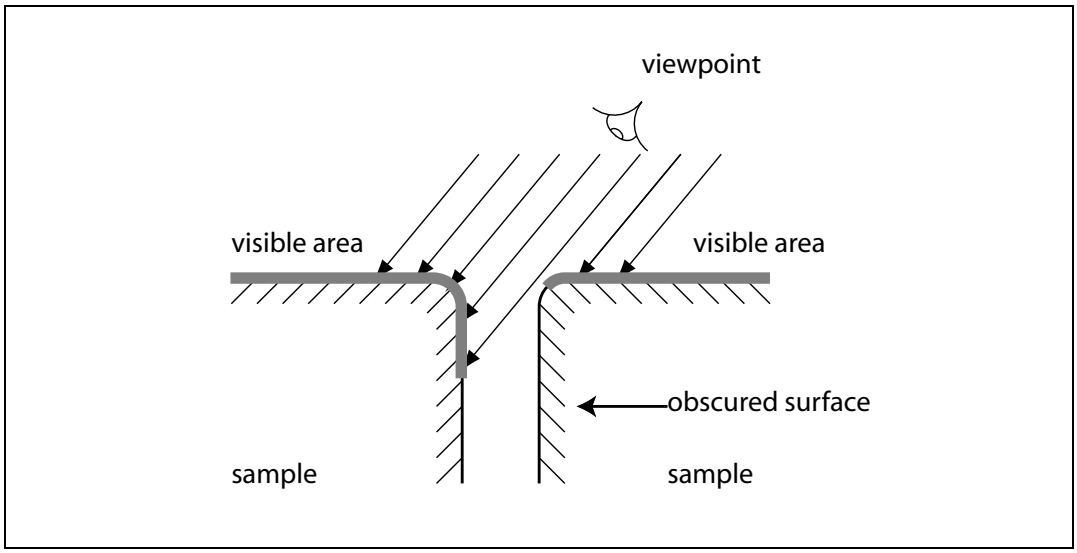

Figure 1-13. Complete measurements of slots and overhangs with optical probes must be done from multiple view points.

The spot is usually imaged onto a one-dimensional detector. The position of the spot may be determined, in the first instance, by looking for the brightest part of the image. Optical filters, tuned to the wavelength of the source, are used to reduce background illumination and increase the contrast in the image. A more precise determination of the spot location is done by fitting a curve to the data. This permits the spot centre to be found at a sub-pixel level, as illustrated in Figure 1-14.

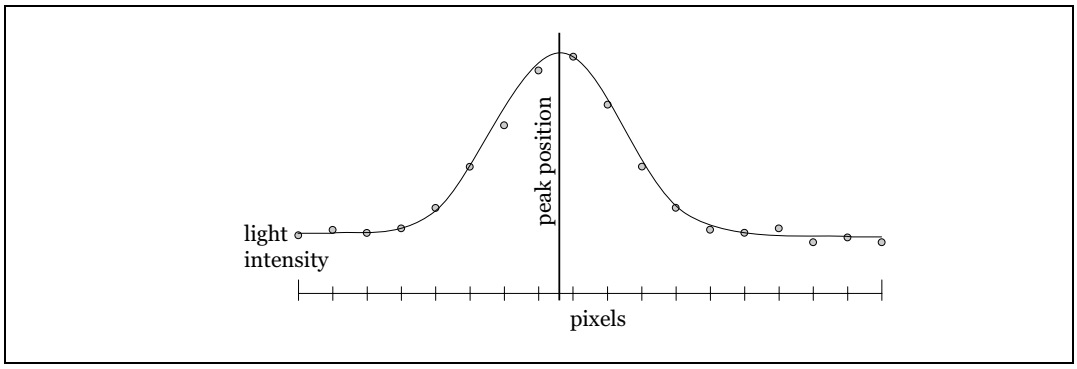

Figure 1-14. The finite size of the spot causes varying intensities of light to fall on the discrete pixels of the detector. The centre of the spot may be accurately determined by fitting a suitable curve to the pixel values, obtaining a sub-pixel location for the peak centre. (courtesy Andrew King)

From Figure 1-12 it is seen that there is a unique relationship between the spot position on the detector to sample distance from the probe and thus the probe is able to record the position of the workpiece.

This can either be repeated in a stepwise fashion, akin to touch-trigger probing (Section 1.1), or scanned along the surface. Probes which work in this manner, such as the Nextec Wizprobe, can sample at about 50Hz, with a precision of 6μm (at 1σ) (Nextec 2005). However, far higher measuring speeds may be obtained by scanning the laser spot perpendicular to the motion of the probe head ('rasterising') and measuring the line that is projected onto the sample with a two-dimensional detector. The image processing is extended to handle two dimensions, and with sufficient computing power (most modern PCs) many more points can be measured per unit time. The Metris probes, such as the LC15 (Figure 1-15), work on this basis, and collect just under twenty thousand points per second across a swath that is 15mm wide. The accuracy for the Metris probe is about 8μm at 1σ (Metris 2005).

Figure 1-15. Metris LC15 laser line scanner

1.3 Confocal sensors

Tactile and optical probes mounted on CMMs are useful tools for samples which are tens to hundreds of millimetres in size. However, with small distortions in the

surface to be measured (±2μm peak to peak), not even the best tactile probes can make sufficiently accurate measurements. In these cases, more specialised systems are required. The first of these that has been used successfully for the contour method (designed by Sebring and others at Los Alamos (Sebring 2001)) is based around the confocal laser probe.

The operating principle for the confocal probe is similar to that of the confocal microscope, both involving a pinhole in the final stage of optics. As seen in Figure 1-16, a coherent monochromatic light source illuminates the sample. The objective lens, through which both light from the source and the subsequent reflections from the passing sample, is coupled to a tuning fork. The rays of light pass through a pinhole before falling on a light sensitive element. The motion of the objective lens causes the quantity of light passing through the pinhole to vary as the sample passes in and out of focus. By correlating the point of highest intensity with the motion of the lens, the location of the focal plane, and thus the sample, can be determined.

Confocal systems, such as those produced by Keyence, have a range of about 0.6mm with a resolution of 10nm (Keyence2005). The shallow range of operation means that samples need to be aligned very precisely before measurements can be taken, and the movement of the camera head needs to be done on well-characterised guides, usually with high precision air bearings.

Los Alamos National Laboratory have used their confocal system for a number of contour method measurements (Prime 2003, Prime 2004a, Prime 2004b). The sample treated with a single laser shock peened spot examined in (Chapter 8) was measured at Los Alamos using their system.

1.4 Atomic force microscopes

One common tool that has not yet been used for the contour method is the atomic force microscope. While all contour method work to date has been on large metallic items, small ceramic samples and MEMS (micro electro-mechanical systems), if a suitable cutting technique were used, might be suitable for measurement with an

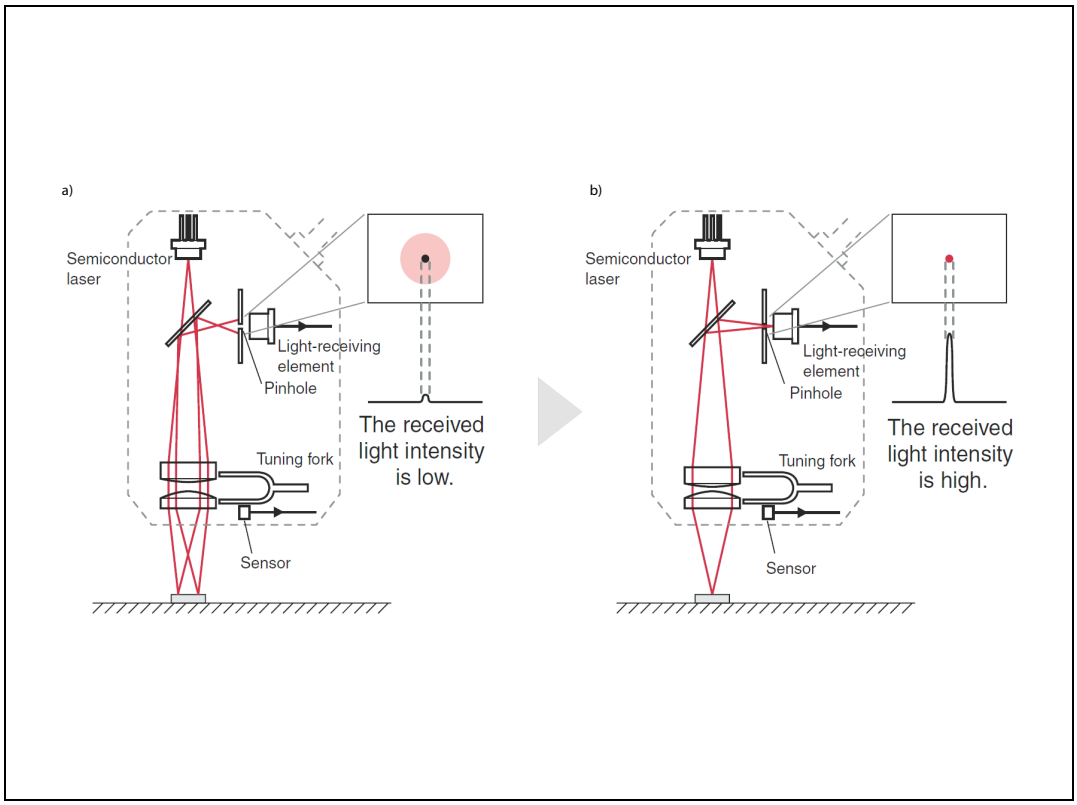

Figure 1-16. The principle of the confocal probe, showing the tuning fork mechanism which moves the objective lens, the pinhole through which the reflected light is received, and the effect of sample distance on detector image. (courtesy Keyence Inc.)

AFM. The principal mode of operation of an AFM is this: a stylus (akin to the stylus of a record player) is lightly placed in contact with the sample surface, and dragged across it. The position of the probe is recorded, either with an interferometer, or more commonly with an optical lever, where light is reflected off the top surface of the stylus and received by a detector situated some distance away (Putman 1992). This geometric magnification permits very precise measurements without the need for expensive instrumentation.

The working volumes are very small (sub-millimetre laterally, 10μm vertically) but for suitably sized samples this avenue would merit investigation.

B FE modelling of bent bar

2.1 Modelling

2.1.1 FEM Geometry

To produce a more complete estimation of the stresses expected on the cut plane of the bent bar, a full three-dimensional finite element model was made. The four point bend procedure was simulated, in conjunction with an elastic-plastic model of the material behaviour, which produced a residual stress state after unloading. The model was built using ABAQUS 6.4 [Abaqus2004].

The four point bend mechanism, as shown previously in Figure 4-9, was modelled as four analytical rigid revolved shells in ABAQUS, each of 20mm diameter.

The steel bar, 300mm in length and 20mm x 20mm in cross section was generated from solid continuum elements. Considerations of symmetry mean that the same results could be obtained with a quarter-model that had appropriate boundary conditions at the axes of reflection, but would only require a quarter of the computational effort to solve. Difficulties in implementing the contact of the rollers with the bar resulted in a compromise of a half-model being executed.

The complete half-model in Figure 2-1 shows the bar and the upper and lower rollers from the right hand side of the model at the end of the loading step, with the ensuing (exaggerated) deformation of the bar.

2.1.2 Boundary conditions

It is very important to ensure that the boundary conditions used in this model are correct (that is to say, they are sufficient to prevent rigid body motion at all steps of the run). Without this, the stiffness matrix that ABAQUS calculates for each iteration in the run is singular, which means that the model moves without restraint. In this specific case, the bottom roller is completely locked ("*encastre*") at all times in

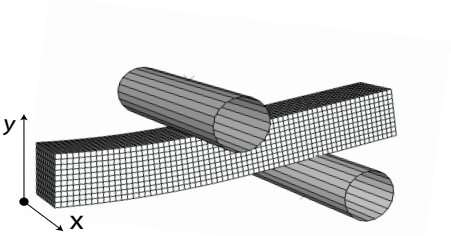

Figure 2-1. The finite element half-model used to simulate the four point bending process. Shown in the fully loaded condition, the left hand side (the cutting plane) is constrained to remain on the centre line, equivalent to the elements at that location in the complete bar. The x- and y-axes are shown. (Exaggerated 3x for clarity)

all degrees of freedom. The upper roller is initially *encastre* but is released to move vertically during loading. In the unloading stage, it is moved back to its original position. The bar is also initially *encastre* but is released after the initial stage (once contact has been established). It is restrained laterally at the end of the bar (right hand side in the figure). The symmetry conditions are set at the middle of the bar (left hand side in the figure).

2.1.3 Contact behaviour

Contact is modelled in ABAQUS as a master-slave relationship between two defined surfaces. These surfaces can either be specified as a grouping of element faces, or from analytically rigid parts. In the bent bar case, the roller cylinder is defined as the master surface (normal pointing outwards) and the matching face on the bar as the slave surface. Although there is nothing to prevent the reverse definition of master and slave, a solution will only be reached when the analytical part is the master. During the iterations in each step, the master surface is actually permitted to penetrate the slave surface, but the opposite is not. In consequence, the slave surface (the bar) must be relatively finely meshed (at least in the region of contact) for the model to be meaningful - otherwise the roller penetrates deeply between the widely spaced nodes of the bar, and the contact modelling is inaccurate. In practise, a uniform mesh spacing of 2mm (with 20mm diameter rollers) was sufficient to avoid problems.

Contact between the rollers and the bar is defined as frictionless (mechanical tangential behaviour settings for contact properties of an interaction, in ABAQUS terms). Numerical precision limits the accuracy of geometric placement of the roller relative to the bar in the assembly construction phase, so this must be done in the Assembly module using Constraint/Contact. Otherwise, the small but finite space will cause zero pivot problems in the simulation.

2.1.4 Simulation steps

Three steps are used in the model. The 'Initial' is an obligatory step created by ABAQUS, which is used to establish the contact between parts. During the 'Loading' step, the load is applied as a concentrated force to the top roller (the bottom roller is unable to move). The force (half of what was used in the real test on account of the two top rollers in the real machine) is applied to a reference point defined on the analytical cylinder. The location of this reference point is not important, but it must be created prior to the definition of the load. The loading force is ramped up linearly over the step duration (1s in simulation time, though this is arbitrary as the model is quasi-static - it has no inertial parameters). The initial step size is set to 0.25s, as it is known that the plasticity that will occur means that the step is not linear and thus will be solved in a piecewise fashion. The third step is the 'Unloading' step, during which the contact interaction of the top roller is removed and the roller moved back to its original position. The bar will straighten elastically, so the initial step size can be set to 1, and the model will be solved for this step with a single iteration.

2.1.5 Meshing

The meshing of the bar is easily done as the geometry is trivial, but it is very important that the correct type of elements are used for the mesh. Hexahedral (cuboid) elements fit much better than tetrahedral as the overall sample is also cuboid. However, there are also a number of classifications of these elements of which some are more suitable to this problem than others.

The full discussion of the meaning of the choices for element formulation is beyond the scope of this text, but the ABAQUS documentation is excellent in this regard

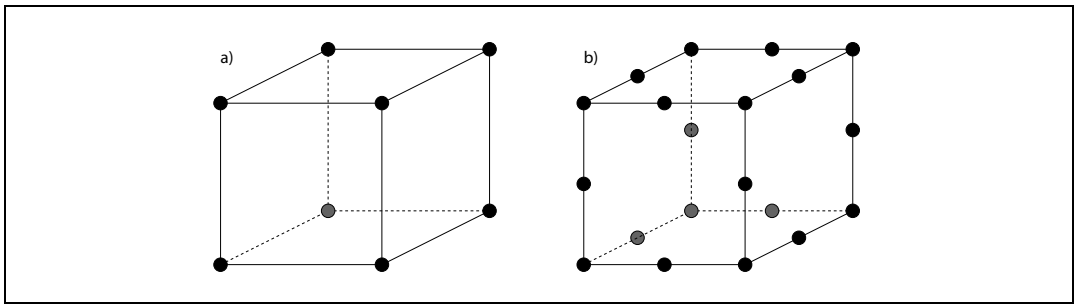

Figure 2-2. Continuum hexahedral elements: a) Linear (first order) and b) Quadratic (second order). The linear element has 8 nodes, whilst the quadratic has 20. All degrees of freedom are only calculated at the node locations, and interpolated (1st or 2nd order respectively) for all other positions in the element.

[Abaqus2004]. However, the bent bar model needs elements suitable for both elastic-plastic simulation and also contact modelling. These issues are dealt with separately below.

2.1.6 Elastic-plastic modelling elements

Once the material has been strained to the point of plasticity, the elements are much reduced in compressibility. This means that the element's volume is constrained to remain constant at it's integration points. In fully integrated second order elements, this overconstrains the element, causing 'volumetric locking' [Abaqus2004] or a stepwise increase in stiffness. First order elements in ABAQUS have a constant volume strain, so can be used without issue in either fully or reduced integration formulations. Reduced integration second order elements can be used when strains are <20% [Abaqus2004]. A linear kinematic hardening model was used.

2.1.7 Contact modelling elements

The ABAQUS recommendations for modelling contact [Abaqus2004] are to use first order elements where possible. If second order elements are used, ambiguities in the force distribution across the element mean that ABAQUS has to add midface nodes to every element on the slave surface.

In this model, C3D8R elements (hexahedral linear reduced integration with hourglass control) were used throughout. Hourglass control is needed to control modes that may propagate with linear reduced integration elements because pure bending of the element generates no strain energy. These details are explained in detail in

section 4.1.2 of the Getting Started with ABAQUS/Standard: Keywords Version [Abaqus2004]. The ABAQUS input deck for this is shown below (Section 2.2).

2.2 ABAQUS input deck

This is the ABAQUS input deck used to perform the simulation of the four point bending mechanism. It has been edited for length - a full working copy is available at http://pwlinda.mt.umist.ac.uk/contourmethod.

```
*Heading
** Job name: fourpointbend Model name: Model-1
*Preprint, echo=NO, model=NO, history=NO, contact=NO
**
** PARTS
**
*Part, name=Bar
*End Part
*Part, name=Roller
*End Part
**
** ASSEMBLY
**
*Assembly, name=Assembly
**
*Instance, name=Bar-1, part=Bar
*Node
      1,          130.,           10.,           20.
      2,          130.,            8.,           20.
      3,          130.,            6.,           20.
      4,          130.,            4.,           20.
      5,          130.,            2.,           20.
      6,          130.,            0.,           20.
      7,          130.,           -2.,           20.
 <snip>
   7984,            0.,           -6.,            0.
   7985,            0.,           -8.,            0.
   7986,            0.,          -10.,            0.
*Element, type=C3D8R
   1,  122,  123,  134,  133,    1,    2,   13,   12
   2,  123,  124,  135,  134,    2,    3,   14,   13
   3,  124,  125,  136,  135,    3,    4,   15,   14
   4,  125,  126,  137,  136,    4,    5,   16,   15
<snip>
6497, 7971, 7972, 7983, 7982, 7850, 7851, 7862, 7861
6498, 7972, 7973, 7984, 7983, 7851, 7852, 7863, 7862
6499, 7973, 7974, 7985, 7984, 7852, 7853, 7864, 7863
6500, 7974, 7975, 7986, 7985, 7853, 7854, 7865, 7864
```

```
** Region: (Section-2:Picked)
*Elset, elset=_PickedSet4, internal, generate
    1,  6500,     1
** Section: Section-2
*Solid Section, elset=_PickedSet4, material=steel
1.,
*End Instance
**
*Instance, name=RollerTop, part=Roller
         50.,           0.,          30.
         50.,           0.,          30.,          50.,          -
1.,          30., 89.9999990194245
*Node
      1,          10.,           0.,           0.
*Nset, nset=RollerTop-RefPt_, internal
1,
*Surface, type=REVOLUTION, name=RigidSurface_, internal
START,          10.,          40.
 LINE,          10.,         -40.
*Rigid Body, ref node=RollerTop-RefPt_, analytical sur-
face=RigidSurface_
*End Instance
**
*Instance, name=RollerBot, part=Roller
        100.,           0.,         -10.
      100.,         0.,       -10.,       100.,         1.,
-10., 89.9999990194245
*Node
      1,          10.,           0.,           0.
*Nset, nset=RollerBot-RefPt_, internal
1,
*Surface, type=REVOLUTION, name=RigidSurface_, internal
START,          10.,          40.
 LINE,          10.,         -40.
*Rigid Body, ref node=RollerBot-RefPt_, analytical sur-
face=RigidSurface_
*End Instance
*Nset, nset=_PickedSet12, internal, instance=Bar-1, generate
 7866,  7986,     1
*Elset, elset=_PickedSet12, internal, instance=Bar-1, generate
 6401,  6500,     1
*Nset, nset=_PickedSet42, internal, instance=RollerTop
 1,
*Nset, nset=_PickedSet46, internal, instance=RollerBot
 1,
*Nset, nset=_PickedSet48, internal, instance=Bar-1, generate
   1,  121,    1
*Elset, elset=_PickedSet48, internal, instance=Bar-1, generate
  1, 100,   1
*Nset, nset=_PickedSet49, internal, instance=RollerTop
```

```
 1,
*Nset, nset=_PickedSet52, internal, instance=Bar-1, generate
   1,  121,    1
*Elset, elset=_PickedSet52, internal, instance=Bar-1, generate
  1, 100,   1
*Nset, nset=_PickedSet53, internal, instance=RollerTop
 1,
*Elset, elset=__PickedSurf36_S3, internal, instance=Bar-1
    1,    2,    3,    4,    5,    6,    7,    8,    9,   10,  101,
102,  103,  104,  105,  106
  107,  108,  109,  110,  201,  202,  203,  204,  205,  206,  207,
208,  209,  210,  301,  302
  303,  304,  305,  306,  307,  308,  309,  310,  401,  402,  403,
404,  405,  406,  407,  408
<snip>
 5903, 5904, 5905, 5906, 5907, 5908, 5909, 5910, 6001, 6002, 6003,
6004, 6005, 6006, 6007, 6008
 6009, 6010, 6101, 6102, 6103, 6104, 6105, 6106, 6107, 6108, 6109,
6110, 6201, 6202, 6203, 6204
 6205, 6206, 6207, 6208, 6209, 6210, 6301, 6302, 6303, 6304, 6305,
6306, 6307, 6308, 6309, 6310
 6401, 6402, 6403, 6404, 6405, 6406, 6407, 6408, 6409, 6410
*Surface, type=ELEMENT, name=_PickedSurf36, internal
__PickedSurf36_S3, S3
*Elset, elset=__PickedSurf44_S5, internal, instance=Bar-1
   91,   92,   93,   94,   95,   96,   97,   98,   99,  100,  191,
192,  193,  194,  195,  196
  197,  198,  199,  200,  291,  292,  293,  294,  295,  296,  297,
298,  299,  300,  391,  392
  393,  394,  395,  396,  397,  398,  399,  400,  491,  492,  493,
494,  495,  496,  497,  498
<snip>
 6295, 6296, 6297, 6298, 6299, 6300, 6391, 6392, 6393, 6394, 6395,
6396, 6397, 6398, 6399, 6400
 6491, 6492, 6493, 6494, 6495, 6496, 6497, 6498, 6499, 6500
*Surface, type=ELEMENT, name=_PickedSurf44, internal
__PickedSurf44_S5, S5
*End Assembly
**
** MATERIALS
**
*Material, name=steel
*Elastic
289000., 0.3
*Plastic
 446.39,          0.
 448.61,    0.000163
 450.05, 0.00044417
  450.9, 0.00089104
 451.48,  0.0016818
```

```
452.73,  0.0027939
454.65,  0.0040813
  457.,  0.0054478
 459.8,  0.0068297
463.14,  0.0080411
466.29,  0.0090901
469.22,   0.010042
472.24,   0.010974
475.34,   0.011885
478.36,   0.012797
481.42,   0.013708
484.54,   0.014634
487.59,   0.015557
490.64,    0.01651
493.64,   0.017483
496.62,   0.018474
499.53,   0.019477
502.51,   0.020501
505.45,   0.021525
508.47,   0.022548
511.41,   0.023569
514.27,    0.02459
517.03,   0.025609
519.75,   0.026628
522.32,   0.027645
524.91,   0.028662
527.47,   0.029678
530.05,   0.030693
532.55,   0.031708
535.01,   0.032721
537.38,   0.033733
539.73,   0.034743
541.96,   0.035753
544.16,   0.036761
546.35,   0.037769
548.47,   0.038775
550.55,   0.039781
552.59,   0.040785
554.63,   0.041789
556.51,   0.042791
558.47,   0.043793
560.34,   0.044793
 562.2,   0.045793
563.94,   0.046791
565.69,   0.047788
567.32,   0.048784
568.92,   0.049779
570.45,   0.050774
572.01,   0.051767
573.56,   0.052759
```

```
 575.09,    0.05375
 576.55,    0.05474
 577.95,    0.05573
 579.34,   0.056718
 580.71,   0.057705
 582.03,   0.058692
 583.34,   0.059677
 584.71,   0.060661
   586.,   0.061645
 587.26,   0.062627
 588.46,   0.063609
 589.65,   0.064589
 590.68,   0.065569
 591.65,   0.066548
 592.63,   0.067525
  593.6,   0.068502
 594.51,   0.069478
  595.5,   0.070453
 596.48,   0.071426
 597.39,   0.072399
  598.3,   0.073371
 599.21,   0.074342
 600.05,   0.075312
  600.9,   0.076281
 601.71,    0.07725
  602.5,   0.078217
 603.27,   0.079183
   604.,   0.080149
 604.65,   0.081113
 605.33,   0.082077
 605.98,   0.083039
 606.65,   0.084001
 607.36,   0.084962
 608.12,   0.085922
 608.78,    0.08688
 609.44,   0.087839
 610.01,   0.088797
 610.53,   0.089753
 610.94,   0.090709
 611.49,   0.091664
 611.97,   0.092618
 612.48,    0.09357
  612.9,   0.094522
 613.41,   0.095473
 613.82,   0.096422
  614.2,   0.097371
**
** INTERACTION PROPERTIES
**
*Surface Interaction, name=Frictionless
```

```
1.,
*Friction
0.,
**
** BOUNDARY CONDITIONS
**
** Name: BarHold Type: Symmetry/Antisymmetry/Encastre
*Boundary
_PickedSet48, ENCASTRE
** Name: BarRestrain Type: Displacement/Rotation
*Boundary
_PickedSet52, 2, 2
** Name: BarSymmetry Type: Symmetry/Antisymmetry/Encastre
*Boundary
_PickedSet12, XSYMM
** Name: RollerHoldBottom Type: Symmetry/Antisymmetry/Encastre
*Boundary
_PickedSet46, ENCASTRE
** Name: RollerRestrainTop Type: Displacement/Rotation
*Boundary
_PickedSet49, 1, 1
_PickedSet49, 2, 2
_PickedSet49, 4, 4
_PickedSet49, 5, 5
_PickedSet49, 6, 6
**
** INTERACTIONS
**
** Interaction: Bottom
*Contact Pair, interaction=Frictionless, small sliding, adjust=0.0
_PickedSurf44, RollerBot.RigidSurface_
** Interaction: Top
*Contact Pair, interaction=Frictionless, small sliding, adjust=0.0
_PickedSurf36, RollerTop.RigidSurface_
** ----------------------------------------------------------------
--
**
** STEP: Load
**
*Step, name=Load
*Static
0.1, 1., 1e-05, 1.
**
** BOUNDARY CONDITIONS
**
** Name: BarHold Type: Symmetry/Antisymmetry/Encastre
*Boundary, op=NEW
** Name: BarRestrain Type: Displacement/Rotation
*Boundary, op=NEW
_PickedSet52, 2, 2
```

```
** Name: BarSymmetry Type: Symmetry/Antisymmetry/Encastre
*Boundary, op=NEW
_PickedSet12, XSYMM
** Name: RollerHoldBottom Type: Symmetry/Antisymmetry/Encastre
*Boundary, op=NEW
_PickedSet46, ENCASTRE
** Name: RollerRestrainTop Type: Displacement/Rotation
*Boundary, op=NEW
_PickedSet49, 1, 1
_PickedSet49, 2, 2
_PickedSet49, 4, 4
_PickedSet49, 5, 5
_PickedSet49, 6, 6
**
** LOADS
**
** Name: Down   Type: Concentrated force
*Cload
_PickedSet42, 2, 0.
_PickedSet42, 3, -16250.
**
** OUTPUT REQUESTS
**
*Restart, write, frequency=1
**
** FIELD OUTPUT: F-Output-1
**
*Output, field, variable=PRESELECT
**
** HISTORY OUTPUT: H-Output-1
**
*Output, history, variable=PRESELECT
*El Print, freq=999999
*Node Print, freq=999999
*End Step
** ----------------------------------------------------------------
--
**
** STEP: Unload
**
*Step, name=Unload
*Static
1., 1., 1e-05, 1.
**
** BOUNDARY CONDITIONS
**
** Name: RollerTopEnd Type: Displacement/Rotation
*Boundary
_PickedSet53, 3, 3
**
```

```
** LOADS
**
** Name: Down   Type: Concentrated force
*Cload, op=NEW
**
** INTERACTIONS
**
** Interaction: Top
*Model Change, type=CONTACT PAIR, remove
_PickedSurf36, RollerTop.RigidSurface_
**
** OUTPUT REQUESTS
**
*Restart, write, frequency=1
**
** FIELD OUTPUT: F-Output-1
**
*Output, field, variable=PRESELECT
**
** HISTORY OUTPUT: H-Output-1
**
*Output, history, variable=PRESELECT
*End Step
```

C Source code for FIT_SPLINE.M

As for the other scripts, the source code contained here is in a constant state of flux as it is modified to increase its usefulness and speed. The most recent version is always available at http://pwlinda.mt.umist.ac.uk/contourmethod. If lifting code from this document, care should be taken as line endings may not be formatted correctly.

```
% FIT_SPLINE.M
% Greg Johnson & Matt Fox
% April 2004
% completely rewritten June 2004 by Greg - now more general
%
% REQUIRES: Spline toolbox and exportfig


% height range - tweak manually
%r=-100:10:100;
%%
r=input('Enter range for colour bar (microns) ([min:step:max] = [-
100:10:100]): ');
if isempty(r)
  return
end

%% produce a colourbar
close all
figure(1)

[x,y]=meshgrid(r,1:2);
contourf(x,y,[r;r],[r])
set(gca,'ytick',[])
set(gca,'xtick',[r])
pos=get(gca,'position');
set(gca,'position',[pos(1) pos(2) pos(3) 0.1])
try
  system('mkdir results');
catch
```

```
  disp('Maybe the "results" directory already exists...')
end
exportfig(gcf,['results/colourbar.eps'],'format','eps2','col-
or','cmyk','preview','none')
saveas(gcf,['results/colourbar.fig']);
print('-djpeg',['results/colourbar.jpg'])

%%



if ~exist('outlinefile','var')
  outlinefile=uigetfile('*.txt','Select the outline file');
  if outlinefile==0
    disp('Cancelled')
    clear outlinefile
    return
  end
end
[xOut,yOut,zOut]=read_three_columns(outlinefile);

if ~(exist('filename1','var') & exist('filename2','var'))
  fnames=uigetfile('*.txt','Select the data files','multise-
lect','on');
  filename1=fnames{1};
  filename2=fnames{2};
  %end
  [xA,yA,zA]=read_three_columns(filename1);
  [xB,yB,zB]=read_three_columns(filename2);

  % estimate point density
 pdensity=max(round(abs(10*median(diff(yA))))/10,round(abs(10*me-
dian(diff(xA))))/10);;

  if pdensity==0
    pdensity=input('Point density estimated at 0 - enter correct
value: ');
  else
    fprintf('Point density estimated at %2.2f: edit this file if
incorrect\n',pdensity);
  end

  disp('Fitting splines to data')

  % only take points every 'decimation' mm

  decimation=pdensity;
  xpad=0.05*(max(xOut)-min(xOut));
  ypad=0.05*(max(yOut)-min(yOut));
```

```
  repx=3;
  repy=repx;

  xrange=min(xOut)-xpad:decimation:max(xOut)+xpad;
  yrange=min(yOut)-ypad:decimation:max(yOut)+ypad;
  [xi,yi,zAi]=griddata(xA,yA,zA,xrange,yrange','nearest');
  [zBi]=griddata(xB,yB,zB,xrange,yrange','nearest');
  zCi=(zAi+zBi)/2;

  disp('Calculating points inside boundary.  Please hold...')
  in=inpolygon(xi(:),yi(:),xOut,yOut);
  disp('Writing averaged data to ''averaged.mat''')
  av.in=in;
  av.zCi=zCi;
  av.z=av.zCi;av.z(~av.in)=NaN;
  av.xi=xi;
  av.yi=yi;
  save('averaged','av')

end


% open log of fit stats
fid=fopen('results/spline_gof.txt','wt');
fprintf(fid,'KnotSpacing(mm)\tOneSig-
ma(um)\tRange(um)\tRMS(um)\n');
close all

%%%%%%%%%%%%%%%%%%%%%%%%%%%%%%%%%%%%
% KNOT SPACING SET HERE
%%%%%%%%%%%%%%%%%%%%%%%%%%%%%%%%%%%%

spacingrange=input('Specify minimum and maximum point spacing (mm)
[x y]: ');
if 0
  spacingset=[spacingrange(2)];
 minspacing=max(pdensity*2,spacingrange(1));  % can't fit splines
with density less than 2x data density
  while spacingset(end)>minspacing
    spacingset(end+1)=spacingset(end)/2;
  end
  %spacingset=spacingset(end:-1:1);
else
  % new attempt here ** greg, april 2005)
  disp('New range done here...')
  spacingset=[spacingrange(1):spacingrange(2)];
end
midpointx=mean([min(xOut) max(xOut)]);
midpointy=mean([min(yOut) max(yOut)]);
```

```
%%%%
if 0
  spacingset=[];
  n=2;
  tmpxrange=max(xrange)-min(xrange);
  tmpyrange=max(yrange)-min(yrange);
  minrange=min(tmpxrange,tmpyrange);
  while minrange/n>2*pdensity
    spacingset(end+1)=minrange/n;
    n=n+1;
  end
  spacingset=spacingset(:);
end
%%%%%%%%%%%%%%%%%%%%
for n=1:length(spacingset)

  knotspacex=spacingset(n);
  %knotspacex=pdensity*2;
  knotspacey=knotspacex;
  %knotspacey=pdensity*4;

  fprintf('Spline knot spacing: X=%2.2f mm  Y=%2.2f
mm\n',knotspacex,knotspacey);

  tmp=midpointx;
  while tmp(end)<max(xOut)
    tmp(end+1)=tmp(end)+knotspacex;
  end
  rhrangex=tmp;

  tmp=midpointx;
  while tmp(end)>min(xOut)
    tmp(end+1)=tmp(end)-knotspacex;
  end
  lhrangex=tmp(end:-1:2);

  tmpx2=[lhrangex rhrangex];
  %%%%%%
  tmp=midpointy;
  while tmp(end)<max(yOut)
    tmp(end+1)=tmp(end)+knotspacey;
  end
  rhrangey=tmp;

  tmp=midpointy;
  while tmp(end)>min(yOut)
    tmp(end+1)=tmp(end)-knotspacey;
  end
  lhrangey=tmp(end:-1:2);
```

```
  tmpy2=[lhrangey rhrangey];

  spline=spap2({augknt(tmpx2,repx),
    augknt(tmpy2,repy)},...
    [repx repy],{xrange,yrange},zCi');

  zerror=fnval(spline,[xi(:) yi(:)]');
  zerror=zCi-reshape(zerror,size(xi));

  zOutC=fnval(spline,[xOut yOut]');

  %%%%%%%%%%%%%%%%%%
  if 0
    figure(1)
    clf
    surf(xi,yi,zCi,'facecolor','none','edgecolor',[.8 .8
.8],'edgealpha',0.7)
    hold on
    fnplt(spline)
    plot3(spline.knots{1},ze-
ros(size(spline.knots{1})),ones(size(spline.knots{1}))*max(zB(:))
,'ro')
    plot3(ze-
ros(size(spline.knots{2})),spline.knots{2},ones(size(spline.knots
{2}))*max(zB(:)),'ro')
    view([1 0 0])
    set(gca,'dataaspectratio',[500 500 1])

    title('Mesh of averaged point clouds (gray) with spline fit');
  end
  %%
  %%%%%%%%%%%%%%%%%%%%
  if 0
    figure(2)
    clf

    fnplt(spline)
    hold on
    plot3(xOut,yOut,zOutC,'.')
    plot3(spline.knots{1},ze-
ros(size(spline.knots{1})),ones(size(spline.knots{1}))*max(zB(:))
,'ko')
    plot3(ze-
ros(size(spline.knots{2})),spline.knots{2},ones(size(spline.knots
{2}))*max(zB(:)),'ko')

    title('Fitted spline, outline of sample')
    set(gca,'clim',[-0.04 0.04])
    view([0 0 1])
  end
```

```
  %%

  zerr2=zerror;
  zerr2(~in)=NaN;

  if 0
    figure(3)
    clf
    mesh(xi,yi,zerr2);view([0 0 1]),axis image
    %hold on
    %plot3(xOut,yOut,zOut,'.')
    title('Error between fitted spline and averaged surfaces')
    xlabel('mm');
    ylabel('mm');
    zlabel('mm');
  end
  e=zerror(in)*1000;
  sperror(n,:)=e;
  onesigma=std(e);
  range1=max(e)-min(e);
  rms=sqrt(mean(e.^2));
 fprintf('STD error: %2.2fum range: %2.2fum RMS: %2.2fum\n\n',one-
sigma,range1,rms);

  fprintf(fid,'%02d\t\t%2.2f\t\t%2.2f\t\t%2.2f\n',spacing-
set(n),onesigma,range1,rms);

  %%
  figure(5)
  % contour plot of spline'd surface
  a=yi;
  b=xi;
  c=reshape(fnval(spline,[xi(:) yi(:)]'),size(xi));
  c(~in)=NaN;
  contourf(a,b,c*1000,r)
  set(gca,'clim',[min(r) max(r)])
  set(gca,'dataaspectratio',[1000 1000 1]);
  axis tight
  xlabel('mm'),ylabel('mm')
  disp('MANUAL COLOUR LIMITS - CHANGE THIS IN FIT_SPLINE.M')

 % colorbar('horizontal','gridlinestyle','-','xgrid','on')

  if floor(spacingset(n))==0
    fname=sprintf('spline00_%03.0f',1000*spacingset(n));
  else
    fname=sprintf('spline%02d_%03.0f',[floor(spacingset(n))
1000*rem(spacingset(n),floor(spacingset(n)))]);
  end
```

```
  titlestr=sprintf('Surface height of averaged data points (um) -
%s',fname);
  title(titlestr,'interpreter','none','fontsize',15)


  disp(['Filename: ',fname]);
  exportfig(gcf,['results/' fname '.eps'],'format','eps2','col-
or','cmyk','preview','none')
  saveas(gcf,['results/' fname '.fig']);
  print('-djpeg',['results/' fname '.jpg'])
  %%
  save([fname '.mat'],'spline')
end

fclose(fid);


%%
figure
%%
clf
numplots=size(sperror,1);
clear ax hp
for n=numplots:-1:1
  subplot(numplots/2,2,numplots+1-n)
  hp(n)=plot(sperror(n,:),'.');
  axis([-inf inf -5 5])
  ax(n)=gca;
  title([num2str(spacingset(n)) 'mm'])
end

hlink=linkprop(ax,{'xlim','ylim'});
%set(ax,'fontsize',14)
set(hp,'markersize',1)
exportfig(gcf,'results/residuals_all.eps','format','eps2','col-
or','cmyk','preview','none')
print('-djpeg',['results/residuals_all.jpg']);

%axis([5200 5500 -5 5])
%set(hp,'markersize',6)
%exportfig(gcf,'results/residuals_zoom.eps','format','eps2','col-
or','cmyk','preview','none')
```

D Source code for CMM_CLEAN.M

The functionality of each button in the cmm_clean display is explained in the fol-

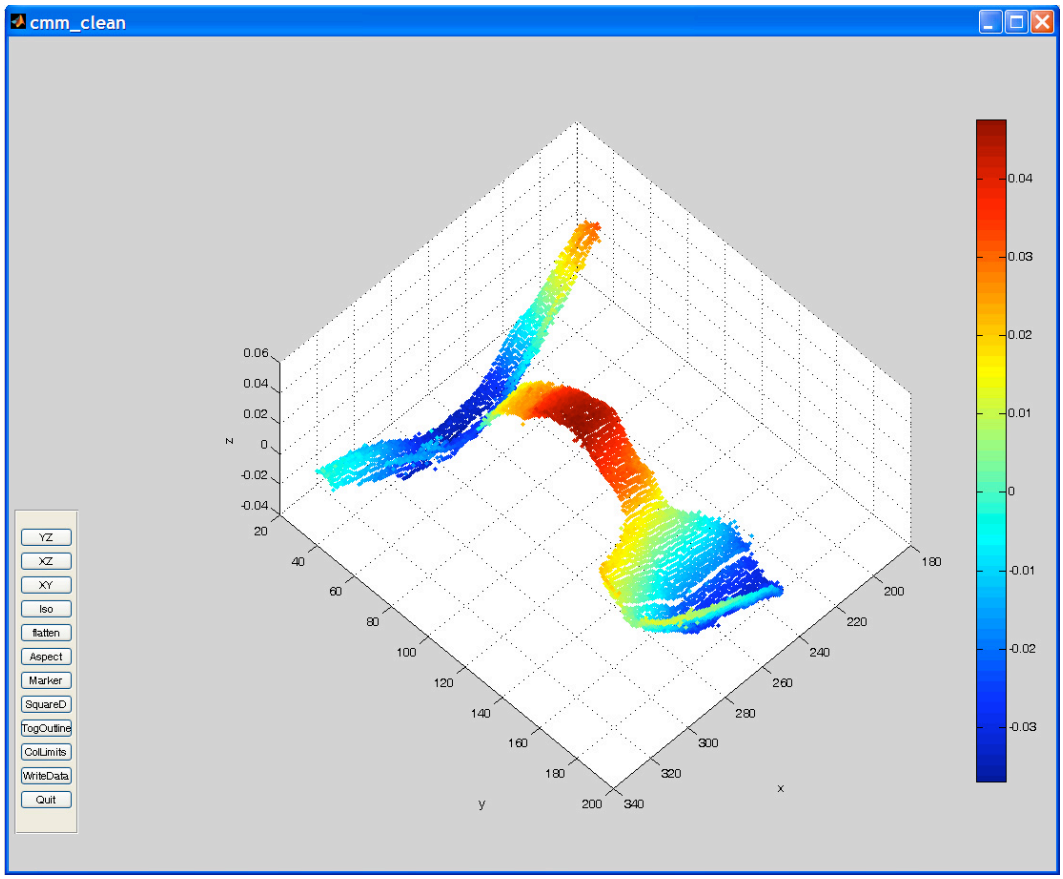

lowing list:

- XZ, YZ, XY, Iso: Viewing angle. Change the camera view to look at the yz, xz, and xy planes, and also an isometric view.
- Flatten: Remove any planar component from the entire dataset. This is implemented by shearing the points, not by true rotation. The measured surface is very close to horizontal, so this approximation is adequate.

- Aspect: When the surface height variations are small, changing the apparent scale of the vertical vs. the horizontal dimensions can make viewing easier.
- Marker: Cycling the marker size for each point. When the data set is fairly sparse, this makes it easier for the operator to recognise surface contours.
- SquareD: If the user has an outline of the sample (the dataset may or may not extend to the edges of the sample), then this function squares off the dataset. Figure 4-23 shows how this process is achieved.
- TogOutline: Toggles the display of the outline, if available.
- ColLimits: The limits to the colour bar are normally automatically taken as the limits of the z values of the dataset. However, if the user wishes to change the colour scaling, they may do so with this button.
- WriteData: Once the required point removal and flattening has been done, this writes the new data to disk. The current filename is used, appended with "_flat".
- Quit: as one would expect.

In any of the planar views (XZ,YZ,XY), the left mouse button may be used to select a rectangular area of the dataset for removal. In addition, the right mouse button may be used to select an area to be used for planar removal - in contrast to the Flatten button which examines the entire dataset for planar content, this examines only the selected area, but corrects the *entire* dataset.

When the dataset is squared off, the rotated dataset is automatically written to a file appended with "_square".

A late and undocumented addition to `cmm_clean` is the 'nudge' function. In cases where the cutting wire has shifted laterally while cutting, steps may appear in the data (as shown in Chapter 6). The assumption of the contour method that the cut is flat must be true, so the nudge function permits the movement of small rectangular areas to align them with the rest of the dataset, and remove the effects of this cutting artefact. This is performed by holding down the Shift (up) and Ctrl (down) keys, while selecting the rectangle with the left mouse button. Once the area has been nudged once, the same area may be nudged further without reselection using the comma (up) and fullstop (down) keys.

As for the other scripts, the source code contained here is in a constant state of flux as it is modified to increase its usefulness and speed. The most recent version is always available at http://pwlinda.mt.umist.ac.uk/contourmethod. If lifting code from this document, care should be taken as line endings may not be formatted correctly.

```
%% CMM_CLEAN.M A simple point cloud editing program
% Greg Johnson, 2003-2004
% Please credit CMM_CLEAN, Greg Johnson, and the University of
Manchester
% for all usage
%
% Try these keys in the figure window:
% f flatten data
% a cycle aspoect ratio
% m cycle marker size
% c set colour limits
% r square off against outline
% u undoes last crop (yahoo!)
% w write data to disk
% o show outline on screen
% z toggle zoom mode (LMB zooms instead of normal)
% q quit without saving
% 1,2,3 4 change view
% LMB drag - crops data
% SHIFT-LMB drag - nudge data up (in z)
% CTRL-LMB drag - nudge data down (in z)
%
% Requires Matlab 7 (Release 14) or later (support for subfunctions)
% and the fit_plane function (from GJ) and also
read_three_columns.m
%
% Modified 16/2/2005
% GJ - added nudge and undo.  Cool beans, eh?

function cmm_clean(varargin)
persistent app
if nargin==0
  % startup
  app=[];
  app.data.fnamedata=uigetfile('*.*','Select the data file');
  if isequal(app.data.fnamedata,0)
    fprintf('Cancelled...\n');
    return
  end
  [app.data.x,app.data.y,app.data.z]=read_three_columns(app.da-
ta.fnamedata);
```

```
  %app.data.x=app.data.x(1:5:end);
  %app.data.y=app.data.y(1:5:end);
  %app.data.z=app.data.z(1:5:end);


  %The following lines are to be uncommented for dealing with badly
scaled
  %data ONLY.
  %app.data.x=app.data.x*0.1;
  %app.data.y=app.data.y*0.4;
  %app.data.z=app.data.z*0.001;

  sfSetupVariables
  sfSetupFigure
else
  if nargin==3
    disp('Ahh!  You want me to look at that data?  OK...')
    app.data.x=varargin{1};
    app.data.y=varargin{2};
    app.data.z=varargin{3};
    sfSetupVariables
    sfSetupFigure
  else
    switch varargin{1}
      case 'mouse'
        sfMouseDrag
      case 'key'
        sfKeyPress
      otherwise
        disp('That sort of thing shouldn''t be allowed...');
    end
  end
end
%%%%%%%%%%%%%%%%%%

%% sfKeyPress
  function sfKeyPress
   app.view.lastkeypress=get(app.view.h_fig,'currentcharacter');
    switch app.view.lastkeypress
      case 'f'
        sfFlattenData
      case 'a'
        sfCycleAspectRatio
      case 'm'
        sfCycleMarkerSize
      case 'r'
        sfSquareData
      case 'o'
        sfToggleOutline
      case 'c'
```

```
        sfSetColourLimits
      case 'u'
        sfUndoLastCrop
      case 'z'
        sfToggleZoomIn
      case 'Z'
        sfZoomOut
      case 'w'
        sfWriteData
      case 'q'
        sfQuit
      case {'1','2','3','4','5','6','7','8'}
        app.view.viewaxis_selector=str2double(app.view.lastkey-
press);
        view(app.view.viewvector(app.view.viewaxis_selector,:));
        set(gca,'cameraupvector',app.view.cameraupvec-
tor(app.view.viewaxis_selector,:));
      case ','
        % bit of a kludge to permit multiple nudges without rese-
lecting...
        app.data.z(app.data.selection)=app.data.z(app.data.selec-
tion)-0.01;
        sfReplotData;
      case '.'
        app.data.z(app.data.selection)=app.data.z(app.data.selec-
tion)+0.01;
        sfReplotData;
      case '<'
        app.data.z(app.data.selection)=app.data.z(app.data.selec-
tion)-0.001;
        sfReplotData;
      case '>'
        app.data.z(app.data.selection)=app.data.z(app.data.selec-
tion)+0.001;
        sfReplotData;
      otherwise
       %disp('Haven''t the faintest idea what you''re asking...');
    end
  end

%% sfMouseDrag
  function sfMouseDrag
    pmask=logical([1 1 1]);
    pmask(app.view.viewaxis_selector)=0;
    seltype=get(gcf,'selectiontype');
    %if strcmp(seltype,'normal')
    %  disp('LMB - pass to zoom')
    %  return
    %end
```

```
    point1 = get(app.view.h_ax,'CurrentPoint');    % button down
detected
    finalRect = rbbox;                   % return figure units
    point2 = get(app.view.h_ax,'CurrentPoint');    % button up de-
tected
    set(gcf,'pointer','arrow')
    point1 = point1(1,pmask);            % extract x and y
    point2 = point2(1,pmask);
    p1 = min(point1,point2);             % calculate locations
    offset = abs(point1-point2);         % and dimensions
    x = [p1(1) p1(1)+offset(1) p1(1)+offset(1) p1(1) p1(1)];
    y = [p1(2) p1(2) p1(2)+offset(2) p1(2)+offset(2) p1(2)];

    u1=x(1);u2=x(3);
    v1=y(1);v2=y(3);

    switch app.view.viewaxis_selector
      case 1
        a=find(app.data.y>u1 & app.data.y<u2);
        b=find(app.data.z>v1 & app.data.z<v2);
      case 2
        a=find(app.data.x>u1 & app.data.x<u2);
        b=find(app.data.z>v1 & app.data.z<v2);
      case 3
        a=find(app.data.x>u1 & app.data.x<u2);
        b=find(app.data.y>v1 & app.data.y<v2);
      otherwise
        a=[];b=[];
    end

    c=intersect(a,b);

    if strcmp(seltype,'normal')
      % LMB, should we crop or zoom?
      if app.view.zoomon
        % zoom
        app.view.axlimits=[u1 u2 v1 v2];
        set(gca,'xlim',app.view.axlimits(1:2),'ylim',app.view.ax-
limits(3:4));

        drawnow
      else
        % crop
        app.data.undoable.x=app.data.x(c);
        app.data.undoable.y=app.data.y(c);
        app.data.undoable.z=app.data.z(c);
        app.data.x(c)=[];
        app.data.y(c)=[];
        app.data.z(c)=[];
      end
```

```
    elseif strcmp(seltype,'extend')
      disp('Nudge up')
      app.data.z(c)=app.data.z(c)+0.01;
      app.data.selection=c;


    elseif strcmp(seltype,'alt')
      disp('Nudge down')
      app.data.z(c)=app.data.z(c)-0.01;
      app.data.selection=c;
      if 0
        % LMB, locally flatten
        % SHOULD NEVER GET HERE!  THIS CODE IS REDUNDANT BUT LEFT
TO SHOW
        % HOW...
        [zfit,zfit2]=fit_plane(app.data.x(c),app.data.y(c),app.da-
ta.z(c),app.data.x,app.data.y);
        app.data.z=app.data.z-zfit2;
      end
    else
      disp('Ooh, an unusual mouse button...')
    end
    % after cropping, reset colormap
    app.view.clim=[min(app.data.z(:)) max(app.data.z(:))];

    sfReplotData
  end


%% sfReplotData
  function sfReplotData
    figure(app.view.h_fig);
    app.view.h_plot=plot3c(app.data.x,app.data.y,app.da-
ta.z,app.data.z,'.');
    xlabel('x');ylabel('y');zlabel('z');
    set(app.view.h_plot,'markersize',app.view.marker-
size(app.view.msize_selector));


    view(app.view.viewvector(app.view.viewaxis_selector,:));
    set(gca,'cameraupvector',app.view.cameraupvec-
tor(app.view.viewaxis_selector,:));
    set(gca,'dataaspectratio',app.view.aspectra-
tio(app.view.ar_selector,:));
    set(gca,'clim',app.view.clim);
    set(gca,'xlim',app.view.axlimits(1:2),'ylim',app.view.axlim-
its(3:4));
    app.view.h_colorbar=colorbar;
    if app.view.showoutline==1
      hold on
```

```
      p=plot3(app.data.xOut,app.data.yOut,(0.1+mean(app.da-
ta.z(:)))*ones(size(app.data.xOut)),'k-')
      set(p,'linewidth',1)
      hold off
    end
  end

%% sfSetupVariables
  function sfSetupVariables
    app.view.viewaxis_selector=1;
    app.view.viewvector=[1 0 0;0 1 0;0 0 1;-0.5 -0.5 1;1 0 0;0 1
0;0 0 1;-0.5 -0.5 1];
    app.view.cameraupvector=[0 0 1;0 0 1;0 1 0;0 0 1;0 1 0;1 0 0;1
0 0;0 0 1];

    app.view.aspectratio=[...
      1e-4 1e-4 1;...
      1e-3 1e-3 1;...
      1e-2 1e-2 1;...
      1e-1 1e-1 1;...
      1e+0 1e+0 1;...
      1e+1 1e+1 1;...
      1e+2 1e+2 1;...
      1e+3 1e+3 1;...
      1e+4 1e+4 1];


    app.view.markersize=[5 15 20 25 30];
    app.view.showoutline=0;

    app.data.z=app.data.z-fit_plane(app.data.x,app.data.y,app.da-
ta.z);

    app.view.clim=[min(app.data.z(:)) max(app.data.z(:))];


    % estimate correct aspect ratio to start with
    rx=max(app.data.x)-min(app.data.x);
    rz=max(app.data.z)-min(app.data.z);
    ratio=rx./rz;
    app.view.ar_selector=find(ratio>app.view.aspectra-
tio(:,1),1,'last');
    app.view.msize_selector=1;

    app.view.zoomon=0;
    app.view.axlimits=[min(app.data.x) max(app.data.x) min(app.da-
ta.y) max(app.data.y)];
    set(gca,'xlim',app.view.axlimits(1:2),'ylim',app.view.axlim-
its(3:4));
```

```
  end

%% sfSetupFigure
  function sfSetupFigure
    % must start with fresh figure!
    app.view.h_fig=figure(1);
    set(gcf,'name','cmm_clean');
    set(gcf,'numbertitle','off');
    set(gcf,'toolbar','none');
    set(gcf,'menubar','none');
    close(app.view.h_fig)
    app.view.h_fig=figure(1);
   % ensure that keystrokes get captured and NOT passed to command
line
    set(app.view.h_fig,'KeyPressFcn','cmm_clean(''key'')');
    set(app.view.h_fig,'WindowButtonDown-
Fcn','cmm_clean(''mouse'')');

    app.view.clim=[min(app.data.z(:)) max(app.data.z(:))];

    clf
    % draw data for the first time
    app.view.h_plot=plot3c(app.data.x,app.data.y,app.da-
ta.z,app.data.z,'.');
    xlabel('x');ylabel('y');zlabel('z');
    app.view.h_ax=gca;
    set(app.view.h_plot,'markersize',app.view.marker-
size(app.view.msize_selector));
    set(gca,'position',[0.2 0.1 0.8 0.8])

    app.view.h_colorbar=colorbar;

    set(gcf,'pointer','crosshair');

    view(app.view.viewvector(app.view.viewaxis_selector,:));
    set(gca,'cameraupvector',app.view.cameraupvec-
tor(app.view.viewaxis_selector,:));
    set(gca,'dataaspectratio',app.view.aspectra-
tio(app.view.ar_selector,:))
    set(gca,'xlim',app.view.axlimits(1:2),'ylim',app.view.axlim-
its(3:4));
    app.gui.uipanel=uipanel('units','pixels','position',[7 40 67
340]);


    bsize=[55 20];

    app.gui.button(1)=uicontrol(gcf,'parent',app.gui.uipanel,...
      'position',[5 300 bsize],'string','YZ',...
      'tooltipstring','Shortcut: 1',...
```

```
      'callback','set(gcf,''currentcharac-
ter'',''1'');cmm_clean(''key'')');
    app.gui.button(2)=uicontrol(gcf,'parent',app.gui.uipanel,...
      'position',[5 275 bsize],'string','XZ',...
      'tooltipstring','Shortcut: 2',...
      'callback','set(gcf,''currentcharac-
ter'',''2'');cmm_clean(''key'')');
    app.gui.button(3)=uicontrol(gcf,'parent',app.gui.uipanel,...
      'tooltipstring','Shortcut: 3',...
      'position',[5 250 bsize],'string','XY',...
      'callback','set(gcf,''currentcharac-
ter'',''3'');cmm_clean(''key'')');
    app.gui.button(4)=uicontrol(gcf,'parent',app.gui.uipanel,...
      'tooltipstring','Shortcut: 4',...
      'position',[5 225 bsize],'string','Iso',...
      'callback','set(gcf,''currentcharac-
ter'',''4'');cmm_clean(''key'')');
    app.gui.button(5)=uicontrol(gcf,'parent',app.gui.uipanel,...
      'tooltipstring','Shortcut: f',...
      'position',[5 200 bsize],'string','flatten',...
      'callback','set(gcf,''currentcharac-
ter'',''f'');cmm_clean(''key'')');
    app.gui.button(6)=uicontrol(gcf,'parent',app.gui.uipanel,...
      'position',[5 175 bsize],'string','Aspect',...
      'tooltipstring','Shortcut: a',...
      'callback','set(gcf,''currentcharac-
ter'',''a'');cmm_clean(''key'')');
   app.gui.button(7)=uicontrol(gcf,'parent',app.gui.uipanel,...
     'position',[5 150 bsize],'string','Marker',...
     'tooltipstring','Shortcut: m',...
     'callback','set(gcf,''currentcharac-
ter'',''m'');cmm_clean(''key'')');
   app.gui.button(8)=uicontrol(gcf,'parent',app.gui.uipanel,...
     'position',[5 125 bsize],'string','SquareD',...
     'tooltipstring','Shortcut: r',...
     'callback','set(gcf,''currentcharac-
ter'',''r'');cmm_clean(''key'')');
   app.gui.button(9)=uicontrol(gcf,'parent',app.gui.uipanel,...
     'position',[5 100 bsize],'string','TogOutline',...
     'tooltipstring','Shortcut: o',...
     'callback','set(gcf,''currentcharac-
ter'',''o'');cmm_clean(''key'')');
   app.gui.button(10)=uicontrol(gcf,'parent',app.gui.uipanel,...
     'position',[5 75 bsize],'string','ColLimits',...
     'tooltipstring','Shortcut: c',...
     'callback','set(gcf,''currentcharac-
ter'',''c'');cmm_clean(''key'')');
   app.gui.button(11)=uicontrol(gcf,'parent',app.gui.uipanel,...
     'position',[5 50 bsize],'string','WriteData',...
     'tooltipstring','Shortcut: w',...
```

```
     'callback','set(gcf,''currentcharac-
ter'',''w'');cmm_clean(''key'')');
   app.gui.button(12)=uicontrol(gcf,'parent',app.gui.uipanel,...
     'position',[5 25 bsize],'string','Quit',...
     'tooltipstring','Shortcut: q',...
     'callback','set(gcf,''currentcharac-
ter'',''q'');cmm_clean(''key'')');

  end

%% sfCycleAspectRatio
  function sfCycleAspectRatio

app.view.ar_selector=mod(app.view.ar_selector,size(app.view.as-
pectratio,1))+1;
    set(app.view.h_ax,'dataaspectratio',app.view.aspectra-
tio(app.view.ar_selector,:));
  end

%% sfCycleMarkerSize
  function sfCycleMarkerSize

app.view.msize_selector=mod(app.view.msize_selector,length(app.vi
ew.markersize))+1;
    set(app.view.h_plot,'markersize',app.view.marker-
size(app.view.msize_selector));
  end

%% sfFlattenData
  function sfFlattenData
    app.data.z=app.data.z-fit_plane(app.data.x,app.data.y,app.da-
ta.z);
    % after flatten, reset the color limits
    app.view.clim=[min(app.data.z) max(app.data.z)];
    sfReplotData
  end

%% sfSetColourLimits
  function sfSetColourLimits
    app.view.clim(1)=input(['Lower value for color scale [' ...
      num2str(app.view.clim(1)) ']: ']);
    app.view.clim(2)=input(['Upper value for color scale [' ...
      num2str(app.view.clim(2)) ']: ']);
    set(app.view.h_ax,'clim',app.view.clim);
    colorbar
  end


%% sfToggleZoom
  function sfToggleZoomIn
```

```
    if app.view.zoomon
      disp('ZoomIn OFF')
      app.view.zoomon=0;
       else
      disp('ZoomIn ON')
      app.view.zoomon=1;
    end
  end

%% sfZoomOut
  function sfZoomOut
    app.view.axlimits=[min(app.data.x) max(app.data.x) min(app.da-
ta.y) max(app.data.y)];
    set(gca,'xlim',app.view.axlimits(1:2),'ylim',app.view.axlim-
its(3:4));
  end
%% sfSquareData
  function sfSquareData
    if ~isfield(app.data,'xOut')
      disp('Reading outline file')
      sfReadOutline
    end
    outline=[app.data.xOut app.data.yOut];
    data=[app.data.x app.data.y app.data.z];
    [outline,data]=sfRotateSquare(outline,data);
    app.data.x=data(:,1);app.data.y=data(:,2);app.data.z=da-
ta(:,3);
    app.data.xOut=outline(:,1);app.data.yOut=outline(:,2);
    dlmwrite([app.data.outlinefile(1:end-4)
'_square.txt'],[app.data.xOut app.data.yOut app.data.zOut],'delim-
iter',' ');
    disp('Written _SQUARE data')
    sfReplotData
  end

%% sfReadOutline
  function sfReadOutline
    app.data.outlinefile=uigetfile('*.*','Select outline file');
    if isequal(app.data.outlinefile,0)
      disp('Cancelled');
    else
      [app.data.xOut,app.data.yOut,app.data.zOut]=textread(app.da-
ta.outlinefile);
    end
  end

%% sfToggleOutline
  function sfToggleOutline
    if ~isfield(app.data,'xOut')
      sfReadOutline
```

```
      if ~isfield(app.data,'xOut')
       % sfReadOutline didn't manage to read the file (cancelled?)
        return
      end
    end
    if app.view.showoutline==1
      app.view.showoutline=0;
    else
      app.view.showoutline=1;
    end
    sfReplotData
  end

%% sfUndoLastCrop
  function sfUndoLastCrop
    app.data.x=[app.data.x; app.data.undoable.x];
    app.data.y=[app.data.y; app.data.undoable.y];
    app.data.z=[app.data.z; app.data.undoable.z];
    sfReplotData
  end


%% sfWriteData
  function sfWriteData
    disp('Writing cleaner FLAT file...')
   dlmwrite([app.data.fnamedata(1:end-4) '_flat.txt'],[app.data.x
app.data.y app.data.z],'delimiter',' ');
  end

%% sfQuit
  function sfQuit
    disp('Quit');
    set(app.gui.button,'enable','off')
    set(app.view.h_fig,'KeyPressFcn',[]);
    set(app.view.h_fig','WindowButtonDownFcn',[])
  end

%% sfRotateSquare
function [outline,data]=sfRotateSquare(outline,data)
  %% SQUAREDATA
 % Samples often have a nominally flat edge to them, so this assumes
that
  % one of those edges is in the bottom 5% of the data, and uses
that edge to
  % rotate the datasets to make the bottom horizontal.  Could go
horribly
  % wrong, but was developed for railway samples and works well
there.  Needs
  % to be done before centering.
  routline=max(outline(:,2))-min(outline(:,2));
```

```
  fivepercentile_outline=min(outline(:,2))+0.01*routline;
 bottomsection_outline=find(outline(:,2)<fivepercentile_outline);

  fit_outline=polyfit(outline(bottomsection_outline,1),out-
line(bottomsection_outline,2),1);

  % small angle approximation could be used here but no benefit
  outline_theta=-tan(fit_outline(1));

  T=[cos(outline_theta) sin(outline_theta);-sin(outline_theta)
cos(outline_theta)];
  % apply T to both outline and datapoints
  outline(:,[1 2])=[outline(:,1) outline(:,2)]*T;
  data(:,[1 2])=[data(:,1) data(:,2)]*T;

end
  %%%%%%%%%%%%%%%%%%
end
```

E Source code for CMM_ALIGN.M

As for the other scripts, the source code contained here is in a constant state of flux as it is modified to increase its usefulness and speed. The most recent version is always available at http://pwlinda.mt.umist.ac.uk/contourmethod. If lifting code from this document, care should be taken as line endings may not be formatted correctly.

```
% CMM_ALIGN.M
% Greg Johnson
% 2004/2005
% Need icp algorithm (C. Pirnog) - in the icp directory

clear all
fnameoutref=uigetfile('*.txt','Select REFERENCE outline file');
if fnameoutref==0
  return
end

fnameref=uigetfile('*.txt','Select REFERENCE DATA file');
if fnameref==0
  return
end
fnameoutfloat=uigetfile('*.txt','Select FLOATING outline file');
if fnameoutfloat==0
  return
end
fnamefloat=uigetfile('*.txt','Select FLOATING DATA file');
if fnamefloat==0
  return
end

fprintf('Reading data...\n');


r=read_three_columns(fnameoutref);
rdata=read_three_columns(fnameref);
f=read_three_columns(fnameoutfloat);
```

```
fdata=read_three_columns(fnamefloat);



%% MIRROR DATA
% Data of the two surfaces usually needs reflectingmirroring, ei-
ther across the x or
% y axis.

mirror=1;  % 1 = mirror in x, 2= mirror in y
if mirror==2
  fprintf('Mirroring data in XZ...\n');
  f(:,2)=-f(:,2);
  fdata(:,2)=-fdata(:,2);
elseif mirror==1
fprintf('Mirroring data in ZY...\n');
  f(:,1)=-f(:,1);
  fdata(:,1)=-fdata(:,1);
else
    fprintf('Not mirroring data - assuming done already...')
end

%% SQUARE DATA
% square off data if slightly squint wrt axis of measurement
% could use radon transform to determine whether (and how) to square
off
% best - would be neater that squaredata which is a bit of a kludge.

if 0
  fprintf('Data IS being squared off - edit cmm_align to change\n')
  [r,rdata]=squaredata(r,rdata);
  [f,fdata]=squaredata(f,fdata);
else
  fprintf('Data is NOT being squared off - edit cmm_align to
change\n');
end

%% CENTRE DATA
% Data is recentred here to a common origin, simply by moving the
centre of
% gravity.  Full alignment is done later on, but this gets the gross
errors
% out of the way

mean_fdata=mean(fdata);
f=f-repmat(mean_fdata,[length(f),1]);
fdata=fdata-repmat(mean_fdata,[length(fdata),1]);
mean_rdata=mean(rdata);
r=r-repmat(mean_rdata,[length(r),1]);
rdata=rdata-repmat(mean_rdata,[length(rdata),1]);
```

```
% we align only in x and y, so set z to zeros
r(:,3)=0;
f(:,3)=0;

%%%%%%%%%
% show starting position...

figure(1)
clf
rorig=r;
forig=f;
fprintf('Optional section removal: ')
if 0
  fprintf('Cropping...\n\n')
  r1=max(r(:,1))-min(r(:,1));
  r2=max(r(:,2))-min(r(:,2));
  if r1>r2
    % remove sections of outline around flashing of LFW
    r(find(r(:,1)>-10 & r(:,1)<10),:)=[];
    f(find(f(:,1)>-10 & f(:,1)<10),:)=[];
  else
    r(find(r(:,2)>-10 & r(:,2)<10),:)=[];
    f(find(f(:,2)>-10 & f(:,2)<10),:)=[];
  end
else
  fprintf('NOT cropping\n\n')
end



clf
plot3(r(:,1),r(:,2),r(:,3),'b.-')
hold on
plot3(f(:,1),f(:,2),f(:,3),'k.-');


plot3(rdata(:,1),rdata(:,2),rdata(:,3),'g.')
hold on
plot3(fdata(:,1),fdata(:,2),fdata(:,3),'r.');
title('Original data after mirroring')

%xlabel('x');ylabel('y');zlabel('z')
set(gca,'dataaspectratio',[1000 1000 1]);
view(0,90)
drawnow
%%

[fnew, tr, rot] = iterativeClosestPoint(r, f, 25,0.050);
```

```
fnew=fnew';
ax1=gca;
%%
figure(2)
clf
plot3(r(:,1),r(:,2),r(:,3),'g.');
hold on
plot3(fnew(:,1),fnew(:,2),fnew(:,3),'r.');

%%
% transform the data points in the same fashion as the outline
fdatanew= transpose(rot*fdata' + repmat(tr.', 1, size(fdata', 2)));
r=rorig;
f=transpose(rot*forig' + repmat(tr.',1,size(forig',2)));

plot3(rdata(:,1),rdata(:,2),rdata(:,3),'g.');
hold on

plot3(fdatanew(:,1),fdatanew(:,2),fdatanew(:,3),'r.');
title('Aligned data')
set(gca,'dataaspectratio',[1000 1000 1]);
view(0,90)
ax2=gca;
hlink=linkprop([ax1 ax2],{'CameraPosition','CameraUpVector'});


% save the data
fprintf('Saving the data to _ALIGNED files\n');

dlmwrite([fnameref(1:end-4) '_aligned.txt'],[rdata],'delimiter','
');
dlmwrite([fnameoutref(1:end-4) '_aligned.txt'],[r],'delimiter','
');


dlmwrite([fnamefloat(1:end-4) '_aligned.txt'],[fdatanew],'delim-
iter',' ');
dlmwrite([fnameoutfloat(1:end-4) '_aligned.txt'],[fnew],'delimit-
er',' ');
```

F Source code for CREATE_INP.M

As for the other scripts, the source code contained here is in a constant state of flux as it is modified to increase its usefulness and speed. The most recent version is always available at http://pwlinda.mt.umist.ac.uk/contourmethod. If lifting code from this document, care should be taken as line endings may not be formatted correctly.

```
% CREATE_INP_displacement.M
% reads a .inp file (generated by Patran) and generates two .inp
files that
% are suitable to be tweaked for the contour method
% Greg Johnson 2004
%
% path should include /cygwin/bin for grep and sed to work

[splinenames,splinepathname]=uigetfile('*.mat','Select spline
files','multiselect','on');
if iscell(splinenames)==0 & splinenames==0
    return
end

[infile,pathname]=uigetfile('*.inp','Select original .inp file');
outfile=[infile(1:end-4) 'ABQ.inp'];
meshfile=[infile(1:end-4) 'mesh.inp'];

material=input('Sample material: ','s');
modulus=input('Young''s modulus (MPa) (ie steel = 209000): ');
poisson=input('Poisson ratio: ');
restraintchoice=input('What nodes for re-
straint(1=BL,2=BR,3=TL,4=TR, specify like [1 2]): ');

disp('Grabbing original mesh...');
% works with ABAQUS (perhaps also PATRAN) generated INP
%cmd=['!c:\cygwin\bin\sed -ne "/*solid/Iq" -ne "/*node/I,$p" '
pathname infile ' > ' meshfile];
```

```
cmd=[‘!c:\cygwin\bin\sed -e “s/*Element.*/&, elset=sample/” -ne “/
*End Instance/Iq” -ne “/*node/I,$p” ‘ pathname infile ‘ > ‘ mesh-
file];
eval(cmd);

% read the nodes to identify the Top set...
disp(‘Reading nodes’);
nodes=read_inp(meshfile);

disp(‘Calculating corner nodes’);
%%
toppoints=[nodes.x(nodes.topnodes)’  nodes.y(nodes.topnodes)’];

%bottom left corner
cornerpoint=[min(nodes.x(nodes.topnodes))-
5,min(nodes.y(nodes.topnodes))-5];
difference=repmat(cornerpoint,length(toppoints),1)-toppoints;
distance=sqrt(difference(:,1).^2+difference(:,2).^2);
[val,ndx]=min(distance);
cornerx=toppoints(ndx,1);
cornery=toppoints(ndx,2);
nodes.cornernode(1)=find(nodes.x==cornerx & nodes.y==cornery &
nodes.z==max(nodes.z));
%%
%bottom right corner
cornerpoint=[max(nodes.x(nodes.topn-
odes))+5,min(nodes.y(nodes.topnodes))-5];
difference=repmat(cornerpoint,length(toppoints),1)-toppoints;
distance=sqrt(difference(:,1).^2+difference(:,2).^2);
[val,ndx]=min(distance);
cornerx=toppoints(ndx,1);
cornery=toppoints(ndx,2);
nodes.cornernode(2)=find(nodes.x==cornerx & nodes.y==cornery &
nodes.z==max(nodes.z));


%top left corner
cornerpoint=[min(nodes.x(nodes.topnodes))-
5,max(nodes.y(nodes.topnodes))+5];
difference=repmat(cornerpoint,length(toppoints),1)-toppoints;
distance=sqrt(difference(:,1).^2+difference(:,2).^2);
[val,ndx]=min(distance);
cornerx=toppoints(ndx,1);
cornery=toppoints(ndx,2);
nodes.cornernode(3)=find(nodes.x==cornerx & nodes.y==cornery &
nodes.z==max(nodes.z));
%%
%top right corner
cornerpoint=[max(nodes.x(nodes.topn-
odes))+5,max(nodes.y(nodes.topnodes))+5];
```

```
difference=repmat(cornerpoint,length(toppoints),1)-toppoints;
distance=sqrt(difference(:,1).^2+difference(:,2).^2);
[val,ndx]=min(distance);
cornerx=toppoints(ndx,1);
cornery=toppoints(ndx,2);
nodes.cornernode(4)=find(nodes.x==cornerx & nodes.y==cornery &
nodes.z==max(nodes.z));



%%
figure(1)
clf
plot3(...
  nodes.x(nodes.topnodes),...
  nodes.y(nodes.topnodes),...
  nodes.z(nodes.topnodes),'r.');
hold on
plot3(...
  nodes.x(nodes.cornernode(restraintchoice)),...
  nodes.y(nodes.cornernode(restraintchoice)),...
  nodes.z(nodes.cornernode(restraintchoice)),'b.','marker-
size',25);
axis equal

view([0 0 1])


%%

fid=fopen(outfile,'wb');
fprintf(fid,'*HEADING\n');
fprintf(fid,'contour method, %s\n',infile);
fprintf(fid,'**\n');
fprintf(fid,'*include,input=%s\n',meshfile);
fprintf(fid,'**\n');

% write the 'top' elset to be the top elements
fprintf(fid,'*ELSET, ELSET=TOP\n');
fprintf(fid,'%d,%d,%d,%d,%d,%d,%d,%d,%d,%d,%d,%d,%d,%d,%d,%d\n',n
odes.topelements);
fprintf(fid,'\n');

%fprintf(fid,'%d, %d, 1\n',min(nodes.topele-
ments),max(nodes.topelements));
%disp('The TOP set generation assumes sequential elements - THIS IS
PROBABLY WRONG!!!!');

fprintf(fid,'*solid section, elset=sample, material=%s\n',materi-
al);
```

```
fprintf(fid,'*material, name=%s\n',material);
fprintf(fid,'*elastic, type=iso\n');
fprintf(fid,' %E,%f\n',modulus,poisson);
fprintf(fid,'**\n');


if iscell(splinenames)==0
  tmp=splinenames;
  clear splinenames;
  splinenames{1}=tmp;
end
splinenames=sort(splinenames);
%% Loop through each spline fit and add a step to the input deck
for n=1:length(splinenames)
  fprintf('Processing spline: %s...\n',splinenames{n})
  % the spline values are negated here
  load([splinepathname splinenames{n}]);
  f=-fnval(spline,[nodes.x(nodes.topnodes)' nodes.y(nodes.topn-
odes)']');
  if 0
    figure(2)
    clf
    plot3(nodes.x(nodes.topnodes),nodes.y(nodes.topn-
odes),f+nodes.z(nodes.topnodes),'.');
    hold on
    plot3(nodes.x(nodes.topnodes),nodes.y(nodes.topn-
odes),nodes.z(nodes.topnodes),'go');
    %set(gca,'dataaspectratio',[1000 1000 1]);
  end

  fprintf(fid,'** STEP (autogenerated by Matlab)\n');
  fprintf(fid,'*step, perturbation, name=%s\n',splinenames{n});
  fprintf(fid,'*static\n');
  fprintf(fid,'*boundary, op=new\n');
  fprintf(fid,'%d,  2,,  0.\n',nodes.cornernode(re-
straintchoice(1)));
  fprintf(fid,'%d, 1,2, 0.\n',nodes.cornernode(re-
straintchoice(2)));
  fprintf(fid,'*boundary, op=new\n');

  disp('Looping through top nodes');
  fprintf(fid,'%d, 3,, %f\n',[nodes.topnodes; f]);

  fprintf(fid,'**\n');
  fprintf(fid,'**\n');
  fprintf(fid,'**\n');

  %fprintf(fid,'*output, field, variable=preselect\n');
  %%fprintf(fid,'*file format, ascii\n');
  %fprintf(fid,'*node print, freq=0\n');
```

```
  %fprintf(fid,'*node file\n');
  %fprintf(fid,'U,RF\n');
  %fprintf(fid,'*el print, pos=integ, freq=0\n');
  fprintf(fid,'*el print, pos=averaged at nodes, elset=top,
freq=1\n');
  fprintf(fid,'S33\n');
  %fprintf(fid,'*el file, pos=averaged at nodes\n');
  %fprintf(fid,'S\n');
  fprintf(fid,'*end step\n');
end

fclose(fid);

disp('Closing file');



% grab everything up to the start of the steps
%cmd=['!sed -n -e "/*node/,/*elset/p" ' infile ' > .\' meshfile];
% this sed command extracts all the nodes and elements, and also
creates
% an element set to be 'rail'.  Sed is cool...

% works with ABQCAE generated INP
%cmd=['!sed -ne "s/*Element.*/\0,elset=rail/"  -ne "/** region/Iq"
-ne "/*node/I,$p" ' infile ' > ' meshfile];
```

G Source code for GEN_OUTLINE.M

As for the other scripts, the source code contained here is in a constant state of flux as it is modified to increase its usefulness and speed. The most recent version is always available at http://pwlinda.mt.umist.ac.uk/contourmethod. If lifting code from this document, care should be taken as line endings may not be formatted correctly.

```
function [varargout]=gen_outline(varargin)
%% GEN_OUTLINE takes cmm boundary data and produces either a Patran
Neutral
% file or a .poly file (for use with Triangle) or a DXF.
%
% Modified September 1st Greg Johnson
% to allow either interactive or parameter driven mode
%
% (outlinefilename,outfilename,pitchflag,val,outputtype)
%
%

% Usage:
% gen_outline(outlinefilename,outfilename,pitchflag,value,output-
type)
% THIS NEEDS EDITING!!
%
% Example:
% gen_outline('outline.txt','../fem/rail2','p',10,'patran')
%
% See http://www-2.cs.cmu.edu/~quake/triangle.html for documenta-
tion for
% the 'triangle' program
%
% Greg Johnson, July 2004

if nargin==0
  outlinefilename=input('Current boundary textfile name: ','s');
  outfilename=input('Name for resulting output file: ','s');
```

```
  pitchflag=input('Pitch (p) or Curvature (c) filtering (or none
()): ','s');
  val=input('Value for filtering (mm or deg (use zero for no fil-
tering)): ');
  outputtype=input('Format for output file (patran, dxf,poly):
','s');

elseif nargin ~=5
  help gen_outline
  return
else
  outlinefilename=varargin{1};
  outfilename=varargin{2};
  pitchflag=varargin{3};
  val=varargin{4};
  outputtype=varargin{5};
end

% read the outline file first
[outline_orig.x,outline_orig.y,outline_orig.z]=read_three_columns
(outlinefilename);

clf
% first decimate the outline by pitch or curvature

if upper(pitchflag)=='P'
  fprintf('Pitch filtering with pitch of %3.3f\n',val)
  outline=filter_pitch(outline_orig,val);
elseif upper(pitchflag)=='C'
  fprintf('Curvature filtering\n')
  outline=filter_curve(outline_orig,val);
elseif upper(pitchflag)=='N'
  disp('No filtering')
  outline=outline_orig;
else
  disp('Horrible problem with pitchflag!! - should be p or c')
  return
end


%%%%%%%
% for quad meshing, MUST have even number of points.
% so we nobble the second last point (arbitrary choice)
if mod(length(outline.x),2)
  outline.x(end-1)=[];
  outline.y(end-1)=[];
end
fprintf('Number of points: %d\n',length(outline.x));
x=outline.x;
y=outline.y;
```

```
plot(x,y,'.-')
axis equal
hold on
plot(x(diff(x)==0 & diff(y)==0),y(diff(x)==0 & diff(y)==0),'ro')
shg

if strcmp(upper(outputtype),'TRIANGLE')
  disp('Writing TRIANGLE format output')
  fid=fopen([outfilename '.poly'],'wt');
  fprintf(fid,'# auto-generated from Matlab\n');
  fprintf(fid,'0 2 0 0 \n');
  fprintf(fid,'# Boundary segments\n');
  fprintf(fid,'%d 1\n',length(x));
  for counter=1:length(x)-1
    fprintf(fid,'%d %d %d 1\n',counter,counter,counter+1);
  end
  fprintf(fid,'%d %d %d 1\n',counter+1,counter+1,1);
  fprintf(fid,'# Number of holes\n');
  fprintf(fid,'0\n');
  fclose(fid);

  fid=fopen([outfilename '.node'],'wt');
  fprintf(fid,'%d 2 0 0\n',length(x));
  for counter=1:length(x)
    fprintf(fid,'%d %f %f\n',counter,x(counter),y(counter));
  end
  fclose(fid);
  % -Pqa20
  cmd=sprintf('!triangle -q %s',[outfilename '.poly'])
  disp('Sizing can be changed...')
  eval(cmd);

elseif strcmp(upper(outputtype),'PATRAN')

  % x=outline_orig.x;
  % y=outline_orig.y;
  disp('Writing PATRAN format output')
  fid=fopen([outfilename '.out'],'wt');
  fprintf(fid,'25      0      0      1      0      0      0
0       0\n');
  fprintf(fid,'PATRAN neutral file generated by Matlab script (Greg
Johnson)\n');
  fprintf(fid,'26      0      0      1      0      0      0
0       0\n');
  % date, time, version - should be fixed
  fprintf(fid,'17--04       10:10:38       3.0\n');

  % write 'grid data' (nodes of boundary)
  for counter=1:length(x)
```

```
fprintf(fid,'31%8d%8d%8d%8d%8d%8d%8d%8d\n',counter,0,1,0,0,0,0,0)
;
    fprintf(fid,'%16.7E%16.7E%16.7E\n',x(counter),y(counter),0);
  end


  for counter=1:length(x)-1
    linecoef=[x(counter) x(counter+1) x(counter+1)-x(counter)
x(counter+1)-x(counter);...
     y(counter) y(counter+1) y(counter+1)-y(counter) y(counter+1)-
y(counter);...
      0 0 0 0]';

    fprintf(fid,'32%8d      0      3      0      0      0
0       0\n',counter);
    fprintf(fid,'%16.7E%16.7E%16.7E%16.7E%16.7E\n',linecoef(1:5));
    fprintf(fid,'%16.7E%16.7E%16.7E%16.7E%16.7E\n',li-
necoef(6:10));
    fprintf(fid,'%16.7E%16.7E',linecoef(11:12));
    fprintf(fid,'%8d%8d\n',counter,counter+1);
  end

  % write last segment manually
  linecoef=[x(end) x(1) x(1)-x(end) x(1)-x(end);...
    y(end) y(1) y(1)-y(end) y(1)-y(end);...
    0 0 0 0]';
 fprintf(fid,'32%8d      0      3      0      0      0      0
0\n',length(x));
  fprintf(fid,'%16.7E%16.7E%16.7E%16.7E%16.7E\n',linecoef(1:5));
  fprintf(fid,'%16.7E%16.7E%16.7E%16.7E%16.7E\n',linecoef(6:10));
  fprintf(fid,'%16.7E%16.7E',linecoef(11:12));
  fprintf(fid,'%8d%8d\n',length(x),1);

 fprintf(fid,'99      0      0      1      0      0      0
0       0');
  fclose(fid);

elseif strcmp(upper(outputtype),'DXF')
  disp('Writing DXF format output')
  fid=fopen([outfilename '.dxf'],'wt');
  fprintf(fid,'0\nSECTION\n2\n');
  fprintf(fid,'ENTITIES\n0\n');
  for counter=1:length(x)-1
    fprintf(fid,...

'LINE\n10\n%f\n20\n%f\n30\n%f\n11\n%f\n21\n%f\n31\n%f\n0\n',...
      x(counter),y(counter),0,x(counter+1),y(counter+1),0);
  end
```

```
  % last line...
  fprintf(fid,...

'LINE\n10\n%f\n20\n%f\n30\n%f\n11\n%f\n21\n%f\n31\n%f\n0\n',...
    x(counter+1),y(counter+1),0,x(1),y(1),0);

  fprintf(fid,'ENDSEC\n0\nEOF\n');
  fclose(fid);

else
  disp('Unknown output type')
end


if nargout>0
  varargout{1}=x;
  varargout{2}=y;
end
if nargin==0
  disp('')
  disp(['You can run ` mfilename ` as a function - like this:']);

  cmd=sprintf('%s(''%s'',''%s'',''%s'',%f,''%s'')',...
    mfilename,...
    outlinefilename,...
    outfilename,...
    pitchflag,...
    val,...
    outputtype);

  disp(cmd)
end


function deg=fixangle(radians);

deg=radians*180/pi;

if deg<0
  deg=deg+360;
end

deg=deg+360;


function outline=filter_pitch(outline_orig,val);
dist=0;
current.x=outline_orig.x(1);
current.y=outline_orig.y(1);
old=current;
```

```
prev=current;
outline.x=[];
outline.y=[];

if val==0
  outline.x=outline_orig.x;
  outline.y=outline_orig.y;
else
  for n=1:length(outline_orig.x)

    dist=dist+dis-
tance([prev.x;prev.y],[outline_orig.x(n);outline_orig.y(n)]);
    prev.x=outline_orig.x(n);
    prev.y=outline_orig.y(n);
    if dist>val
      if dist>2*val
        % fill in really long gaps
        if ~isempty(outline.x)
          xrange=linspace(out-
line.x(end),outline_orig.x(n),1+ceil(dist/val));
          yrange=linspace(out-
line.y(end),outline_orig.y(n),1+ceil(dist/val));
        else
          xrange=linspace(outline_orig.x(n-
1),outline_orig.x(n),1+ceil(dist/val));
          yrange=linspace(outline_orig.y(n-
1),outline_orig.y(n),1+ceil(dist/val));
        end
        outline.x=[outline.x xrange(2:end-1)];
        outline.y=[outline.y yrange(2:end-1)];

      end

      dist=0;
      old=current;
      outline.x=[outline.x outline_orig.x(n)];
      outline.y=[outline.y outline_orig.y(n)];
      plot(outline.x,outline.y,'r.-')
      axis equal
      drawnow
    end
  end
  plot(outline.x,outline.y,'r.-');
  axis equal
  drawnow
end

function outline=filter_curve(outline_orig,val)
% curvature based filtering
```

```
orig_length=length(outline_orig.x);

outline.x=[];
outline.y=[];
curveflag=0;
range=round(orig_length/40);
init=1;

for n=1:orig_length
  if n+range > orig_length
    % wrap around if necessary
    segment.x=[outline_orig.x(n:end); outline_orig.x(1:range-
(orig_length-n))];
    segment.y=[outline_orig.y(n:end); outline_orig.y(1:range-
(orig_length-n))];
  else
    segment.x=[outline_orig.x(n:n+range)];
    segment.y=[outline_orig.y(n:n+range)];
  end

  xA1=segment.x(1);   yA1=segment.y(1);
  xA2=segment.x(end); yA2=segment.y(end);

  if curveflag~=0 | init==1
    init=0;
    yB1=segment.y(1);
    yB2=segment.y(round(end/2));
    xB1=segment.x(1);
    xB2=segment.x(round(end/2));
  end

  theta1=fixangle(atan2(yA2-yA1,xA2-xA1));
  theta2=fixangle(atan2(yB2-yB1,xB2-xB1));

  dt1=abs(theta1-theta2);
  dt2=abs(dt1-360);
  difftheta=min([dt1 dt2]);

  if difftheta>val
    curveflag=round(orig_length/50);  % was /50
    % if angle > threshold specified by user
    outline.x=[outline.x xB1];
    outline.y=[outline.y yB1];
    plot(xB1,yB1,'ro')
    hold on

  elseif curveflag>1
    % add a few extra points after things go flat again
    curveflag=curveflag-1;
    outline.x=[outline.x xA1];
```

```
    outline.y=[outline.y yA1];

  end

end

if curveflag==0
  % in straight section as we finished
  % delete first point
  outline.x(1)=[];
  outline.y(1)=[];
  % connect first and last points
  %   outline.x(end+1)=outline.x(1);
  %   outline.y(end+1)=outline.y(1);
end
```

H Source code for GEN_CMMSCAN.M

As for the other scripts, the source code contained here is in a constant state of flux as it is modified to increase its usefulness and speed. The most recent version is always available at http://pwlinda.mt.umist.ac.uk/contourmethod. If lifting code from this document, care should be taken as line endings may not be formatted correctly.

8.1 Usage

The software that controls the Mitutoyo Euro-C-Apex CMM used in this dissertation, COSMOS, is a scriptable program. So-called 'part programs' for performing measurements are written once and may be run numerous times. With the use of internal variables, the origin of the measurement program may be moved, as might be useful when measuring a number of identical parts laid out on the instrument table. It is also possible to write ASCII versions of part programs, which, after compilation by COSMOS, are then available to be executed.

In order to automate the measurement procedure for surfaces of arbitrary samples for contour method investigation, the author has developed a Matlab routine called `gen_cmmscan`. It is used as part of the following sequence:

1. Lay the sample on the CMM bed, with cut surface upwards, aligned nominally to the axes of the machine (within 10° is sufficient).
2. Measure the perimeter of the sample using the SP600 probe in continuous mode with a suitable resolution (sufficient to capture the features of the sample) and export this as a 'Transpak' text file.
3. Run `gen_cmmscan` from within Matlab. Parameters include the outline text file, the height of the surface of the sample, the name of the part program that is to be generated, the name of the results file for the measurements, the pitch of the measurements that are desired, and a choice of discrete or continuous mea-

surement types. This will generate a filename with a '.agw' extension, which is an ASCII version of the part program as suitable for compilation by COSMOS. The outline will be drawn on screen at the conclusion of the program, complete with the measurement points that have been calculated. This stage may take a considerable amount of time if the outline is complex and the point density is high - five to ten minutes is not unusual.

4. From within COSMOS, read and compile the AGW file using the "CMM/ASCII Geopak-Converter" menu item from the Part Manager. This will create a part in the current part folder with the name that was specified to `gen_cmmscan`.
5. Run the part program. The measured data will be written to the specified text file as a series of rows, each row having the <*x,y,z*> coordinates of the measured point.

8.2 Code

```
function gen_cmmscan(outlinefile,ztop,partprogram,measurement-
filename,pitch,type)
% generates a grid of points within part boundary
% Usage:
% gen_cmmscan(outlinefile,ztop,partprogram,measurementfilena-
me,pitch,type)

if nargin~=6
  help(mfilename)
  return
end

disp('This has been modified to speed up measurements - but it may
not')
disp('work anymore.  Look in the code for  *** to comment out the
new code')

tic
close all
disp('Specify the FULL path for the results file - otherwise it goes
to c:/cosmosXvY/exe ');
pitchx=pitch;
pitchy=pitch;

[x,y,z]=textread(outlinefile);
plot3(x,y,z,'.-','markersize',1);
axis equal

bbox=[min(x) min(y) max(x) max(y)];  % left front back right
hold on
meanz=mean(z);
```

```
startx=bbox(1);
starty=bbox(2);
endx=bbox(3);
endy=bbox(4);
zclearance=ztop+100;
zmeasurement=ztop-2;
zstandoff=ztop+2;



xrange=startx-2:pitchx:endx+2;
yrange=starty-2:pitchy:endy+2;


xpos=zeros(1,length(xrange)*length(yrange));
ypos=zeros(1,length(xrange)*length(yrange));

n=1;
for a=xrange
  for b=yrange
    xpos(n)=a;
    ypos(n)=b;
    n=n+1;
  end
end



if strcmp(upper(type),'DISCRETE')
  disp('If you have a high point density this next step might take
30 minutes!!!');
  disp('Thinking hard...')
  inside=inpolygon(xpos,ypos,x,y);


  fid=openPartProgram(partprogram);
  discreteheaderPartProgram(fid,zmeasurement,zclearance,zstandoff)
  points=1;
  contourndx=1;
  totalnumlines=0;
  additionalParts=0;
  disp('Generating code...');
  first=find(inside==1,1,'first');
  hp=plot3(xpos(first),ypos(first),meanz,'r.','markersize',1);
  hold on
  sprintf('Number of measurement points: %d Estimate time for scan:
%fs',length(find(inside==1)),length(find(inside==1))*2);
  for point=find(inside==1)
    plot3(xpos(point),ypos(point),meanz,'r.','markersize',1);
```

```
    % *** commented out the next two lines to try and speed things
up...
    % fprintf(fid,'GOTO/CART, %3.3f, %3.3f, ''ZSTANDOFF''\n',...
    %  xpos(point),ypos(point));
    fprintf(fid,'PTMEAS/CART,%3.3f,%3.3f,''ZMEASUREMENT'',VEC-
COMP,0,0,-1\n',...
      xpos(point),ypos(point));
    totalnumlines=totalnumlines+2;
    if points>1500
      %disp(['Contour ' num2str(contourndx)]);
      drawnow
      fprintf(fid,'ENDMES\n');
      if contourndx==1  % overwrite any exisiting file
        fprintf(fid,['CONTOUR/EXPORT,"Scan",NUMBER=1,"' measure-
mentfilename '"\n']);
      else  % append to existing file
        fprintf(fid,['CONTOUR/EXPORT,"Scan",NUMBER=1,"' measure-
mentfilename '",APPEND\n']);
      end
      fprintf(fid,'CONTOUR/MEAS, "Scan", NUMBER=1\n');
      points=1;
      contourndx=contourndx+1;
      % *** next line also changed from +2 to +1
      totalnumlines=totalnumlines+1;
    else
      points=points+1;
    end
    if totalnumlines>40000
      disp('got a problem here - will probably throw away data!')
      plot3(xpos(point),ypos(point),meanz,'go');
      totalnumlines=1;
      additionalParts=additionalParts+1;
      fprintf(fid,'ENDMES\n');%added by CG 10-02-06
      fprintf(fid,['CONTOUR/EXPORT,"Scan",NUMBER=1,"' measurement-
filename '",APPEND\n']);
      closePartProgram(fid);
      fid=openPartProgram([partprogram sprintf('%02d',additional-
Parts)]);
     discreteheaderPartProgram(fid,zmeasurement,zclearance,zstand-
off);
    end

  end

  if points~=1
    disp(['Contour ' num2str(contourndx)]);
    fprintf(fid,'ENDMES\n');
    if contourndx==1  % overwrite any exisiting file
      fprintf(fid,['CONTOUR/EXPORT,"Scan",NUMBER=1,"' measurement-
filename '"\n']);
```

```
    else  % append to existing file
      fprintf(fid,['CONTOUR/EXPORT,"Scan",NUMBER=1,"' measurement-
filename '",APPEND\n']);
    end

  end
  closePartProgram(fid)
  fprintf('Number of lines in last program ~= %d\n',totalnumlines);


elseif strcmp(upper(type),'CONTINUOUS')
  % attempt scanning measurements
  % calculate start and end points for each contour
  disp('Continuous scanning')


  convex_ndx=convhull(x,y);
  inside=inpolygon(xpos,ypos,x(convex_ndx),y(convex_ndx));
  disp('Generating code...');

  edges=find(diff(inside)~=0);
  %plot3(xpos(edges),ypos(edges),repmat(meanz,size(edges)),'go')
  xtmp=xpos(edges);ytmp=ypos(edges);
  measspeed=6;
  meassafe=1;
  contourndx=1;

  fid=openPartProgram(partprogram);

  for n=1:2:length(edges) %edges should always be an even number
    plot3(xtmp(n:n+1),ytmp(n:n+1),[meanz meanz],'r-o')
    hold on
    fprintf(fid,'DRIVE/ZAXIS, %f\n',meanz+6);
    fprintf(fid,'GOTO/CART,%f,%f,%f\n',xtmp(n),ytmp(n),meanz+6);
    fprintf(fid,'CONTOUR/MEAS, "Scan", NUMBER=1\n');
    fprintf(fid,'AUTOM/CONTOUR,$\n');
    fprintf(fid,'YZPLAN,$\n');
    fprintf(fid,'CART,$\n');
    fprintf(fid,'%3.3f,%3.3f,%3.3f,$\n',xtmp(n),ytmp(n),meanz);
    fprintf(fid,'%3.3f,%3.3f,%3.3f,$\n',xtmp(n+1),yt-
mp(n+1),meanz);
    fprintf(fid,'VECCOMP,   0.0000,   1.0000,  0.0000,$\n');
    fprintf(fid,'PITCH =%3.3f,$\n',pitch);
    fprintf(fid,'SCNVEL=%3.3f,$\n',measspeed);
    fprintf(fid,'SAFETY=%3.3f,$\n',meassafe);
    fprintf(fid,'LEFT,$\n');
    fprintf(fid,'IGNORE_1ST,$\n');
    %fprintf(fid,'NOCOMP,$\n'); % Comment this line for COMPON
    fprintf(fid,'DISPLACEMENT=   0.2500\n');
    % fprintf(fid,'PATCH = 56\n');
```

```
    fprintf(fid,'ENDMES\n');
    if contourndx==1  % overwrite any exisiting file
      fprintf(fid,['CONTOUR/EXPORT,"Scan",NUMBER=1,"' measurement-
filename '"\n']);
      contourndx=0;
    else  % append to existing file
      fprintf(fid,['CONTOUR/EXPORT,"Scan",NUMBER=1,"' measurement-
filename '",APPEND\n']);
    end
    fprintf(fid,'ENDFIL\n');
    fclose(fid);

  end

else
  disp('Scan type can be ''discrete'' or ''continuous''');
  return
end

axis equal
toc



function fid=openPartProgram(partprogram)
%% start part program
fid=fopen([partprogram '.agw'],'wt');
fprintf(fid,'$$ Matlab generated scan lines\n');
fprintf(fid,'\n');
fprintf(fid,['FILNAM/ "' partprogram '"\n']);
fprintf(fid,'\n');
fprintf(fid,'SNSLCT/1\n');
fprintf(fid,'DATSET/MCS\n');

fprintf(fid,'CNCON / MESVEL = DEFALT, POSVEL = HIGH, APPRCH =
0.5\n');
fprintf(fid,'\n');


function discreteheaderPartProgram(fid,zmeasurement,zclear-
ance,zstandoff)
fprintf(fid,'CONTOUR/MEAS, "Scan", NUMBER=1\n');
fprintf(fid,'\n');
fprintf(fid,'ASSIGN/''ZMEASUREMENT''="%f",FIXP=4\n',zmeasure-
ment);
fprintf(fid,'ASSIGN/''ZCLEAR''="%f",FIXP=4\n',zclearance);
fprintf(fid,'ASSIGN/''ZSTANDOFF''="%f",FIXP=4\n',zstandoff);
fprintf(fid,'DRIVE/ZAXIS,''ZCLEAR''\n');

fprintf(fid,'\n');
```

```
function closePartProgram(fid)

fprintf(fid,'ENDFIL\n');
fclose(fid);
```

Bibliography

Abaqus 2004 — ABAQUS, *ABAQUS/Standard Documentation Version 6.5*, Pawtucket, Rhode Island: ABAQUS, Inc. 2004

Aliabadi 1992 — Aliabadi, M. H. , Rooke, David P., *Numerical Fracture Mechanics*, Springer, 1992

AllMetal 2004 — All Metal Services, Certificate of Conformity (BSI) RS 052.: Birmingham, UK. 2004.

Askar 1963 — Askar, C. and E. Moroz, Pressure on evaporation of matter in a radiation beam. *Journal of Experimental and Theoretical Physics Letters*, (16) p1638-1644, 1963.

ASTM 1999 — ASTM, Standard Practice for Determining Residual Stresses by Hole- Drilling Strain-Gage Method, Standard E837-95: West Conshohocken, PA. 1999.

Baldwin 1975 — Baldwin G. C., Origin of Synchrotron Radiation, *Physics Today*, 28(1): p9, 1975.

Benedict 1987 — Benedict G.F., *Non-Traditional Manufacturing Processes*, chapter Electrical discharge machining (EDM), Marcel Dekker, Inc, New York & Basel (1987), pp. 231–232.

Besl 1992 — Besl, P.J. and N.D. McKay, A method for registration of 3-d shapes. *IEEE Transactions Pattern Analysis and Machine Intelligence*, 14(2): p. 239-256, 1992.

Bishop 1995 — Bishop C. M., *Neural networks for pattern recognition*. Oxford University Press, p. 372-375. 1995.

Bonner 1996 — Bonner, N.W., *Measurement of residual stresses in thick section steel welds*. PhD thesis, Mechanical Engineering,University of Bristol, 1996.

Bonner 1996b — Bonner, N.W. and D.J. Smith, *Residual stresses in design, fabrication, assessment and repair*, chapter Measurement of residual stresses using the deep hole method. American Society of Mechanical Engineers: New York. p. 53-65. 1996.

Boothroyd 1989 — Boothroyd G. and A.K. Winston, *Fundamentals of Machining*. chapter Non-conventional machining processes. Marcel Dekker, Inc, p. 491. 1989.

Boresi 2003 — Boresi A., Schmidt R., *Advanced mechanics of materials*, 6th ed. Wiley & Sons 2003.

Brass 2005 — Brass Bow Music Company, http://www.thebrassbow.com

Britannica 2001 — *Metallurgy, friction welding*. Encyclopædia Britannica, www.britannica.com. Vers. 2001 1999-2001.

Brown 1983 — Brown, K.R. *Strength of Metals and Alloys*,1983.

Bueckner 1958 — Bueckner, H.F., The propagation of cracks and the energy of elastic deformation. *Transactions ASME*, 80: p. 1225-1230. 1958.

Chakrabarti 1996 — Chakrabarti, D.J. and et al., *Materials Science Forum*, 1085: p. 217-222. 1996.

Charmilles 2020 — Charmilles, Robofill 2020. http://www.gfac.com

Cheng 1986 — Cheng, W. and I. Finnie, *Journal of Engineering Materials and Technology*,. 108: p. 87-92. 1986.

Clauer 1976 — Clauer, A.H., B.P. Fairand, and B.A. Wilcox, Laser Shock Hardening of Weld Zones in Aluminium Alloys. *Metallugical and Materials Transactions*, 8A: p. 1871-1876. 1976.

Clauer 1977 — Clauer, A.H., B.P. Fairand, and B.A. Wilcox, Pulsed Laser Induced Deformation in an Fe-3 Wt Pct Si Alloy. *Metallugical and Materials Transactions*, 8A: p. 119-125. 1977.

Cullity 1978 — Cullity, B.D., *Elements of x-ray diffraction*. 2nd ed. New York: Addison-Wesley. 1978.

Daymond 2003 — Daymond, M.R. and N.W. Bonner, Measurement of strain in a titanium linear friction weld by neutron diffraction. *Physica B: Condensed Matter*, 325: p. 130-137, 2003.

Deepcyrogenics 2005 — Deep Cryogenics Ltd, http://www.dynat.com

DeJong 1980 — DeJong, H.F., *Engineering Fracture Mechanics*,. 13: p. 175, 1980.

Devaux 1993 — Devaux, D., et al., Generation of shock waves by laser-induced plasma in confined geometry. *Journal of Applied Physics*, 74(4): p. 2268-2273, 1993.

DeWald 2001 — DeWald, A.T. and M.R. Hill, *Residual Stress in a Thick Steel Weld Determined Using the Contour Method*. 2001.

DeWald 2004 — DeWald, A.T., et al., Assessment of Tensile Residual Stress Mitigation in Alloy 22 Welds Due to Laser Peening. *Journal of Engineering Materials and Technology*, 126(4): p. 465-473, 2004.

Dynat 2005 — Dynat Inc., http://www.dynat.com

Edwards 2005 — Edwards, L., Private communication. 2005.

Evans 2004 — Evans, A. and A. King, Private communication. 2004.

Evans 2005 — Evans, A., *Near surface residual stresses in aerospace materials*. PhD thesis, University of Manchester, 2007.

Fairland 1974 — Fairland, B.P., A.H. Clauer, and R.G. Jung, Quantitative Assessment of Laser-Induced Stress Waves Generated at Confined Surface. *Applied Physics Letters*, 25(8): p. 431-433, 1974.

Fairland 1976a — Fairland, B.P. and A.H. Clauer, Use of Laser Generated Shocks to Improve the Properties of Metals and Alloys. *Industrial Application of High Power Laser Technology*, 86: p. 112-119, 1976.

Fairland 1976b — Fairland, B.P. and A.H. Clauer, Effect of Water and Paint Coatings on the Magnitude of Laser-Generated Shocks. *Optical Communications*, 18(4): p. 588-591, 1976.

Fairland 1979 — Fairland, B.P. and A.H. Clauer, Laser Generation of High Amplitude Stress Waves in Materials. *Journal of Applied Physics*, 50(3): p. 1497-1502, 1979.

Fathallah 1994 — Fathallah, R., et al., Comparison of residual stresses determined by X-ray diffraction, neutron diffraction and the hole drilling method in aerospace shot peened materials. ICRS-4: p. 834-843, 1994.

Fisher 2005 — Fisher, R., http://pwlinda.mt.umist.ac.uk/contourmethod/links/GJ_PhD, 2005.

Frankel 2005 — Frankel, Private communication. 2005.

Frankel 2008 — Frankel, Private communication. 2008.

Fridrici 2001 — Fridrici, V., S. Fouvry, and P. Kapsa, Effect of shot peening on the

fretting wear of Ti-6Al-4V. *Wear*, 250: p. 642-649, 2001.

Ganguly 2004 — Ganguly, S., *Non-destructuve measurement of residual stresses in welded aluminium 2024 airframe alloy.* PhD thesis, Open University, 2004.

George 2000 — George, D., *Determination of residual stresses in large section stainless steel welds*. PhD thesis, University of Bristol, 2000.

Grant 2002a — Grant, P.V., http://matcmn020.pdf, 2002.

Grant 2002b — Grant, P.V. and J. Lord, An Evaluation of Four Hole Drilling Analysis Techniques with respect to Non-Uniform Residual Stress Fields. 2002.

Haykin 1999 — Haykin S., Neural networks: a comprehensive foundation. Prentice Hall, p. 213-218, 1999.

Heyn 1911 — Heyn, E. and O. Bauer, On Stresses in Cold Drawn Metal. Internationals Zeitsckrift fur Metallographic, 1: p. 16-50, 1911.

Hill 2003 — Hill, M.R., Laser Peening Technology. *Advanced Materials & Processes*, 161(8): p. 65-67, 2003.

Ho 2003 — Ho K.H. and S.T. Newman, State of the art electrical discharge machining (EDM). *International Journal of Machining Tools and Manufacturing*. 43(13), pp. 1287–1300, 2003.

Honeycomb 1995 — Honeycomb and Bhadeshia, *Steels*: Edward Arnold. 1995.

Huntress 1978 — Huntress E.A., Electrical discharge machining. *American Machinist* 122 8, pp. 83–98, 1978.

ISO 2002 — ISO, Geometrical Product Specifications (GPS) -- Acceptance and reverification tests for coordinate measuring machines (CMM) -- Part 2: CMMs used for measuring size. 2001.

James 1996 — James, M.R., Introduction, in Handbook of Measurement of Residual Stresses, J. Lu, Editor. The Fairmont Press: Lilburn, GA. p. 1-4, 1996.

Jameson 2001 — Jameson E.C., Description and development of electrical discharge machining (EDM). In: Electrical Discharge Machining, Society of Manufacturing Engineers, Dearbern, Michigan, p. 16, 2001.

Johnson 1966 — Johnson, P.C., B.A. Stein, and R.S. Davis, *Inertia Welding*, Caterpillar Tractor Co. 1966.

Karadge 2005a — Karadge, M. and R. Moat, Personal Communication.

Karadge 2005b — Karadge, M., Neutron measurements on IFW1 at POLDI, Switzerland. 2005.

Kelleher 2003 — Kelleher, J., et al., The Measurement of Residual Stress in Railway Rails by Diffraction and Other Methods. *Journal of Neutron Research*, 11(4): p. 187-193, 2003.

Keyence 2005 — Keyence, Confocal probe specifications - LT class. 2005.

King 2005 — King, A., Private communication. 2005.

King 2008 — King, A., Private communication. 2008.

Krar 1997 — Krar S.F. and A.F. Check, Electrical discharge machining. In: Technology of Machine Tools, Glencoe/McGraw-Hill, New York, p. 800, 1997.

Lambert 2002 — Lambert, T.A. and K.D. Murphy, Modal convection and its effect on the stability of EDM wires. *International Journal of Mechanical Sciences*, 44(1): p. 207-216, 2002.

Leggatt 1996 — Leggatt, R.H., et al., Development and experimental validation of the deep hole method for residual stress measurement. *Journal of Strain Analysis*, 31: p. 177, 1996.

Li 1997 — Li, K.Y., Optics and Lasers in Engineering, 27: p. 125-136, 1997.

Lodini 2001 — Lodini A., The recent development of neutronic techniques for determination of residual stresses. *Radiation Physics and Chemistry*, **61**, p 226-233, 2001.

Lord 2000 — Lord, J., http://pwlinda.mt.umist.ac.uk/contourmethod/links/GJ_PhD

Macherauch 1986 — Macherauch E., Kloss K.H., *Proceedings of the International Conference on Residual Stresses*, Garmisch-Partenkirchen, FRG, p167-174. 1986.

Makino 1997 — Makino, A. and D. Nelson, J. Eng. Mater. Technol. (Trans ASME), 119(95-103), 1997.

Marrow 2004a	Marrow, T.J., et al., High resolution X-ray tomography of short fatigue crack nucleation in austempered ductile cast iron. *International Journal of Fatigue*, 26(7): p. 717-725, 2004.
Marrow 2004b	Marrow, T.J., et al. High-resolution, in-situ, tomographic observations of stress corrosion cracking. in EICM-2. Banff, Canada. 2004.
Martineau 2004	Martineau, R.L., M.B. Prime, and T. Duffey, Penetration of HSLA-100 steel with tungsten carbide spheres at striking velocities between 0.8 and 2.5km/s. *International Journal of Impact Engineering*, 30(5): p. 505-520, 2004.
Mary 2006	Mary C., Jahazi M., Linear friction welding of IN-718 process optimization and microstructure evaluation. 11th International Ceramics Congress, p. 357, 2006.
Mathar 1934	Mathar, J., Determination of Initial Stresses by Measuring Deformation Around Drilled Holes. Trans ASME, 56(4): p. 249-254, 1934.
Masubuchi 2003	Masubuchi K., Residual stresses and distortion in welds. Encyclopedia of Materials: Science and Technology. Buschow et al., Eds. Elsever, Oxford, p8121-8126, 2003.
McGeough 1988	J.A. McGeough J.A., Electrodischarge machining. in: Advanced Methods of Machining, Chapman & Hall, London, p130, 1988.
McGrath 2000	McGrath, P.J., et al., A Novel 8-Element Gauge for Residual Stress Assessment Using the High Speed Centre Hole Drilling Method. 2000.
Measurement 2000	http://pwlinda.mt.umist.ac.uk/links/GJ_PhD, 2000.
Metris 2005	Metris, Optical probing products - specifications for the LC15, 2005.
Milbradt 1951	Milbradt, K.P., Ring Method Determination of Residual Stresses. Proceedings SESA, 9(1): p. 63-74, 1951.
Mitutoyo 2001	Mitutoyo, Mitutoyo Product Catalogue. 2001.
Montross 2002	Montross, C.S., et al., Laser shock processing and its effect on microstructure and properties of metal alloys: a review. *International Journal of Fatigue*, 24: p. 101-1036, 2002.

Nextec 2005	Nextec, http://http://www.nextec-wizprobe.com
Nickola 1986	Nickola, W.E. Practical Subsurface Residual Stress Evaluation By The Hole-Drilling Method. in Proceedings of the Spring Conference on Experimental Mechanics. New Orleans: Society for Experimental Mechanics, 1986.
OneCryo 2005	OneCyro, Inc., http://www.onecryo.com, 2005.
Orringer 1996	Orringer, O., et al., Residual stress and its consequences on both sides of the wheel-rail interface. *Wear*, 191(1-2): p. 25-34. 1996.
Pain 1993	Pain, H.J., The physics of vibrations and waves. 4th edition ed., Chichester: Wiley, 1993.
Pang 2003	Pang, J.W.L., et al., Effects of tooling on the residual stress distribution in an inertia weld. *Materials Science and Engineering*, A356: p. 405-413, 2003.
Petropolous 2004	Petropoulos, G., N.M. Vaxevanidis, and C. Pandazaras, Modeling of surface finish in electro-discharge machining based upon statistical multi-parameter analysis. *Journal of Materials Processing Technology*, 155-156: p. 1247-1251, 2004.
Peyre 1996	Peyre, P., et al., Laser Shock Processing of Aluminium Alloys: Application to High Cycle Fatigue Behaviour. *Mater. Sci. Eng*., 210A: p. 102-113, 1996.
Pintchovius 1982	Pintchovius L., Jung V., Macherauch E., Schafer R., Vohringer O,. Sagamore Army Materials Research Conference Proceeding, 28: p. 461-482, 1982.
Pirnog 2004	Pirnog, C., No longer available on web, 2004
Polmear 1995	Polmear I.J., Light alloys: metallurgy of the light metals. Arnold, New York. 4th ed. 1995
Preuss 2002	Preuss, M., et al., Metall. Mater. Trans. A, 33: p. 3327-3234, 2002.
Preuss 2004	Preuss M., Quinta da Fonseca J., Steuwer A., Wang L., Withers P.J., Bray S., Residual stress in linear friction welded IMI55. *Journal of Neutron Research*, 12: p. 165-173, 2004.
Preuss 2005	Preuss, M., Personal communication. 2005.
Preuss 2005b	Preuss, M., Discussion on measurements of inertia friction welds.

2005.

Prevey 1993 — Prevéy, P.S., X-ray diffraction characterization of residual stresses produced by shot peening, in Shot Peening Theory and Application. II-TT International. p. 81-93, 1990.

Prevey 2000 — Prevéy, P.S. FOD Resistance and Fatigue Crack Arrest in Low Plasticity Burnished IN718. in Proceedings of the 5th National Turbine Engine High Cycle Fatigue Conference. Chandler, Arizona. 2000.

Prime 1999 — Prime, M.B., Residual stress measurement by successive extension of a slot: The crack compliance method. *Applied Mechanics Reviews*, 52(2): p75, 1999.

Prime 2000 — Prime, M.B. and A.R. Gonzales. The Contour Method: Simple 2-D Mapping of Residual Stresses. in 6th Int Conf. on Residual Stresses. Oxford, 2000.

Prime 2000b — Prime, M.B., P. Rangaswamy, and M.A.M. Bourke. Measuring Spatial Variation of Residual Stresses in a MMC Using Crack Compliance. in Proc. 7th Int. Conf. on Composites Engineering. Denver, Colorado, 2000.

Prime 2001 — Prime, M.B., Cross-Sectional Mapping of Residual Stresses by Measuring the Surface Contour After a Cut. *Journal of Engineering Materials and Technology*, 123: p. 162-168, 2001.

Prime 2002 — Prime, M.B. and M.R. Hill, Residual stress, stress relief, and inhomogeneity in aluminium plate. *Scripta Materialia*, 46(1): p. 77-82, 2002.

Prime 2002b — Prime, M.B., et al. Residual Stress Mapping in Welds Using The Contour Method. in 6th Int. Conf. Trends in Welding Research. Pine Mountain, GA: ASM International, 2002.

Prime 2002c — Prime, M.B. and R.L. Martineau, Mapping Residual Stresses After Foreign Object Damage Using The Contour Method. *Materials Science Forum*, 404-407: p. 521-526, 2002.

Prime 2003 — Prime, M.B., M.A. Newborn, and J.A. Balog, Quenching and Cold-Rold Residual Stresses in Aluminium Hand Forgings: Contour Method Measurement and FEM Prediction. *Materials Science Forum,* 426-432: p. 435-440, 2003

Prime 2004	Prime, M.B., et al., Laser Surface-Contouring and Spline Data-Smoothing for Residual Stress Measurement. *Experimental Mechanics*, 44(2): p. 176-184, 2004.
Prime 2004b	Prime, M.B., et al. Contour-Method Determination of Parent-Part Residual Stresses Using a Partially Relaxes FSW Test Specimen. in 2004 SEM X Int. Congress & Exposition on Experimental and Applied Mechanics. Costa Mesa, CA., 2004.
Prime 2005	Prime, M.B., Personal Communication. 2005.
Prime 2005b	Prime, M.B., Personal Communication. 2005.
Prime 2008	Personal communications, 2008
Puri 2005	Puri A.B. and B. Bhattacharyya, An analysis and optimization of the geometrical inaccuracy due to wire lag phenomenon in WEDM. *Int. J. Mach. Tools Manuf*. 43-2 , pp. 151–159, 2003.
Putman 1992	Putman, C.A.J., et al., A detailed analysis of the optical beam deflection technique for use in atomic force microscopy. *Journal of Applied Physics*, 71(1): p. 6-12, 1992.
Raj 1987	Raj, K. and R.J. Boulton, Ferrofluids -- Properties and applications. *Materials & Design*, 8(4): p. 233-236, 1987.
Ramasawmy 2004	Ramasawmy, H. and L. Blunt, Effect of EDM process parameters on 3D surface topography. *Journal of Materials Processing Technology*, 148(2): p. 155-164, 2004.
Rangaswamy 2005	Rangaswamy, P., et al., Residual stresses in LENS® components using neutron diffraction and contour method. *Materials Science and Engineering*, 2005.
Rendler 1966	Rendler, N.J. and I. Vigness, Hole-drilling Strain-Gage Method of Measuring Residual Stresses. *Experimental Mechanics*, 6(12): p. 577-586, 1966.
Renishaw 2003	Renishaw, TP200 precision touch trigger probe. 2003.
Renishaw 2004	Renishaw, 2004 - Reseating reproducability of touch trigger probe. 2004.
Ritchie 1987	Ritchie, D. and R.H. Leggatt, The measurement of the distribution of residual stresses through the thickness of a welded joint. *Strain*, p. 61-70, 1987.

Rotadata 2005 Rotadata, Personal Communication. 2005.

Russell 2005 Russell, R., Personal Communication. 2005.

Sachs 1927 Sachs, G., Evidence of residual stresses in rods and tubes. *Zeitch fur Metalljunde*, 19: p. 352, 1927.

Satyanarayana 2005 Satyanarayana, V.V., M. G., and M. B., Dissimilar metal friction welding of austenitic–ferritic stainless steels. *Journal of Materials Processing Technology*, 160: p. 128-137, 2005.

Schajer 1981 Schajer, G.S., Application of Finite Element Calculations to Residual Stress Measurements. *Journal of Engineering Materials and Technology*, 103: p. 157-163, 1981.

Schajer 1988a Schajer, G.S., Measurement of non-uniform residual stresses using the hole-drilling method, Part I - stress calculation procedures. *Journal of Engineering Materials and Technology*, Transactions of ASME, 110: p. 338-343, 1988.

Schajer 1988b Schajer, G.S., Measurement of non-uniform residual stresses using the hole-drilling method, Part II - Practical application of the integral method. *Journal of Engineering Materials and Technology*, Transactions of ASME,. 110: p. 344-349, 1988.

Schajer 1994 Schajer, G.S. and L. Yang, Residual-stress Measurement in Orthotropic Materials Using the Hole-drilling Method. *Experimental Mechanics*, 34(12): p. 324-333, 1994.

Schajer 1996 Schajer, G.S., et al., Hole-drilling and Ring Core Methods, in Handbook of Measurement of Residual Stresses, J. Lu, Editor, Fairmount Press. p. 11, 1996.

Schajer 1997 Schajer, G.S. and M. Tootoonian, A New Rosette Design for More Reliable Hole-Drilling Residual Stress Measurements. *Experimental Mechanics*, 37(3): p. 299-306, 1997.

Schoenberg 1946 Schoenberg, I.J., Contributions to the Problem of Approximation of Equidistant Data by Analytic Functions. *Quarterly of Applied Mathematics*, 4(1,2): p. 45-99 & 112-141, 1946.

Sebring 2001 Sebring, R., et al. Non-Contact Optical Three Dimensional Liner Metrology. in Proc. 28th IEEE International Conference on Plasma Science and The 13th IEEE International Pulsed Power Conference. Las Vegas, NV: IEEE, 2001.

Shobert 1983	Shobert E.I., What happens in EDM. in: E.C. Jameson, Editor, Electrical Discharge Machining: Tooling, Methods and Applications, Society of Manufacturing Engineers, Dearbern, Michigan, pp. 3–4, 1983.
Smith 1994	Smith, D.J. and N.W. Bonner, Measurement of residual stresses in a thick section steel weld, in Engineering Integrity Assessment, J.H. Edwards, J. Kerr, and P. Stanley, Editors. Chameleon Press: Birmingham, 1994.
Smith 2000	Smith, D.J., P.J. Bouchard, and D. George, Measurement and prediction of residual stresses in thick section steel welds. Journal of Strain Analysis, 39: p. 117-124, 2000.
Soete 1950	Soete, W. and R. Vancrombrugge, An Industrial method for the Determination of Residual Stresses. Proceedings SESA, 8(1): p. 17-28, 1950.
Stone 2008	Stone, H.J., K.D.H. Bhadeshia and P.J. Withers, In situ monitoring of weld transformations to control weld residual stresses. in: *Materials Science Forum* Vols. 571-572, pp 393-398, 2008.
Talyscan 2001	Hobson, T., Talyscan 250 specifications. 2001.
TechSpec 2005	TechSpec Incorporated, http://www.cryometals.com 2005.
Threadgill 2001	Threadgill, P., http://pwlinda.mt.umist.ac.uk/contourmethod/links/GJ_PhD, 2001
Three 2005	http://www.300below.com, 2005
Tiitto 1996	Tiitto, S., Magnetic Methods, in Handbook of Measurement of Residual Stresses, J. Lu, Editor, Fairmount Press. p. 45, 1996.
Toupin 1963	Toupin, R.A., A dynamical theory of elasic dielectrics. *International Journal of Engineering Science*. 1(1): p. 101-126, 1963.
Ueda 1980	Ueda, Y. and K. Fukuda, New measuring method of three dimensional welding residual stresses based on newly proposed principle of inherent strain. *Naval Architecture and Engineering* (Japan)., 18: p. 146-163, 1980.
Ueda 1997	Ueda, Y., Sectioning methods, in Handbook of measurement of residual stresses, J. Lu, Editor, The Fairmont Press. p. 49-70,

1996.

Vaidyanathan 1971 — Vaidyanathan, S. and I. Finnie, Determination of residual stresses from stress intensity factor measurements. *Journal of Basic Engineering*, 93: p. 242-246, 1971.

Vairis 1998 — Vairis, A. and M. Frost, High frequency linear friction welding of a titanium alloy. *Wear*, 218: p. 117-131, 1998.

Vaughan 2005 — Vaughan, T., Personal Communication.Discussions concerning EDM cutting at Rotadata, 2005.

Virkkunen 2001 — Virkkunen, I., *Thermal Fatigue of Austenitic and Duplex Stainless Steels*. PhD thesis, Helsinki University, 2001.

Wang 1975 — Wang K.K., Friction welding, *Welding Research Council Bulletin* **204**. p1-22. 1975

Webster 2001 — Webster, G.A. and A. Ezeilo, *International Journal of Fatigue*, 23: p. S375-S383, 2001.

White 1963 — White, R.M., Elastic wave generation by electron bombardment or electromagnetic wave absorption. *Journal of Applied Physics*, 34: p. 2123-2124, 1963.

Withers 2000 — Withers, P.J. and H.K.D.H. Bhadeshia, Residual stress: Part 1 - Measurement techniques. *Material Science and Technology*, 17: p. 355-365, 2000.

Withers 2001 — Withers, P.J. and P.J. Webster. Neutron and synchrotron x-ray scanning. *Strain*, 37(1):9–33, 2001.

Withers 2003 — Withers, P.J., Analysis of residual stress by diffraction using neutron and synchrotron radiation, in Use of synchrotron x-ray radiation for stress measurement, Taylor and Francis, 2003.

Withers 2003 — Withers P. J., *Analysis of residual stress by diffraction using neutron and synchrotron radiation*, Fitzpatrick, M.E. and A. Lodini , ed. CRC Press, 2003.

XDB 2001 — Thompson, A., et al., *X-ray Data Booklet*, Lawrence Berkeley Nation Laboratory, 2001.

Yin 2000 — Yin, Q. Residual Stresses in Unsymmetric Laminated Carbon Fiber Composites. in OSJ-SPIE Conference. Yokohama, 2000.

Zhang 2002 Zhang, Y., M.E. Fitzpatrick, and L. Edwards, Measurement of the Residual Stresses around a Cold Expanded Hole in an EN8 Steel Plate Using the Contour Method. *Materials Science Forum*, 404-407: p. 527-532, 2002.

Zhang 2003 Zhang, Y., *Numerical and Experimental Exploration of the Contour Method for Residual Stress Evaluation*. PhD thesis, Materials Science & Engineering,Open University, 2003.

Zhang 2004 Zhang, Y., et al., Cross-sectional mapping of residual stresses in a VPPA weld using the contour method. *Acta Materialia*, 52(17): p. 5225-5232, 2004.

Zhuang 2001 Zhuang, W.Z. and G.R. Halford, Investigation of residual stress relaxation under cyclic load. *International Journal of Fatigue*, 23: p. S31-S37, 2001.